Finite element modelling of grain-scale heterogeneities in polycrystalline aggregates

Héba Resk

▶ **To cite this version:**

École Doctorale n°364 : Sciences Fondamentales et Appliquées

Doctorat ParisTech

T H È S E

pour obtenir le grade de docteur délivré par

l'École nationale supérieure des mines de Paris

Spécialité « Mécanique Numérique »

présentée et soutenue publiquement par

Héba RESK

le 03 décembre 2010

Finite element modelling of grain-scale heterogeneities in polycrystalline aggregates

~ ~ ~

Modélisation par Éléments Finis des hétérogénéités à l'échelle granulaire au sein d'agrégats polycristallins

Directeur de thèse : **Thierry COUPEZ**
Co-encadrement de la thèse : **Roland LOGÉ**

Jury
L. DELANNAY, Professeur, iMMC, Université catholique de Louvain   Président
A. HAZOTTE , Professeur, LETAM, Université de Metz   Rapporteur
O. CASTELNAU , Directeur de recherche, PIMM, Arts et Métiers ParisTech   Rapporteur
T. COUPEZ, Professeur, CEMEF, MINES ParisTech   Examinateur
R. LOGÉ, Docteur, CEMEF, MINES ParisTech   Examinateur
M. BERNACKI, Docteur, CEMEF, MINES ParisTech   Examinateur

T
H
È
S
E

The Road Not Taken

Two roads diverged in a yellow wood,
And sorry I could not travel both
And be one traveler, long I stood
And looked down one as far as I could
To where it bent in the undergrowth;

Then took the other, as just as fair,
And having perhaps the better claim
Because it was grassy and wanted wear,
Though as for that the passing there
Had worn them really about the same,

And both that morning equally lay
In leaves no step had trodden black.
Oh, I marked the first for another day!
Yet knowing how way leads on to way
I doubted if I should ever come back.

I shall be telling this with a sigh
Somewhere ages and ages hence:
Two roads diverged in a wood, and I,
I took the one less traveled by,
And that has made all the difference.

Robert Frost, (1874 - 1963)

Acknowledgments

Understanding the physics of materials at the microscopic level has always fascinated me and I am very grateful to the Universe for completing my thesis work in this particularly challenging and interesting field. This work, would not have been possible though, without the contribution of a lot of people, who helped me, either on the professional or the personal level, or both.

My first acknowledgements go to the CEMEF and its directors, Jean-Loup Chenot and Yvan Chastel, for recruiting me and giving me the opportunity to achieve this work. Secondly, I would like to thank my thesis advisors Thierry Coupez and Roland Logé as well as my close collaborator Marc Bernacki, for helping me, each in their own way. I owe Thierry my sense of autonomy and my obsession for achieving a clear understanding of the problem at hand. I would like to thank him for his stinging, yet useful remarks, and for giving me the opportunity to be part of the CIM group. I would like to thank Roland for his valuable contributions, especially regarding the physics of the problem and for the numerous discussions we had. I really appreciate Marc's regular involvement and help in the more numerical aspects of this work. I am grateful for their complementary guidance.

I would like to express my thanks to the members of the jury of this thesis, Pr. Alain Hazotte, Dr. Olivier Castelnau and Pr. Laurent Delannay. Special thanks to Laurent for his contributions, help and support I would like to thank the EU for their funding and for allowing me to work with other scientists from European and American universities, who participated in the DIGIMAT project, namely the Centre des Matériaux (CDM) of Mines Paristech, Carnegie Mellon University (CMU), Eötvös University (ELTE), Princeton University and Imperial College (IC). Special mention to R. Quey for supplying the experimental data used in chapter 6.

I would like to thank Luisa Silva, Hugues Digonnet and Julien Bruchon of the CIM group for answering my numerous questions and for helping me achieve my goals. My appreciation goes also to all my former colleagues of the CIM group, who nourished my work. I would like to express my gratitude to all the CEMEF staff. Special mention to Gilbert Fiorucci, Bernard Triger, all people from the workshop for their lovely spirit, the IT department team (EII), who always solved my problems in a timely manner and the CEMEF's administrative director Patrick Coels for his availability. The Ladies of the CEMEF played an important role in making my life easier on campus, professionally and personally. Special thanks to Marie-Francoise, Sylvie,

Abstract

Macroscopic properties of crystalline solids depend inherently on their underlying microscopic structure. Studying the mechanisms operating at the microstructural scale during the various thermomechanical processes to which such materials may be subjected offers a valuable insight into their final in-use properties. The objective of this work is to investigate grain scale heterogeneities in polycrystalline aggregates subjected to large strains using the Crystal Plasticity Finite Element Method (CPFEM). For this purpose, highly resolved simulations, where each grain is represented explicitly, are needed. The first part of this work is devoted to a detailed account of the numerical framework implemented for such simulations. A classical elastic-viscoplastic crystal plasticity model is combined to a non-linear parallel finite element framework. The discretization of the digital microstructures is performed using non-conforming unstructured meshes. Most importantly, a level set approach is used to describe grain boundaries and to guide an adaptive anisotropic meshing strategy. Automatic remeshing, with appropriate transport of variables, is introduced in the proposed framework. In the second part of this work, the robustness and flexibility of our approach is demonstrated via different CPFEM applications. The deformation energy is used to assess heterogeneities in polycrystalline aggregates, highlighting the need to perform adaptive meshing so as to achieve a good compromise between accuracy and computation time. These grain-scale heterogeneities are to be accurately predicted during the deformation simulation if subsequent static recrystallization modelling is to be performed. An example of linking between the deformation and static recrystallization steps, using the proposed common approach, is illustrated. In terms of global texture predictions, the CPFEM framework is validated for a highly resolved model polycrystal subjected to more than 90 % thickness reduction in rolling. The importance of automatic remeshing in avoiding excessive mesh distortion, in such applications, is demonstrated. Most importantly, microtexture analysis is performed on digital microstructures that correspond, in a discrete sense, to an actual microstructure observed experimentally. Intragranular misorientation predictions and virtual 2D orientation maps are compared to the experimental ones, highlighting the difficulties pertaining to the validation of such grain-scale predictions.

Résumé

Les matériaux cristallins, notamment métalliques, sont des matériaux hétérogènes. Leurs propriétés macroscopiques sont fondamentalement déterminées par leurs caractéristiques microstructurales. L'étude des mécanismes opérant à l'échelle du grain permet de mieux comprendre et ainsi mieux contrôler les caractéristiques des pièces fabriquées afin de réduire leur coût et optimiser leur performance.

Cette thèse s'inscrit dans le cadre de la méthode dite "CPFEM" qui couple la plasticité cristalline à la méthode des Éléments finis (EF). L'objectif de ce travail est d'étudier les hétérogénéités à l'échelle du grain au sein d'agrégats polycristallins soumis à de grandes déformations. Pour ce faire, une représentation explicite de la microstructure est nécessaire. Le travail réalisé, ainsi que ce manuscrit, s'articule autour de deux axes principaux: (i) la mise en place d'un cadre numérique robuste adapté à des calculs intensifs en grandes déformations; (ii) la validation de ce cadre à travers différents cas tests, qui permettent, notamment, d'étudier les hétérogénéités locales.

Dans le chapitre 2, le comportement du matériau est modélisé par une loi élastoviscoplastique cristalline, qui ne prend cependant pas en compte le développement d'une sous-structure dans sa formulation. Cette loi est couplée à une formulation EF mixte en vitesse pression. L'approche EF, détaillée dans le chapitre 3, peut être considérée comme le modèle polycristallin idéal vu le respect, au sens numérique faible, de l'équilibre des contraintes et la compatibilité des déformations. Dans le chapitre 4, l'approche utilisée pour construire, représenter et discrétiser un volume polycristallin est détaillée. La microstructure est représentée, soit par des polyèdres de Voronoi, soit par des voxels, si elle est construite à partir de données expérimentales. L'agrégat polycristallin est discrétisé avec une approche "monolithique", où un seul maillage, non structuré et non-conforme aux interfaces entre les grains, est utilisé. Une approche level set permet alors de décrire l'interface entre les grains de façon implicite et sert de base pour la construction d'un maillage adaptatif anisotrope. Le remaillage, avec un transport approprié des variables du problème, se fait de façon naturelle et automatique si la carte de métrique, associée au maillage, est calculée avant la procédure de remaillage.

Dans le chapitre 5, les hétérogénéités inter- et intragranulaire sont appréhendées à travers une étude de la distribution d'une fraction de l'énergie de déformation. Cette fraction est considérée, dans une première approche, comme étant représentative de l'énergie stockée durant

la déformation. Une analyse de sensibilité, au degré et au type de maillage utilisé, permet de mettre en évidence l'apport d'une stratégie de maillage anisotrope. Ces données locales sont particulièrement importantes à calculer lors de la déformation d'agrégats polycrystallins si l'objectif est de modéliser le phénomène de recristallisation statique qui suit l'étape de déformation. Un cas test 3D permet d'illustrer le cha"nage de la simulation de la déformation et de la recristallisation, toutes deux réalisées dans le même cadre numérique.

Dans le chapitre 6, notre approche numérique est, dans un premier temps, validée à l'aide d'un cas test de laminage pour un polycrystal statistiquement représentatif d'une texture expérimentale. Une réduction d'épaisseur de plus de 90 % est réalisée. Le remaillage, dans ce type d'application, s'avère plus que nécessaire. Dans la seconde partie de ce chapitre, une étude approfondie de la microtexture, développée au sein de microstructures virtuelles, est effectuée. Dans ce cas, ces microstructures "digitales" correspondent à une microstructure réelle dans un sens discret. Les prédictions de désorientations, d'orientations cristallographiques moyennes ainsi que les cartes d'orientation 2D virtuelles, sont comparés à l'expérience à l'échelle de chaque grain, mettant ainsi en évidence les facteurs à l'origine de certaines des différences observées.

Contents

Chapter 1

Introduction

I   Micromechanical modelling of polycrystalline materials

Metallic materials exhibit a crystalline structure and are in essence heterogeneous materials. They are in fact polycrystals, composed of several crystals or grains. These latter are defined as regions of continuous lattice orientation. At a lower scale, as seen on figure 1.1, one finds dislocations, which are linear defects in the crystal lattice, which is otherwise a perfect arrangement of atoms.

| Sample | Polycrystal | Crystals | Dislocations | Atoms |
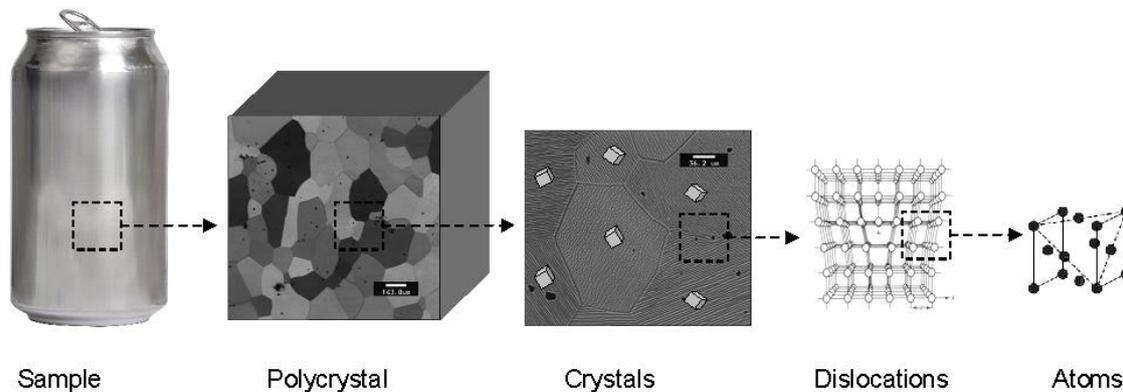
Fig. 1.1: From sample level to atoms

Crystal plasticity theory [Kocks, 1998a] provides a first level of linking between macroscopic properties and microscopic features (crystallographic orientation...). It is intended to represent the behavior of polycrystals at the mesoscopic scale without modelling explicitly the motion of individual dislocations or individual atoms, which are the concern of dislocation dynamics models and atomistic models. During processing, metallic parts are subjected to various thermomechanical treatments. Microstructural evolution triggered by plastic deformation and/or recrystallization determine the final in-use properties of these components. The motivation behind the micromechanical modelling of polycrystalline metallic materials, based on crystal plasticity is twofold:

- from a technological point of view, assist the design of thermomechanical processes by taking into consideration these microstructural features, such as crystallographic orientation, in order to account for macroscopic anisotropic behavior such as the earing in deep-drawn aluminum cans (fig. 1.2),

- from a more fundamental point of view, increase our understanding of the mechanisms operating at the microstructural scale.

Fig. 1.2: Earing in aluminum cans [AluMATTER, 2009]

Although first simulations based on crystal plasticity were initiated a while ago, with the pioneering work of Pierce and co-workers [Peirce et al., 1982, 1983], their added-value for the understanding of macroscopic anisotropy has not been fully apprehended as their development is directly linked to improvements in computational methods and optimization of computational resources. In real-scale Finite Element (FE) simulations of metal forming processes like in figure 1.3(a), each material point (integration point) represents a set of crystals i.e orientations with no account for topological arrangement of grains or for their shapes. In such formulations, a polycrystal model is needed in order to link the micro and the macro scales. The chosen transition rule could be more or less satisfactory in terms of deformation compatibility and stress equilibrium, depending on the way the interaction between the grains is accounted for. These two-level models are then used in much the same way as any other macroscopic constitutive law, but providing better predictions of the final mechanical properties of the sample [Dawson et al., 1994; Delannay et al., 2005; Kalidindi et al., 1992].

Crystal plasticity theory can also be used in "small scale" FE simulations, in which the grains are represented explicitly (fig. 1.3(b)). In this case, the microstructure could either represent a model polycrystal in a statistical sense, or, in some specific cases, an actual microstructure observed experimentally. Small scale FE simulations can be assimilated to in-situ observations performed during virtual mechanical testing. They can be very useful for studying the local micro-mechanical fields that develop within a polycrystalline aggregate subjected to loading. It should be noted that a relatively recent approach based on the Fast Fourier Transform (FFT) algorithm has been adapted to compute the deformation of viscoplastic 2D and 3D polycrystals [Lebensohn et al., 2008, 2005]. This approach seems to be a viable alternative to the FEM but is however limited to viscoplastic behaviors. Other limitations associated with

this approach are the boundary conditions, which are are necessarily periodic, and the mesh (structured grid) which does not deform. The FEM remains the most widely used procedure in the domain of small scale crystal plasticity simulations due to its versatility and robustness. Compared to polycrystal models, the FE approach does not obviously require a transition rule, as the scale at which the simulation is performed is actually the grain's scale. The Crystal Plasticity Finite Element Method, also known as CPFEM, has been used extensively in the last two decades[BATE, 1999]. Numerous examples are found in the literature [BARBE et al., 2001a,b; MIKA and DAWSON, 1998; SARMA et al., 2002] and could be differentiated on the basis of, on the one hand, their intended objectives and, on the other hand, the crystal plasticity models, the FE formulation and the numerical tools used to represent and mesh the microstructure. Due to its inherent nature, FE results are obviously quite sensitive to microstructure representation and mesh discretization. Depending on the intended objectives and the computational limitations, the use of different numerical strategies is justified. In effect, one can be interested in several types of analyses, which can be classified in two main categories:(i) predicting the global response of the polycrystal such as the stress-strain curve or the ODF or other global texture evolution measurements; (ii) focusing on the local heterogeneities of stress, strain and lattice orientation . It should be noted that care should be taken while interpreting the huge amount of microstructural data that can be extracted from such simulations. The presence of a large variety of approaches could hinder the formulation of general conclusions. This is all the more true because of the difficulties pertaining to the validation of such micromechanical predictions against experimental measurements.

(a) (b)
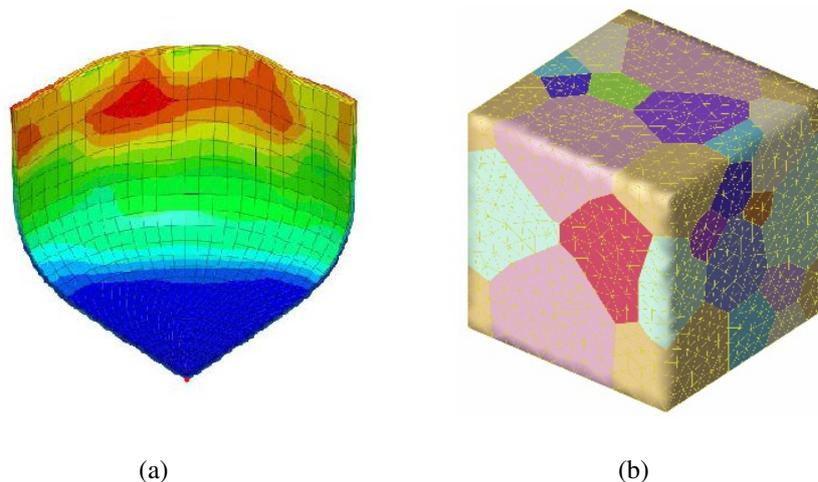
Fig. 1.3: Real-scale and small scale FE simulations: (a) simulation of deep drawing process using polycrystal plasticity [ROUSSELIER et al., 2009]; (b) A meshed polycrystal made of 17 grains [MANIATTY et al., 2007]

II Experimental characterization and investigation at the grain scale: the limits

The validation of the results of small scale simulations entails first the ability to generate virtual 3D microstructures that correspond to the real microstructures and then to compare the numerical predictions to relevant experimental results. The construction of the microstructure is in fact a challenge, whether the digital microstructure is intended to represent a model polycrystal or an actual microstructure observed experimentally. Two distinct but complementary types of information are needed to fully describe a polycrystal: geometric features regarding grain morphology and topology and the corresponding spatial distribution of physical quantities like the crystallographic orientation. In the case of a model polycrystal, the digital microstructure is considered representative of the real material if it contains a sufficient number of grains and if it matches the real material in a statistical sense both in its geometrical (morphology-topology) features and in the spatial sampling of its physical attributes. In the case of an exact microstructure replicate, these microstructural features have to be respected in a discrete and exact sense. While the numerical algorithms needed to fit experimental data are far from being perfect [BHANDARI et al., 2007; ROLLETT et al., 2007], the first limiting factor regarding the construction of digital polycrystals lies in the actual 3D characterization of the microstructure before deformation and whether or not such characterization is destructive. There are essentially two methods available nowadays for characterizing microstructures in 3D: 2D sectioning based on electron back-scatter diffraction (EBSD), also known as orientation imaging microscopy (OIM), and 3D X-ray diffraction (3DXRD) microscopy.
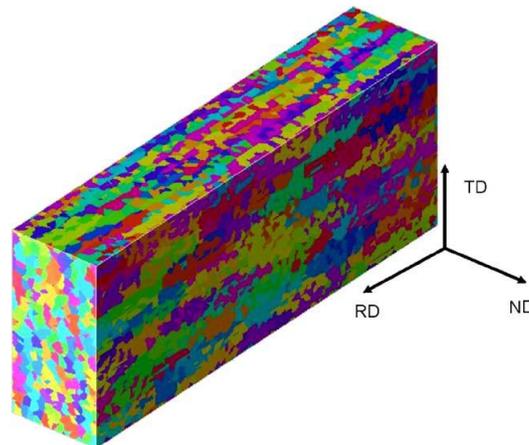
Fig. 1.4: Example of a model polycrystal: voxelization of a rolled microstructure including crystallographic orientation data based on the Microstructure Builder approach (Carnegie Mellon University) [BRAHME et al., 2006]

In orientation imaging microscopy, thin successive layers of the material are polished and scanned using EBSD and the obtained regular pixelized grids are then assembled to obtain the

final 3D microstructure [ERIEAU, 2003; GOSH et al., 2008]. Without dwelling on the difficulties pertaining to the alignement of the successive layers, the major drawback of such technique is related to its destructive nature. In the same vein, the Microstructure Builder approach [BRAHME et al., 2006] is based on EBSD scans of two orthogonal planes (fig. 1.4). While this approach optimizes the scanning effort, it is only pertinent if the digital microstructure is to represent a model polycrystal. Indeed, if this is the objective, then the destructive nature of these two methods are insignificant as the simulation predictions can be compared to any other specimen of the same polycrystal. On the other hand, in the case of "real" microstructures, researchers have also used EBSD scans in order to follow the same set of grains before and after deformation. Due to the 2D nature of the scans, these studies were sometimes limited to multicrystalline specimens, where the microstructure is essentially composed of one layer of crystals [DELAIRE et al., 2000; KALIDINDI et al., 2004]. In other cases, authors have confined their investigations to the layer located on the free surface of the specimens [BUCHHEIT et al., 2005; LEBENSOHN et al., 2008] while "guessing" the rest of the microstructure. The split sample method, originally introduced in the early 40's [BARRETT and LEVENSON, 1940] and more recently adapted and perfected to channel die compression [PANCHANADEESWARAN et al., 1996; QUEY, 2009], is used to follow the grains in the bulk of the polycrystalline specimens. Nevertheless, the indetermination regarding the surrounding microstructure remains a problem if 3D simulations are compared to such measurements.

3D X-ray diffraction microscopy (fig. 1.5) is a non destructive technique currently used to follow grains in the bulk of millimeter-centimeter thick polycrystals [SØRENSEN et al., 2006]. This tool can be considered as state-of-the-art technique in the characterization of grains and sub-grains. It has been used to follow grain growth in annealed specimens [SØRENSEN et al., 2006] and the deformation of grains inside specimens subjected to relatively low strains [POULSEN et al., 2003]. The low strain limitation is due to the fact that all the grains diffract at the same time and excessive grain fragmentation leads to overlapping of diffraction spots.
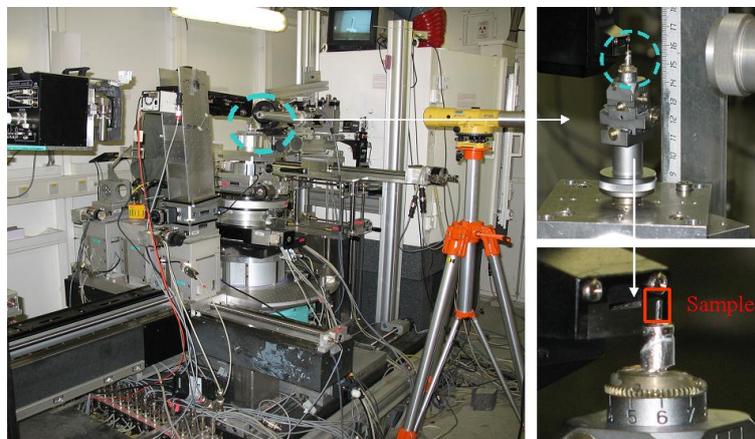
Fig. 1.5: 3DXRD microscope stationed at the ESRF beamline ID11 in Grenoble, France

III   Objectives of the present work and thesis outline

In this work, a CPFEM modelling strategy is used to approach the micromechanics of polycrystalline aggregates. In *Chapter 2*, modeling assumptions about single crystal behavior are reviewed briefly before presenting the actual single crystal model used in this study, thus highlighting the limits of the chosen approach. The model used is a classical elastic-viscoplastic formulation that satisfies the basic objective of taking into account crystal plasticity theory while minimizing the important computational cost that could be associated with a more complex model.

Given the behavior of the single crystal, the different ways to account for the behavior of the polycrystal are reviewed in *Chapter 3*, namely classical polycrystal plasticity theory and more advanced models that strive to fill the gap between the actual physics behind grain deformation and the simplified modelling assumptions of classical models. In that scope, the FE approach is presented as a limiting case as no assumption is made about grain interaction. Different FE formulations found throughout the literature are briefly reviewed before presenting the framework used in this work, whereby 3D polycrystals are deformed using an updated Lagrangian scheme. This framework is implemented in a parallel multi-component C++ library, called CimLib, developed in CEMEF [Digonnet et al., 2007].

Generating and meshing the microstructure is a pre-requisite for performing FE simulations. In *Chapter 4*, different meshing strategies are highlighted. In this work, a specific approach is introduced, namely an unstructured "monolithic" mesh is used, not necessarily conforming to actual grain boundaries, while a level set framework is used to implicitly locate grains. Adaptive meshing techniques, based on this level set description, is used to define precisely the interfaces of the grains while optimizing computation time. Most importantly, automatic remeshing is introduced as a necessary tool for reaching important strains (true strain > 1). Such strains are typically encountered in metal forming processes like rolling for example.

In *Chapter 5*, applications of the proposed framework for the investigation of local stress and strain heterogeneities is illustrated. The deformation energy measure is used as a parameter to assess such heterogeneities. Energy that is stored in the material during deformation is the driving force for further microstructural evolution that takes place during deformation or annealing. Dynamic or static recrystallization phenomena inevitably occur. Complex multi-scale models are in theory necessary for accurately describing the deformation and the associated recrystallization phenomena [Logé et al., 2008]. However, before moving to such complicated schemes, one of the first bottleneck to overcome is the ability to transpose all the deformation simulation results to the recrystallization simulation. In *Chapter 5*, such linking between deformation simulation and recrystallization simulation is illustrated. The common numerical framework used for both is shown to be an elegant way of achieving this.

One typical objective of CPFEM simulations is deformation texture prediction. In *Chap-*

ter 6, a brief overview of crystallographic texture measures and representations is given. Global texture prediction ("macrotexture") is investigated in a model polycrystal deformed by plain strain compression up to 90 % thickness reduction. Such strain levels can only be obtained if proper remeshing operations are performed at regular intervals. The rest of the chapter is dedicated to the investigation of lattice orientation heterogeneities in an experimental microstructure deformed by channel die compression. The experimental part of this investigation has been performed by R. Quey from the Ecole Nationale Supérieure des Mines de Saint Etienne [QUEY, 2009] who followed the microtexture evolution of individual grains in the bulk of a polycrystalline aluminum sample. One of the objectives of this chapter is to evaluate the ability of our CPFEM framework to allow the construction of the "equivalent" virtual test and to assess its microtexture predicting capability. Different assumptions are made on the constitutive behavior of the surrounding material due to the lack of experimental data. Highly resolved 3D simulations are performed and the OIM software is used to probe a slice of the virtual specimen. Virtual OIM maps are compared to experimental ones and a discussion is held on the topological distribution of orientation gradients and the possibility to predict them with a standard crystal plasticity based constitutive law.

This work is part of the DIGIMAT project (EU/NSF) which aims at developing a framework for a thorough understanding and simulation of static recrystallization. Other academic partners include Centre des Matériaux (CDM) of Mines Paristech, Carnegie Mellon University (CMU), Eötvös University (ELTE), Princeton University and Imperial College (IC). The work in this thesis has contributed to the following written communications:

- LOGÉ, R., RESK, H., SUN, Z., DELANNAY, L., and BERNACKI, M. (2010). Modelling plastic deformation and recrystallization of polycrystals using digital micro-structures and adaptive meshing techniques. In *Proceedings Metal Forming 2010, submitted for publication in Steel Research international*

- RESK, H., DELANNAY, L., BERNACKI, M., COUPEZ, T., and LOGÉ, R. (2009). Adaptive mesh refinement and automatic remeshing in crystal plasticity finite element simulations. *Modelling and Simulation in Materials Science and Engineering*, 17(7):075012

- BERNACKI, M., RESK, H., COUPEZ, T., and LOGÉ, R. (2009). Finite element model of primary recrystallization in polycrystalline aggregates using a level set framework. *Modelling and Simulation in Materials Science and Engineering*, 17(6):064006

- LOGÉ, R., BERNACKI, M., RESK, H., DELANNAY, L., DIGONNET, H., CHASTEL, Y., and COUPEZ, T. (2008). Linking plastic deformation to recrystallization in metals using digital microstructures. *Philosophical Magazine*, 88(30):3691–3712

- BERNACKI, M., CHASTEL, Y., DIGONNET, H., RESK, H., COUPEZ, T., and LOGÉ, R. (2007a). Development of numerical tools for the multiscale modelling of recrystallization in metals based on a digital material framework. *Computer Methods in Material Science*, 7:142–149

- BERNACKI, M., DIGONNET, H., RESK, H., COUPEZ, T., and LOGÉ, R. (2007b). Development of numerical tools for the multiscale modelling of recrystallization in metals, based on a digital material framework. In *Materials Processing and Design: Modeling, Simulation and Applications, AIP conference proceedings, NUMIFORM 2007*, volume 908, pages 375–380, Porto, Portugal

and the following oral communications:

- RESK, H., BERNACKI, M., CHASTEL, Y., COUPEZ, T., DELANNAY, L., and R.LOGÉ (2008a). Numerical modelling of plastic deformation and subsequent primary recrystallization in a polycrystalline volume element, based on a level set framework. In *WCCM8-ECCOMAS 2008*, Venice, Italy

- RESK, H., BERNACKI, M., COUPEZ, T., DELANNAY, L., and R.LOGÉ (2008b). Adaptive mesh refinement in crystal plasticity finite element simulations of large deformations in polycrystalline aggregates. In *ICOTOM 15*, Pittsburgh PA, USA

Chapter 2

Single crystal plasticity

In crystal plasticity theory, plastic deformation is modelled using the slip system activity concept. Dislocations are assumed to move across the crystal lattice along specific crystallographic planes and directions. As the material is subjected to loading, the applied stress resolved along the slip direction on the slip plane initiates and controls the extent of dislocation glide. This latter has the effect of shearing the material, while the volume remains constant and the crystal lattice remains unchanged. Moreover, the crystal lattice can deform elastically, but elastic strains are small compared to plastic strains and are sometimes neglected in crystal plasticity models. Finally, the crystal lattice can also rotate to accommodate the applied loading. This lattice rotation (or spin), is responsible for texture development. The concept of lattice rotation in crystal plasticity is not, at first hand, easy to grasp, especially compared to material rotation (or rigid body rotation). [PEETERS et al., 2001] illustrate well this fundamental difference with figure 2.1.
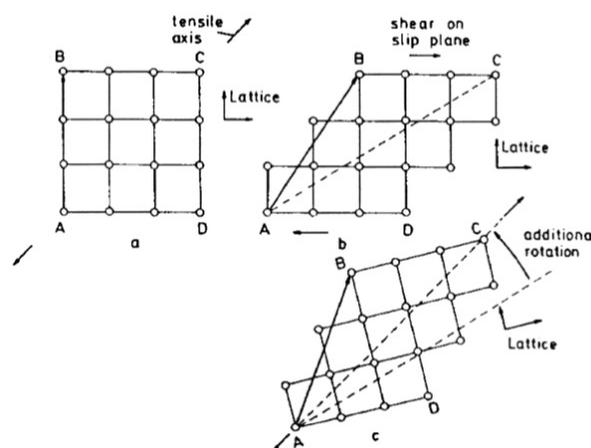
Fig. 2.1: "(a) and (b) A shear γ on a slip plane does not cause the lattice to rotate, although a material vector may rotate; (b) and (c) An additional rotation - which also causes the crystal lattice to rotate - will bring the crystal in a position corresponding to the strain forced upon it: e.g. pure elongation in the direction AC" [PEETERS et al., 2001]

These considerations form the basics of classical crystal plasticity theory. Other modes of deformation in polycrystals like twinning or grain boundary sliding are not tackled in this discussion. Also, more recent concepts in crystal plasticity modelling, attempting to account for the discrete nature of dislocation glide (*non-local theory*) are briefly highlighted in section III.4.

I   Components of a single crystal model

In order to account for the mechanics of grain structure heterogeneous deformation, crystal plasticity models are based on microstructural variables such as crystallographic orientation or dislocation densities. Polycrystal models are based on single crystal models as illustrated by figure 2.2 and are discussed in the next chapter.
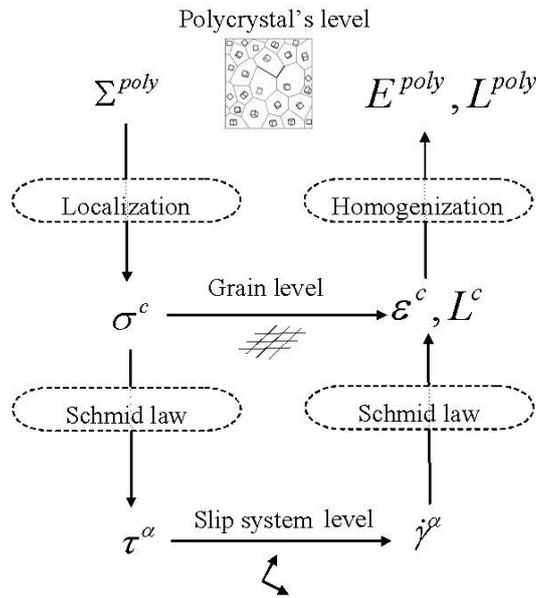
Fig. 2.2: From Polycrystal level to slip system level

In order to describe the behavior of a single crystal, three components are needed:

1. A kinematic framework describing the motion of the single crystal. The kinematic decomposition used in crystal plasticity is in the majority of models a multiplicative decomposition as opposed to an additive decomposition which is generally used for small deformations [Shabana, 2008]. In classical plasticity theory, if the elastic behavior is considered, the decomposition is composed of a plastic and an elastic term.

2. Elastic relations describing the elastic behavior depending on the crystal structure of the material. Elastic strains are small compared to plastic ones but are sometimes important to consider if the objective of the simulations is to compute residual stresses for example [Marin and Dawson, 1998a]. The assumption of small elastic strains enables nevertheless

simplifications in the governing equations [M$_{\text{ARIN}}$ and D$_{\text{AWSON}}$, 1998b]. In other applications where elasticity is not a concern, the elastic behavior is neglected [B$_{\text{EAUDOIN}}$ et al., 1995].

3. Evolution rules for the intragranular variables of the model, namely a flow rule and a hardening rule. Different forms of these equations can be found in the literature and a brief overview is given in this section.

II   Flow rule

The Schmid law [S$_{\text{CHMID}}$ and B$_{\text{OAS}}$, 1935] determines the resolved stress on slip system α ,i.e the shear stress τ^α as follows:

$$\tau^\alpha = \boldsymbol{T} : \boldsymbol{M}^\alpha = \boldsymbol{T} : (\boldsymbol{b}^\alpha \otimes \boldsymbol{n}^\alpha)_{Sym} \quad , \tag{2.1}$$

where $\boldsymbol{T}$ is the applied stress, $\boldsymbol{b}^\alpha$ is the slip direction, $\boldsymbol{n}^\alpha$ is the slip plane normal, $\boldsymbol{M}^\alpha$ is the Schmid tensor which is the symmetric part of the orientation tensor $\boldsymbol{t}^\alpha = (\boldsymbol{b}^\alpha \otimes \boldsymbol{n}^\alpha)$.

II.1   Ideal plastic flow

At low homologous temperatures, the behavior of single crystals is assumed to be ideally plastic. In this case, the flow is modelled using the Schmid yield criterion. The Schmid yield criterion or the "generalized Schmid law" postulates that yield occurs on a given slip system α if the resolved stress on this slip system (τ^α) reaches a critical value (τ_c^α) [K$_{\text{OCKS}}$, 1998a]. It can be expressed as follows:

$$\left.\begin{array}{l} \tau^\alpha = \tau_c^\alpha \\ \dot{\tau}^\alpha > 0 \end{array}\right\} \Rightarrow \dot{\gamma}^\alpha > 0 \quad . \tag{2.2}$$

where $\dot{\gamma}^\alpha$ is the slip rate for slip system α. This yield criterion defines a yield surface which indicates the direction in which the flow occurs, i.e the straining direction, for a given stress state. The yield surface is in fact a five dimensional convex polyhedron in stress space, with each facet corresponding to the activation of a single slip system. Straining occurs along the normal to the facets of this polyhedron. At the vertices, the straining direction is undetermined and is bounded by the normals to the facets intersecting at those vertices. Figure 2.3 illustrates the concept in a 2D projection of the stress space.
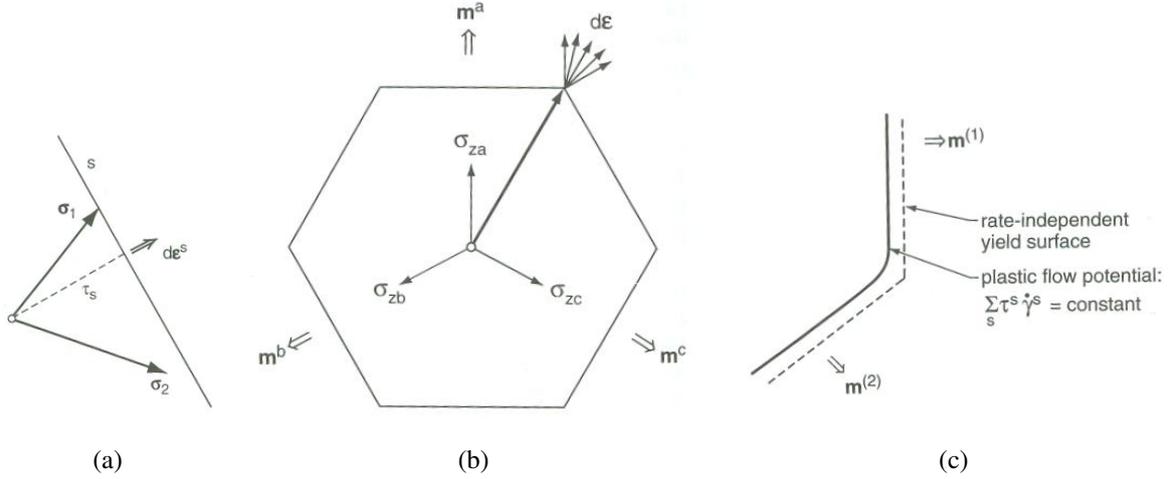
Fig. 2.3: 2D projection of yield surface in stress space (a) single slip representation; (b) multiple slip representation;(c) rate independent vs rate dependent plasticity [Kocks, 1998a]. Here s stands for slip system and m is the Schmid tensor

The vertices correspond to a case where more than one slip system is activated, i.e a case of multiple slip. In Taylor's analysis [Taylor, 1938], five independent slip systems are in fact required to accommodate a given deformation rate (taking into consideration the incompressibility condition). Taylor also proposed a way of solving the indetermination regarding the straining direction, i.e regarding the selection of the active slip systems that operate for a given vertex stress state. Assuming that all slip systems have the same initial critical resolved shear stress and that they all harden equally, he postulated that the active slip systems are the ones which minimize the energy dissipated during slip (minimum internal work principle). This can be formulated as follows:

$$\sum_{\alpha} \tau^{\alpha} |\dot{\gamma}^{\alpha}| \leq \sum_{\alpha} \tau^{\alpha} |\dot{\gamma}^{\alpha*}| , \tag{2.3}$$

$$\sum_{\alpha} |\dot{\gamma}^{\alpha}| \leq \sum_{\alpha} |\dot{\gamma}^{\alpha*}| , \tag{2.4}$$

where $\dot{\gamma}^{\alpha*}$ is any possible set of slips satisfying the incompressibility condition.

Later on, in order to solve the same indetermination, Bishop and Hill looked at the problem from the stress point of view, i.e one is to find the stress state that allows for multiple slip. In their analysis, the "correct" stress σ is the one that maximizes plastic work (maximum work principle). This can be formulated as follows:

$$(\sigma - \sigma^*) : E \geq 0 , \tag{2.5}$$

where E is the applied strain tensor and σ^* is any possible stress state that activates a minimum of five slip systems. It has been shown that Taylor's minimimum internal work principle is actually equivalent to the maximization principle of the plastic work but only if hardening is taken equal for all slip systems [Bishop and Hill, 1951]. For this reason, Taylor's analysis and Bishop and Hill's analysis are described as the "Taylor-Bishop-Hill model".

Ideal plasticity, also known as multi-surface plasticity or "rate independent plasticity", has been used since in numerical applications [Anand and Kothari, 1996; Knockaert et al., 2000; Peirce et al., 1982; Schmidt-Baldassari, 2003]. Robust numerical procedures are needed for selecting the active slip systems and avoiding singular matrices related to the non-uniqueness of the set of active slip systems. Additional constitutive assumptions are also needed to compute the actual amount of slip on the selected systems. It is important to mention that the robustness of the numerical schemes used in rate independent formulations depends on the chosen hardening law, which completes the constitutive framework [Busso and Cailletaud, 2005], and is discussed in section III.

II.2   Viscoplastic flow

Two reasons motivate the use of a viscoplastic form for the flow rule: (i) describing the behavior of metals exhibiting rate sensitivity, especially in applications where localization phenomena is studied, (ii) avoiding the previously mentioned difficulties associated with rate independence . As seen on figure 2.3(c), the use of a rate dependent formulation has the effect of rounding the yield surface, thus avoiding the vertex indetermination. Typically, the viscoplastic behavior is described by an exponential law, first introduced by [Hutchinson, 1977]:

$$\dot{\gamma}^{\alpha} = \dot{\gamma}_0 \left| \frac{\tau^{\alpha}}{\tau_c^{\alpha}} \right|^{1/m} sign(\tau^{\alpha}) \, , \tag{2.6}$$

where τ^{α} is the resolved shear stress, $\dot{\gamma}_0$ is a reference slip rate, m the rate sensitivity exponent, and τ_c^{α} the critical resolved shear stress for slip system α. Clearly, this expression assumes that all slip systems are active and the slip rates (slip increments) are directly determined. Rate independence corresponds to the limiting case when $m \to 0$ and can therefore be theoretically approximated using this expression. Nevertheless it is worth mentioning that, when m is very small, the convergence of the numerical integration scheme of the constitutive equations is more difficult as highlighted by [Anand and Kothari, 1996]. The computational costs of a rate dependent formulation compared to the rate independent one could therefore be more important [Delannay et al., 2002] depending on the adopted value of m.

Equation 2.6 has been frequently used since [Delannay et al., 2006; Erieau and Rey, 2004; Marin and Dawson, 1998b]. This type of flow rule can also be expressed in terms of variables such as dislocation densities thus relating it to more elementary physical mechanisms of the theory of crystal plasticity [Fivel, 1997]. In the same vein, [Cheong and Busso, 2004; Cheong et al., 2005] base their flow rule on the thermally activated motion of dislocations:

$$\dot{\gamma}^{\alpha} = \dot{\gamma}_0 \left[-\frac{F_0}{\kappa T} \left(1 - \left\langle \frac{|\tau^{\alpha}| - S^{\alpha}\mu/\mu_0}{\hat{\tau}_0\mu/\mu_0} \right\rangle^p \right)^q \right] sign(\tau^{\alpha}) \, , \tag{2.7}$$

where S^{α} is the total slip resistance to dislocation motion, μ/μ_0 is the shear moduli ratio at the absolute temperature θ and 0 K, F_0 is the Helmholtz free energy of activation, κ the Boltzmann constant, $\hat{\tau}_0$ is the maximum lattice friction resistance and p and q sensitivity exponents.

From a more phenomenological perspective, the flow rule introduced by [Cailletaud, 1987] and used later on by several authors [Barbe et al., 2001a; Diard et al., 2005], is given by:

$$\dot{\gamma}^\alpha = \left\langle \frac{|\tau^\alpha - x^\alpha| - r^\alpha}{K} \right\rangle^{1/m} sign(\tau^\alpha - x^\alpha) \, , \tag{2.8}$$

where K is a material parameter, r^α is an isotropic hardening variable and x^α is a kinematic hardening variable.

III   Hardening

In order to complete the constitutive framework, hardening has to be taken into account. The hardening rule represents the strain-induced evolution of the material resistance to plastic deformation. It can take the following generic expression:

$$\dot{\tau}_c^\alpha = \sum_\beta h^{\alpha\beta} \left| \dot{\gamma}^\beta \right| \, , \tag{2.9}$$

where the $h^{\alpha\beta}$ terms are the components of the hardening (modulus) matrix. The hardening (modulus) matrix reflects the dependence of hardening upon the history of slip, more specifically on the shearing rate on the different slip systems. The diagonal terms $h^{\alpha\alpha}$ account for the hardening of slip system α due to its own slip activity, i.e. self-hardening. The off-diagonal elements $h^{\alpha\beta}|_{\alpha\neq\beta}$ reflect the hardening of slip system α due to the slip activity on the slip system β, i.e latent hardening. The hardening matrix can have different forms depending on the actual physical mechanisms and phenomenological behaviors that are accounted for and the simplifying assumptions adopted. Proportional and latent hardening are presented below. More elaborate expressions including kinematic hardening and gradient effects are then briefly discussed.

III.1   Proportional hardening

An example of proportional hardening is Taylor's model. In this latter, all components of the hardening matrix are taken equal and are constant over time:

$$h^{\alpha\beta} = h \, . \tag{2.10}$$

The hardening is said to be isotropic as all system harden at the same rate (isotropic hardening). More specifically, in Taylor's original work, the critical resolved shear stress was taken equal for all systems, making the hardening actually proportional (i.e the single crystal yield surface only changes size : there is no motion or shape change). These assumptions do not actually reflect the phenomenology of hardening in single crystals. Hardening is not constant as the deformation proceeds and data from single crystal experiments have shown that latent hardening rate could sometimes be higher than the self hardening one [Jackson and Basinski, 1967; Kocks and Brown, 1966].

III.2   Latent hardening

One way of differentiating self and latent hardening effects is by taking the latent harden-ing terms to be proportional to the self hardening ones, which are in general specified. A simple hardening model is then given by:

$$h^{\alpha\alpha} = h \quad \text{and} \quad h^{\alpha\beta} = qh \quad \text{if } \alpha \neq \beta \,. \tag{2.11}$$

The parameter q is termed the latent hardening ratio and it is generally defined as a constant in the range $1.0 < q < 1.4$ which seems to encompass much of the experimentally measured data [PEIRCE et al., 1983] although experimental investigations have shown that q evolves with the deformation [FRANCIOSI et al., 1980]. In [PEIRCE et al., 1983], the common term h is given by:

$$h = h(\gamma_{cum}) = h_0 sec^2 \left(\frac{h_0 \gamma_{cum}}{\tau_{sat} - \tau_0} \right) \,, \tag{2.12}$$

where h_0 is a hardening coefficient, τ_0 and τ_{sat} represent the initial and the saturation values of τ_c. The term τ_0 is generally taken equal for all slip systems as it is actually quite difficult to experimentally identify the initial strength of the individual slip systems. The term γ_{cum} is the accumulated slip defined by:

$$\gamma_{cum} = \int_0^t \sum_\alpha |\dot{\gamma}^\alpha| \, dt \,. \tag{2.13}$$

Latent hardening is reflected in the anisotropic evolution of the yield surface. Besides the fact that it affects the slip system hardenesses, it also has a more or less important impact on the global mechanical response of the polycrystal and on texture predictions as it influences "tex-ture" or "geometric" hardening [BASSANI, 1994; MILLER and DAWSON, 1997].

III.3   Including kinematic hardening

As mentioned previously in section II.2, [CAILLETAUD, 1987] included in his model not only an isotropic hardening variable r^α, but also a kinematic one x^α:

$$\begin{cases} r^\alpha = r_0 + Q^\alpha \sum_\beta h^{\alpha\beta} \left(1 - e^{-b\gamma_{cum}} \right) \,, \\ x^\alpha = cs^\alpha \qquad \text{with } \dot{s}^\alpha = \dot{\gamma}^\alpha - ds^\alpha |\dot{\gamma}^\alpha| \,, \end{cases} \tag{2.14}$$

where r_0, Q^α, b, c and d are material-dependent parameters. Clearly, the use of a kinematic variable accounts for kinematic hardening (which is translated as a shift of the single crystal yield surface). The saturation of hardening could therefore be described not only during mono-tonic but also cyclic loading. Besides, latent hardening effects are taken into account via the coefficients Q^α and the interaction matrix $h^{\alpha\beta}$ which is constant. It is worth mentioning that these terms appear only in the expression of the isotropic variable r^α as the Bauschinger effect is not generally related to the interaction between slip systems, but is linked to the interaction of each individual slip system with its environment.

III.4 Using dislocation densities and including gradient effects

In the same way as for the flow rule, hardening models can be more physically-based if expressed in terms of dislocation densities and if the basic mechanisms of dislocation generation and annihilation are considered. Moreover, strain gradient concepts, which account for example for size-dependent effects, can be introduced directly at the level of the hardening model. For this purpose [CHEONG et al., 2005](see section II.2 for the flow rule) define the total dislocation density on slip system α as:

$$\rho_T^\alpha = \rho_S^\alpha + \rho_G^\alpha \,. \tag{2.15}$$

In this expression, ρ_S^α and ρ_G^α refers to statistically stored dislocations (SSD) and geometrically necessary dislocations (GND) respectively. As expressed in [FLECK et al., 1994], which reported experimental evidence of size-dependent effects, "dislocations become stored for two reasons : they accumulate by trapping each other in a random way or they are required for compatible deformation of various parts of the crystal. The dislocations which trap each other randomly are referred to as statistically stored dislocations ... gradients of plastic shear result in the storage of geometrically necessary dislocations". These dislocations contribute to the total slip resistance S^α as follows:

$$S^\alpha = \lambda \mu_0 b^\alpha \sqrt{\sum_\beta h_S^{\alpha\beta} \rho_S^\beta + \sum_\beta h_G^{\alpha\beta} \rho_G^\beta} \,, \tag{2.16}$$

where b is the magnitude of the Burgers vector and λ a statistical coefficient accounting for the deviation from regular spatial arrangements of SSDs and GNDs (different values for b and λ could also be used for SSDs and GNDs). Latent hardening is represented by the two matrices $h_S^{\alpha\beta}$ and $h_G^{\alpha\beta}$ which are in fact reduced to the two coefficients h and q as given by equation 2.11 (h is taken constant and not a function of the accumulated slip).

Evolutionary equations for SSDs

SSDs are decomposed into pure edge $\rho_{S_e}^\alpha$ and screw components $\rho_{S_{sw}}^\alpha$ in order to account for their different mobilities, hardening and recovery processes. Dislocations generation is assumed to be related to Frank-Read sources and the annihilation is assumed to occur due to sign differences between the same type of parallel dislocations. The evolutionary equations are written as balance laws between dislocation generation and dislocation annihilation and are given by:

$$\begin{cases} \dot{\rho}_{S_e}^\alpha = \dfrac{C_e}{b^\alpha} \left[K_e \sqrt{\sum_\beta \rho_T^\beta} - 2d_e \rho_{S_e}^\alpha \right] |\dot{\gamma}^\alpha| \,, \\[4mm] \dot{\rho}_{S_{sw}}^\alpha = \dfrac{C_{sw}}{b^\alpha} \left[K_{sw} \sqrt{\sum_\beta \rho_T^\beta} - \rho_{S_{sw}}^\alpha \left(K_{sw} \pi d_{sw}^2 \sqrt{\sum_\beta \rho_T^\beta} + 2d_{sw} \right) \right] |\dot{\gamma}^\alpha| \,. \end{cases} \tag{2.17}$$

In this expression, d_e and d_{sw} are critical distances for spontaneous annihilation of opposite sign edge and screw dislocations respectively. C_e and C_{sw} represent the relative contributions of edge and screw dislocations to the slip produced by SSDs while K_e and K_{sw} are related to the their respective mean free path.

Evolutionary equations for GNDs

For describing the evolution of GNDs, a vector ρ_G^α related to the GND density is introduced. and is expressed in a local reference system defined by the slip direction b^α, the slip plane normal n^α and the orientation tensor $t^\alpha = (b^\alpha \otimes n^\alpha)$ [Busso et al., 2000]. The terms $\rho_{G_{sw}}^\alpha$, $\rho_{G_{en}}^\alpha$ and $\rho_{G_{et}}^\alpha$ are the components in the b^α, n^α and t^α directions respectively. In rate form, we obtain:

$$\dot{\rho}_G^\alpha = \dot{\rho}_{G_{sw}}^\alpha b^\alpha + \dot{\rho}_{G_{et}}^\alpha t^\alpha + \dot{\rho}_{G_{en}}^\alpha n^\alpha . \tag{2.18}$$

Nye's dislocation tensor [Nye, 1953] is used to define a tensorial measure of the GND densities which can be related to the resultant Burger's vector of all GNDs, yielding the following evolutionary equation:

$$b^\alpha \left(\dot{\rho}_{G_{sw}}^\alpha b^\alpha + \dot{\rho}_{G_{et}}^\alpha t^\alpha + \dot{\rho}_{G_{en}}^\alpha n^\alpha \right) = curl \left(\dot{\gamma}^\alpha n^\alpha F^p \right) , \tag{2.19}$$

where F^p is the plastic deformation gradient. The *curl* term translates the dependence of the GND density evolution on the spatial gradient of the slip rate, hence the *non-local* terminology which is sometimes used to describe strain-gradient plasticity concepts.

Non-local models have thrived in the last decade in an attempt to overcome the shortcomings of standard *local* models. Indeed, standard models have shown to yield results in fair agreement with experiments in terms of stress strain curves [Buchheit et al., 2005] or global texture predictions [Bachu and Kalidindi, 1998]. It is however admitted that such constitutive models often do not represent realistically the operating microstructural mechanisms related to the discrete nature of dislocation glide. Modelling efforts have therefore been directed towards improving the constitutive model by including gradient effects which are in fact the expression of the spatial distribution of dislocations. One way of taking into account these effects is by including gradient terms at the level of the evolutionary rules of the internal slip system variables as it is done above and in other instances [Acharya and Beaudoin, 2000; Arsenlis and Parks, 2001; Bassani, 2001; Huang et al., 2004]. Another approach in phenomenological yield surface gradient plasticity consists of incorporating higher order strain-gradient terms and couple stresses and requires sometimes the use of non-standard boundary conditions [Fleck et al., 1994; Gudmundson, 2004]. [Gerken and Dawson, 2008] find yet another way of incorporating non-local effects by including in the standard kinematic framework mentioned in section I a third term that accounts for long range strain.

It has been shown that such enhancements yield results that are in better accordance with experimental data in terms of local fields [Ma et al., 2006]. An excellent synthetic account of

applications where non-local effects are important to consider and of the different formulations available in the literature is given in [GERKEN and DAWSON, 2008]. In general the more physically sound the model is, the more computationally demanding it becomes [CAILLETAUD et al., 2003].

IV   Single Crystal model used in this work

IV.1   formulation

The single crystal model used in this work relies on an elastic-viscoplastic formulation. The main concepts are highlighted in this section and more details can be found elsewhere [DELANNAY et al., 2006]. In this model, plastic deformation is achieved by dislocation slip, along the {111} <110> crystallographic systems for FCC crystals deforming at low temperatures. The kinematics of the single crystal is a combination of dislocation slip, lattice rotation and elastic stretch. Figure 2.4 illustrates the multiplicative decomposition used in this work.
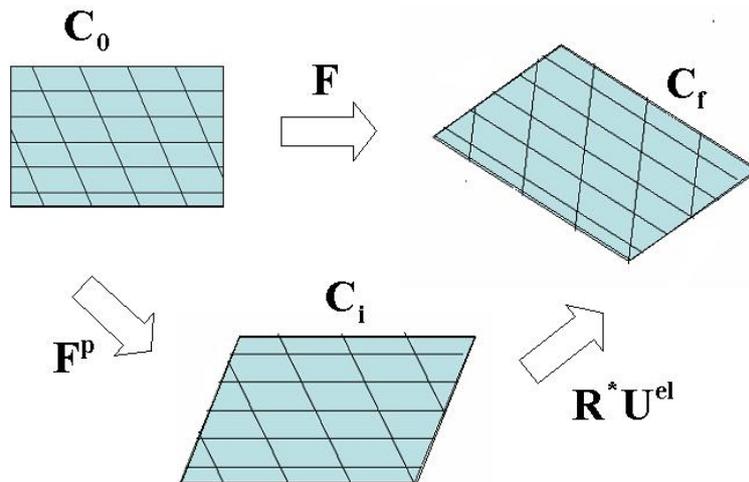
Fig. 2.4: Crystal kinematics: initial (C_0), intermediate (C_i) and final configuration (C_f)

The deformation gradient tensor $\boldsymbol{F}$, typically considered in finite strain kinematics, is decomposed as follows:

$$\boldsymbol{F} = \boldsymbol{F}^{el}\boldsymbol{F}^p = \boldsymbol{R}^*\boldsymbol{U}^{el}\boldsymbol{F}^p \,, \tag{2.20}$$

where $\boldsymbol{F}^p$ is the plastic deformation gradient that accounts for slip, $\boldsymbol{R}^*$ is the lattice rotation and $\boldsymbol{U}^{el}$ is the elastic stretch. The intermediate configuration C_i corresponds to a stress-free configuration or "relaxed" configuration obtained by elastically unloading the crystal in the final configuration C_f and rotating it. An additional fictitious configuration could be introduced between C_i and C_f as in [MARIN and DAWSON, 1998b] where it is obtained by elastically unloading C_f to a relaxed state but without rotation. The crystal constitutive equations could be written in any of these configurations and the choice conditions the procedure and scheme used

to integrate them. In this work, the equations are written in the intermediate configuration C_i. The velocity gradient tensor L is given by:

$$L = \dot{F}F^{-1} = \dot{R}^* R^{*T} + R^* \left(\dot{U}^{el} U^{el^{-1}} \right) R^{*T} + R^* U^{el} \left(\dot{F}^p F^{p^{-1}} \right) U^{el^{-1}} R^{*T} . \qquad (2.21)$$

The plastic velocity gradient L^p, accounting for dislocation slip, is then written as follows:

$$L^p = \dot{F}^p F^{p^{-1}} = \sum_{\alpha} M^{\alpha} \dot{\gamma}^{\alpha} . \qquad (2.22)$$

In this expression, M^{α} is the Schmid tensor of slip system α and $\dot{\gamma}^{\alpha}$ is the corresponding rate of dislocation slip. The Schmid tensor has the same expression in the initial and intermediate configuration as crystallographic slip does not distort the lattice.

The elastic strain tensor E is calculated with respect to the intermediate configuration and is therefore given by:

$$E = \frac{1}{2} \left(F^{el^T} F^{el} - 1 \right) = \frac{1}{2} \left(U^{el^T} U^{el} - 1 \right) . \qquad (2.23)$$

The work-conjugate measure of stress is the second Piola-Kirchhoff stress T. This latter is related to the Cauchy stress σ through:

$$T = \det(F^{el}) F^{el^{-1}} \sigma F^{el^{-T}} = \det(U^{el}) U^{el^{-1}} R^{*T} \sigma R^* U^{el^{-1}} . \qquad (2.24)$$

The elasticity relation between T and E is given by:

$$T = CE , \qquad (2.25)$$

where C is a fourth order anisotropic elasticity operator. For cubic symmetry, the corresponding matrix has a form identical to the isotropic case, except that three independent constants are needed to fully describe the matrix [Hosford, 1993]. This form allows for the separation of the deviatoric and spherical components of T.

Infinitesimal elastic strains assumption

For materials subjected to important plastic strains, the elastic strains are small compared to plastic one. Typically, in metal forming operations, they never exceed 1%. It is then assumed that they are small compared to unity. This assumption yields:

$$U^{el} = \mathbb{1} + \boldsymbol{\varepsilon}^{el} , \qquad (2.26)$$

where $\mathbb{1}$ is the identity tensor, $\boldsymbol{\varepsilon}^{el}$ is a symmetric tensor with $\left\| \boldsymbol{\varepsilon}^{el} \right\| \ll 1$. Neglecting higher order terms in $\boldsymbol{\varepsilon}^{el}$ leads to:

$$U^{el^{-1}} = \left(\mathbb{1} - \boldsymbol{\varepsilon}^{el} \right) ,$$

$$\det(U^{el}) = \det(\mathbb{1} + \boldsymbol{\varepsilon}^{el}) = 1 + \text{tr}(\boldsymbol{\varepsilon}^{el}) .$$

For the same sake of simplification, for any tensor X, $\boldsymbol{\varepsilon}^{el} : X$ is neglected compared to X. Bearing these assumptions in mind, the velocity gradient tensor can be rewritten as:

$$L = \dot{R}^* R^{*^T} + R^* \left(\dot{\boldsymbol{\varepsilon}}^{el} + \sum_\alpha M^\alpha \dot{\gamma}^\alpha \right) R^{*^T} , \tag{2.27}$$

and equations 2.23, 2.24 and 2.25 simplify to:

$$T = C\boldsymbol{\varepsilon}^{el} = R^{*^T} \sigma R^* . \tag{2.28}$$

Flow rule and hardening model

In order to complete the single crystal model, the viscoplastic exponential law is used as a flow rule:

$$\dot{\gamma}^\alpha = \dot{\gamma}_0 \left| \frac{\tau^\alpha}{\tau_c} \right|^{1/m} sign(\tau^\alpha) , \tag{2.29}$$

where $\tau^\alpha = T : M^\alpha$ is the resolved shear stress, $\dot{\gamma}_0$ is a reference slip rate, m the sensitivity exponent, and τ_c the critical resolved shear stress which is assumed to be identical for all slip systems. A rate sensitive formulation is used here in order to avoid the non-uniqueness problem associated with the identification of the active slip systems in rate independent formulations.

Regarding the hardening, it is assumed that all slip systems have the same τ_c and that they all harden equally according to the following rule:

$$\tau_c = \tau_{c0} \left(1 + \frac{\Gamma_{tot}}{\Gamma_0} \right)^n \quad \text{with} \quad \Gamma_{tot} = \int_0^t \sum_\alpha |\dot{\gamma}^\alpha| \, dt , \tag{2.30}$$

where τ_{c0}, Γ_0 and n are material parameters. Increase in slip resistance is therefore directly related to the total shear accumulated on all slip systems. A Voce type saturation law is also implemented as follows:

$$\dot{\tau}_c = H_0 \left(\frac{\tau_{sat} - \tau_c}{\tau_{sat} - \tau_0} \right) \sum_\alpha |\dot{\gamma}^\alpha| , \tag{2.31}$$

where τ_0 and τ_{sat} represent the initial and the saturation values of τ_c and H_0 a hardening coefficient.

IV.2 Time integration scheme of the constitutive law

To summarize, the equations describing the elasto-viscoplatic model can be listed as follows:

$$\textit{Kinematics:} \qquad \boldsymbol{L}_{sym} \rightarrow \boldsymbol{D} = \boldsymbol{R}^* \left(\dot{\boldsymbol{\varepsilon}}^{el} + \sum_\alpha \frac{1}{2}(\boldsymbol{M}^\alpha + \boldsymbol{M}^{\alpha^T})\dot{\gamma}^\alpha \right) \boldsymbol{R}^{*^T} , \qquad (2.32a)$$

$$\textit{Kinematics:} \qquad \boldsymbol{L}_{anti} \rightarrow \boldsymbol{W} = \dot{\boldsymbol{R}}^* \boldsymbol{R}^{*^T} + \boldsymbol{R}^* \left(\sum_\alpha \frac{1}{2}(\boldsymbol{M}^\alpha - \boldsymbol{M}^{\alpha^T})\dot{\gamma}^\alpha \right) \boldsymbol{R}^{*^T} , \qquad (2.32b)$$

$$\textit{Elasticity:} \qquad \boldsymbol{T} = \boldsymbol{C}\boldsymbol{\varepsilon}^{el} , \qquad (2.32c)$$

$$\textit{Schmid Law:} \qquad \tau^\alpha = \boldsymbol{T} : \boldsymbol{M}^\alpha , \qquad (2.32d)$$

$$\textit{Flow:} \qquad \dot{\gamma}^\alpha = \dot{\gamma}_0 \left| \frac{\tau^\alpha}{\tau_c} \right|^{1/m} sign(\tau^\alpha) , \qquad (2.32e)$$

$$\textit{Hardening:} \qquad \tau_c = \tau_{c0} \left(1 + \frac{\Gamma_{tot}}{\Gamma_0} \right)^n , \Gamma_{tot} = \int_0^t \sum_\alpha |\dot{\gamma}^\alpha| \, dt . \qquad (2.32f)$$

The objective of the integration of the constitutive model is to compute the model-dependent variables at time $t + \Delta t$, given that their values are known at time t and that the applied deformation is known for every crystal ($\boldsymbol{L}$ or equivalently $\boldsymbol{D}$ and $\boldsymbol{W}$). In the previous system, the unknown independent variables are: the crystal stresses $\boldsymbol{T}|_{t+\Delta t}$ (or equivalently the elastic deformation $\boldsymbol{\varepsilon}^{el}|_{t+\Delta t}$), the slip resistance $\tau_c|_{t+\Delta t}$ and the lattice orientation $\boldsymbol{R}^*|_{t+\Delta t}$. These constitute the state variables of the problem. In order to simplify the time integration procedure, one can choose to eliminate the lattice rotation from this system (and hence the evolutionary equation 2.32b) which is approximated by $\widetilde{\boldsymbol{R}}^*$ as follows:

$$\boldsymbol{R}^*|_{t+\Delta t} \approx \widetilde{\boldsymbol{R}}^* = \boldsymbol{W}\Delta t \boldsymbol{R}^*|_t .$$

As mentioned in [DELANNAY et al., 2006], the impact of such an approximation is negligible in metal forming simulations such as those performed in this work. The update of the lattice orientation is performed later, after the integration of the rest of the equations, as it is explained below.

Equations 2.32a, 2.32c and 2.32d are combined in order to find the crystal stresses $\boldsymbol{T}|_{t+\Delta t}$. A fully implicit time integration scheme yields the following discretized equations:

$$\boldsymbol{T}|_{t+\Delta t} = \boldsymbol{T}|_t + \boldsymbol{C}\left[\widetilde{\boldsymbol{R}}^{*^T} \boldsymbol{\Delta D} \widetilde{\boldsymbol{R}}^* - \frac{1}{2}(\boldsymbol{M}^\alpha + \boldsymbol{M}^{\alpha^T})\Delta\gamma^\alpha \right] , \qquad (2.33a)$$

$$\Delta\gamma^\alpha = \dot{\gamma}^\alpha|_{t+\Delta t}\Delta t = \dot{\gamma}_0 \left(\frac{\boldsymbol{M}^\alpha : \boldsymbol{T}|_{t+\Delta t}}{\tau_c|_{t+\Delta t}} \right)^{1/m} sign(\boldsymbol{M}^\alpha : \boldsymbol{T}|_{t+\Delta t})\Delta t , \qquad (2.33b)$$

$$\tau_c|_{t+\Delta t} = \tau_{c0} \left(1 + \frac{\Gamma_{tot}|_{t+\Delta t}}{\Gamma_0} \right)^n \text{ with } \quad \Gamma_{tot}|_{t+\Delta t} = \Gamma_{tot}|_t + \sum_\alpha |\Delta\gamma^\alpha| . \qquad (2.33c)$$

A two level iterative scheme is used to solve this system. A first Newton-Raphson procedure is used to solve equation 2.33a. A second one is used to compute the slip increments $\Delta\gamma^\alpha$ based

on the stress estimate. Slip resistance is computed subsequently. Finally, regarding lattice reorientation, equation 2.32b is integrated using an exponential map ([SIMO and HUGHES, 1998]). In practice, all these equations are expressed in the crystal reference frame so that M^α is identical in crystals belonging to the same phase. At the beginning of the simulation, the orientation of each grain is recorded and used to shift from the sample coordinate system to the crystal coordinate system ($R_0 R^{*^T}$).

Link with the Finite Element formulation

The Cauchy stress, used by the finite element model, is updated according to 2.28, yielding:

$$\sigma|_{t+\Delta t} = R^* T|_{t+\Delta t} R^{*^T} . \tag{2.34}$$

Moreover, a consistent algorithmic tangent operator is used by the finite element formulation, as highlighted in the next chapter. It is given by:

$$\mathbb{C} = \frac{\partial \Delta \sigma}{\partial \Delta D} \approx R^*|_{t+\Delta t} \widetilde{R}^{*T} \frac{\partial T|_{t+\Delta t}}{\partial (\widetilde{R}^{*T} \Delta D \widetilde{R}^*)} \widetilde{R}^* R^{*T}|_{t+\Delta t} , \tag{2.35}$$

where

$$\frac{\partial T|_{t+\Delta t}}{\partial (\widetilde{R}^{*T} \Delta D \widetilde{R}^*)} = \left[C^{-1} + \sum_\alpha \frac{1}{2} (M^\alpha + M^{\alpha^T}) \otimes \frac{\partial \Delta \gamma^\alpha}{\partial T|_{t+\Delta t}} \right]^{-1} . \tag{2.36}$$

This last equation is obtained by differentiating equation 2.33a with respect to the deformation increment. The last term in equation 2.36 is obtained from the solution of the following linear set:

$$\sum_\alpha \left[\delta_{\alpha\beta} + \frac{\Delta \gamma^\alpha}{\partial m \tau_c|_{t+\Delta t}} \frac{\partial \tau_c|_{t+\Delta t}}{\partial \Delta \gamma^\beta} \right] \frac{\partial \Delta \gamma^\alpha}{\partial T|_{t+\Delta t}} = \frac{\Delta \gamma^\beta}{m M^\beta : T_{t+\Delta t}} M^\beta , \tag{2.37}$$

where

$$\frac{\partial \tau_c|_{t+\Delta t}}{\partial \Delta \gamma^\beta} = n \tau_{c0} \left(1 + \frac{\Gamma_{tot}|_{t+\Delta t}}{\Gamma_0} \right)^{n-1} \frac{sign \Delta \gamma^\beta}{\Gamma_0} . \tag{2.38}$$

The assessment of the time integration scheme can be found elsewhere [DELANNAY et al., 2006].

V   Conclusion

As seen in this chapter, the behavior of a single crystal could be modelled in a more or less complex fashion so as to reflect the actual physical mechanisms operating at the microstructural level. The slip system concept represents a homogenized way of taking into consideration the motion of individual dislocations that glide through the crystal lattice under the effect of the (resolved) stress. The flow rule reflects the non-linear relationship between strain rate and stress. It is phenomenological in nature, even if various authors have strived to incorporate more

"physics" into their models by, for example, considering dislocation densities as primary variables, distinguishing the behavior of statistically stored dislocations from geometrically necessary ones, and therefore including strain gradients effects so as to account for non-local or long-range influences. Local models, such as the one used in this work, are blind to those influences and, thus, do not include any length scale. They are, therefore, not expected to yield satisfactory results in several instances, including, for example, the prediction of the Hall-Petch effect, which is one of the most well-known macroscopic manifestation of size-related effects in metallic materials. Most importantly, they can not capture all grain scale heterogeneities, particularly those that appear under the influence of strain gradients. Bearing these limitations in mind, the single crystal model is in general combined with another model at the level of the polycrystal in order to account for the interaction between each grain and its neighbors. Assumptions about grain interaction are as significant as the single crystal model in determining the outcome of the modelling effort, as seen in the following chapter.

Chapter 3

Accounting for grain interaction

Single crystals are in general part of a polycrystal and therefore, when this latter is subjected to loading, the behavior of each crystal (and that of the ensemble) is affected by the presence of the other constituents. The objective of polycrystal theories is to account for the individual behavior of the crystals and that of the polycrystal by defining:

- The way the deformation is partitioned among the crystals and the interaction between the grain and its neighbors,

- Whether or not the grain is considered as an homogeneous entity.

The CPFEM approach can be considered as being the ultimate polycrystal model. Its assumptions regarding deformation and stress equilibrium are the closest to the actual physics of the problem compared to classical polycrystal models and more elaborate "N-site" models, as highlighted in this chapter.

I   Polycrystal theories

Polycrystal models are based on the *Representative Volume Element (RVE)* concept. The RVE polycrystal should be small enough compared to the macroscopic scale but large enough to reflect microstructural heterogeneities. In homogenization theory, the RVE is such as the loading and displacement conditions at its boundary are uniform and the volume average of stress, strain and velocity gradient over all grains are equal to the overall stress Σ^{poly}, strain (E^{poly}) and velocity gradient (L^{poly}) at its boundary [HILL, 1967]. This could be expressed as

follows:

$$
\begin{cases}
\boldsymbol{\Sigma}^{poly} = \langle \boldsymbol{\sigma}^c \rangle = \dfrac{1}{V} \displaystyle\int_V \boldsymbol{\sigma}^c dV \,, \\[18pt]
\boldsymbol{E}^{poly} = \langle \boldsymbol{\varepsilon}^c \rangle = \dfrac{1}{V} \displaystyle\int_V \boldsymbol{\varepsilon}^c dV \,, \\[18pt]
\boldsymbol{L}^{poly} = \langle \boldsymbol{L}^c \rangle = \dfrac{1}{V} \displaystyle\int_V \boldsymbol{L}^c dV \,,
\end{cases}
\tag{3.1}
$$

where V is the volume of RVE, c stands for the crystal and *poly* for the polycrystal. Polycrystal models are basically composed of: (i) single crystal constitutive relations and (ii) a localization rule which is used to partition the macroscopic deformation among the grains (see figure 2.2). They are in essence statistical models. Several approaches, with their own variants, are present in the literature. Only the main ones are recalled here. These models are needed in Finite Element simulations where each integration point represents a group of crystals. They incorporate more or less complex assumptions in order to account for the interactions between the grains inside a polycrystal. After briefly discussing the earliest of them all, the *Sachs* model, the *Taylor (Full-Constraints)* model is presented followed by classical Taylor-Type models (*Relaxed-Constraints*) and more elaborate Taylor-Type models that strive to take into account the direct neighborhood of each grain by considering "clusters" of grains (*N-site*). While these models are based on short-range interactions, the *Self-Consistent* approach incorporates the long-range interactions between one cluster (a grain or a group of grains) and the rest of the polycrystalline matrix.

I.1   Sachs model

In this model [SACHS, 1928] and its variants, grains are assumed to experience the same state of stress as the macroscopic polycrystal one and achieve deformation by activating only one slip system like unconstrained single crystals. No link or assumption is made about the deformation of each grain or the interaction between the grains. Therefore each grain deforms independently. While stress equilibrium is forced upon the system with the uniform stress assumption, compatible deformation is not achieved. This model is often presented as a "lower-bound".

I.2   Taylor full-constraint model (FC)

Taylor's original analysis [TAYLOR, 1938] is motivated by the violation of compatibility (or equivalently the assumption of single slip) in Sach's model. Taylor assumed that all grains deform in the exact same manner as the polycrystal. In fact, if a polycrystal is subjected to important strains, one could assume that the behavior of each individual grain is not that different

from its neighbor and from the overall behavior. This compatibility requirement, which guaranties a perfect fit at the grain boundaries is achieved at the expense of local stress equilibrium. In rate form, the Taylor assumption can be expressed as follows:

$$\boldsymbol{L}^c = \boldsymbol{L}^{poly} \, . \tag{3.2}$$

The Taylor model is very simple to implement in numerical applications and the associated computational costs are small compared to other polycyrstalline models. In large scale applications, texture-induced anisotropy is fairly predicted [MARIN and DAWSON, 1998a], especially for materials exhibiting a high degree of crystal symmetry (like cubic crystals) and subjected to strains well beyond the elastic limit. On the other hand, some major characteristics of deformation texture evolution are not well accounted for.

I.3   Relaxed constraints models (RC)

Constraining completely the motion (the deformation) of the grains in the Taylor FC approach was thought of being potentially responsible for the shortcomings of the model regarding deformation texture predictions. Relaxed constraints models are based on the idea of freeing some degrees of freedom of each individual grain with the intended objective of improving texture predictions. Relaxing the kinematic constraints on the grains can be physically justified in some contexts. Typically, during rolling for example, grains become flat or elongated and the polycrystal can be regarded as a group of lamellae or thin brick shaped grains, which remain parallel to each other during the deformation. The kinematic constraints on those grains could therefore be relaxed, allowing possible misfits at the grain boundaries while satisfaction of local stress equilibrium is enhanced.

Relaxing the constraints entails prescribing, on the grain's level, only some components of the polycrystal velocity gradient. In the *lath* model for example, the local shear component $\boldsymbol{L}^c_{13}$ (l_{13} in figure 3.1(b)) is not set equal to the macroscopic one $\boldsymbol{L}^{poly}_{13}$ which is equal to zero in ideal rolling. This reduces by one the number of equations, thus yielding only four independent equations to be solved for the slip rates (increments) as opposed to the five independent ones in the Taylor FC model. Consequently, only four slip systems are active in this case. Another variant, the *pancake* model relaxes yet another component, the transverse shear $\boldsymbol{L}^c_{23}$, thus activating only three slip systems in this case. A general mathematical framework describing these "Generalized Relaxed Constraints" (GRC) models is given in [VAN HOUTTE, 2005]. The partitioning rule is expressed as:

$$\boldsymbol{L}^c = \boldsymbol{L}^{poly} - \sum_{r=1}^{R} \widetilde{\boldsymbol{K}}^r \dot{\gamma}_r^{RLX} \, , \tag{3.3}$$

where R is the number of relaxations ($R = 1$ for the *lath* model and $R = 2$ for the *pancake*), $\dot{\gamma}_r^{RLX}$ are unknown relaxation shear rates and $\widetilde{\boldsymbol{K}}^r$ are the relaxation modes. These latter (expressed in

the macroscopic frame) are given by:

$$\widetilde{K}^1 = \begin{bmatrix} 0 & 0 & 1 \\ 0 & 0 & 0 \\ 0 & 0 & 0 \end{bmatrix} \quad , \quad \widetilde{K}^2 = \begin{bmatrix} 0 & 0 & 0 \\ 0 & 0 & 1 \\ 0 & 0 & 0 \end{bmatrix} . \tag{3.4}$$

It can be shown that relaxing specific components of the velocity gradient entails the satisfaction of equilibrium of the corresponding stress components [VanHoutte et al., 2004].

<table>
<tr><td>(a)</td><td>(b)</td></tr>
</table>
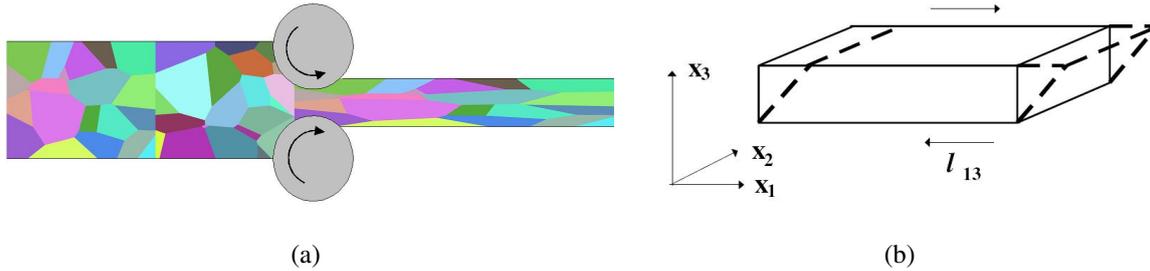
Fig. 3.1: Flattening of grains during rolling: (a) rolling process; (b) the lath model ($x_1 = RD, x_2 = TD$)[Van Houtte, 2005]

One of the main conceptual faults of the GRC models is the fact that the volume average of the velocity gradients over the whole polycrystal might not equal the macroscopic one. Indeed, nothing in these models is done to ensure that the contribution of the extra terms that were added, i.e the contribution of the relaxation shear rates, is equal to zero over the entire volume. Practically speaking, RC *pancake* models, for example, have not yielded much improvement regarding deformation texture prediction [Van Houtte, 2005]. Sometimes the predictions are even worse than the Taylor FC model [Delannay, 2001].

I.4 *N-site* models

As opposed to FC and RC models, *N-site* models consider what happens to more than one grain at a time. The main concept is to incorporate short-range interaction during the deformation of each grain by considering a cluster of *N* grains. In the LAMEL and advanced LAMEL (or multisite) models, two crystals are considered while a cluster of eight crystals is considered in the Grain Interaction (GIA) model.

I.4.1 The LAMEL model

The LAMEL model assumptions are quite similar to those of GRC models. Consequently, its applicability is also limited to special cases where grains are flattened as in the rolling process. In order to overcome the major shortcoming of the GRC models in terms of satisfaction of volume averages, the LAMEL model considers a lamellae composed of two crystallites which

are meant to achieve *together* the macroscopic deformation. Practically speaking, two crystals are chosen randomly from the pool of discretized orientations constituting the texture of the polycrystal and assigned to the top and bottom grain as illustrated by figure 3.2. Several relaxation modes are considered with the basic requirement that the interface remains coherent i.e grain boundary sliding is not permitted. Type I and II relaxation modes are equivalent to the relaxation modes of the *pancake* model as seen on figure 3.3. They leave the interface between the two grains unrotated and undeformed. In Type III, the shear components act in the same direction (instead of opposite directions as in type I and type II) which leaves the interface deformed, which is therefore a special case compared to the other two relaxation modes.
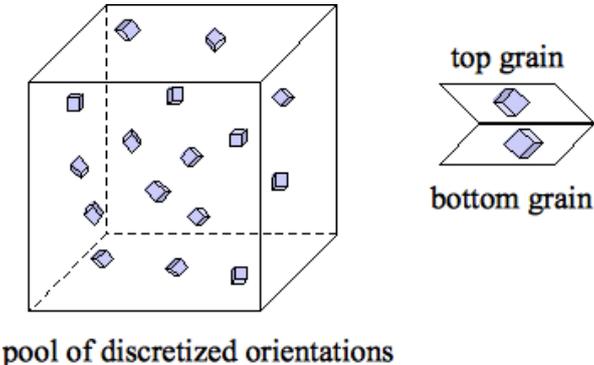
Fig. 3.2: Illustration of the LAMEL orientation selection procedure
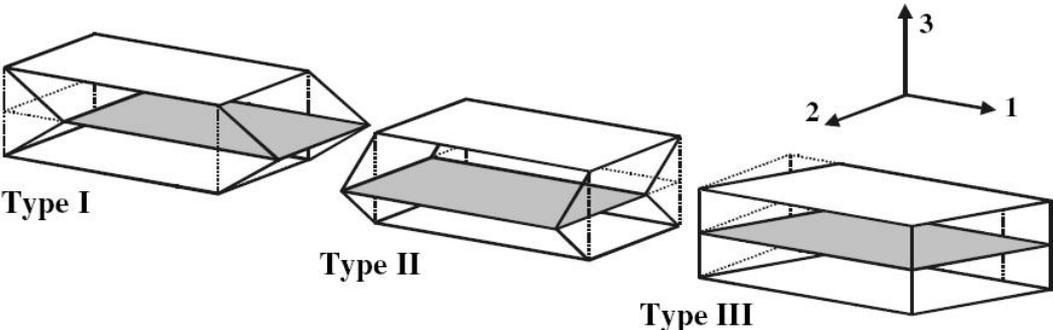
Fig. 3.3: the LAMEL relaxation modes ($1 = RD$, $2 = TD$) [VAN HOUTTE, 2005]

While it is only applicable to rolling, the LAMEL model has been successful in improving the predictions of texture evolution in steels for example [VAN HOUTTE et al., 1999].

I.4.2 The Advanced LAMEL model and the "multisite" model

The multisite model [DELANNAY et al., 2009] is the elastic-viscoplastic extension of the advanced LAMEL model (ALAMEL) developed initially by [VAN HOUTTE, 2005]. Regarding the treatment of grain's interaction, both models are equivalent. The first characteristic feature

of the multisite model is that no assumption is made regarding the grain shape, which makes the model applicable in any context. The interaction of the grain with several neighbors is taken into account which is equivalent to considering the grain as a non-homogeneous entity as illustrated by figure 3.4. With these assumptions, the multisite model strives to overcome the shortcomings of the previous models by sticking more closely to the actual physics of the problem, whereby every grain is generally surrounded by more than one neighbor. The crystallographic orientation of different regions of the grain evolves therefore differently and its contribution is considered in the texture evolution of the polycrystal. The interactions considered in the multisite model are the same as those considered in the LAMEL model (Type I and II). In the same vein, the GIA model takes into consideration the interaction between neighboring grains by relaxing the constraints inside a cluster composed of eight grains [ENGLER et al., 2005]. The grains are allowed to relax under an energy penalty term.
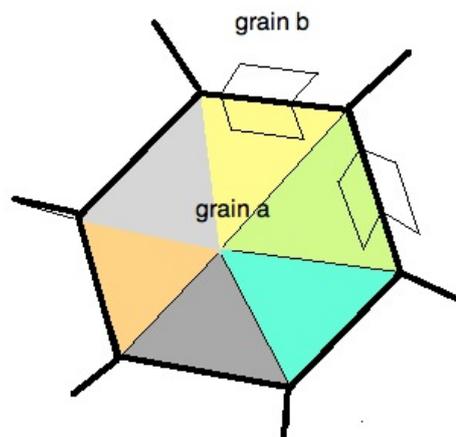
Fig. 3.4: Ilustration of the multisite model

When compared to FC and RC models, the Advanced LAMEL and GIA models yield results that are in better agreement with experimental data in terms of texture evolution. This is sometimes also true when compared to low resolution CPFEM simulations [VANHOUTTE et al., 2004].

I.5 Self-Consistent models

As opposed to the Taylor model which violates stress equilibrium, self-consistent models were designed to satisfy both equilibrium and compatibility in an average sense. They are based on the original work of [ESHELBY, 1957] who considered the problem of determining the stress and strain in an elastic ellipsoidal inclusion surrounded by a unbounded elastic medium having the same properties as the inclusion. The self-consistent approach, as illustrated by figure 3.5, relies on the concept of eigenstrain and the extension of Eshebly's remarkable result to the case

of ellipsoidal inhomogeneities included in an unbounded domain having unknown effective properties and subjected to the macroscopic strain or stress (ε^0 or σ^0) as a far-field strain or stress.
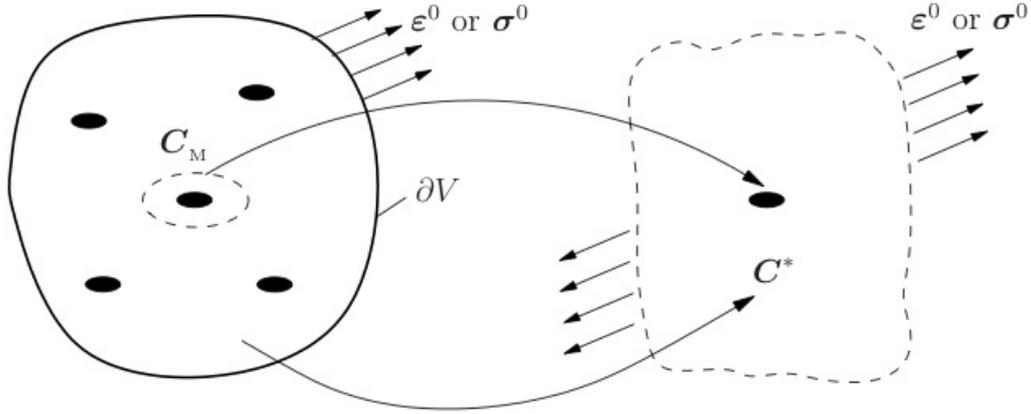
Fig. 3.5: Self-consistent principle[Gross and Seelig, 2006]

Applying this concept to polycrystalline aggregates, each grain (defined as one crystal with a given crystallographic orientation) is considered as an inclusion embedded in polycrystalline matrix composed of *all* other grains. In this case, the behavior of the matrix is then determined by considering successively different grains (considered as representative of all other grains having the same orientation). The overall behavior is then computed as the average response of all those representative grains. As opposed to multisite and LAMEL model, where next-neighbor interaction is addressed, the self-consistent approach takes into consideration long-range interactions, as each grain "feels" the influence, not only of its direct neighbors, but of all other grains constituting the polycrystalline matrix.

A first self-consistent model was proposed by [Kröner, 1961] and extended later by [Budiansky and Wu, 1962]. In this model, each grain is regarded as an elastic-plastic spherical inclusion embedded in an elastic infinite medium. The grain and the matrix are considered elastically isotropic and have the same linear elastic properties. The interaction between the grain and the aggregate is elastic. Considering an Eshelby problem and the previous assumptions yields the following expression for the stress σ^c inside a spherical crystal [Khan and Huang, 1995]:

$$\sigma^c = \Sigma^{poly} - 2G(1 - \zeta)(\boldsymbol{E}_p^{poly} - \boldsymbol{\varepsilon}_p^c) \quad \text{with } \zeta = \frac{2(4 - 5v)}{15(1 - v)} , \tag{3.5}$$

where $\boldsymbol{E}_p^{poly}$ is the overall plastic strain, $\boldsymbol{\varepsilon}_p^c$ is the local plastic strain, G is the shear modulus and v the Poisson's ratio.

Due to the model's assumption, it is limited to small strains. Later on, other authors con-

sidered the elastic-plastic [BERVEILLER and ZAOUI, 1979; HILL, 1965] response of the polycrystal in the interaction. Others considered viscoplasticity [HUTCHINSON, 1976; LEBENSOHN and TOMÉ, 1993; MOLINARI et al., 1987].

II   The CPFEM approach - brief literature review of FE formulations

The characteristics of the Finite Element approach in the treatment of crystal plasticity problems, where each grain is represented (meshed) explicitly can be summarized as follows:

- No micro to macro linking hypothesis is needed

- The compatibility requirement is fulfilled on the local level

- Equilibrium is also fulfilled locally in a weak sense

- In simulations, where more than one element is used to discretize the grain, in-grain heterogeneities can be represented. Stress, strain and lattice orientation gradients are predicted.

- Next-neighbor interactions are included. Long-range interactions are indirectly taken into consideration as the influence of far away grains is transmitted to a given grain in much the same way as the last ball in a Newton's cradle. Consequently, no assumptions for the interactions are needed and their influence is included in the outcome of the Finite Element computations.

The Finite element model is composed of a representation and meshing of the microstructure, and of the finite element formulation used to solve the mechanical problem. Representation and meshing of the microstructure is tackled in the next chapter. In this section, some formulations used in the literature are reviewed briefly before presenting the finite element formulation used in this work. Finite element simulations in solid mechanics are dominated either by displacement /velocity based formulations or by mixed formulations. In these latter, in addition to the primary variable (displacement / velocity), a second primary unknown is introduced. In practice, the pressure has often been used yielding mixed displacement/pressure or velocity/pressure formulations. In crystal plasticity applications, the focus is set primarily on the constitutive behavior and the Finite Element formulation is discussed by only a few authors. In many applications, the traditional displacement formulation is used either through in-house codes [DELAIRE et al., 2000] or through commercial finite element codes like ABAQUS [DELANNAY et al., 2006]. These formulations are a priori more economical than mixed methods due to the use of one primary vectorial unknown. However a known problem associated with

this formulation and the use of first-order elements is locking, which occurs when modelling incompressible or nearly incompressible materials [Bathe, 1996]. One way to overcome this is to use second order elements, which lack the simplicity (in terms of numerical implementation) offered by linear elements. Another alternative is to use mixed formulations, which have been applied in the context of crystal plasticity applications in form of displacement/pressure formulations as in [Maniatty et al., 2007] or velocity/pressure formulation as in [Marin and Dawson, 1998a]. In these formulations, it is necessary that the combination of interpolation functions for displacement /velocity and for pressure satisfy the Brezzi-Babuska condition [Brezzi and Fortin, 1991] in order to ensure stability. Dawson and his collaborators often used mixed formulations where the pressure is piecewise constant over the element and the velocity is interpolated using linear shape functions (P1/P0 formulation). They noted that such a formulation converges well in the case of an elastic-viscoplastic constitutive behavior while failing in the case of rigid viscoplastic one [Marin and Dawson, 1998a]. Sharp discontinuities across elements due to the single crystal anisotropy is mainly responsible for such numerical problems. For this purpose they proposed a Hybrid formulation [Beaudoin et al., 1995] which is based on the concept of defining subdomains within a body while applying contraints between them.

Another classification of finite element formulations considers the scheme used to handle the deformation of the body. In crystal plasticity applications, like in many solid mechanics problems, the Lagrangian scheme is generally adopted. In the case of large strain applications, the updated Lagrangian scheme is very useful [Maniatty et al., 2007; Sarma et al., 2002] whereas the Eulerian approach is more rare [Barton et al., 2004].

In this work, a mixed velocity pressure finite element formulation is used with appropriate combination of interpolation functions. More specifically, the mini-element (P1+/P1) with linear continuous pressure and linear velocity with a bubble function added at its center for this latter, is used. Specific details of the formulations are found below.

III Finite element formulation in this work

III.1 Balance laws

The resolution of the mechanical problem is based on balance of momentum and conservation of mass coupled with the appropriate boundary conditions and constitutive equations. In local form, the conservation of linear momentum and the conservation of mass are written as:

$$div\boldsymbol{\sigma} + \rho\boldsymbol{g} = \rho\frac{d\boldsymbol{v}}{dt} \,, \tag{3.6}$$

$$\frac{d\rho}{dt} + \nabla \cdot (\rho\boldsymbol{v}) = 0 \,, \tag{3.7}$$

where $\boldsymbol{v}$ is the velocity vector, $\boldsymbol{\sigma}$ is the Cauchy stress tensor, ρ the density and $\boldsymbol{g}$ the gravity.

Appropriate surface traction and velocity boundary conditions are given by:

$$v = v_{app} \text{ on } \Gamma_v \,, \tag{3.8}$$

for the velocity vector v, and:

$$\sigma n = t = t_{app} \text{ on } \Gamma_t \,, \tag{3.9}$$

for the traction vector t where $\Gamma = \Gamma_v \cup \Gamma_t$ is the boundary of the domain Ω.

In the present work, we restrict our attention to isothermal, quasi-static deformation of polycrystalline aggregates. Also neglecting body forces, equation 3.6 is reduced to:

$$div\sigma = 0 \,. \tag{3.10}$$

The Cauchy stress tensor σ can be decomposed into its deviatoric and spherical pressure components. However, such decomposition is only meaningful if the constitutive law, that is to be solved in concert with this equation, can give the evolution of the deviatoric and pressure components separately. Besides, for constitutive models that account for the elastic behavior, equation 3.7 is replaced by the volumetric response of the elasticity relations, as the density can be directly determined once the motion of the body is obtained. Bearing these hypotheses in mind, the final system of equations to be solved may be written as:

$$\begin{cases} div S - \nabla p = 0 \,, \\ tr\dot{\varepsilon} + \dfrac{\dot{p}}{\chi} = 0 \,, \end{cases} \tag{3.11}$$

where S and p are respectively the deviatoric and pressure components of σ, χ the bulk (elastic) modulus, and $\dot{\varepsilon}$ the strain rate tensor defined as:

$$\dot{\varepsilon} = \frac{1}{2}\left(\nabla v + \nabla v^T\right) \,. \tag{3.12}$$

III.2   Variational formulation

The formulation of the finite element problem is based on the weak integral form of the system presented in 3.11. The procedure for obtaining the weak form consists of first multiplying the equations by test functions $v^* \in V$ and $p^* \in P$ where V and P are appropriate functional spaces given by:

$$\begin{cases} V = \{v, v \in H^1(\Omega)^d \,|v = v_{app} \text{ on } \Gamma_v\} \,, \\ V_0 = \{v, v \in H^1(\Omega)^d \,|v = 0 \text{ on } \Gamma_v\} \,, \\ P = \{p, p \in L^2(\Omega)\} \,, \end{cases} \tag{3.13}$$

with d the space dimension, V the space of kinematically admissible velocity fields and V_0 the space of kinematically admissible velocity fields to zero.

Integration over the volume of the domain Ω and the use of the Green formula yields the following variational problem:

find $(v, p) \in (V, P)$ *such that* $\forall (v^*, p^*) \in (V_0, P)$:

$$\begin{cases} \int_\Omega S(v) : \dot{\varepsilon}(v^*) d\Omega - \int_\Omega p \cdot \nabla v^* d\Omega - \int_\Gamma t \cdot v^* d\Gamma = 0 \,, \\ \int_\Omega \left(tr\dot{\varepsilon} + \frac{\dot{p}}{\chi} \right) p^* d\Omega = 0 \,. \end{cases} \qquad (3.14)$$

III.3   Time discretization

The large deformation of the microstructure is modelled using an updated Lagrangian framework. In this incremental approach, the total simulation time t_{tot} is discretized into N increments such that $t_{tot} = \cup_{i=0}^{N-1} [t_i, t_i + \Delta t_i]$. At time t the configuration of the body Ω^t is known and the solution (v^t, p^t) satisfying the balance laws at that time, can be determined based on stresses calculated at time $t + \Delta t$. The new configuration is then updated using a finite difference scheme, namely an Euler explicit scheme as follows:

$$x^{t+\Delta t} = x^t + v^t \Delta t \,, \qquad (3.15)$$

with x the node coordinate vector and v^t the velocity vector solution of the mechanical problem on the current configuration.

III.4   Spatial discretization

In order to compute the solution of the variational problem 3.14 using the finite element method, the domain Ω is discretized such that:

$$\Omega_h = \bigcup_{K \in \mathcal{T}_h(\Omega)} K \,, \qquad (3.16)$$

where Ω_h is a spatial discretisation of the domain Ω, $\mathcal{T}_h(\Omega)$ a finite element mesh of the domain Ω, K a simplex and h a parameter denoting the mesh size.

We introduce the functional vector spaces of finite dimensions V_h and P_h close to the continuous spaces V and P of infinite dimension, such that the discrete solution $(v_h, p_h) \in (V_h, P_h)$ is close to the "real" one $(v, p) \in (V, P)$. The spaces V_h and P_h have to be chosen in such a way that the existence and the uniqueness of the solution is guaranteed. For this purpose, these spaces cannot be chosen independently. They have to satisfy the Brezzi Babuska stability conditions [BREZZI and FORTIN, 1991]. In this respect, the MINI-element P1+/P1, first introduced in CEMEF by [COUPEZ and MARIE, 1997], is a convenient and an appropriate choice.

III.4.1 The MINI-element

The MINI-element is an isoparametric triangle in 2D and tetrahedron in 3D with a linear interpolation for the pressure field. On the other hand, the velocity field interpolation has a linear component and a nonlinear one, the so-called bubble function, which is a added at the center of the element as shown in figure 3.6 for the 3D case.

Velocity   Pressure
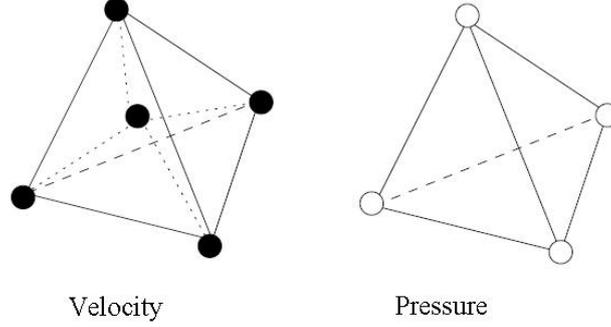
Fig. 3.6: MINI-Element P1+/P1

For such element, the finite element spaces can be written as:

$$
\begin{cases}
W_h = V_h \bigoplus B_h \,, \\
W_{h_0} = V_{h_0} \bigoplus B_h \,, \\
V_{h_0} = \{v_h \in (\varepsilon^0(\Omega_h))^d : v_h|_K \in \mathbb{P}_1(K) \,, v_h|_{\Gamma_{K_{v_h}}} = 0\} \,, \\
V_h = \{v_h \in C^0(\Omega_h)^d : v_h|_K \in \mathbb{P}_1(K) \, v_h|_{\Gamma_{K_{v_h}}} = v_{app}\} \,, \\
B_h = \{b_h \in C^0(\Omega_h)^d : b_h|_{K_i} \in \mathbb{P}_1(K_i) \text{ and } b_h|_{\Gamma_K} = 0\} \,, \\
P_h = \{p_h \in C^0(\Omega_h) : p_h|_K \in \mathbb{P}_1(K)\} \,,
\end{cases}
\tag{3.17}
$$

where d is the space dimension, $K_i, i = 1 \ldots d+1$ are the $d+1$ subsimplexes composing K.

Denoting N^l and N^b the linear and bubble shape functions respectively, the discretized velocity and pressure fields can be written as:

$$
\begin{aligned}
w_h &= v_h + b_h = \sum_{i=1}^{Nbnode} N_i^l(x)v_i + \sum_{j=1}^{Nbelt} N_j^b(x)b_j \,, \\
p_h &= \sum_{i=1}^{Nbnode} N_i^l(x)p_i \,,
\end{aligned}
\tag{3.18}
$$

where *Nbnode* and *Nbelt* are the total number of nodes and elements in the mesh respectively. On the local level, for each element, the velocity and pressure unknowns are written as:

$$
\begin{aligned}
w_h &= v_h + b_h = \sum_{i=1}^{D} N^l(x)V_i + N^b(x)b_j \,, \\
p_h &= \sum_{i=1}^{D} N_i^l(x)P_i \,,
\end{aligned}
\tag{3.19}
$$

where $D = d + 1$ and N^b is a linear function defined on each of the $d + 1$ sub-elements.

For each element K, the bubble function has the following fundamental properties:

$$\left|\begin{array}{l} \int_K \mathbb{A} : \nabla b_h d\Omega_K = 0 \quad \text{for any constant tensor } \mathbb{A}, \text{ therefore } \int_K \nabla v_h : \nabla b_h d\Omega_K = 0 \,, \\[3mm] \int_K v_h \nabla \cdot b_h d\Omega_K = - \int_K \nabla v_h \cdot b_h d\Omega_K \,, \\[3mm] b_h = 0 \text{ on } \Gamma_K \,. \end{array}\right. \tag{3.20}$$

III.4.2 The discrete problem

The discrete problem is formulated as follows:

find $(w_h = v_h + b_h, p_h) \in (W_h, P_h)$ such that $\forall(w_h^* = v_h^* + b_h^*, p_h^*) \in (W_{h_0}, P_h)$:

$$\left\{\begin{array}{l} \int_{\Omega_h} S(w_h) : \dot{\varepsilon}(w_h^*)d\Omega - \int_{\Omega_h} p \cdot \nabla w_h^* d\Omega - \int_\Gamma t \cdot w_h^* d\Gamma = 0 \,, \\[3mm] \int_{\Omega_h} \left(tr\dot{\varepsilon}(w_h) + \dfrac{\dot{p}}{\chi} \right) p_h^* d\Omega = 0 \,. \end{array}\right. \tag{3.21}$$

Taking into consideration the decomposition $w_h = v_h + b_h$ and $w_h^* = v_h^* + b_h^*$, the previous system can be rewritten as:

$$\left\{\begin{array}{l} \int_{\Omega_h} S(v_h + b_h) : \dot{\varepsilon}(v_h^*)d\Omega - \int_{\Omega_h} p_h \cdot \nabla v_h^* d\Omega - \int_\Gamma t \cdot v_h^* d\Gamma = 0 \,, \\[3mm] \int_{\Omega_h} S(v_h + b_h) : \dot{\varepsilon}(b_h^*)d\Omega - \int_{\Omega_h} p_h \cdot \nabla b_h^* d\Omega - \int_\Gamma t \cdot b_h^* d\Gamma = 0 \,, \\[3mm] \int_{\Omega_h} \left(tr\dot{\varepsilon}(v_h + b_h) + \dfrac{\dot{p}_h}{\chi} \right) p_h^* d\Omega = 0 \,. \end{array}\right. \tag{3.22}$$

It has been shown [Jaouen, 1998] that in the case of an elastic-viscoplastic constitutive law, the deviatoric component S can be decomposed into a linear $S(v_h)$ and a bubble part $S(b_h)$. This yields:

$$\left\{\begin{array}{l} \int_{\Omega_h} S(v_h) : \dot{\varepsilon}(v_h^*)d\Omega + \int_{\Omega_h} S(b_h) : \dot{\varepsilon}(v_h^*)d\Omega - \int_{\Omega_h} p_h \cdot \nabla v_h^* d\Omega - \int_\Gamma t \cdot v_h^* d\Gamma = 0 \,, \\[3mm] \int_{\Omega_h} S(v_h) : \dot{\varepsilon}(b_h^*)d\Omega + \int_{\Omega_h} S(b_h) : \dot{\varepsilon}(b_h^*)d\Omega - \int_{\Omega_h} p_h \cdot \nabla b_h^* d\Omega - \int_\Gamma t \cdot b_h^* d\Gamma = 0 \,, \\[3mm] \int_{\Omega_h} \left(tr\dot{\varepsilon}(v_h + b_h) + \dfrac{\dot{p}_h}{\chi} \right) p_h^* d\Omega = 0 \,. \end{array}\right. \tag{3.23}$$

In practice, the system 3.23 is equivalent to the following system:

$$
\begin{cases}
\displaystyle\sum_{K\in\mathcal{T}_h(\Omega)} \Big[\int_K \boldsymbol{S}(\boldsymbol{v}_h) : \dot{\boldsymbol{\varepsilon}}(\boldsymbol{v}_h^*)d\Omega_K + \int_K \boldsymbol{S}(\boldsymbol{b}_h) : \dot{\boldsymbol{\varepsilon}}(\boldsymbol{v}_h^*)d\Omega_K - \int_K p_h \cdot \nabla\boldsymbol{v}_h^* d\Omega_K - \int_{\Gamma_K} \boldsymbol{t}\cdot\boldsymbol{v}_h^* d\Gamma_K \Big] = 0\,,\\[2mm]
\displaystyle\sum_{K\in\mathcal{T}_h(\Omega)} \Big[\int_K \boldsymbol{S}(\boldsymbol{v}_h) : \dot{\boldsymbol{\varepsilon}}(\boldsymbol{b}_h^*)d\Omega_K + \int_K \boldsymbol{S}(\boldsymbol{b}_h) : \dot{\boldsymbol{\varepsilon}}(\boldsymbol{b}_h^*)d\Omega - \int_K p_h \cdot \nabla\boldsymbol{b}_h^* d\Omega_K - \int_{\Gamma_K} \boldsymbol{t}\cdot\boldsymbol{b}_h^* d\Gamma_K \Big] = 0\,,\\[2mm]
\displaystyle\sum_{K\in\mathcal{T}_h(\Omega)} \Big[\int_K \Big(tr\dot{\boldsymbol{\varepsilon}}(\boldsymbol{v}_h + \boldsymbol{b}_h) + \frac{\dot{p}_h}{\chi} \Big) p_h^* d\Omega_K \Big] = 0\,.
\end{cases}
\tag{3.24}
$$

Thanks to the properties of the bubble function 3.20, we obtain:

$$
\int_K \boldsymbol{S}(\boldsymbol{v}_h) : \dot{\boldsymbol{\varepsilon}}(\boldsymbol{b}_h^*)d\Omega_K = \int_{\Omega_h} \boldsymbol{S}(\boldsymbol{b}_h) : \dot{\boldsymbol{\varepsilon}}(\boldsymbol{v}_h^*)d\Omega_K = 0
\tag{3.25}
$$

$$
\int_{\Gamma_K} \boldsymbol{t}\cdot\boldsymbol{b}_h^* d\Gamma_K = 0
\tag{3.26}
$$

Bearing these properties and removing the subscript h for more clarity, the system 3.24 simplifies to:

$$
\begin{cases}
\displaystyle\sum_{K\in\mathcal{T}_h(\Omega)} \Big[\int_K \boldsymbol{S}(\boldsymbol{v}) : \dot{\boldsymbol{\varepsilon}}(\boldsymbol{v}^*)d\Omega_K - \int_K p \cdot \nabla\boldsymbol{v}^* d\Omega_K - \int_{\Gamma_K} \boldsymbol{t}\cdot\boldsymbol{v}^* d\Gamma_K \Big] = 0\,,\\[2mm]
\displaystyle\sum_{K\in\mathcal{T}_h(\Omega)} \Big[\int_K \boldsymbol{S}(\boldsymbol{b}) : \dot{\boldsymbol{\varepsilon}}(\boldsymbol{b}^*)d\Omega_K - \int_K p \cdot \nabla\boldsymbol{b}^* d\Omega_K \Big] = 0\,,\\[2mm]
\displaystyle\sum_{K\in\mathcal{T}_h(\Omega)} \Big[\int_K \Big(tr\dot{\boldsymbol{\varepsilon}}(\boldsymbol{v} + \boldsymbol{b}) + \frac{\dot{p}}{\chi} \Big) p^* d\Omega_K \Big] = 0\,.
\end{cases}
\tag{3.27}
$$

This system is non-linear due to the non-linearity of the constitutive behavior, which is here chosen to be elastic-viscoplastic. The non-linearity related to the material behavior does not require fundamental reformulation of the problem, as opposed to geometric non-linearities. However, as it is often the case, the constitutive law and the system of equations are written in incremental form. Small step increments are in fact needed to correctly account for path dependance and obtain physically sound solutions. In incremental form, the problem can then be formulated as follows:

Given $\boldsymbol{S}_n, p_n, \boldsymbol{t}_n$ and Ω_n such that equilibrium is satisfied at time t, $\forall(\boldsymbol{v}^* + \boldsymbol{b}^*, p^*) \in (W_0, P)$:

$$
\begin{cases}
\displaystyle\sum_{K\in\mathcal{T}_h(\Omega_n)} \Big[\int_K \boldsymbol{S}_n(\boldsymbol{v}) : \dot{\boldsymbol{\varepsilon}}(\boldsymbol{v}^*)d\Omega_K - \int_K p_n \cdot \nabla\boldsymbol{v}^* d\Omega_K - \int_{\Gamma_K} \boldsymbol{t}_n \cdot \boldsymbol{v}^* d\Gamma_K \Big] = 0\\[2mm]
\displaystyle\sum_{K\in\mathcal{T}_h(\Omega_n)} \Big[\int_K \boldsymbol{S}_n(\boldsymbol{b}) : \dot{\boldsymbol{\varepsilon}}(\boldsymbol{b}^*)d\Omega_K - \int_K p_n \cdot \nabla\boldsymbol{b}^* d\Omega_K \Big] = 0\\[2mm]
\displaystyle\sum_{K\in\mathcal{T}_h(\Omega_n)} \Big[\int_K \Big(tr\dot{\boldsymbol{\varepsilon}}_n(\boldsymbol{v} + \boldsymbol{b}) + \frac{\dot{p}_n}{\chi} \Big) p^* d\Omega_K \Big] = 0
\end{cases}
\tag{3.28}
$$

Find $\boldsymbol{v}_{n+1}$ kinematically admissible, $\boldsymbol{S}_{n+1}, p_{n+1}, \boldsymbol{t}_{n+1}$ and Ω_{n+1} that satisfies the equilibrium

at time $t + \Delta t$, $\forall (v^* + b^*, p^*) \in (W_0, P)$:

$$
\begin{cases}
\displaystyle \sum_{K \in \mathcal{T}_h(\Omega_{n+1})} \left[\int_K S_{n+1}(v) : \dot{\varepsilon}(v^*) d\Omega_K - \int_K p_{n+1} \cdot \nabla v^* d\Omega_K - \int_{\Gamma_K} t_{n+1} \cdot v^* d\Gamma_K \right] = 0 \\[4mm]
\displaystyle \sum_{K \in \mathcal{T}_h(\Omega_{n+1})} \left[\int_K S_{n+1}(b) : \dot{\varepsilon}(b^*) d\Omega_K - \int_K p_{n+1} \cdot \nabla b^* d\Omega_K \right] = 0 \\[4mm]
\displaystyle \sum_{K \in \mathcal{T}_h(\Omega_{n+1})} \left[\int_K \left(tr\dot{\varepsilon}_{n+1}(v + b) + \frac{\dot{p}_{n+1}}{\chi} \right) p^* d\Omega_K \right] = 0
\end{cases}
\tag{3.29}
$$

In practice, if the time step is taken sufficiently small so as to enable small strain increments, Ω_{n+1} is taken equal to Ω_n. The configuration of the body is then updated via equation 3.15.

III.5 Resolution

III.5.1 Non linear system of equation to be solved

The nonlinear algebraic system of equations 3.24can be written as global residuals as follows:

$$
\mathcal{R} = \begin{cases}
\mathcal{R}^v (v_h, b_h, p_h) = \mathcal{R}^{vv} + \mathcal{R}^{vb} + \mathcal{R}^{vp} + \mathcal{F}^v = 0 \,, \\
\mathcal{R}^b (v_h, b_h, p_h) = \mathcal{R}^{bv} + \mathcal{R}^{bb} + \mathcal{R}^{bp} + \mathcal{F}^b = 0 \,, \\
\mathcal{R}^p (v_h, b_h, p_h) = \mathcal{R}^{pv} + \mathcal{R}^{pb} + \mathcal{R}^{pp} = 0 \,,
\end{cases}
\tag{3.30}
$$

Taking into consideration the various simplifications, the actual discrete problem 3.27 yields the following system, decoupled in terms of v_h and b_h:

$$
\mathcal{R} = \begin{cases}
\mathcal{R}^v (v_h, p_h) = \mathcal{R}^{vv} + 0 + \mathcal{R}^{vp} + \mathcal{F}^v = 0 \\
\mathcal{R}^b (b_h, p_h) = 0 + \mathcal{R}^{bb} + \mathcal{R}^{bp} + 0 = 0 \\
\mathcal{R}^p (v_h, b_h, p_h) = \mathcal{R}^{pv} + \mathcal{R}^{pb} + \mathcal{R}^{pp} = 0
\end{cases}
\tag{3.31}
$$

In a more general form, if a stands for a vector containing the discretization parameters (pressure and velocity), the incremental problem consists of solving $\mathcal{R}(a_{n+1}) = 0$ starting from a (pseudo) equilibrium solution at $\mathcal{R}(a_n) = 0$ such that $a_{n+1} = a_n + \Delta a_n$.

III.5.2 Resolution of the non linear system

A Newton-Raphson method is used to solve the non linear system 3.31. The Newton-Raphson method is the most widely used procedure for solving non-linear problems. It converges quite rapidly, providing that the initial guess is within the actual zone containing the solution. If this is the case, the convergence is quadratic, otherwise it diverges.

The method consists of linearizing the residu $\mathcal{R}(a_{n+1})$ with respect to the discretization parameter a. This yields:

$$\mathcal{R}(a_{n+1}^{i+1}) \cong \mathcal{R}(a_{n+1}^i) + \left(\frac{\partial \mathcal{R}}{\partial a}\right)_{n+1}^i \delta a_n^i = 0 , \tag{3.32}$$

where i stands for the iteration counter. The iterative correction is then given by:

$$\left(\frac{\partial \mathcal{R}}{\partial a}\right)_{n+1}^i \delta a_n^i = -\mathcal{R}(a_{n+1}^i) . \tag{3.33}$$

Once convergence is achieved, the variables are updated as follows:

$$a_{n+1}^{i+1} = a_{n+1}^i + \delta a_n^i = a_n + \Delta a_n^i . \tag{3.34}$$

Applying this procedure to the system 3.31 yields, on the level of each element, the following algebraic system:

$$\begin{pmatrix} K^{vv} & 0 & K^{vp} \\ 0 & K^{bb} & K^{bp} \\ K^{pv} & K^{pb} & K^{pp} \end{pmatrix}_{n+1}^i \begin{pmatrix} \delta v \\ \delta b \\ \delta p \end{pmatrix}_n^i = - \begin{pmatrix} \mathcal{R}^v \\ \mathcal{R}^b \\ \mathcal{R}^p \end{pmatrix}_{n+1}^i \tag{3.35}$$

where K^{xy} are the local stiffness matrix components. These are given by:

$$K^{xy} = \frac{\partial \mathcal{R}^{xy}}{\partial z}$$

with $(x, y) \in \{v, b, p\}$.

A condensation of the bubble is used at the local level in order to eliminate the extra degree of freedom δb associated with the bubble [Jaouen, 1998]:

$$\delta b = - \left(K^{bb}\right)^{-1} \left(\mathcal{R}^b + K^{bp}\delta p\right) . \tag{3.36}$$

This yields the following local system, where the unknowns are the pressure and the three components of the velocity field:

$$\begin{pmatrix} K^{vv} & K^{vp} \\ K^{pv} & K^{pp} - K^{bp^t}\left(K^{bb}\right)^{-1} K^{bp} \end{pmatrix}_{n+1}^i \begin{pmatrix} \delta v \\ \delta p \end{pmatrix}_n^i = - \begin{pmatrix} \mathcal{R}^v \\ \mathcal{R}^p - K^{bp^t}\left(K^{bb}\right)^{-1} \mathcal{R}^b \end{pmatrix}_{n+1}^i . \tag{3.37}$$

In effect, the use of the bubble function in the mini-element is equivalent to adding stabilizing terms to the local (and so to the global) stiffness matrix of the problem. These stabilizing terms are responsible for the versatility of the mini-element, which can be used in all contexts (compressible or nearly incompressible materials).

III.5.3 General solution procedure and numerical implementation

In order to solve the mechanical problem, the constitutive law has to be coupled to this finite element scheme. It is important to note that, given the type of element used in this work, there is only one Gauss point per element for the integration of the constitutive equations. The solution procedure at a given time step can be summarized as follows:

1. calculate the initial estimate of the velocity vector (solution of the previous increment),

2. compute the elemental velocity gradient used as input to the constitutive model,

3. iterate at the constitutive law level in order to compute state variables at time $t + \Delta t$ and the tangent modulus,

4. solve the global system of equations for the velocity and pressure fields at time $t + \Delta t$ using a Newton-Raphson algorithm and go back to point 2 until convergence is achieved,

5. if convergence occurs, update the velocity and pressure fields and the configuration of the body and move on to the next increment,

The computations presented in this work are carried out using the C++ library *CimLib* [DIGONNET et al., 2007] on a 192 cores Opteron 2,4 Ghz linux cluster. *CimLib* is a parallel multi-component library that includes all the necessary tools for the resolution of the finite element problem. Practically speaking, the solution of the corresponding linearized system of equations is obtained with PETSC (Portable, Extensible Toolkit for Scientific Computation) [BALAY et al., 1997] using a preconditionned iterative solver, namely the generalized minimum residual method. An automatic time stepping algorithm is used to ensure that the strain increments remain small so as to ensure optimum convergence of the procedure. Moreover an automatic subincrementation algorithm is used in order to ensure accurate integration of the constitutive equations. The call to the constitutive law is done in two ways depending on the form in which its is used. In effect, in this work, most applications are performed using the constitutive law in its single crystal form, while in some case, the mean-field form of the law is used, namely, the Taylor transition rule is used to compute a polycrystal behavior at each integration point instead of a single crystal one. In the first case, the constitutive equations are solved for all elements at the same time and the computed state variables are stored in order to be used during the construction of the local matrices. When the polycrystal form and the single crystal form of the constitutive law are used together, as it is the case in *chapter 6*, the constitutive law is called during the actual construction of the local system of equations for each element as illustrated by the dotted line in figure 3.7. In this case, the statements (A-1) and (D-1) are not executed as the loop on all elements is done through the linear solver. This second procedure enables the use of different constitutive behaviors (crystal/polycrystal or even the use of any other constitutive law) but it is computationally more expensive compared to the first procedure.
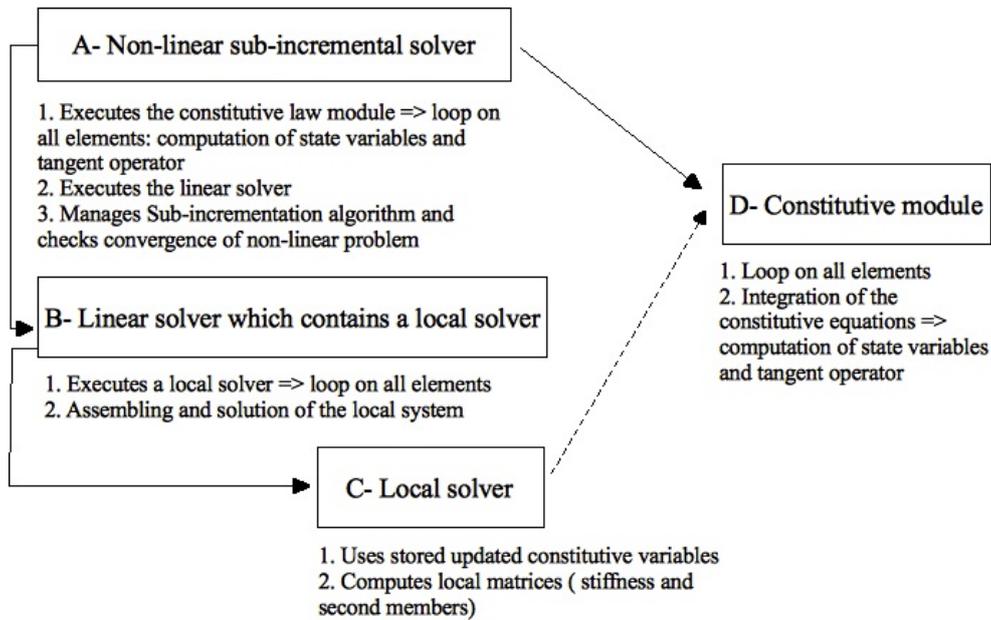
Fig. 3.7: CimLib resolution procedure

IV   Conclusion

In this chapter, we presented some of the strategies used to account for grain interaction and for the partitioning of the deformation among the grains of a polycrystalline aggregate. On the one hand, there are simplified grain interaction models that have the advantage of being simple enough to implement and use, for example, in large scale finite element simulations of metal forming processes. Authors have strived to incorporate more physically based assumptions in their models so as to optimize them while maintaining their simplicity. On the other hand, CPFEM simulations, where grains are represented explicitly, represent the ultimate grain interaction model, as seen in this chapter. Moreover, if more than element is used to discretize each grain, grain-scale heterogeneities can be predicted. In the following chapter, the tools necessary for generating and meshing the microstructure are presented as well as the level set representation, which is one of cornerstones of our numerical approach.

Chapter 4

Generating and Meshing polycrystalline aggregates

I Microstructure generation and meshing overview

Throughout the literature, different approaches for representing the microstructure have been implemented depending on the intended objective and the computational limitations. Indeed, the more complicated and resolved the microstructure is, the more computationally expensive the resolution of the finite element problem becomes. Using as low as one element per grain (with more than one integration point though) is sufficient for providing results that are in fair agreement with experimental texture measurements for example. [BACHU and KALIDINDI, 1998; KALIDINDI et al., 1992; SARMA and DAWSON, 1996] used cubes or bricks to represent grains with this intended objective as illustrated by figure 4.1. The relatively good predictions provided by such models is actually not surprising, given the fact that the Taylor FC polycrystal model provides, until today, a relatively adequate approximation of texture evolution, while neglecting microstructure representation altogether. However, such representations do not make use of the advantages of the CPFEM method as discussed previously in accounting for in-grain heterogeneities. Moreover, this type of representation (and elements) lead to simplified geometrical description of grains and their boundaries, whereas taking the grain shape into account is important when investigating local fields. The influence of grain shape on local stress and strain fields has been highlighted by several studies. Delannay and co-workers showed that using grains shaped as truncated octahedrons instead of bricks enabled better predictions of local strain heterogeneities [DELANNAY et al., 2006]. A similar argument was developed by Mika and Dawson while using rhombic dodecahedra [MIKA and DAWSON, 1998]. More recently, Ritz and Dawson compared cubic, rhombic, dodecahedral and truncated octahedral shaped grains in terms of stress variations [RITZ and DAWSON, 2009]. The grain shape and topological arrangement has also an important influence if individual grain rotation and local orientation gradients are investigated. This is all the more important if the digital microstructure is representing an

actual real microstructure as in [BHATTACHARYYA et al., 2001; KALIDINDI et al., 2004].

(a)   (b)
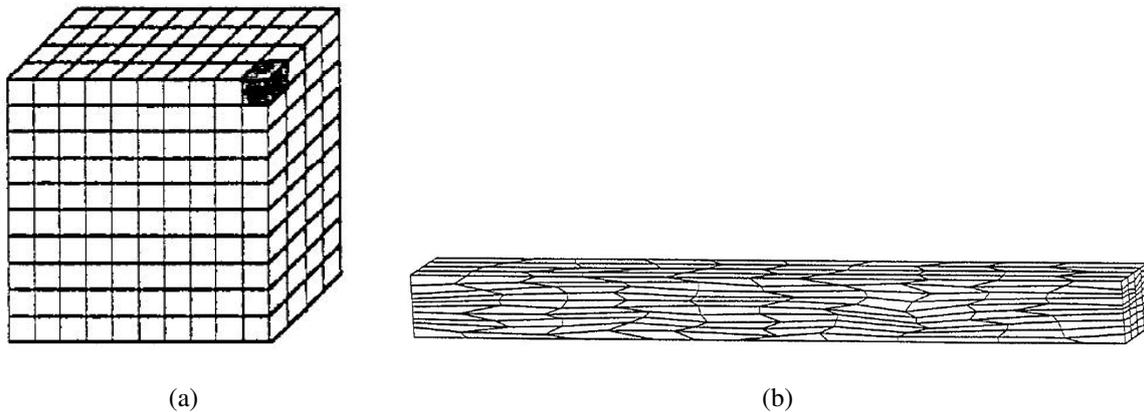
Fig. 4.1: Finite-element polycrystal with brick shaped grains (one element per grain): (a) initially; (b) after 70 % height reduction [BACHU and KALIDINDI, 1998]

The finite element method also requires the discretization of the microstructure into a given finite element mesh. The mesh can be structured ("regular") or unstructured ("free") with various degrees of mesh refinement. In order to compare the results of different simulations throughout the literature in terms of mesh sensitivity, the element interpolation scheme has to be taken into account. However, some general remarks can be made. Coarse discretization, used in general in conjunction with regular meshes and the previously mentioned simplified representation of grains, is relatively adequate for texture evolution predictions [SARMA and DAWSON, 1996]. Other authors have shown that increasing mesh refinement has very little impact on the global stress-strain response of the polycrystal in studies using conventional crystal plasticity [BARBE et al., 2001a,b; BUCHHEIT et al., 2005; DIARD et al., 2005] while a relatively more important impact is observed when using non-local approaches [CHEONG et al., 2005]. All agree that finely discretized meshes are needed to capture local details of microstructure evolution and local gradients, regardless of the choice of mesh type or the choice of the constitutive model. Most importantly, if one is interested in capturing local effects related to grain boundaries, the finite element mesh has to correctly describe the actual grain boundary geometries. Diard and co-workers, in [DIARD et al., 2005], highlight the drawbacks of using regular meshes in the case of Voronoi-based topologies as they badly describe grain boundaries. A comparison is made between a structured and unstructured conforming mesh (see fig. 4.2) and it is shown that gradients across grain boundaries are not well captured with a structured mesh . Zhao and coworkers develop a similar argument [ZHAO et al., 2007] . As the mesh used is structured, they decide to represent grains using truncated octahedrons in order to correctly describe grain boundaries (see fig. 4.3).

<center>(a)   (b)</center>
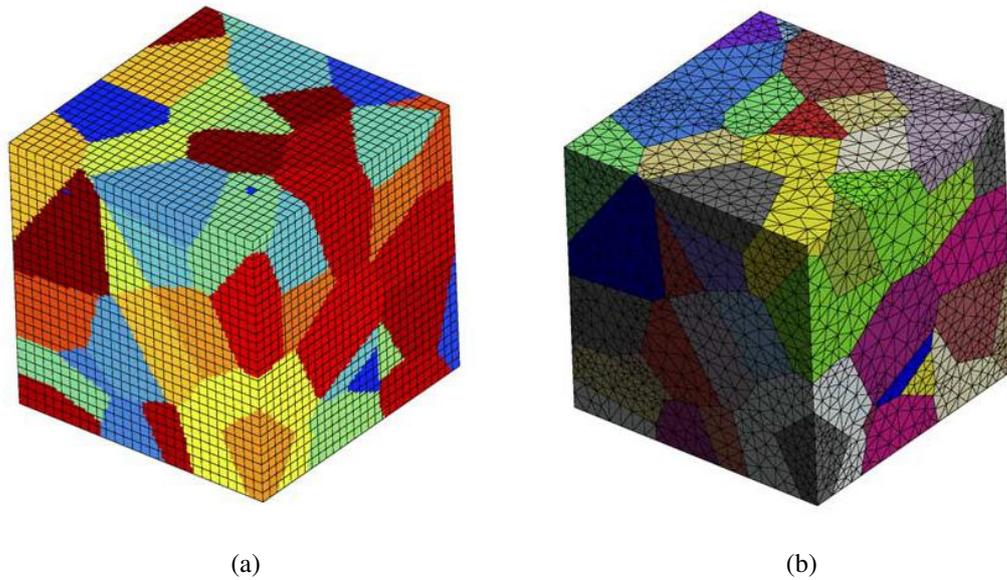
Fig. 4.2: A Voronoi based polycrystal: (a) regular mesh; (b) unstructured conforming mesh where the boundaries of the grains are explicitly described by the mesh nodes[DIARD et al., 2005]

Two main reasons seem to hinder the use of 3D microstructures discretized using highly refined unstructured meshes.The first reason is related to the prohibitive computational cost, associated with the computational time needed for the integration of the constitutive law, and the important computational capacity which is required in order to solve the FE problem. Very little quantitative information is available in the literature on the computational costs of the different formulations and it is very difficult to assess such information anyway as numerical tools and hardware configurations vary. However, this limitation has pushed several authors to limit their studies to 2D meshes, 3D meshes with only one element in the thickness [ERIEAU and REY, 2004] or 3D meshes with as large as ≈ 12000 elements per grain [ZHAO et al., 2007]. The second problem is related to the need to reconstruct the mesh, especially in simulations carried out in a Lagrangian context where element degeneracy occurs quite rapidly. Eulerian approaches provide one possible remedy to this problem [BARTON et al., 2004]. The Lagrangian approach is still the most used and element distortion poses substantial problems, especially in applications related to large deformations or localization phenomena (e.g. rolling, friction stir welding (FSW), equal channel angular pressing (ECAP), shear bands formation...). Reconstruction of the mesh was only reported in relatively large deformation studies (70 % strain) where structured meshes were used [DAWSON et al., 1994; SARMA et al., 1998]. The reconstruction of such meshes is then quite straightforward. Unstructured meshes were used either in small strain applications [DIARD et al., 2005] or in large strain applications as reported by Maniatty and co-authors where moderate strains were achieved (56 % macroscopic compression) without the need for remeshing [MANIATTY et al., 2007].

<center>55</center>

(a)   (b)
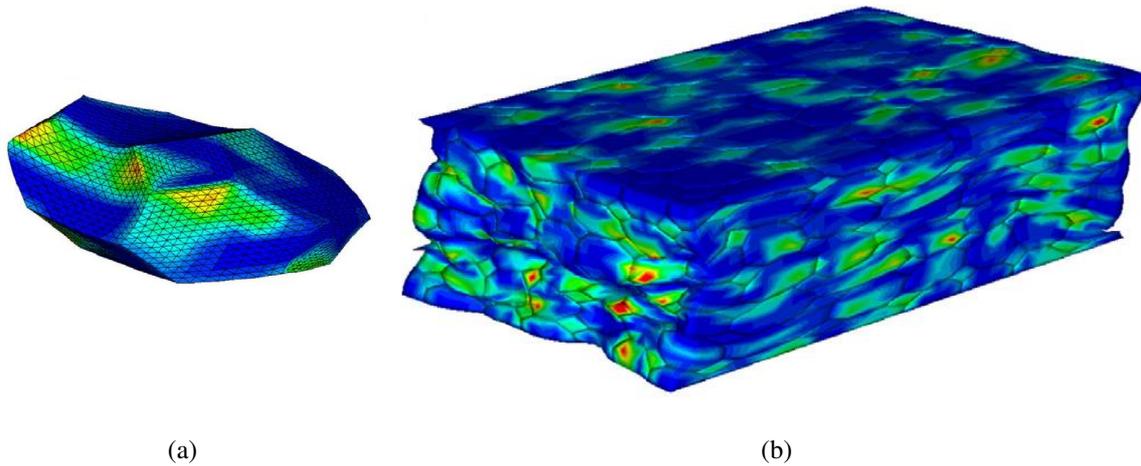
Fig. 4.3: Truncated octahedron polycrystal after 50 % plain strain compression: (a) the mesh of one grain in the deformed configuration (12,288 elements); (b) deformed polycrystal. Color indicates the misorientation between the initial and deformed configurations. [ZHAO et al., 2007]

Thus, in large strain applications where local information is sought, several numerical requirements can be highlighted: the ability to correctly represent grains and grain boundaries, the possibility to use highly refined unstructured meshes but at the same time optimized in order to reduce the computational burden, and finally the possibility to reconstruct such meshes whenever it is needed.

II   Generating digital microstructures

The digital microstructure may either correspond to an idealized polycrystalline aggregate or to an experimentally observed one. Robust experimental and numerical techniques are needed for the 3D characterization of the microstructure [GROEBER et al., 2008a] and the subsequent reconstruction step [GROEBER et al., 2008b]. The DIGIMICRO software, currently under development, represents a first step towards this objective. It provides a window-based plateform for constructing 2D or 3D microcrostructures [BERNACKI et al., 2007a]. The programming work is done in C++, and a user friendly interface with interactive menus is available. The software is based on the Digital material concept introduced by Dawson [DAWSON et al., 2005]. The idea is to generate virtual/ digital samples and to probe them after their construction in order to obtain microstructures that match specific experimental criteria. Typically, a model polycrystal would be generated exhibiting a desired texture or grain boundary texture, grain size ditribution, a specific grain or subgrain morphology...etc. At its current development stage, the DIGIMICRO software can be used to construct virtual microstructures based on a recursive Voronoï tessellation algorithm. This latter can also be used to construct subgrains. Figure 4.4 shows two model polycrystals created with the DIGIMICRO software.
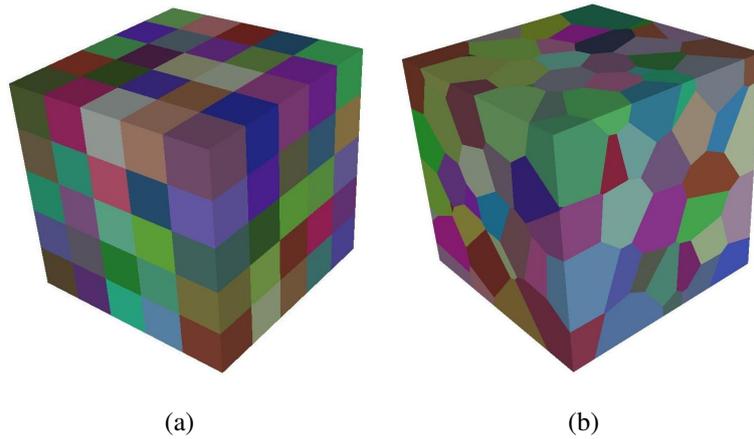
Fig. 4.4: A model polycrystal with (a) cubic grains; (b) Voronoi shaped grains. The color scheme is representative of the grains numbering

The DIGIMICRO software can also read pixelized or voxelized experimental data. Typically, microstructures images obtained using orientation image microscopy software can be first converted into the DIGIMICRO format giving a pixelized 2D microstructure. A 3D polycrystal is then constructed by performing an extrusion in the third dimension as seen in figure 4.6 thereby yielding a columnar microstructure. Also a Monte-Carlo (MC) algorithm, intended for simulating recrystallization, can be used to evolve a given microstructure and obtain different instantiation of a given microstructure as seen in figure 4.5. The MC algorithm can also be used to evolve a 2D experimental microstructure and then combine different 2D layers in order to reconstruct a 3D non-columnar microstructure as seen in figure 4.7 where only 10 grains are illustrated for the sake of clarity. This is used for generating the non-columnar microstructure in chapter 6.
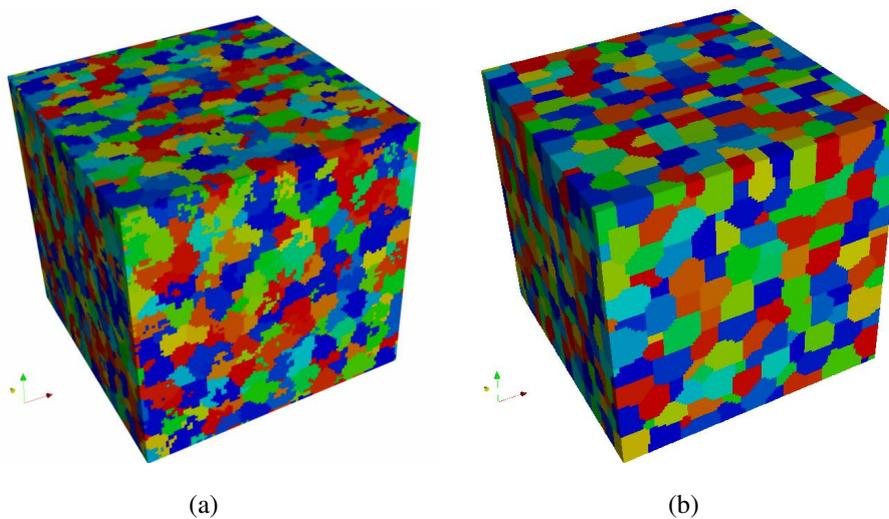
Fig. 4.5: (a) Voxelized microstructure and (b) the same microstructure after application of the MC algorithm
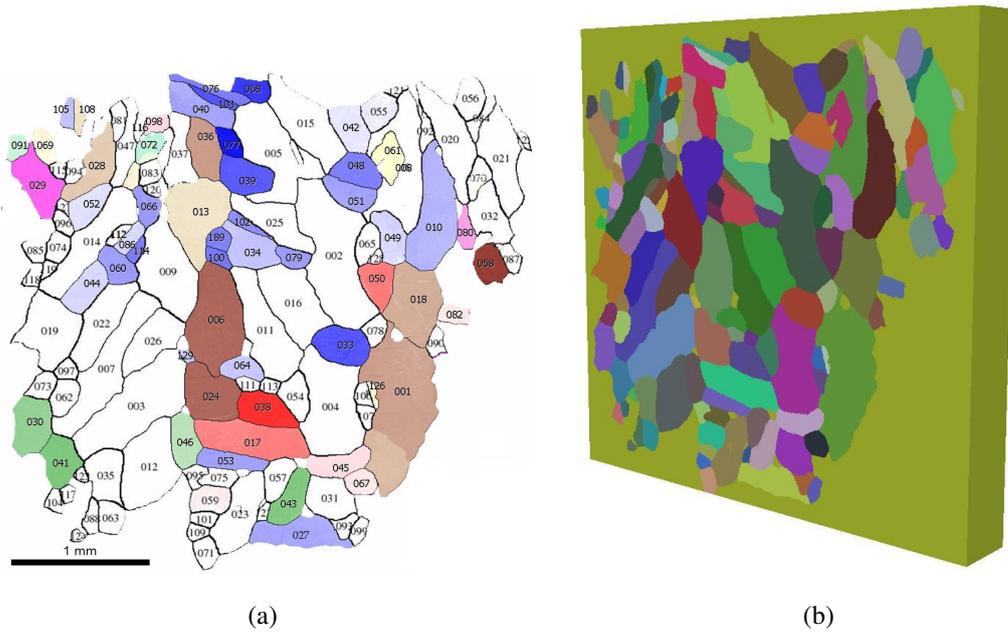
Fig. 4.6: (a) Experimental microstructure and (b) the corresponding DIGIMICRO extruded voxelized polycrystal
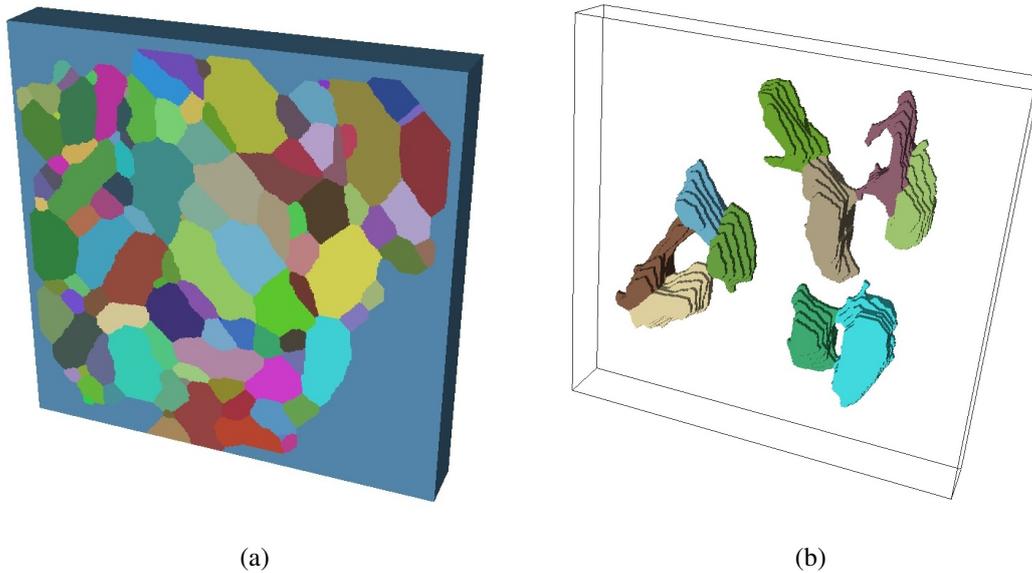
Fig. 4.7: (a) A 3D non-columnar polycrystal based on the 2D experimental microstructure of figure 4.6(a) , (b) ten grains of the microstructure

Finally, regarding grain properties, each individual grain shape is approximated by a fitting ellipsoid as seen in figure 4.8(b). Probing algorithms can then measure particular instantiations of a microstructure, e.g. grain volume and grain shape distribution as seen on figure. The obtained geometrical features can be combined manually according to desired criteria of sizes and shapes. Crystallographic orientation is assigned either randomly or based on an input file provided by the user. More advanced algorithms for discretizing a given texture are not avail-

able yet. Such discretization, when necessary is performed in collaboration with the Université Catholique de Louvain [MELCHIOR and DELANNAY, 2006].
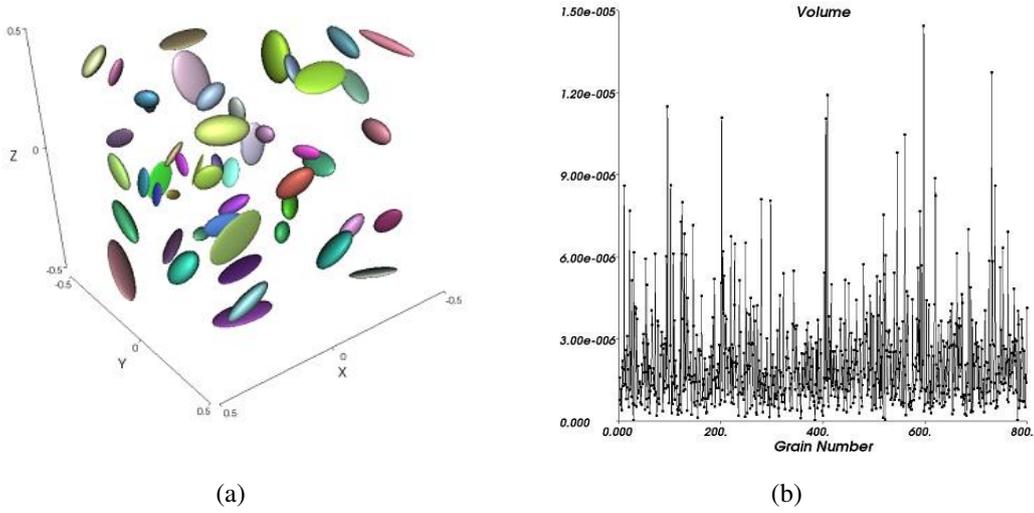
Fig. 4.8: (a) Approximation of grain shape by fitting ellipsoids, (b) Grain volume distribution

It is worth noting that generating simple microstructures, typically Voronoï based ones, can also be performed in CimLib. However, all treatments of voxelized microstructures are performed using the DIGIMICRO software.

III From geometrical representation to FE computations

III.1 Initial mesh generation

The MTC mesh generator, developed by T. Coupez, constructs 2D triangular and 3D tetrahedral unstructured meshes. MTC is a topological mesh generator in the sense that it transforms a given topology into a mesh by requiring that the sum of the volumes of the generated elements be equal to the volume of the part being meshed [COUPEZ, 2000]. To be more precise, a minimum volume principle ensures that the generated topology ends up being a proper mesh of the domain (i.e no element overlaps and no gaps) while also respecting a minimum quality criterion. In practice, the mesh is generated by iterative local optimization using cut and paste operations while improving simultaneously the quality of the elements, as illustrated by figure 4.9. The quality of an element K is defined through a normalized shape factor given by:

$$c(K) = c_0 \frac{|K|}{l(K)^d} \, , \tag{4.1}$$

where c_0 is a normalisation coefficient, $|K|$ the volume of the element, $l(K)^d$ the average length of the edges of the element and d the space dimension.
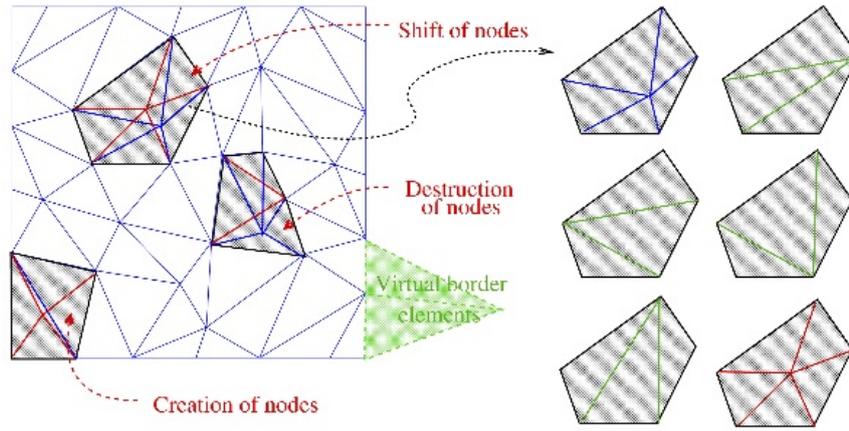
Fig. 4.9: Local Mesh optimization process in MTC [MESRI et al., 2008]

Regarding the meshing of 3D microstructures, an initial, isotropic, homogeneous mesh is constructed using the MTC mesh generator. The meshing strategy chosen here is based on a "monolithic" approach i.e there is only one mesh over the whole domain, which is here the polycrystal. No information about individual domains (which are here represented by the grains) is given to MTC. Consequently, the constructed mesh does not conform to grain boundaries i.e. the interfaces are not explicitly described by nodes of the mesh. In the approach presented here, the boundaries are located implicitly using level set functions.

III.2 Level-set framework for grain representation

For a given grain, the level set function is defined as a signed distance function ϕ . For each node of the mesh, the distance to the closest grain boundary is computed and considered positive if the node is located inside the grain and negative outside. Linear shape functions are then used to interpolate nodal values over the whole domain. The iso-zero of the level set function represents the grain boundary, Γ, and the gradient of the level set function defines the normal to the boundary. More precisely, any distance function ϕ satisfies inherently the following properties [OSHER and SETHIAN, 1988]:

$$\|\nabla\phi\| = 1, \;\; \boldsymbol{n} = \frac{\nabla\phi}{\|\nabla\phi\|} = \nabla\phi\,. \tag{4.2}$$

Figure 4.10 illustrates, in 2D, this strategy for a square grain. The color scheme corresponds to the distance to the grain boundary Γ . As clearly seen, the boundary Γ crosses the triangular elements.
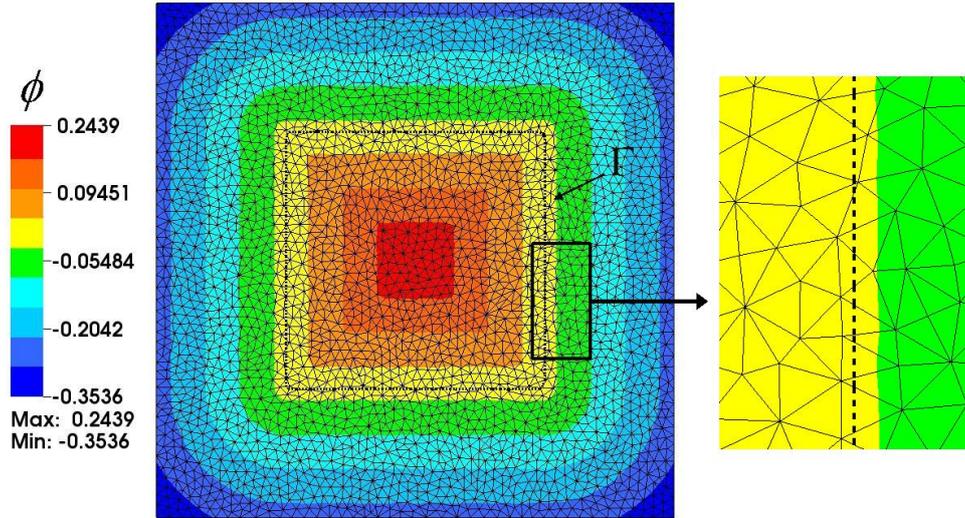
Fig. 4.10: Level set function for a square grain. The dotted line is the boundary of the grain Γ.

When dealing with a polycrystalline aggregate, an individual level set function is used for each grain: $\{\phi_i, 1 \leq i \leq N_G\}$ with N_G the total number of grains in the aggregate. One can also define a global level set function as [RESK et al., 2009]:

$$\phi_{glob} = max\{\phi_i, 1 \leq i \leq N_G\}. \tag{4.3}$$

The zero value of ϕ_{glob} corresponds to the grain boundary network. Figure 4.11 illustrates the global distance function for a 300 grains polycrystal generated by Voronoi tessellation. This level set framework is compatible with any type of microstructure (e.g. idealized Voronoi-based topologies or any other type of microstructure where grain boundaries are not necessarily flat).

(a)   (b)
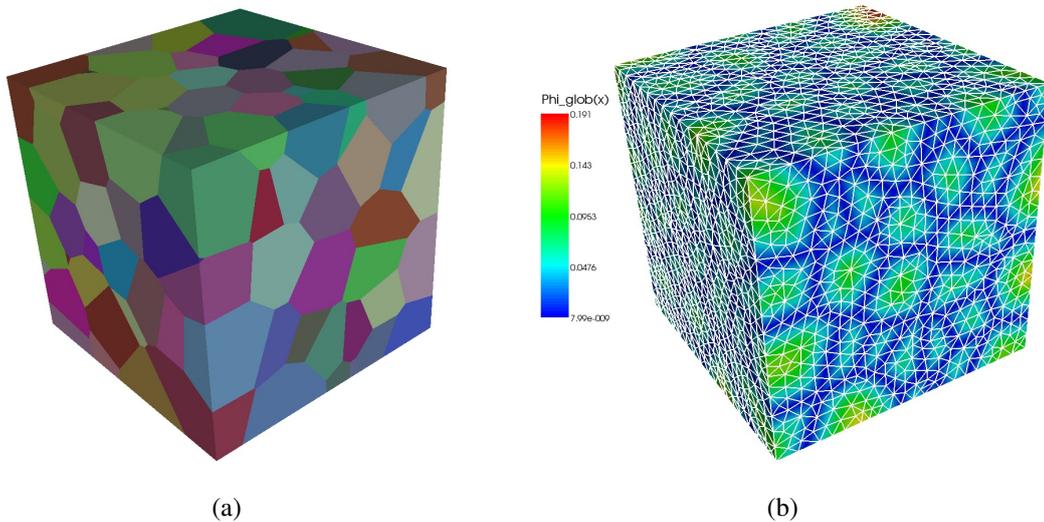
Fig. 4.11: (a) a 300 grains polycrystal and; (b) the corresponding global distance function ϕ_{glob}. Color scheme corresponds to the distance to the grain boundary network.

Level set methods are commonly used to track moving interfaces in various numerical applications [SETHIAN, 1996]. In this work, the level set function of each grain moves according to the material velocity, which corresponds here to the mesh velocity as the deformation is carried out in a Lagrangian context. As such, it enables the identification of the grains during the deformation and the analysis of local fields with respect to the distance to the grain boundaries. Although the level set function is constructed initially as a distance function, it looses its properties as the computation proceeds. As the mesh deforms, the level set function and its gradient are distorted and the properties (eq 4.2) are not preserved. This problem is overcome using a standard re-initialization technique based on the solution of a Hamilton-Jacobi equation [SETHIAN, 1996]. In practice, such re-initialization is performed periodically, typically every few time steps, which prevents the level set function from becoming too irregular as illustrated in figure 4.12, and preserves the position of the iso-zero (in black).

(a)   (b)
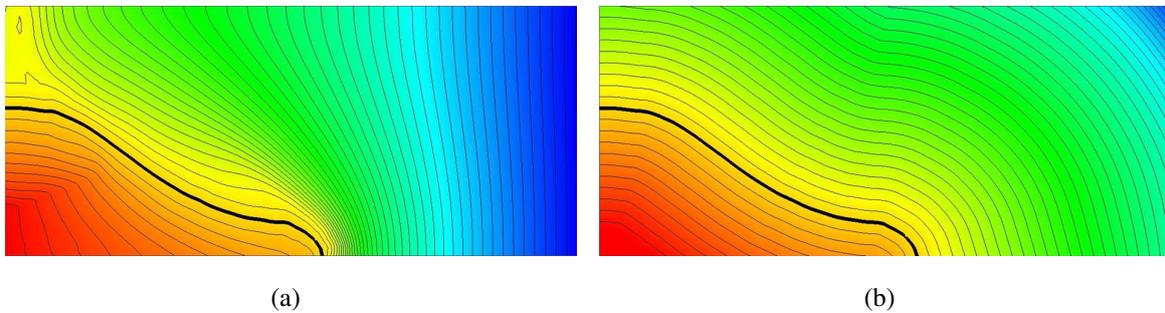
Fig. 4.12: A level set function (a) after a few time steps ; (b) after re-initialization. Color scheme corresponds to the distance function and the bold line is the interface of the domain Γ

III.3   Mesh adaptation

III.3.1   Metric definition

When MTC generates an isotropic mesh, it does so based on a metric field. A metric $\mathcal{M}$ is a real symmetric positive definite matrix used to change length calculations in a local base. As such, a new scalar product and a new norm are defined. For two vectors x and $y \in \mathbb{R}^3$, we have:

$$\begin{cases} \langle x, y \rangle_{\mathcal{M}} = x^T \mathcal{M} y \\ \|x\|_{\mathcal{M}} = \left(x^T \mathcal{M} x \right)^{1/2} \end{cases} \tag{4.4}$$

When such a metric is used to construct FE meshes, the size of all elements is prescribed to one in the local basis. In the usual Euclidian space, the element size in the direction ν_i then becomes $1/\sqrt{\lambda_i}$, where λ_i is the ith eigenvalue of the metric, and ν_i the associated eigenvector. If the three eigenvalues are equal and if they are uniform over the whole domain, the resulting mesh is isotropic and homogeneous. However, with a non uniform metric field, the mesh size and mesh refinement directions can be controlled locally, leading to an "anisotropic" mesh.

III.3.2 Anisotropic mesh adaptation

The level set functions provide the information needed for the construction of a metric field : grain boundaries are accurately identified by the iso-zero of the level set functions, and their normals are aligned with the gradient of the level set functions. As a starting point, let us consider a single level set function ϕ. Within a layer of thickness e (fig. 4.13(a)) close to the grain boundary, let h_2 be the desired mesh size in the direction of $\nabla\phi$ and let h_1 be the desired mesh size in directions perpendicular to $\nabla\phi$. Let us finally require an isotropic mesh size equal to h_1 outside the grain boundary layer. The metric $\mathcal{M}$ is then expressed as follows [Resk et al., 2009]:

$$\mathcal{M} = C\,(\nabla\phi \otimes \nabla\phi) + B\mathbb{1}\,, \tag{4.5}$$

where $\mathbb{1}$ is the identity tensor, B and C scalars given by:

$$B = \frac{\mathbb{1}}{h_1^2}\,, \quad C = \begin{cases} 0 & \text{if } |\phi| > \dfrac{e}{2} \\ \dfrac{1}{h_2^2} - \dfrac{1}{h_1^2} & \text{if } |\phi| \leq \dfrac{e}{2} \end{cases}. \tag{4.6}$$

The eigenvalues of the metric near the boundary are:

$$\begin{cases} \lambda_2 = \left(\dfrac{1}{h_2^2} - \dfrac{1}{h_1^2}\right)\|\nabla\phi\|^2 + \dfrac{1}{h_1^2} = \dfrac{1}{h_2^2}\,, \\ \lambda_1 = \lambda_3 = \dfrac{1}{h_1^2}\,, \end{cases} \tag{4.7}$$

where λ_2 is associated with the eigenvector $\nu_2 = \nabla\phi$ while the two other eigenvalues are associated to the basis vectors (ν_1, ν_3) of the plane tangent to the boundaries. Clearly, if h_2 is chosen much smaller than h_1, $\nabla\phi$ corresponds to the refinement direction and the elements are stretched in the plane tangent to the boundaries as shown (in 2D) in figure 4.13(b). When dealing with a polycrystalline aggregate where multiple level set functions are used (one for each grain), a general procedure is needed for defining, at any point x of the domain, the appropriate refinement directions and the corresponding metric. Two cases can be considered:

(A) $\phi(x) > e/2$ for $\{1 \leq i \leq N_G\}$, which means that x lies in the "bulk" of the grains, i.e. far from any boundary. In figure 4.13(b), these points correspond to the isotropic regions with mesh size h_1

(B) $\phi(x) \leq e/2$ for $\{1 \leq i \leq N_G\}$ for n grains, $n \leq N_G$. Typically, in an isotropic Voronoï tesselation, planar grain boundaries (where $n = 2$) intersect along edges (where $n = 3$), and edges intersect at vertices (where $n > 3$). The n vectors $\nabla\phi_i$ along which refinement is required define a space V of dimension 1, 2, or 3.

In case (B), if V is one-dimensional, there is only one direction of mesh refinement and the metric takes the form given by equations 4.5 and 4.6. When V is three-dimensional, an isotropic

metric is chosen, this time with a mesh size h_2. When V is two-dimensional, the required refinement is obtained with the following metric:

$$\boldsymbol{M} = C \left(\nabla\phi_1 \otimes \nabla\phi_1\right) + C \left(\nabla\phi_1^{\perp V} \otimes \nabla\phi_1^{\perp V}\right) + B\mathbb{1} \,. \tag{4.8}$$

Here, V is the plane defined by vectors $(\nabla\phi_1, \nabla\phi_1^{\perp V})$. The metric 4.8 prescribes a mesh size h_2 in the plane V, and a mesh size h_1 in the direction normal to V [Resk et al., 2009].

As the ϕ_i functions are linearly interpolated over an element, $\nabla\phi_i$ are piecewise constant. Since the mesh generator considers metrics as nodal values of the mesh, a standard conversion is performed, by which a nodal value of $\nabla\phi_i$ is calculated as a volume average of the neighboring elements values. This, in turn, has the effect of smoothing out discontinuities in $\nabla\phi_i$ which may arise at grain boundary corners or edges. The outcome is illustrated in figure 4.13(b), where the mesh is 2D for the sake of clarity.

(a)   (b)
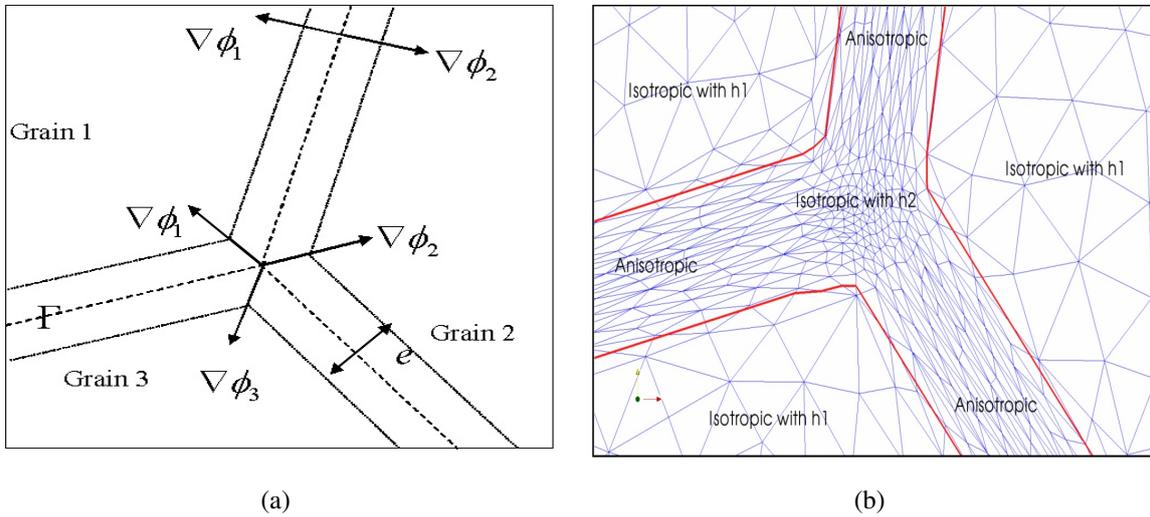
Fig. 4.13:   (a) 3 grains in 2D ; (b) the corresponding adapted anisotropic mesh [Resk et al., 2009].

As mentioned above, MTC, when generating (or adapting) the mesh according to a given metric, ensures, as much as possible, that the elements generated respect a given quality, as defined by equation 4.1. In this equation, the length and volume calculations take the local metric into account [Gruau and Coupez, 2005]. For an isotropic metric, this shape factor gives the highest quality when all edges of the element have the same length. The worst quality corresponds to elements which tend to degenerate from a volume to a surface (in 3D), or from a surface to a segment (in 2D). For an anisotropic mesh, the highest quality corresponds to an element which fits best the given metric [George and Bourouchaki, 1998]. Stretched elements may be acceptable with respect to an anisotropic metric while their quality is low if calculated in the usual Euclidean space. Figure 4.14 shows an example of the anisotropic meshing of 4 cubic grains in 3D and figure 4.15 illustrates the anisotropic 3D mesh of the microstructure shown in figure 4.11.
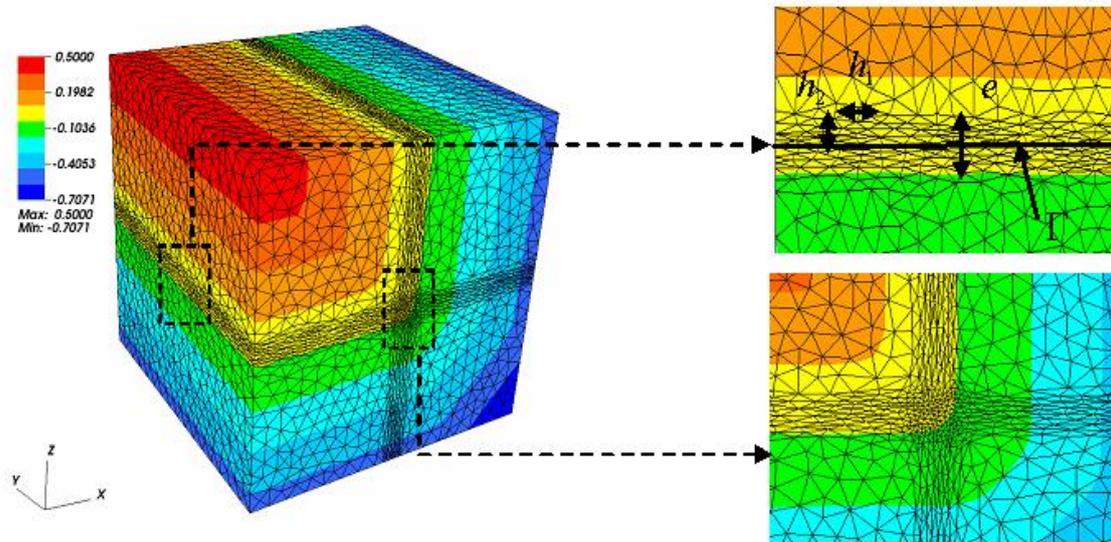
Fig. 4.14: Anisotropic adaptive meshing of a polycrystal made of four grains. The level set function of one grain is shown and a close up view of the region between two grains (top) and a close up of the central region (bottom)
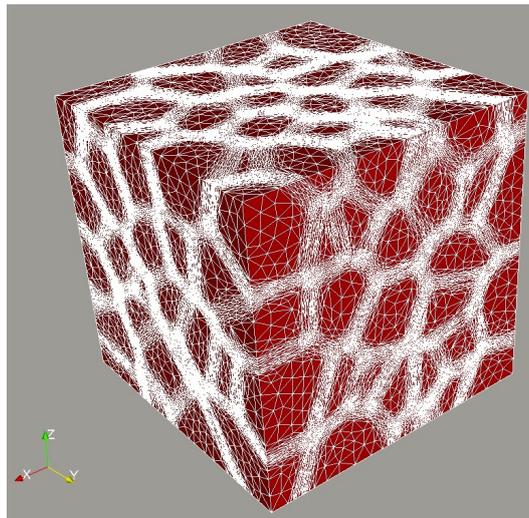
Fig. 4.15: A 300 grains polycrystal anisotropically meshed

III.4 Microstructural variable assignment

As the mesh does not conform exactly to grain boundaries, the microstructure is not perfectly reproduced. Because of the finite element interpolation scheme, there is only one Gauss point per element for the integration of the constitutive equations. A single crystallographic orientation is thus assigned to each element before the simulation. The lattice orientation is assigned depending on the position of the Gauss point (i.e. the center of gravity of the element) with respect to the interface Γ. The element belongs to grain i if $\phi_i \geq 0$. As seen in figure 4.16, mesh refinement near the interface enables a better reproduction of the grain boundary geome-

try. The advantage of using an anisotropic mesh is that it optimizes the number of nodes used for a given geometric accuracy. Indeed, as the elements are stretched in the direction tangent to the interface Γ, the number of nodes (and elements) in this direction is smaller compared to the isotropic case.

<center>(a)   (b)</center>
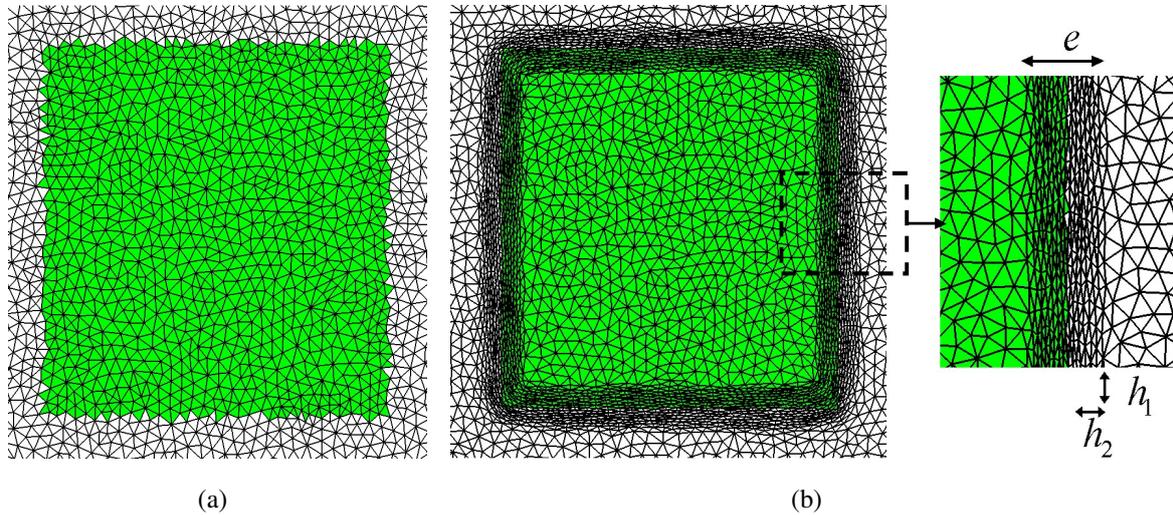
Fig. 4.16: (a) Isotropic mesh ; (b) anisotropic mesh. Color indicates the elements belonging to a rectangular grain.

III.5 Remeshing

The mesh generator reconstructs the mesh as often as needed if fed with the appropriate metric field. From the MTC point of view, remeshing is equivalent to the initial mesh construction. Most importantly, the issue of variables transport after remeshing is important. The technique used to transport variables from the old mesh to the new one depends on the order of interpolation of the element. In this work, the linear mini-element P1+/P1 is used. The corresponding procedure used can be summarized as follows. As seen on figure 4.17, the new node is first located with respect to an element of the old mesh. For nodal values, like level set function values, a linear interpolation scheme is used. For mechanical variables, or state variables, which are constant by element, a zero-order transport is performed, whereby the value of an element of the old mesh is directly transferred to the closest element in the new mesh based on the position of their respective Gauss points (centers of gravity).
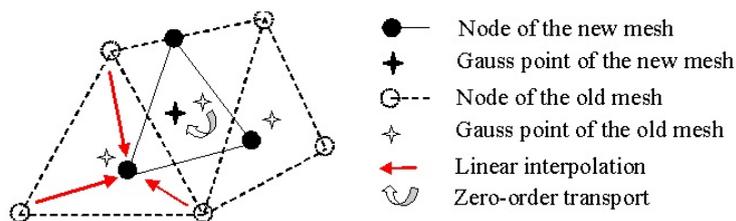
Fig. 4.17: Transport of variables after remeshing

Obviously, this transport operation go hand in hand with loss/distortion of information. For nodal values, a little diffusion is expected because of linear interpolation. The transported fields are somehow smoothed in the newly constructed mesh. For elemental variables, spatial distortion of their distribution is expected and some values might be "left out", typically if the new elements are bigger than the old ones. However, if the new mesh is "close" to the old one (if the elements size and shape are close i.e if the same metric is used to reconstruct the mesh), then this potential problem should be limited. One important transported variable during computation is the crystallographic orientation, which is one of the state variables of the constitutive law, and which determines the final crystallographic texture of the polycrystal, as it will be discussed in more details in chapter 6. The following test case allows a first assessment of the transport of crystallographic orientations in a global way.

(a)   (b)

(c)
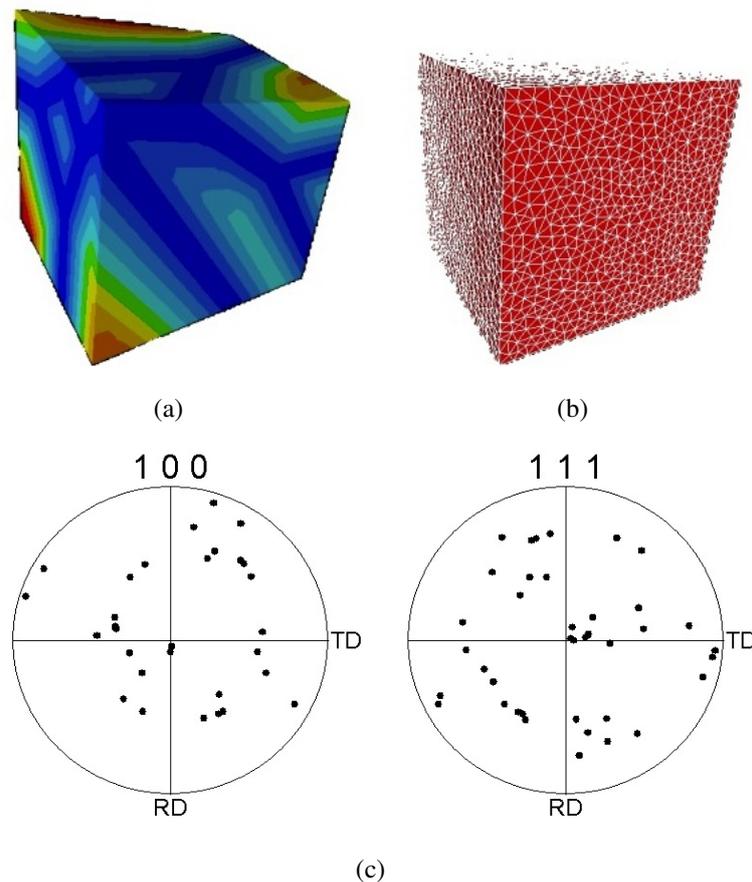
Fig. 4.18: (a) Global distance function for 10 grains; (b) initial isotropic mesh composed of 97968 elements and 18451 nodes and (c) initial {100} and {111} pole figures.

A ten grains polycrystal (see figure 4.18(a)) is subjected to pure uniaxial compression. The mesh used is isotropic and the computations were carried out on 8 processors of the cluster described in chapter 3 section III.5.3. Remeshing was performed automatically every 5 % thickness reduction. Total computation time, for a true strain of 42.5 %, without remeshing is approximately 5h and 7h30 with automatic remeshing. Figure 4.19 shows the deformation of the

10 grains after 12.5 % and 42.5 % true strain with and without remeshing and the corresponding {100} and {111} pole figures. Globally, as one can see, the texture evolution is not that sensitive to the diffusion that occurs during the re-mapping of the crystallographic orientations. Figure 4.20 illustrates the capability of the remeshing procedure to allow more straining, in this case up to 53.7 % true strain. Element degeneracy is avoided. However, in this last computation, the mechanical anisotropy of the grains leads to important physical folding which eventually causes the computation to breakdown.

(a)

(b)
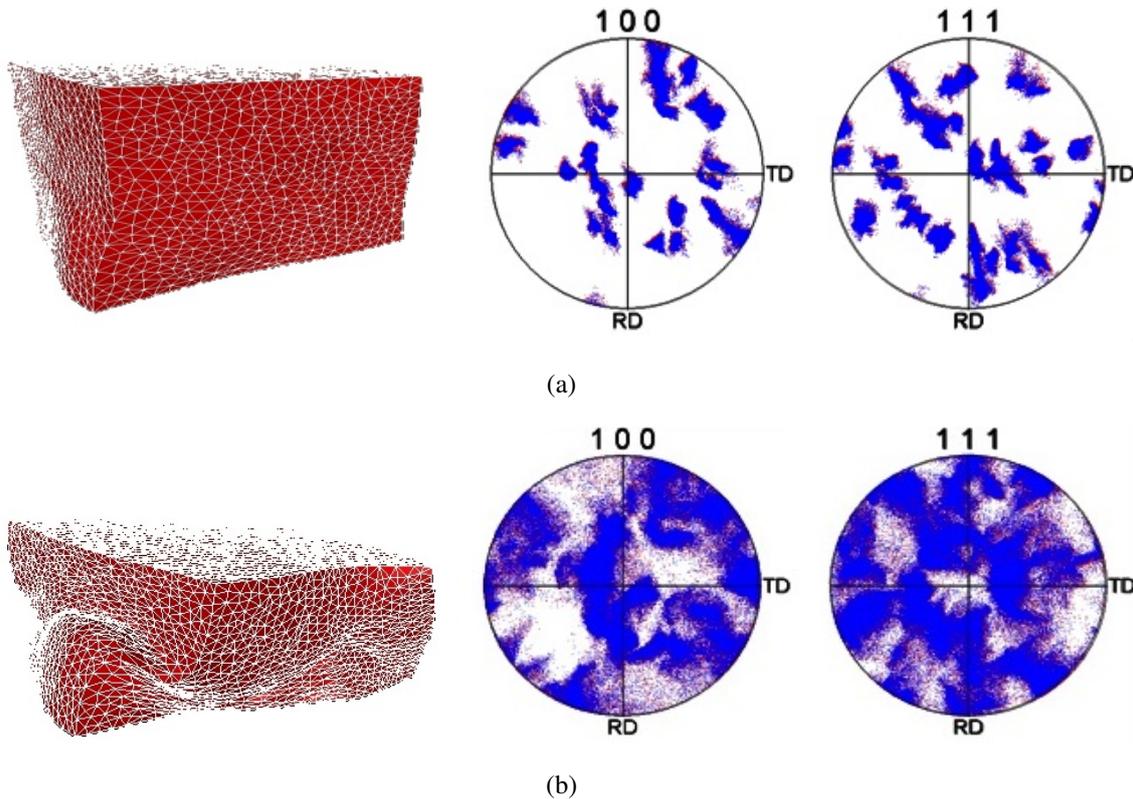
Fig. 4.19: Deformed mesh and the corresponding {100} and {111} pole figures: (a) after 12.5 % true strain; (b): after 42.5 % true strain. The pole figures with and without remeshing are superposed, the red being obtained without remeshing and the blue after remeshing.
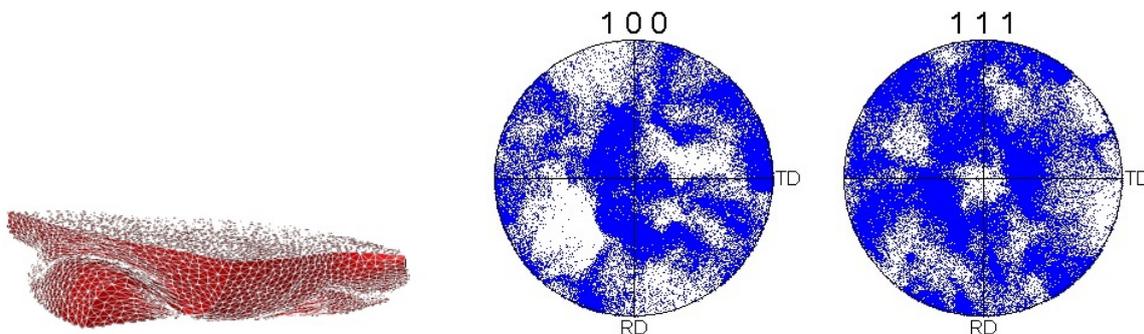
Fig. 4.20: Deformed mesh in the case of remeshing after 53.7 % true strain and the corresponding {100} and {111} pole figures.

The motivations behind performing remeshing can be multiple. In general, remeshing is performed in order to avoid element degeneracy. This latter occurs in several contexts. Typically, in Lagrangian contexts where large deformations are achieved, the elements end up severely distorted and the computations break down. Reconstruction of the mesh is mandatory if we need to carry out the computations further. Element distortion can also be due to strain/strain rate localization that could occur if the physics of the problem dictates it, even if relatively low deformation is achieved. Moreover, if a certain metric field is defined, based on moving boundaries (in Lagrangian or Eulerian contexts), the mesh should be regularly reconstructed so as to match the desired metric. Another important issue that needs to be considered is when to perform such remeshing. In the previous test case, a simple automatic criterion based on the amount of thickness reduction is used. Other criteria based on strain localization and element quality can also be considered as will be discussed in the next chapter.

III.6 Boundary conditions

For CPFEM computations on polycrystalline aggregates, appropriate boundary conditions are to be applied. Periodic Boundary conditions can be applied, if the RVE is to be considered as embedded in an infinite medium. Periodic boundary conditions require that the digital microstructure be periodic itself, in terms of grain geometry and properties (crystallographic orientation). Periodicity is then enforced during computation by requiring that the velocity (displacement) of pairs of points facing one another on opposing faces of the RVE be equal. For structured meshes, this is quite straightforward as in [DELANNAY et al., 2006] because for every node of the mesh on one face, there is an exact corresponding node on the opposing face. This is not the case for unstructured meshes like the ones used in this work. Other types of boundary conditions can be applied in CPFEM applications. In the previous test case, the four lateral faces of the cubic volume are left free which leads to folding and the breakdown of the computation. Mixed type boundary conditions, where only the normal components of the velocity (displacement) vector are prescribed can be used, as in [BACHU and KALIDINDI, 1998; ERIEAU and REY, 2004; SARMA et al., 1998]. Mixed boundary conditions do not ensure that the response of the polycrystal is homogeneous if the material behavior is homogeneous (i.e if the polycrystal is replaced by a single crystal). It is therefore preferred to apply homogeneous boundary conditions in strain or stress. In this work, we apply homogeneous strain rate boundary conditions: at every node belonging to the boundary of the domain $\partial\Omega$, the three components of the velocity vector $\boldsymbol{v}$ are prescribed according to the following equation:

$$\boldsymbol{v} = \boldsymbol{L}\boldsymbol{x} \quad \text{on } \partial\Omega\,, \tag{4.9}$$

where $\boldsymbol{L}$ represents the velocity gradient tensor and $\boldsymbol{x}$ the position vector in the current configuration. Figure 4.21 illustrates the boundary conditions in the case of plain strain compression.
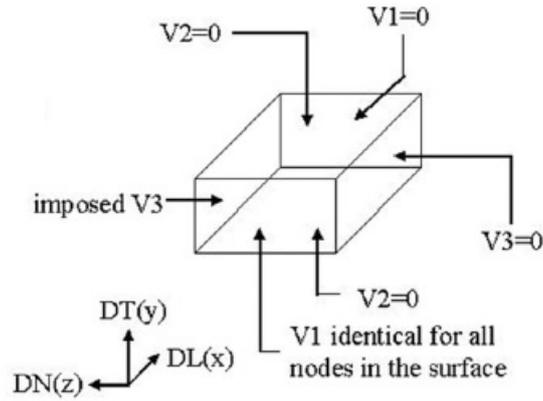
Fig. 4.21: Homogeneous strain rate boundary conditions in plane strain compression

IV Conclusion

Although the generation of 3D polycrystalline aggregates is not trivial, especially if the digital microstructure is to correspond, as much as possible, to an experimentally observed one, one of the bottlenecks to performing highly resolved CPFEM simulations in large strain applications is flexible meshing and remeshing. The mesh generator, used in this work, allows the generation of unstructured meshes that respect a given metric field. Remeshing is also readily performed with appropriate transport of elemental and nodal variables. The third characteristic of our numerical framework is the introduction of level sets to describe grain boundaries. The level set formulation is used to define an anisotropic metric. Based on this metric, an adaptive mesh, enabling an accurate geometric description of grain boundaries, is generated [RESK et al., 2009]. In this mesh, the elements are stretched in the plane tangent to the boundaries. The directional accuracy is demonstrated in chapter 5 while investigating stress and strain heterogeneities. Such heterogeneities can readily be analyzed with the level of mesh refinement achieved in the simulations. Also, the linking with static recrystallization simulation is performed. The construction of the initial topology, in the recrystallization simulation, is facilitated, given the common level set framework used to describe grains in the deformation and recrystallization simulations. Other typical applications are macrotexture predictions as illustrated in chapter 6. Most importantly, as highlighted in chapter 2, even-though the single crystal model does not include strain gradient effects in its formulation, the high level of discretization reveals in-grain misorientations due to varying slip activities from one element to the other as shown in chapter 6.

Chapter 5

Stress and strain rate heterogeneities: investigation & application

CPFEM has the capability to model various physical phenomena, depending on the type of constitutive law used and on the degree of mesh refinement. However, as mentioned by [BATE, 1999], even with a simple constitutive model, such as the one used in this work, much can be investigated with the CPFEM method. In-grain heterogeneities, due to the interaction with the surrounding grains, are put into light, if sufficient mesh density is used. However, other origins for the development of in-grain heterogeneities, as evidenced by single crystal experiments, are not taken into consideration. As mentioned by [DELANNAY, 2001], the Taylor ambiguity is one such origin as it reflects the fact that different regions of a grain could activate different set of slip systems, selected from the "pool" of possible combinations. Most importantly, dislocation patterning associated with the formation of substructure governed by individual dislocation motion, superimposes a layer of lower scale gradients on the already mentioned gradients associated with grain interaction. Such patterning can only be represented if the discrete nature of dislocation glide is taken into consideration via appropriate constitutive models.

With the use of conventional crystal plasticity models, several authors have investigated grain-scale heterogeneities of stress and strain that develop inside a polycrystal for various motivations. With damage applications in mind, [DIARD et al., 2005] analyzed intra-granular and inter-granular stress (and strain) fields in order to highlight critical regions with high stress concentrations. In our case, we want to establish a link with the occurrence of static recrystallization during a heat treatment. The first part of this chapter is therefore dedicated to a brief overview of recrystallization modelling. The main parameters needed for a first modelling effort towards an integration of a deformation and recrystallization simulation are highlighted. A mesh sensitivity analysis, based on the deformation energy distribution, is conducted and followed by a test case where deformation and recrystallization are successfully linked.

I   Overview of Recrystallization modelling

I.1   The physics: importance of deformation history

During plastic deformation, dislocations are multiplied throughout the metallic material, therefore raising the overall energy of the "system". This stored energy is released through three distinct microstructure evolution processes: recovery, recrystallization and grain coarsening. During recovery, the system lowers its energy by rearranging the dislocations into sub-grain structures. During grain coarsening, grains increase their size so as to decrease the total grain boundary area, therefore reducing their associated energy. During recrystallization, certain point-like regions of the deformed microstructure with very small defects densities grow at the expense of the rest. These nuclei finally lead to a new grain structure as illustrated by figure 5.1.

<table>
<tr><td>(a) Initial microstructure</td><td>(b) Deformed microstructure</td></tr>
<tr><td>(c) Nucleation</td><td>(d) Recrystallized microstructure</td></tr>
</table>
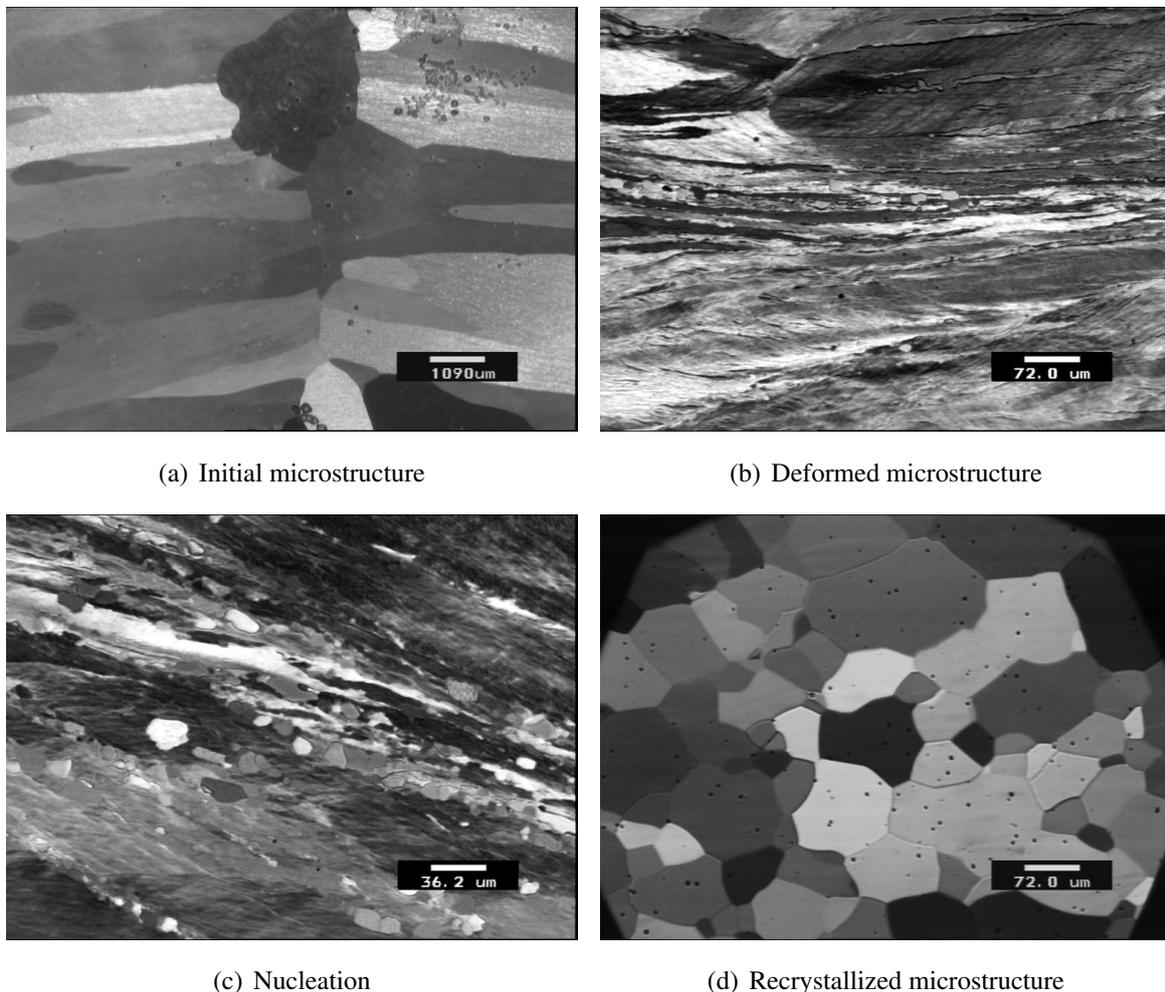
Fig. 5.1: Recrystallization phenomena

Nucleation and grain growth characterize recrystallization phenomena. The term "nuclei formation" is misleading as these nuclei are actually embedded in the deformed microstructure. As highlighted by [DOHERTY et al., 1997], understanding nucleation phenomena and establish-

ing nucleation criteria are far from being resolved. However, two conditions seem to match experimental findings: a critical size, preventing the new nucleus from shrinking, and adjacent high local misorientation, giving the nucleus enough mobility to grow into new grains. Possible nucleation sites could coïncide with existing high angle grain boundaries of the deformed microstructure. The growth of the new grains is then determined by gradients in stored strain energy, as well as properties of the boundary, namely boundary mobility, curvature and energy. Primary recrystallization refers to the process where the main driving force is the strain energy, which is the case in highly deformed materials. In secondary recrystallization, it is important to consider boundary energy and boundary curvature in the growth kinetics of the newly formed grains. Finally, recrystallization phenomena could occur, either dynamically during the actual deformation process, particularly during hot deformation, or subsequently as it is the case in static recrystallization.

To summarize, as nicely expressed in [DOHERTY et al., 1997], "the entire recrystallization process is latent in the deformed state". The parameters of the deformed microstructure that will determine the newly recrystallized one are : (i) stored energy distribution, (ii) crystallographic orientations, (iii) local misorientations, (iv) microstructure topology.

I.2   Approaches to recrystallization modelling

No generic model is currently available to describe the recrystallization behavior of a wide class of metallic alloys. Over the last decade, considerable progress has been made in the numerical simulation of recrystallization phenomena [MIODOWNIK, 2002]. Common approaches include the Monte Carlo (MC) method [ROLLETT and RAABE, 2001], the cellular automaton (CA) methods [RAABE, 1999; ROLLETT and RAABE, 2001], the phase field method [CHEN, 1995] and the level set method [ZHAO et al., 1996]. The first two are probabilistic techniques, which deliver evolving grain structures. They are associated with a 2D or 3D geometric representation of the microstructure, discretized on a regular grid made of 'cells', which are allocated to the grains.

The standard MC method as derived from the Potts model (multistate Ising model) applies probabilistic rules to update each cell at each time step of the simulation. The use of this model in 3D is relatively easy and efficient [HASSOLD and HOLM, 1993]. However, the comparison between MC results and experiments is not straightforward [ROLLETT, 1997]. Furthermore, the standard form of the model does not result in a linear relationship between stored energy and migration rate. The CA method, on the other hand, uses physically based rules to determine the rate at which a transformation front propagates across neighboring cells [RAABE, 1999] and can, therefore, be related to the microstructure and kinetics of a real system. In the case of primary recrystallization, the switch rule is simple: an unrecrystallized cell switches to the recrystallized state if one of its neighbours is already recrystallized. A major drawback of the CA method is the absence of an appropriate method to treat nucleation phenomena [ROLLETT, 1997]. The two

others methods; i.e. the phase field and level set methods, have many common points. They both have the advantage of avoiding numerical difficulties related to interface tracking. The principle of the phase-field model consists of describing the location of phases by introducing an order parameter (the phase field), which varies smoothly from one to zero (or minus one to one) through a diffuse interface [COLLINS and LEVINE, 1985]. The concept has been extended to deal with more complex problems involving more than two phases and also to model microstructure evolution [CHEN, 2002; KARMA, 2001]. As for the MC or CA methods, the topological events are treated in a natural way as a result of energy minimization. In the case of 2D ideal normal grain growth, published results illustrate the potential of the approach [CHEN, 2002]. However, the main difficulty of this method remains the construction of the free energy density function. Furthermore, the energy minimization of each order parameter can involve very expensive and intensive calculations, particularly for three-dimensional systems [KRILL and CHEN, 2002]. In contrast, the level set method [OSHER and SETHIAN, 1988; SETHIAN, 1996] is now commonly used to follow propagating fronts in various models [SUSSMAN et al., 1994]. The level set method has been extended to model the motion of multiple junctions when more than two regions or grains intersect [MERRIMAN et al., 1994].

Previous attempts to use digital microstructures for the modelling of plastic deformation and subsequent static recrystallization have been reported. In [RAABE and BECKER, 2000], a 2D digital sample was meshed, mechanical testing was performed with crystal plasticity finite element simulations and thermal treatment involving recrystallization was done subsequently using a CA approach. A Monte Carlo (MC) approach can replace the CA approach, as done in [BAUDIN et al., 2005; ERIEAU, 2003; ERIEAU and REY, 2004; VOLOVITCH et al., 2005]. In both methods, the finite element mesh needs to be converted into appropriate "voxel" grids. In doing so, some details of the microstructures may be lost, e.g. those related to grain boundary curvature. This aspect is important if grain growth is to be modelled after primary recrystallization. Furthermore, in some cases, it is useful to simulate further deformation of the digital aggregate following partial recrystallization, e.g. when studying multi-pass (industrial) processing. Transforming the voxel structure back to the finite element mesh then implies a new loss of information (boundary curvature, but also distribution of residual strains/stresses, etc.).

I.3 Linking deformation and recrystallization simulations

In the approach presented here, a common platform is used for the simulation of the cold deformation and for subsequent recrystallization. First, there is only one conversion of the initial digital aggregate into a finite element mesh. The deformation simulation, based on an updated Lagrangian framework, is carried out. The level set framework is used to initially identify the grains (i.e assign microstructural variables). The distance functions uniquely define the topology of the aggregate and the corresponding allocation of properties, even when automatic

remeshing operates. Their continuous update allows keeping track of the boundaries until the end of the deformation simulation. Digital heat treatment is then performed directly on the 3D finite element mesh obtained at the end of the deformation step. All variables updated during the deformation simulation are ready for use as input to the static recrystallization simulation. Most importantly, the stored energy distribution that dictates the kinetics of microstructural evolution during recrystallization is readily available from the deformation simulation. In this work, the influence of the grain boundary energy is neglected with respect to that of the strain energy i.e only primary recrystallization is considered.

The stored energy is directly related to dislocation multiplication. A relatively accurate way of computing the stored energy is to base it on dislocation densities, if such variables are computed by the crystal plasticity law. Dislocation densities are not used in the crystal plasticity model used in the work. A simple approach would consist in describing both the critical resolved shear stress τ_c (see chapter 2) and the stored energy E as a function of the dislocation density ρ as used by [Sarma et al., 1998]:

$$\left.\begin{array}{l} \tau_c = \tau_{c0} + \dfrac{1}{2} Gb \sqrt{\rho} \\ E = \dfrac{1}{2} \rho Gb^2 \end{array}\right\} \Rightarrow E = \dfrac{2}{G} (\tau_c - \tau_{c0})^2 \,, \tag{5.1}$$

where G is the shear modulus of the material. Another simple approach is to use the plastic work. Although the largest part of the plastic work is dissipated into heat during deformation, the plastic work, may, as a first approximation, be considered proportional to the energy stored in dislocation structures during the deformation. As elastic strains are small compared to plastic ones, the plastic work and the total deformation energy are very close. This deformation energy is then used as a measure of the stored energy. This latter is computed from:

$$E = \delta.W = \delta. \int_0^t \boldsymbol{\sigma} : \dot{\boldsymbol{\varepsilon}} dt \,, \tag{5.2}$$

where W is the deformation energy, δ defines the fraction of strain energy which is actually stored in the material and not dissipated into heat.

Predicting the distribution of the deformation energy is therefore important. The effect of mesh refinement, mesh adaptation and remeshing on the global and the local deformation energy is investigated. Local heterogeneities of stresses and strain are therefore apprehended. Finally, the use of this energy measure and the linking between the deformation and recrystallization is illustrated at the end of the chapter. More details on the recrystallization simulations can be found in appendix B where the published papers [Logé et al., 2008] and [Bernacki et al., 2009] are attached.

II Effect of mesh type, mesh refinement and remeshing in highly resolved polycrystalline simulations

A polycrystal composed of 50 randomly oriented grains is considered [Resk et al., 2009]. The unit cubic domain shown in figure 5.3 is subjected to homogeneous strain rate boundary conditions under plane strain compression. The material is an aluminum alloy with the material parameters presented in table 5.1.

$C_{11}(GPa)$	$C_{12}(GPa)$	$C_{44}(GPa)$	m	$\dot{\gamma}_0(s^{-1})$	$\tau_0(GPa)$	$\tau_{sat}(GPa)$	$H_0(GPa)$
107.3	60.9	28.3	20.0	0.001	0.1	0.3	0.03

Table 5.1: Material parameters

Table 5.2 summarizes the different meshes which were used. The mesh size h is equal to 0.05. Meshes M_1 to M_6 are isotropic. Meshes M_7 and M_8 are generated based on the anisotropic metric and are hence characterized by an element size h_1 far from the interface and an element size h_2 close to the interface in its perpendicular direction. For both anisotropic meshes, the anisotropic layer e defined in chapter 4 (see section III.3) has a length of 0.1 M_7 has the same mesh size as M_1 far from the interface ($h_1 = h$), while having the same mesh size as M_4 near the grain boundary ($h_2 = h/2.5$) as illustrated in figure 5.2. Similarly, M_8 has the same mesh size as M_1 far from the interface ($h_1 = h$), while having the same mesh size as M_5 near the grain boundary ($h_2 = h/3$). It should be noted that the coarsest mesh corresponds to 1500 integration points per grain (M_1) while the finest mesh (M_6), which is our reference mesh for analyzing the effect of mesh refinement and remeshing, corresponds to 115 000 integration points per grain. In order to evaluate the effect of remeshing, results obtained with meshes M_4 and M_7 are compared. This latter is shown in figure 5.3(c).
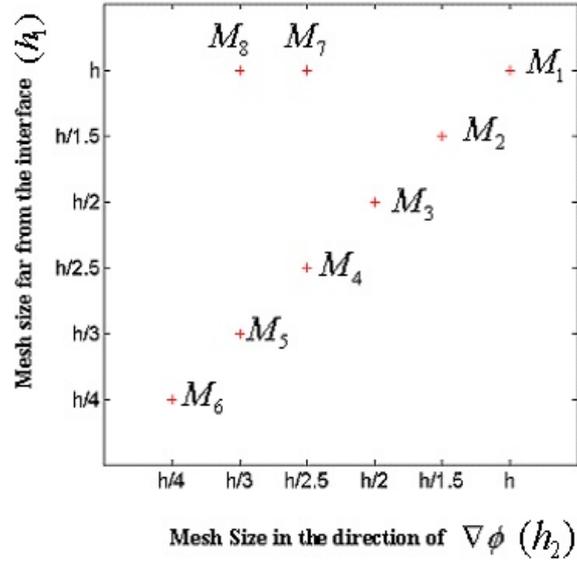
Fig. 5.2: Mesh size relationships

Mesh	Mesh size	# of elements	# of nodes
M_1	h	75039	14292
M_2	$h/1.5$	268708	49807
M_3	$h/2$	661806	122153
M_4	$h/2.5$	1175040	213442
M_5	$h/3$	2196912	395829
M_6	$h/4$	5819925	1035454
M_7	$h_1 = h$ $h_2 = h/2.5$	339555	44916
M_8	$h_1 = h$ $h_2 = h/3$	483389	60467

Table 5.2: Description of the different meshes used
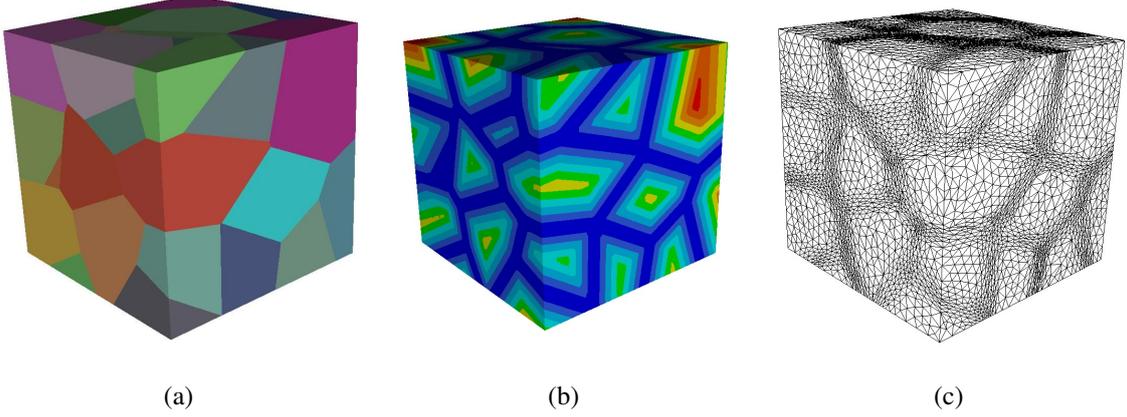
Fig. 5.3: (a) A 50 grains polycrystal, (b) the corresponding global distance function ϕ_{glob} (dark blue corresponds to zero) and (c) mesh M_7

II.1 Error Analysis

The accuracy of the FE simulations is evaluated based on the deformation energy (see equation 5.2). A first prediction of the deformation energy field is performed using a highly refined mesh M_6. This prediction is considered as a reference solution. The simulation is repeated with a coarser mesh and the result, which is constant by element, is mapped onto the reference mesh using zero-order transport as shown in figure 5.4. The local absolute error is then written as follows for each element K, $K \in \mathcal{T}_h(\Omega)$ with $\mathcal{T}_h(\Omega)$ denoting the finite element discretization of Ω for the mesh M_6:

$$e_{abs}(K) = |\widetilde{w}(K) - \hat{w}(K)| \, , \tag{5.3}$$

where $\widetilde{w}_K$ is the mapped value and $\hat{w}_K$ is the reference value. The local relative error for each element is then given by:

$$e_{rel}(K) = \frac{e_{abs}(K)}{|\hat{w}(K)|}(\%) \, . \tag{5.4}$$

Based on the L^2 norm of the deformation energy, the relative error integrated over the whole polycrystal can be written as:

$$e_{\Omega}(K) = \frac{\|e\|_{L^2(\Omega)}}{\|\hat{w}\|_{L^2(\Omega)}} = \frac{\left[\int_{\Omega} e_{abs}^2(K)d\Omega\right]^{1/2}}{\left[\int_{\Omega} \hat{w}(K)^2 d\Omega\right]^{1/2}} = \frac{\left[\sum_{K \in \mathcal{T}(\Omega)} |K| e_{abs}^2(K)\right]^{1/2}}{\left[\sum_{K \in \mathcal{T}(\Omega)} |K| \hat{w}(K)^2\right]^{1/2}}(\%) \, , \tag{5.5}$$

where $|K|$ is the volume of the element K.

In order to have topological information regarding the distribution of the local errors with respect to the closest grain boundary, a binning strategy, based on the global distance function ϕ_{glob} (see chapter 4 section III.2) is implemented. The procedure can be summarized as follows.

Let I_p be an interval of grain boundary distance defined by (see figure 5.4):

$$I_p = \left[p \frac{\phi_{glob_{max}}}{N_{bin}}, (p+1) \frac{\phi_{glob_{max}}}{N_{bin}} \right[, \qquad (5.6)$$

where N_{bin} is the number of bins, $p \in \{0, 1, \ldots, N_{bin} - 1\}$ and $\phi_{glob_{max}} = \max_{\Omega}[\phi_{glob}(x)]$.
Let Ω_p be a sub-domain such that:

$$\Omega_p = \bigcup_{K \in \mathcal{L}_p} K \quad \text{with} \quad \mathcal{L}_p = \{K \in \mathcal{T}_h(\Omega) | \phi_{glob}(G_K) \in I_p\} , \qquad (5.7)$$

where G_K is the Gauss point (center of gravity) of the element K . The relative error for each Ω_p is then given by:

$$e_{\Omega_p}(K) = \frac{\|e\|_{L^2(\Omega_p)}}{\|\hat{w}\|_{L^2(\Omega_p)}} = \frac{\left[\int_{\Omega_p} e_{abs}^2(K)d\Omega \right]^{1/2}}{\left[\int_{\Omega_p} \hat{w}_K^2 d\Omega \right]^{1/2}} = \frac{\left[\sum_{K \in \mathcal{L}_p} |K| e_{abs}^2(K) \right]^{1/2}}{\left[\sum_{K \in \mathcal{L}_p} |K| \hat{w}_K^2 \right]^{1/2}}(\%) . \qquad (5.8)$$
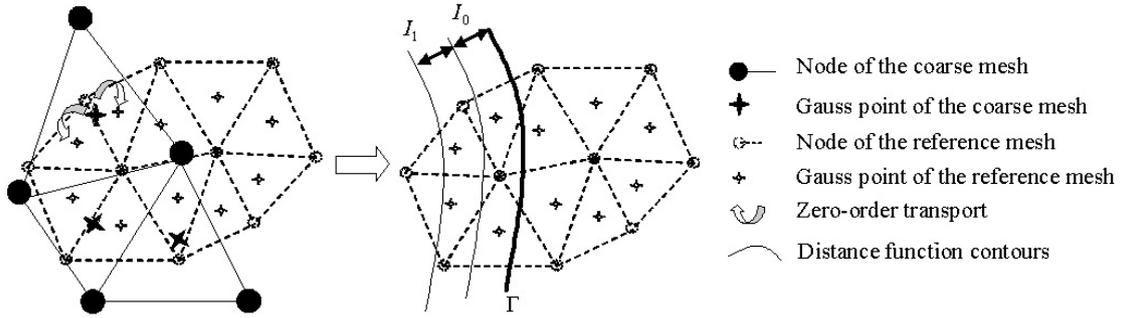
Fig. 5.4: Illustration of the error analysis methodology [RESK et al., 2009].

II.2 Mesh size effects

Figure 5.5 illustrates the macroscopic compression stress averaged over the whole polycrystal versus the macroscopic true strain for the different meshes. As expected, there are minor differences. The simulation is performed up to a true strain of about 1.1 for the coarsest isotropic mesh M_1 and a true strain of 0.7 for the reference mesh M_6. After these strains, without remeshing, the analysis cannot be extended further as large element distortion hinders the convergence of the solution. Element distortion can be measured through element quality as defined previously in equation 4.1. Figure 5.6 illustrates the evolution of the average and minimum element quality calculated in the usual Euclidean space for the isotropic mesh M_1 and the anisotropic mesh M_7. As observed, the minimum element quality which corresponds to the quality of only one element in the whole mesh is close to zero for M_1 when reaching a true strain around 1.1, i.e when the computation stops converging. As expected, the initial shape quality of the stretched

elements of the mesh M_7 is relatively low and the simulation in this case breaks down earlier (0.8 true strain).

Elements are distorted because of strain localization. The latter is properly captured only when the mesh is highly resolved, giving some insight into this physical mechanism. However, without reconstruction of the mesh, elements may be deformed so much that the computation breaks down by lack of convergence. The computed equivalent strain rate gives an indication of how fast the elements are distorted and it can be used as a remeshing criterion in order to avoid excessive element distortion. Figure 5.7 shows the evolution of the maximum equivalent strain rate ($\dot{\varepsilon}^{max}$) normalized with respect to the average equivalent strain rate ($\dot{\varepsilon}^{avg}$) for the different meshes. The maximum equivalent strain rate is reasonable for 15 % height reduction (0.16 true strain) but literally explodes for all mesh sizes after 30 % height reduction (0.36 true strain) unless remeshing is performed. As expected, when the mesh size decreases, strain localization occurs earlier in the computation. When remeshing is performed periodically (every 5% height reduction), excessive strain localization is prevented up to very large strains (see M_4 case with remeshing in figure 5.7).
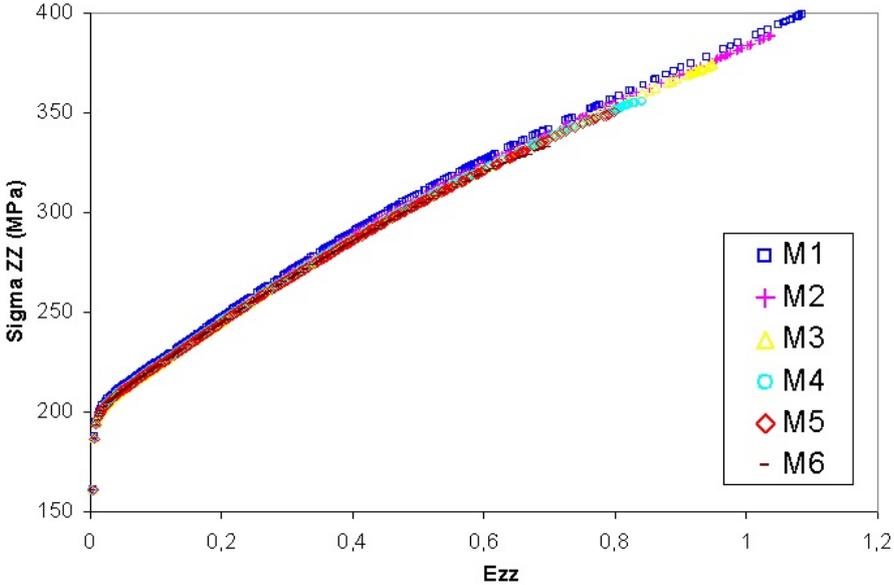
Fig. 5.5: Stress-strain curve for the different isotropic meshes
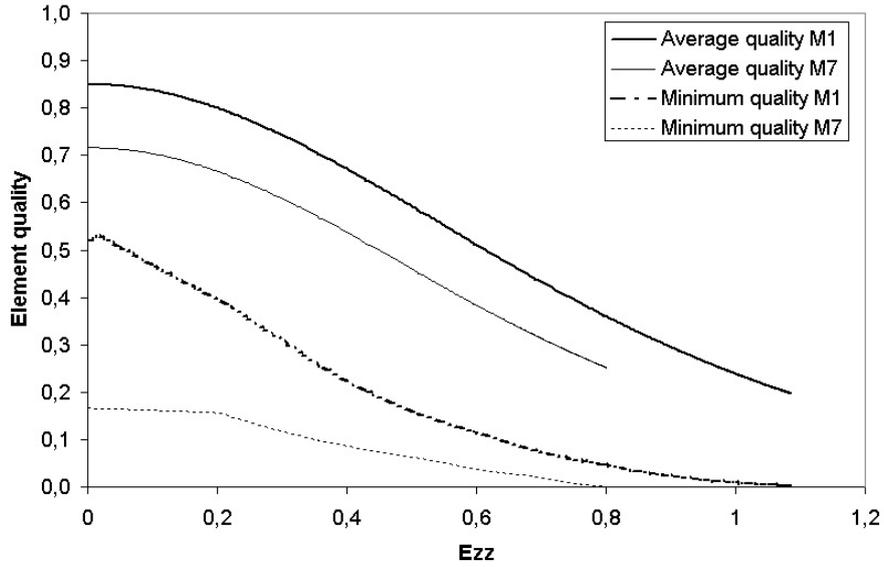
Fig. 5.6: Evolution of the average and minimum element quality $c(K)$ for mesh M_1 and M_7
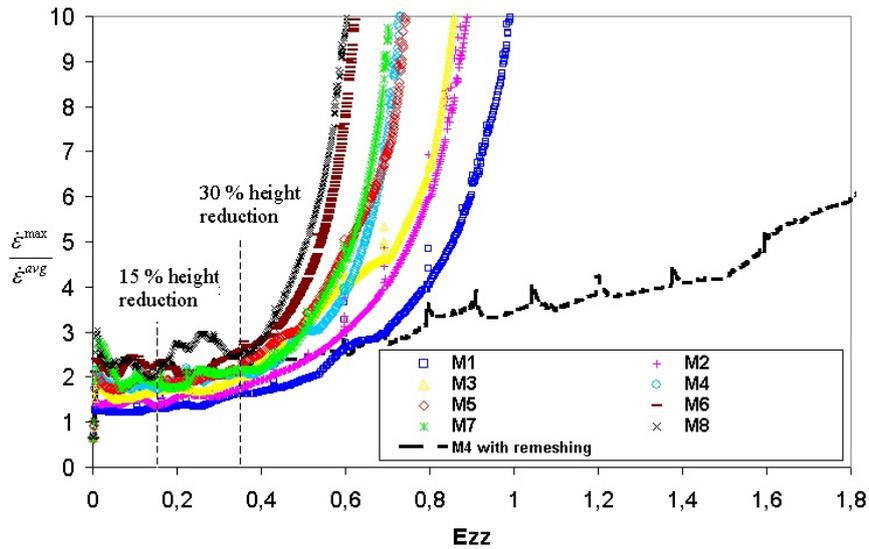
Fig. 5.7: Evolution of $\dot{\varepsilon}^{max}/\dot{\varepsilon}^{avg}$ for the different meshes [Resk et al., 2009].

As the mesh is refined, it is expected that the total relative error e_Ω would decrease. For the isotropic meshes and after 15 % height reduction, e_Ω is of the order of 10 % for M_1 (1500 elements per grain) and 5 % for M_5 (45000 elements per grain) as illustrated in figure 5.8. Using the binning strategy presented in section II.1, the relative error e_{Ω_p} after 15 % height reduction is computed and shown in figure 5.9. The error predicted with all isotropic meshes is largest near grain boundaries, corresponding to the zero value of the global level set function ϕ_{glob}. As we move away from the boundaries, this error decreases significantly. This is is also confirmed by the results shown in figure 5.10, where the relative error e_{rel} for the mesh M_5 is illustrated. As observed, the maximum values of e_{rel} occur near the grain boundaries, but this is not the case for all grain boundaries.
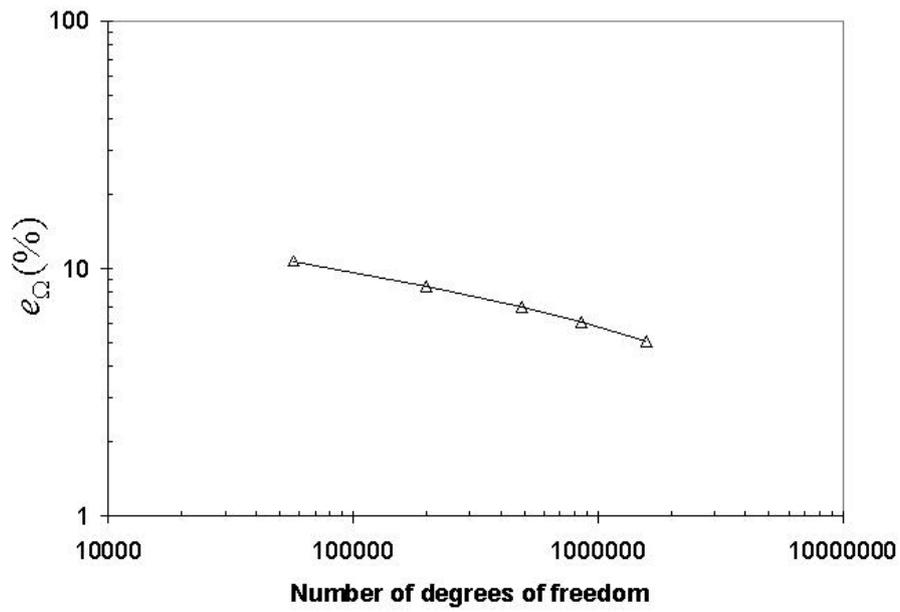
Fig. 5.8: $e_\Omega(\%)$ versus the number of degrees of freedom for 15% height reduction (isotropic meshes)
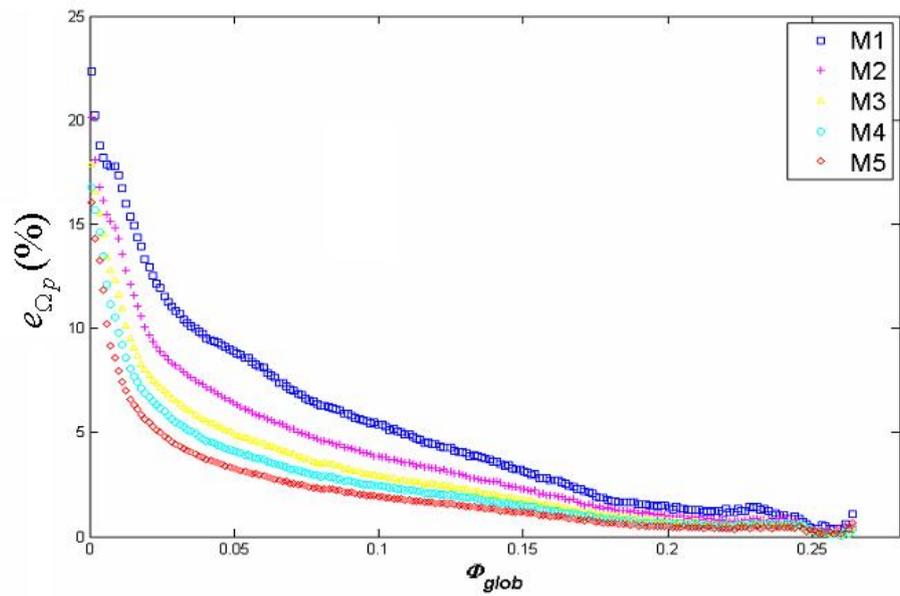
Fig. 5.9: $e_{\Omega_p}(\%)$ after 15 % height reduction with respect to ϕ_{glob} (isotropic meshes)
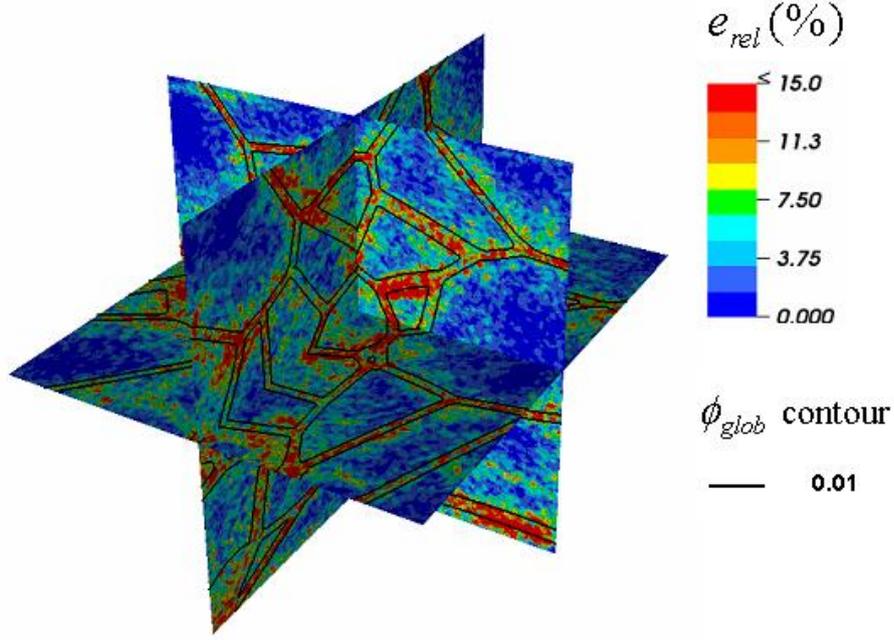
Fig. 5.10: Three slices along the X, Y and Z directions revealing the local relative error $e_{rel}(\%)$ and the 0.01 contours of ϕ_{glob} after 15% height reduction for mesh M_5

In section III.4 of chapter 4, it is shown that the use of an adaptive mesh is essential for guaranteeing geometric accuracy. Indeed, given the meshing generation strategy and the element interpolation scheme, a highly refined mesh near grain boundaries is needed and the anisotropic mesh offers a good compromise between computational cost and geometric accuracy. The question now is to check if the refinement near grain boundaries offered by such a strategy is justified in terms of distribution of mechanical fields such as the deformation energy field. In figure 5.11, the error e_{Ω_p} predicted with the isotropic mesh M_4 is plotted on the same graph as the one predicted by the anisotropic mesh M_7, which has the same mesh size h_2 as M_4 near the grain boundary and same mesh size h_1 as M_1 far from the boundary (see figure 5.2). The results for the anisotropic mesh M_8 and the corresponding isotropic mesh M_5 are also shown on the same graph. The anisotropic meshes and the refined isotropic ones lead to comparable errors very close to the interface. This means that reducing the mesh size in the direction perpendicular to the interface is enough to limit errors (i. e. reducing mesh size in the other directions is not needed). As we move away from the interface, the error e_{Ω_p} obtained with the anisotropic meshes is lower than that of the coarsest mesh M_1, but higher than the refined isotropic ones, even in the anisotropic layer (i.e $\phi_{glob} < e/2$). As we move out of the anisotropic layer, the anisotropic meshes generate lower errors than the coarsest mesh M_1 (i.e. $\phi_{glob} < 3e/2$). Finally, the coarsest mesh and the anisotropic meshes produce similar errors far away from the interface (i.e.$\phi_{glob} > 3e/2$). If one compares the isotropic meshes M_4 and M_5 to the equivalent anisotropic ones M_7 and M_8 in terms of number of elements and nodes (see table 5.2), the difference is significant. An anisotropic mesh refinement strategy thus offers a good

compromise between accuracy and computation time, as justified in the following section.
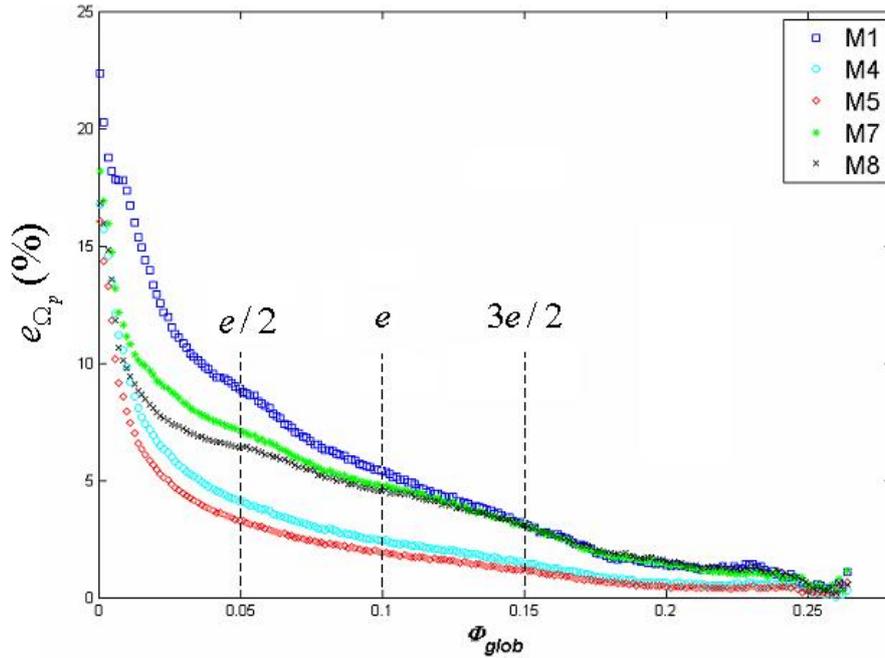
Fig. 5.11: $e_{\Omega_p}(\%)$ after 15% height reduction for the anisotropic and isotropic meshes [RESK et al., 2009].

II.3   Remeshing Effects

Computations with and without automatic remeshing were performed on 12 processors of the cluster described in chapter 3 section III.5.3. The initial meshes were M_4 and M_7. Remeshing was performed systematically, every 5% height reduction.

As seen in table 5.3 , the computational cost of the automatic remeshing after 3 remeshing operations is negligible. For such meshes, the integration of the constitutive equations is more expensive than other numerical operations. After 30 % thickness reduction and 6 remeshing operations, remeshing even enables one to gain time in the isotropic case. Indeed, after 30 % thickness reduction, the mesh is quite distorted unless remeshing is performed (figure 5.7) and element distortion impedes fast convergence of the iterative solution. This explains the increase of the computation time in the absence of any remeshing.

When the mesh is anisotropic, remeshing is much more computationally demanding than in the isotropic case. Indeed, the computation of the metric (which takes each individual level set function into account, see chapter 4 section III.3) and the topological operations are far more expensive. Hence, the computational cost for an anisotropic mesh is always more important if remeshing is performed as opposed to the same mesh without remeshing. Nevertheless, when comparing the computational cost of the anisotropic and isotropic cases, the anisotropic mesh remains advantageous. For example, table 5.3 shows that the computation time for reaching

30 % height reduction with remeshing is 478 minutes for M_4 as opposed to 197 minutes for M_7. The original construction of the anisotropic mesh was not taken into account in the present analysis.

	Computation time (min) for M_4		Computation time (min) for M_7	
% height reduction	With remeshing	Without remeshing	With remeshing	Without remeshing
15	247	245	96	90
30	478	494	197	175

Table 5.3: Computational cost of automatic remeshing for M_4 and M_7

(a) Without remeshing   (b) With remeshing (6 remeshing operations)
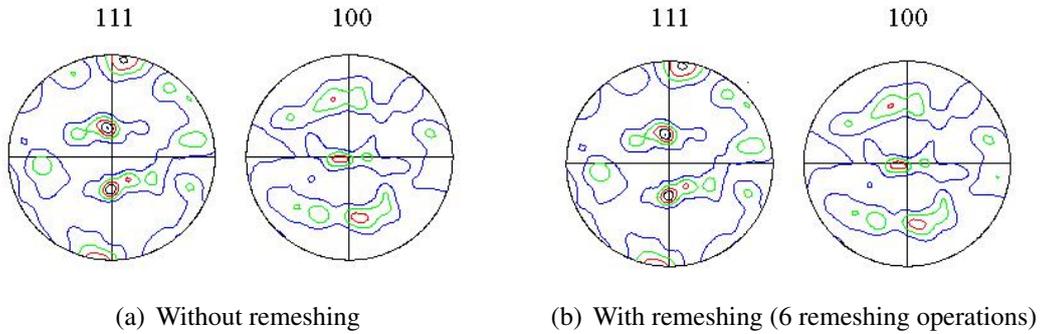
Fig. 5.12: {111} <100> pole figures after 30% height reduction for mesh M_7. Contour lines correspond to the multiples of random intensity

In order to validate the zero-order transport of state variables applied during remeshing, the predicted textures were compared in terms of pole figures. The predicted textures are indistinguishable with and without remeshing. Figure 5.12 shows the pole figures for M_7 after 30 % height reduction as an illustration. Hence there is no significant loss of information during the remeshing operations in terms of global texture evolution. In terms of the deformation energy field, table 5.4 describes the evolution of the total relative error e_Ω as the computation is carried out. The slight differences observed between the remeshed and non remeshed cases confirm that the diffusion, related to the remeshing procedure, is low. Even after 6 remeshing operations (30 % height reduction), the differences are quite small for the isotropic and the anisotropic cases. It is worth mentioning that the deformation textures obtained using mesh M_4 and M_7 are identical, if compared using pole figures. Global texture predictions are insensitive to the mesh refinement at such high resolutions.

	$e_\Omega(\%)$ for M_4		$e_\Omega(\%)$ for M_7	
% height reduction	With remeshing	Without remeshing	With remeshing	Without remeshing
15	6.01	6.09	7.71	7.36
30	6.16	6.19	8.37	7.44

Table 5.4: Total relative error $e_\Omega(\%)$ with and without remeshing

III   Deformation and recrystallization simulation test case

A common numerical framework is used for the simulation of the deformation and subsequent recrystallization of polycrystalline aggregates. The same level set framework is used to locate grains and follow the evolution of the microstructure. In the case of the deformation simulation, a Lagrangian approach is adopted, whereby the level set function of each grain moves according to the mesh velocity. For recrystallization modelling, the level set framework is applied in a Eulerian framework. In this case, given a velocity field v defined over a domain Ω, the level set method consists in evolving each distance function ϕ_i according to a convection equation as follows [BERNACKI et al., 2009]:

$$\begin{cases} \dfrac{\partial \phi_i}{\partial t} + v.\nabla\phi_i = 0 \\ \phi(t = 0, x) = \phi_i^0(x) \end{cases} , \forall i \in \{1, \dots, N_G\} . \tag{5.9}$$

At any time t the interface Γ_i of grain G_i is given implicitly by the equation $\phi_i(t, x) = 0$. The idea is then to establish the kinetic law describing the evolution of the velocity field v.

The link with the deformation simulation is done in three respects. First the deformed microstructure at the end of the deformation simulation is used as input to the recrystallization simulation. The level set approach common to both simulations allows working directly on the deformed mesh, without loosing / distorting any information. The stored energy is readily available, and, as it will be seen below, dictates the evolution of the recrystallized microstructure, with no need to construct a free energy density function (as in phase field methods). When dealing with primary recrystallization, nucleation of new grains also need to be modelled. Position and time of appearance of each new nucleus can be based on different criteria. In this work, the gradient of the stored energy is used as discussed below.

III.1   Kinetic law and nucleation modelling

It is generally assumed for pure metals that the kinetic law for grain boundary motion is well approximated by [HUMPHREYS and HATHERLY, 2004; KUGLER and TURK, 2006]:

$$v = M\Delta f n , \tag{5.10}$$

86

where M corresponds to the grain boundary mobility, Δf to the driving force per unit area, and $\boldsymbol{n}$ to the outward unit normal to the grain boundary. Generally, as in [KUGLER and TURK, 2004], M is calculated with:

$$M = \frac{b\delta D_b}{kT} exp\left(\frac{Q_b}{RT}\right) , \tag{5.11}$$

where b is burger's vector, δ is the characteristic grain boundary thickness, D_b the boundary self diffusion coefficient, Q_b the boundary diffusion activation energy and k the Boltzmann's constant. The driving force Δf is defined by [HUMPHREYS and HATHERLY, 2004]:

$$\Delta f = \Delta E - 2\gamma\kappa , \tag{5.12}$$

where γ is the grain boundary energy, which is function of the boundary misorientation, κ the curvature of the grain boundary and ΔE is the stored energy difference across the boundary. If one can compute the dislocation density throughout the polycrystal this energy difference can be expressed as $\Delta E = \xi\Delta\rho$ where ξ corresponds to the dislocation line energy and $\Delta\rho$ the total dislocation density difference across the interface [KUGLER and TURK, 2004]. In this work, several approximations are introduced. First, it is assumed that the material is highly deformed before it undergoes primary recrystallization. The second term of Equation 5.12, related to the grain boundary energy, is therefore neglected compared to the first term, related to stored strain energy. Secondly, the stored energy is computed according to equation 5.2. The absolute values of E do not always matter, e.g. only the relative values play a role in determining the topological evolution of the grain boundary network. Therefore the exact value of the proportionality variable δ in equation 5.2 does not need to be known.

Although the kinetic law for grain boundary motion seems quite simple, several challenges regarding its implementation in a level set framework have been identified and addressed [BERNACKI et al., 2009]. In order to avoid the development of overlaps or vaccuum, the velocity field has to be defined over the whole domain Ω while taking into account each individual level set function corresponding to a each grain. The velocity field has to be as regular as possible, which is not straightforward when multiple junctions are considered (the intersection of 3 or more grains). Moreover, in order to compute it correctly according to equation 5.10, the normal to the interface, given by the gradient of the level set function $\nabla\phi$ (see chapter 4 section III.2) has to be determined precisely. Most importantly, the approach and the proposed solutions to these issues are strongly related to the accuracy of level set function calculations around the interfaces. Indeed, a little disturbance of the levels around an interface leads to an error in the velocity estimation and consequently in their own evolution. During the deformation simulation, we have showed that anisotropic meshes, with refinement close to the boundaries, offer a good compromise between accuracy and computational cost [RESK et al., 2009]. Also, such meshes have proved to be necessary for a correct computation of the velocity field during the recrystallization step [BERNACKI et al., 2009]. Therefore, in order to avoid any loss of information when linking the deformation and recrystallization steps, the use of anisotropic meshes

with refinement close to the grain boundary during the deformation simulation is important. Finally, reinitialization of the level set functions as mentioned previously (see chapter 4 section III.2) is done periodically in order to ensure a correct computation of the velocity field. This is done more frequently in the case of recrystallization simulation compared to the deformation simulation, due to inherent sensitivity of the approach.

Regarding nucleation modelling and disappearance of grains, the level set framework is particularly useful. Disappearance of grains are handled automatically. Indeed, for a given grain G, the corresponding level set function ϕ_G becomes negative in the whole domain as the grain disappears, thereby stopping all computations related to that level set function. In a similar way, it is possible to introduce new regions (grains), based on given criteria. For example, new grains can nucleate during primary recrystallization, with an assumed low (taken here as zero) stored energy. A very simple method to create a nucleation site is to build a new function at a desired time increment and at a given spatial position. Spontaneous growth occurs if a zero stored energy is assumed inside the new region. Different rules have been developed for the time and space nucleation laws [Bernacki et al., 2009]. For example, at each time step of the simulation, a probabilistic or deterministic law of nucleation can be used considering a set of possible nucleation sites. This set can be chosen in different ways: (i) randomly in the domain Ω, (ii) only at grain boundaries (recalling that nucleation occurs near high local misorientations), or (iii) according to specific criteria based on crystallographic or mechanical variables calculated from the previous deformation step in the polycrystal . In this work, one has noticed significant intergranular and intragranular variations of the stored energy E, which result in maxima in the norm of the stored energy gradient $\|\nabla E\|$ mainly at grain boundaries. This latter quantity is then used to define a criterion for nucleation.

III.2   Simulation of deformation and subsequent recrystallization

A ten grains Voronoi microstructure is subjected to plane strain compression. A 20 % reduction in height is applied and the computed stored energy and the norm of the stored energy gradient $\|\nabla E\|$ are illustrated in figure 5.13. The calculated stored energy field is used as an input to model recrystallization. A normalized average of the stored energy is computed for each grain G_i, and the distribution of $\|\nabla E\|$ is used to define the set of potential nucleation sites. The selection of 1000 potential sites is done by choosing the nodes of the mesh for which $\|\nabla E\|$ is the highest, while considering a safe distance between two neighbouring nuclei equal to 3 times the average element size. A newly activated site is effectively taken into account if it does not belong to the existing recrystallized volume fraction of the domain. Figure 5.14 illustrates the increasing recrystallized volume fractions and the corresponding recrystallized front in blue. The simulation was performed in 6 hours on 16 processors of the cluster described in chapter 3 section III.5.3 and the final microstructure is made of 27 grains.
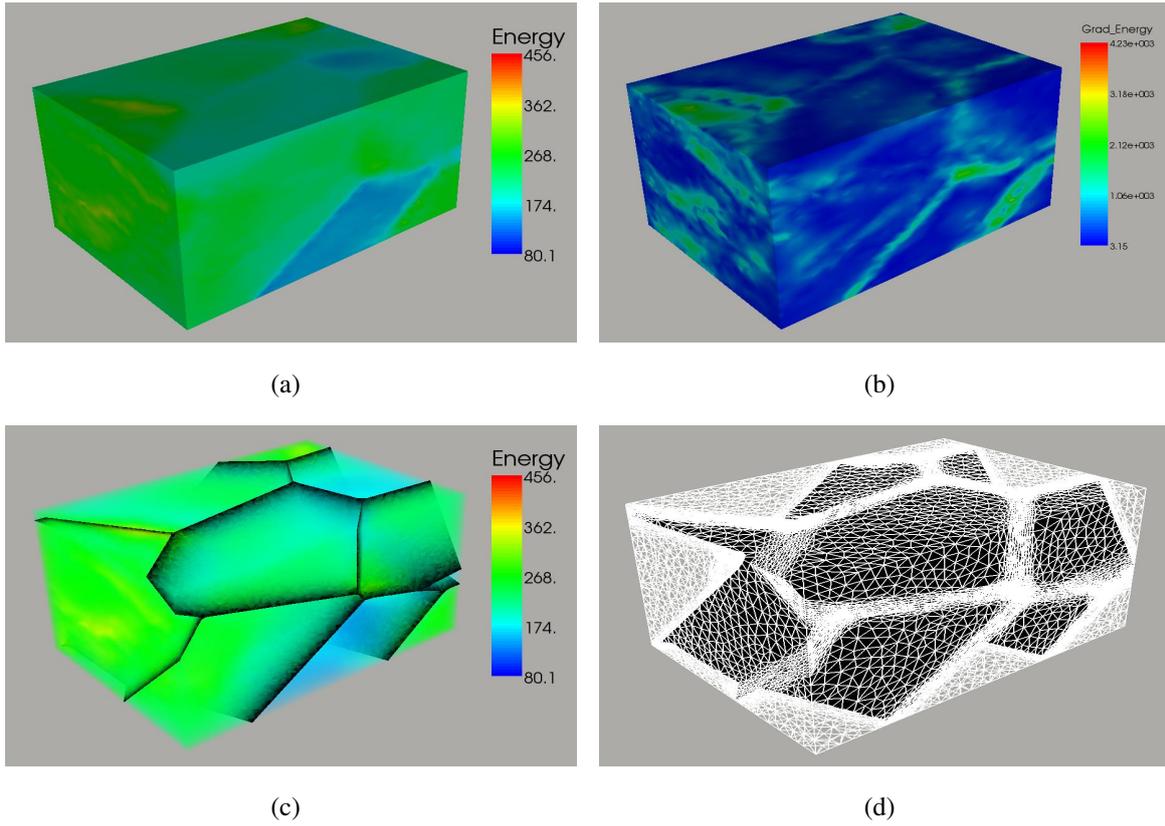
Fig. 5.13: A 3D ten grains microstructure after plastic deformation: (a) external surface view of stored energy, (b) corresponding norm of the stored energy gradient,(c)volumetric view of the stored energy with grain boundaries in black and (d) adaptive and anisotropic meshing in white, grain boundaries in black
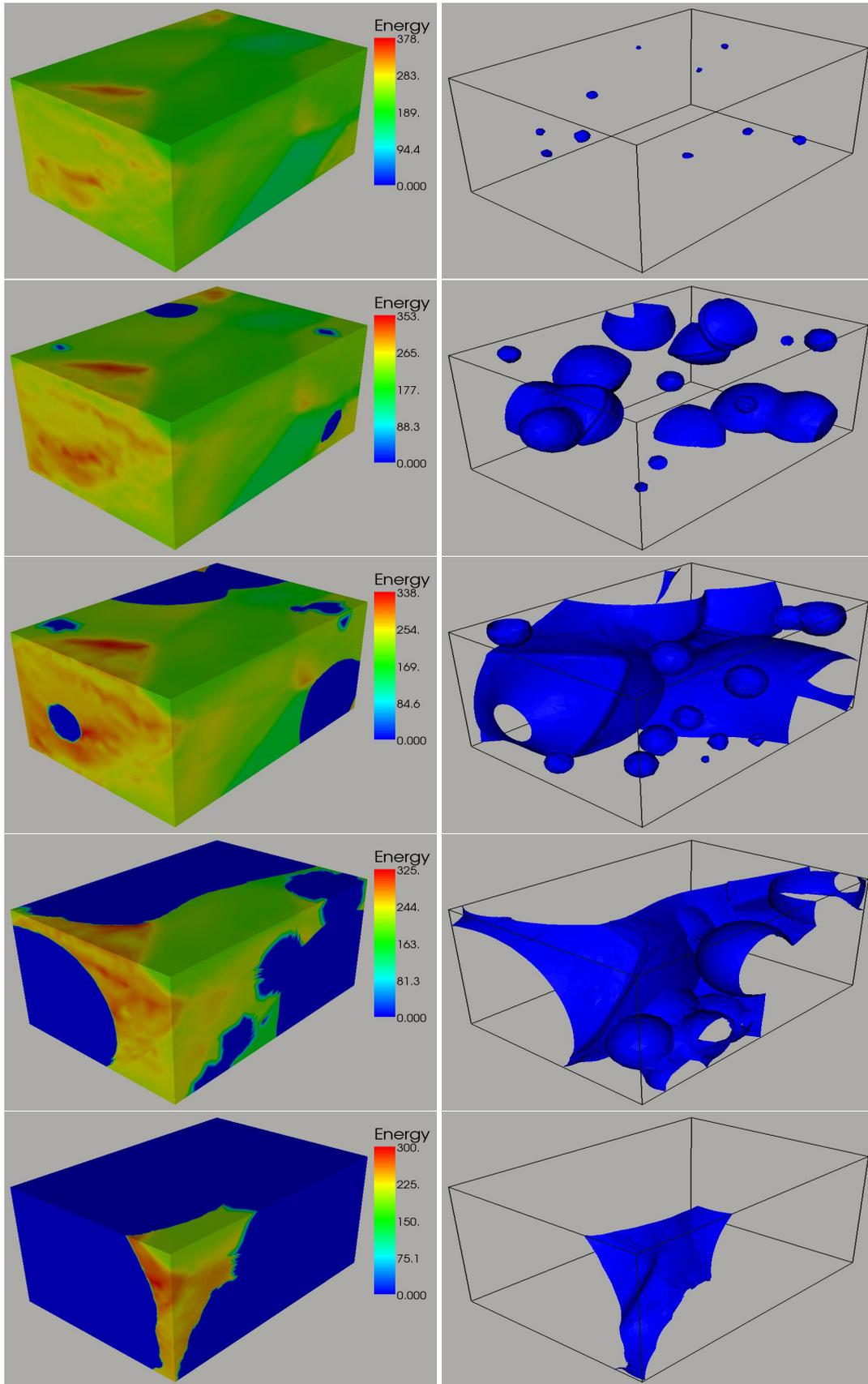
Fig. 5.14: 3D recrystallization with a non uniform initial stored energy field. From top to bottom: external surface view of the stored energy for recrystallized volume fractions of 1%, 15%, 58%, 80% and 95%, and the corresponding recrystallized front in blue

90

IV Conclusion

In CPFEM simulations, the anisotropy of the solution is driven by the geometry of the grains and differences in crystallographic orientation. Using meshes that conform to grain boundaries is therefore of prime importance, especially when local microstructural information is sought. Highly refined unstructured meshes could be used. However, the gains obtained in terms of local discrepancies are negligible compared to the increase in computational cost. In this chapter, it has been shown that an adaptive meshing strategy, leading to a highly refined anisotropic mesh respecting grain boundary geometry, offers a good compromise between resolution and computation time [Resk et al., 2009]. On the other hand, such resolution is not needed along all grain boundaries in a given polycrystal. Further mesh optimization could therefore be accomplished using error estimators, which provide a dynamic way of measuring discretization errors during the computation. An example of an a posteriori anisotropic error estimator is presented by Mesri and coworkers [Mesri et al., 2008]. This estimator can be used to provide better guidance to the adaptive meshing procedure presented in this work. Indeed, the mesh can be adapted dynamically during the computation based on both the level set functions representing grain boundaries and the local errors estimates. Moreover, a further constraint in terms of number of elements in the mesh can be included in this strategy, thereby introducing an additional parameter allowing the control of the number of elements per grain. In their analysis regarding the influence of grain shape on local stress variations, Ritz and Dawson highlight the drawbacks of not being able to control the number of elements in each grain as they vary the grain shape [Ritz and Dawson, 2009]. Regarding remeshing, it has been shown that the global (texture predictions) and local (plastic work) discrepancies associated with the transport of state variables are not significant. Reconstruction of the mesh is necessary in order to avoid important element distortion. The latter poses substantial problems in terms of accuracy and, ultimately, causes the breakdown of simulations carried out in a Lagrangian context if remeshing is not performed (see figure 5.7). Such distortion is connected to strain localization phenomena, which are best captured by high mesh resolution simulations, such as those presented in this chapter.

In the second part of this chapter, we presented a first modelling effort towards linking CPFEM simulations and static recrystallization simulations using a common numerical framework, based on the FE method and a level set formulation. Such modelling effort presents the advantage of minimizing loss of information when transferring required data from the deformation step to the recrystallization step. Energy stored during the deformation is the driving force for recrystallization. In this work, a fraction of the deformation energy is considered as a measure of the stored energy. With highly resolved FE simulations, significant intergranular and intragranular variations of the stored energy E have been observed, with maxima in the norm of the stored energy gradient $\|\nabla E\|$ mainly at grain boundaries. This latter quantity is used to define a criterion for nucleation. More elaborate nucleation criteria can be based on intergranular

and intragranular misorientations. As seen in chapter 4, all elements belonging to a grain are initially assigned the same orientation. The partition of the deformation among the elements, as the outcome of the FE problem after deformation, results in varying slip system activities from one element to the other and consequently, as per equation 2.32b, varying lattice spins, hence the development of misorientation. As noted by [MIKA and DAWSON, 1999] and highlighted in the next chapter, these misorientations have the same origin as geometrically necessary dislocations (GNDs). In the next chapter, more detailed definitions of orientations and misorientations are investigated as they are specifically applied for two other applications of CPFEM simulations. Macrotexture predictions for a model polycrystal and microtexture analysis for a digital microstructure, representing a replicate of a measured microstructure, are performed.

Chapter 6

Deformation texture prediction

In this chapter, a brief overview of crystallographic orientation measures and representation is given and the concept of misorientation and orientation deviation is introduced. The macrotexture in a model polycrystal deformed up to important strains is investigated. The rest of the chapter is dedicated to the investigation of the deformation and texture evolution in an experimental microstructure.

I Orientation

I.1 Orientation description

The crystallographic orientation of a grain or a crystal in a polycrystalline sample is usually defined as the rotation required to bring the sample reference frame (R_s) into coincidence with the crystal reference frame (R_c) as illustrated by figure 6.1. As such, it is used as a reference axes transformation of tensorial quantities (vectors, stress tensor ...). Traditionally, the symbol "g" is used for denoting the orientation. This latter could be represented by an orthogonal matrix as in the following equation:

$$R_c = gR_s = \begin{bmatrix} a_{11} & a_{12} & a_{13} \\ a_{21} & a_{22} & a_{23} \\ a_{31} & a_{32} & a_{33} \end{bmatrix} R_s \ . \tag{6.1}$$
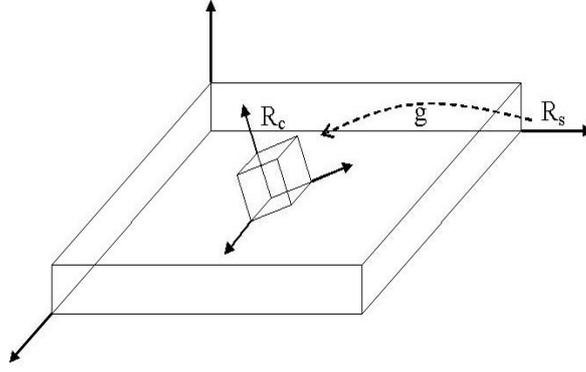
Fig. 6.1: Definition of the orientation of a crystal

Orthogonal matrices are one possible way of representing orientations. Other descriptions are available [KOCKS, 1998b]. Miller Indices specifies the alignment of a plane normal {hkl} and a direction $< uvw >$ within the crystal with the third and the first axis of the sample respectively. Typically, they are used to define *texture components* (or certain ideal or typical orientations) that might appear during rolling for example (see figure 6.2). In this case, the {hkl} plane normal is parallel to the Normal direction (ND) of the sample and the $< uvw >$ is parallel to the rolling direction (RD) of the sample. Miller indices are mathematically and numerically cumbersome. The most common orientation representation is based on the three Euler angles and is expressed as $g = g(\varphi_1, \Phi, \varphi_2)$. The Three angles correspond to three successive rotations according to a specific sequence or convention (Bunge, Roe, symmetric, the first one being the most common). The set of all orientations defined as Euler angles define the Euler Space. The orientation can also be represented by a rotation about an axis c by an angle w and can therefore be written as $g = g(c, w)$. The Rodrigues-Frank vector r combine both the rotation axis and the angle into one vector representation with $r = tan(w/2)c$. In the same vein, quaternion description combine all needed information into a single vector $(q_0, q_1, q_2, q_3) = (\cos w/2, c_x \sin w/2, c_y \sin w/2, c_z \sin w/2)$. This description is particularly useful as composition of rotations, inversions ...etc are translated into simple algebraic operations. Conversions between the different descriptions are possible and the formulae used in this study are summarized in appendix A. For crystals with symmetries under rotation, different orientations could be equivalent. Namely for cubic crystals, there are 24 symmetrically equivalent orientations.

Given a group of m discrete orientations described by quaternions q_i, one can compute a mean orientation $\bar{q}$ given by [PANTLEON et al., 2008]:

$$\bar{q} = \frac{1}{N} \sum_m q_i \text{ with } N = \left| \sum_m q_i \right| . \tag{6.2}$$

In order to compute this average, crystal symmetry has to be taken into consideration. In fact, 24 symmetry operators with switching symmetry are to be applied ($24 \times 2 = 48$) in order to put

the orientations into the fundamental zone (asymmetric unit). Special care has to be taken in the computations as mentioned by [GLEZ and DRIVER, 2001]. In this work, the average orientation has been computed either using the TSL-OIM software or using the routines available from [QUEY, 2008].

I.2   Orientation representation

An orientation described by Euler angles is represented by a point in the 3D cartesian representation of Euler space. Pole figures and inverse pole figures are particularly useful when analyzing the orientation evolution of one or several grains. Pole figures are 2D projections (stereographic, equal area, equal angle) used to represent the 3D orientations with respect to the sample reference frame. An inverse pole figures plots the position of a sample direction (RD,TD and ND for rolled specimens for example) relative to the crystal reference frame.
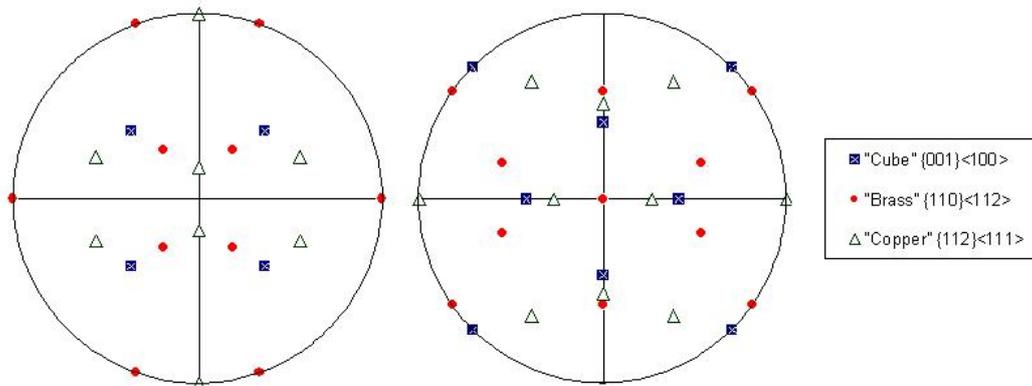
Fig. 6.2: 111 and 100 pole figures showing typical texture components that might appear during rolling

Pole figures and inverse pole figures give an indication of grain rotation as evidenced by the rotation of the points across the figures. They also give an indication of grain fragmentation that could occur as the material is deformed. Initial orientation represented by concentrated points spread out in a cloud as seen on figure 6.3. In a standard Taylor Full constraint model (see chapter 3 section I.2), such fragmentation cannot be predicted by the model as opposed to the Finite Element simulations.
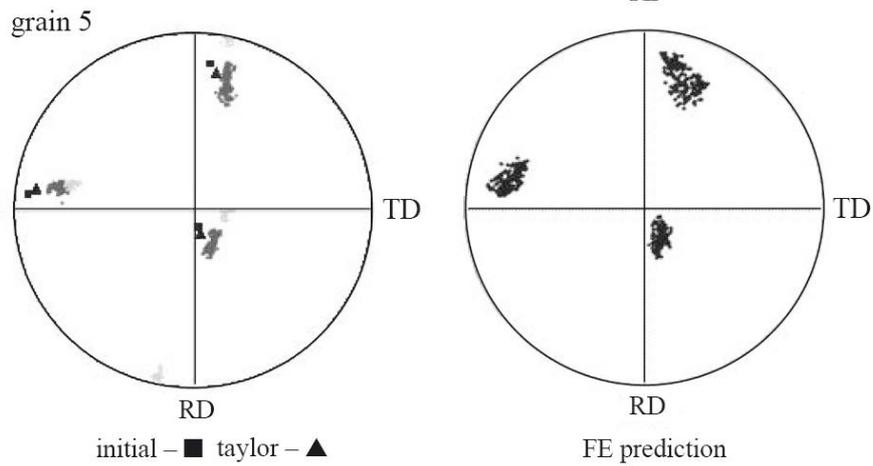
Fig. 6.3: (100) pole figures showing the initial orientation, the Taylor FC prediction and the cloud experimentally measured after 40 % plain strain compression on the left-hand side, and the finite element (FE) prediction after on the right-hand side for a particular grain [Kalidindi et al., 2004]

I.3 Texture analysis

In order to describe the evolution of crystallographic orientations for an important number of grains, a statistical methodology is needed. The orientation distribution function (ODF) provides a means to describe the texture or preferred orientation of a polycrystal. This concept is central in texture analysis. The ODF provides a continuous description of the distribution of the discrete orientation data. More specifically, the orientation distribution function $f(g)$ is a probability density function . It describes the probability of finding a given orientation g (i.e. the volume fraction of material with orientation g) within a given distance in orientation space dg. As mentioned previously, the orientation space can correspond to the Euler space if Euler angles are used. Quaternions and Rodriguez vectors are can also be used as they constitute an appropriate space for the continuous description of rotations. Mathematically, the ODF is given by:

$$\frac{dV/V}{dg} = f(g) = f(\varphi_1, \Phi, \varphi_2) .$$

$$(6.3)$$

Because of the definition of f, the following equation is satisfied:

$$\oint f(g)dg = 1 .$$

$$(6.4)$$

In general, ODFs are represented as two-dimensional sections of the 3D cartesian Euler space as seen in figure 6.4.
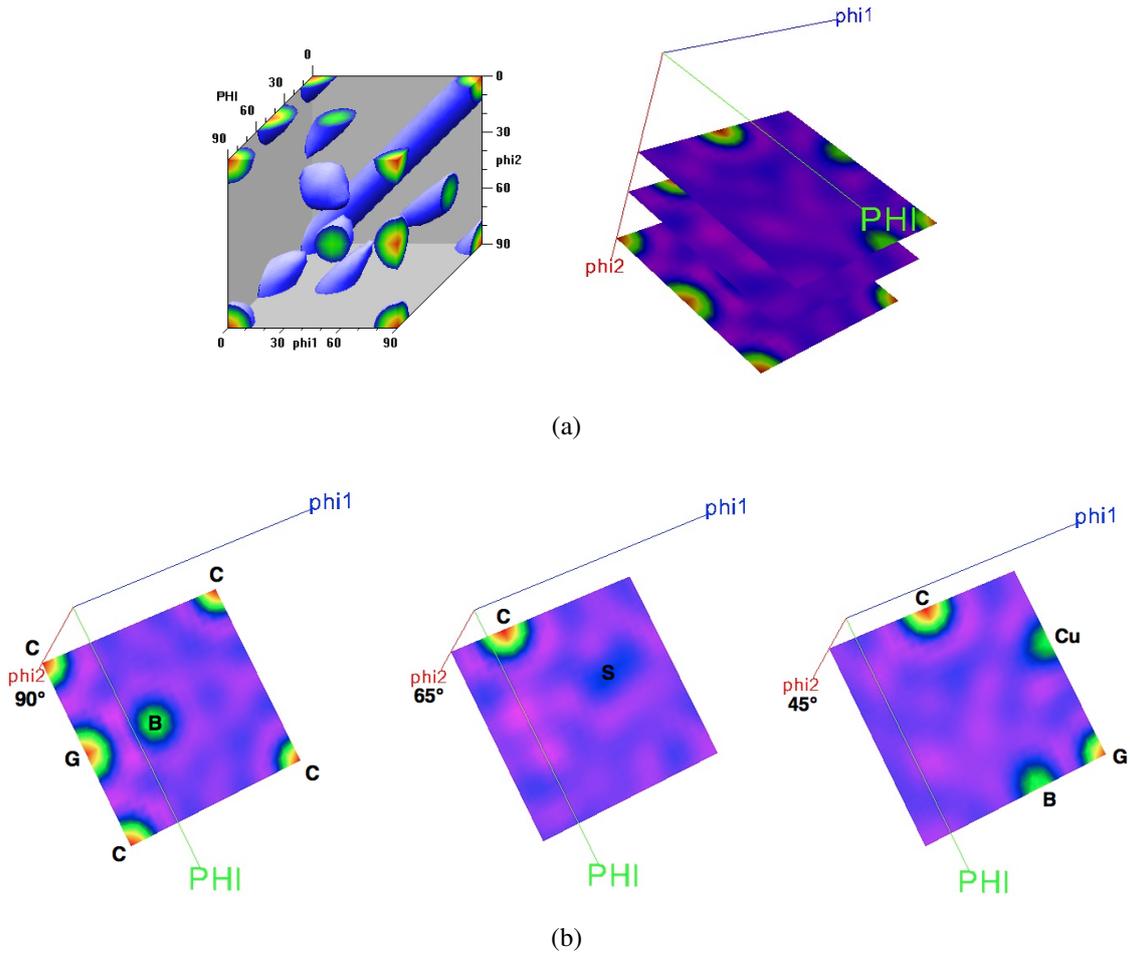
Fig. 6.4: (a) 3D Euler space featuring ideal texture components that appear during rolling of an FCC metal. The isosurface represents: Cube (C), Copper(Cu), Brass(B), Goss (G) and S components; (b) three typical sections along φ_2 (phi2 = constant).

Historically, discrete pole figures obtained via X-Ray or neutron diffraction were used to generate the ODF. OIM analysis now allows for the direct determination of the ODF from the OIM data. There are actually two ways for calculating the ODF: direct methods and series expansions of generalized spherical harmonics which is used in this work via the TSL-OIM software.

After computing the ODF, one can also use pole figures and inverse pole figures to represent texture. Other detailed analysis include texture fiber analysis such as in [ZHAO et al., 2007] which consists in following a characteristic line across the Euler space that defines quantitatively specific texture components.

II   Misorientation

II.1   Basic definition

The misorientation represents the difference in orientation between two orientations or two grains. It is basically the axis transformation required to bring the crystal lattice of one grain into coincidence with the other. If g_1 and g_2 are the orthogonal matrices representing respectively the orientation of the first and second grain, then the misorientation, commonly denoted by Δg, is given by:

$$\Delta g = g_2 . g_1^T = g_2 . g_1^{-1} . \tag{6.5}$$

As for orientation, the same descriptors apply for misorientation. Nevertheless, the axis/angle representation is commonly used. Using equation 6.5, the rotation axis corresponding to Δg, which is the common crystallographic axis between the two lattices, is expressed in crystal coordinates. Inverting the order of the combination of the two orientations would result in a rotation whose axis is expressed in the sample reference frame. In general, the crystal reference frame is chosen for most common applications of the misorientation concept is the description of the boundary separating two grains and it is hence more physically meaningful to express Δg in the local frame.

II.2   Some misorientation measures

II.2.1   Disorientation

The disorientation is the minimum rotation angle between two lattices. Computing the disorientation angle requires putting the misorientation into the fundamental zone (angle is minimum and misorientation axis is located inside the standard stereographic triangle). For this purpose, crystal symmetry has to be applied. As mentioned previously, there are 24 symmetrically equivalent orientations. Because the misorientation involves two lattices, two sets of 24 symmetry operators should be used as well as switching symmetry ($24 \times 24 \times 2 = 1152$ equivalent misorientations) if the misorientation is expressed in the crystal reference frame. If the sample frame is used, then only 24 operators with switching symmetry are to be applied ($24 \times 2 = 48$ equivalent misorientations). If the angle of rotation is the only parameter used to describe disorientation, then only one set of 24 operators needs to be applied as the angle is the same regardless of the reference frame used (invariance under axis transformation). This could be achieved using quaternions as described in the appendix A. The term misorientation and disorientation are used interchangeably in this dissertation to refer to the disorientation angle.

II.2.2 Orientation deviation

In this work, "orientation deviation" is used in the context of grain fragmentation that occurs during deformation. For a given grain, the mean orientation is first computed. The orientation deviation refers then to the *disorientation angle* between the orientation of a given point belonging to the same grain and the mean orientation of that grain. A frequency distribution for the orientation deviation can be plotted giving a first quantitative insight into the orientation heterogeneity inside a grain but with no topological information. An average value of the orientation deviation could also be computed for each grain. This value is sometimes termed "grain orientation spread" but some authors also use the term "grain average misorientation" to refer to this measure. A distribution of this average value gives then an insight into the heterogeneity of grain substructure in a polycrystalline sample. Figure 6.5 illustrates such a distribution.
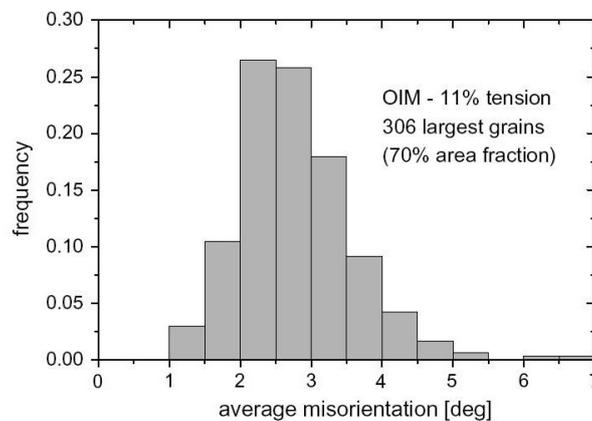
Fig. 6.5: Average orientation deviation distribution for a copper specimen after 11% tension [Lebensohn et al., 2008]

II.2.3 Local misorientation

One could also compute the misorientation in the neighborhood of a given point. Intergranular misorientations refers to the difference in orientation from one grain to the other. As such, they represent one component used to describe grain boundaries. Typically, for randomly oriented cubic crystals, the intergranular misorientations exhibit the MacKenzie distribution [Kocks, 1998b].

Intragranular misorientations refers to local misorientations that develop inside a grain as the deformation proceeds. These local misorientations are in fact the manifestation of the presence of grain substructure. Transmission electron microscopy (TEM) has been used to directly investigate grain dislocation structures (dislocation walls ... see figure 6.6) at the micron or sub-micron level. Nonetheless, intragranular lattice misorientations, measured by EBSD or predicted by relatively high resolution finite element simulations, are indicative of crystal substructure. As reported in [Dawson et al., 2002], "the volume of a crystal is divided into

subregions of like lattice orientation with the boundaries between the subregions exhibiting lattice misorientations".
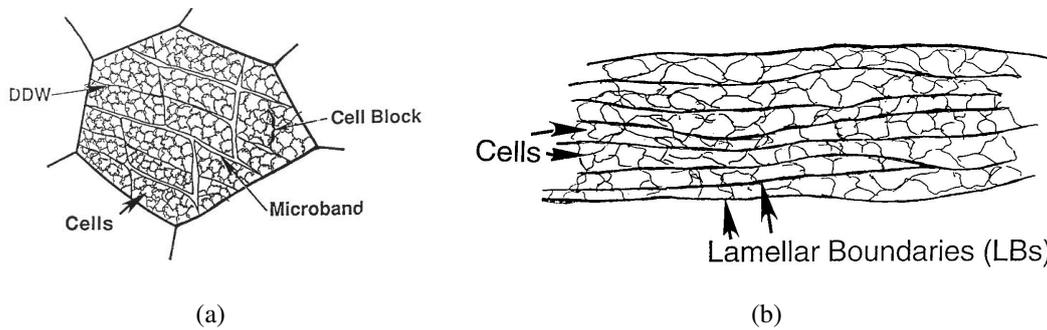
Fig. 6.6: Schematic of grain subdivision: (a) at low strain and (b) high strains [DOHERTY et al., 1997]

Frequency distributions of intracrystalline misorientations are yet another way of apprehending grain subdivision. In this work, the term "misorientation" is used to refer to this measure. An average misorientation can therefore be computed. Both measures, the average *local* misorientation and the average orientation deviation (orientation spread) give complementary information about the orientation heterogeneity inside a grain as seen in figure 6.7.
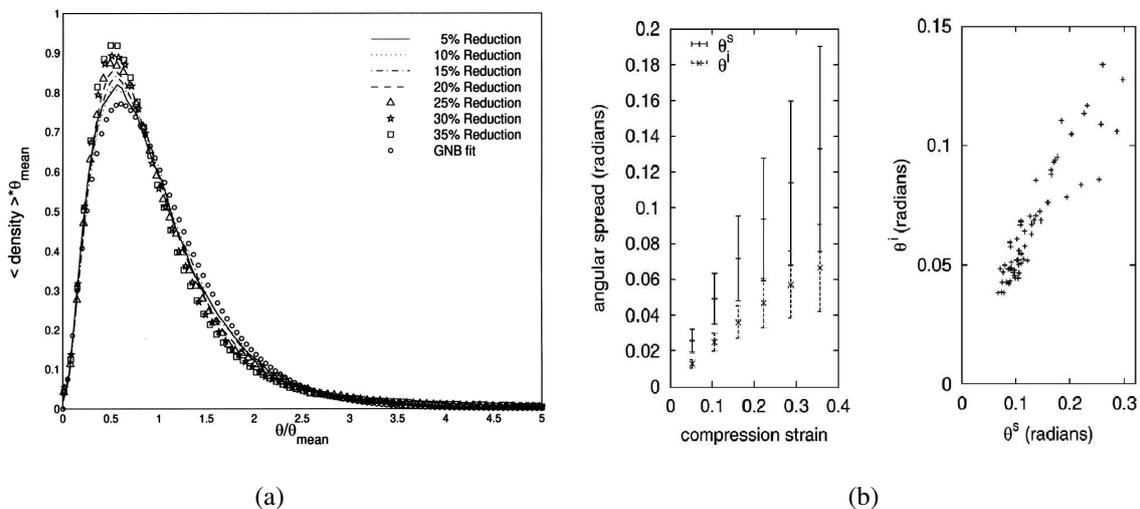
Fig. 6.7: (a) Intragranular misorientation scaled with the average misorientation for a group of crystals and fit from [HUGHES et al., 1997] (b) Correlation between grain orientation spread θ^s and grain average misorientation θ^i and their evolution with compressive strain [DAWSON et al., 2002]

One can also define a Kernel misorientation as the average misorientation between a given point and all of its neighbors, excluding misorientations greater than a given value (in general taken as 15°). As with orientations, one can also define a misorientation distribution function (MODF). The MODF concept is used to statistically describe grain boundaries in a polycrystal, which are defined by a lattice misorientation axis and angle and a boundary plane. MODF

is defined in the same way as the ODF with *g* representing a misorientation rather than an orientation weighted with areas instead of volumes, since boundaries are planar entities.

III   Orientation image microscopy

Figure 6.8 summarizes the principle of *Orientation Imaging microscroscopy (OIM)*. Electrons of a scanning electron microscope (SEM) are diffracted by the crystallographic planes of a tilted specimen (70° for optimum diffraction). The acquisition of an EBSD (electron backscatter diffraction) pattern enables the determination of the phase and the crystallographic orientation at specific locations on the surface of the specimen. The scanning step determines how far apart the measurements are acquired and therefore determines the spatial resolution of the acquisition. Step size as small as 0.3-0.5 μm can be achieved. Higher resolutions, with step sizes as small as 0.05 to 0.01 μm can be reached with a Field Emission Gun Scanning Electron Microscope (FEG-SEM). The process is in general automated which makes the OIM technique quite useful even-though only 2D microstructural information is obtained. However, the acquisition is in general time-consuming so only a selected region of the surface of the specimen is scanned. Also, the angular accuracy of the obtained maps depends on the quality of the diffraction image and on system/software dependent parameters such as the mathematical algorithm for pattern indexing. Various subsequent processing and analysis can be performed based on the collected EBSD patterns, ranging from visualizing crystallographic orientation maps to texture analysis, misorientation computations, grain boundary maps. They can be classified in two groups: statistical analysis on the level of the whole sample e.g. texture analysis (ODF, pole figures...etc) and microtexture investigation on the level of individual grains. One of the interesting features, related to this technique, is the fact that the reconstructed maps give an "image" of the actual microstructure. Therefore topological information regarding the spatial distribution of orientation gradient is, in theory, readily obtained. Grain subdivision can be spotted, by obtaining frequency distributions such as those shown in figure 6.5 but also the maps enable the visualization of the location of such subdivision. However, new insights into such subdivision is possible only if the scanning step is small enough to capture such gradients. The technique in its present status can not compete with the one based on transmission electron microscope (TEM), which allows the details sketched in figure 6.6 to be revealed, especially at high strains. Indeed, regions of high dislocation content are difficult to index with EBSD (black regions in the orientation map of figure 6.8).
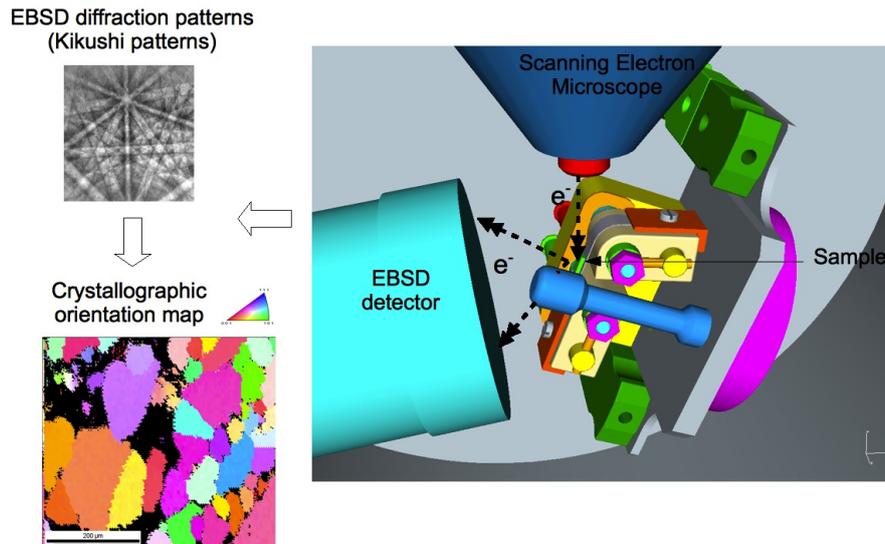
Fig. 6.8: OIM principle

In this work, the TSL-OIM software (version 4.0.5) is used to investigate experimental measured microstructures as well as numerical data provided by the FE simulations. The experimental data was obtained elsewhere [QUEY, 2009] and was put in the TSL-OIM software format for further investigation. Regarding numerical data, any 2D numerical data can be used in TSL-OIM as long as it is cast in the correct format, even if no EBSD map is associated with it. The software recognizes any file cast in the form of grid of points (x,y position and three Euler angles). It can be used as any texture analysis software. In this work, 3D digital tests are performed and the microstructure is probed, as it is done on the real sample. The method consists in making a 2D projection on a much finer structured mesh is first performed as seen on figure 6.9 (the projection consists of giving each 2D element the value of the nearest 3D element that "crosses" it). The center of gravity of these elements was then taken as the (x,y) position of the equivalent grid point in OIM. There is an error associated with this procedure, nevertheless, it is significantly reduced if the 2D projection mesh is very fine compared to the 3D mesh. Using this procedure, the whole digital 2D slice of the 3D microstructure can be analyzed. Individual grains can also be probed, based on the presence function, discussed in chapter 4 section III.4, by assigning a fictitious phase number for each grain. The software statistical capabilities can therefore be applied for each grain, without relying on the standard procedure which is used to determine to which grain each point belongs. In the standard procedure, grains are defined using two parameters determined by the user, namely a grain size and a tolerance angle. This latter represents the maximum point-to-point misorientation that is allowed inside a given grain. Using a fictitious phase number for each point, based on the presence function, allows all points belonging to a given grain to be included in the analysis, regardless of their misorientation with respect to their neighbors.
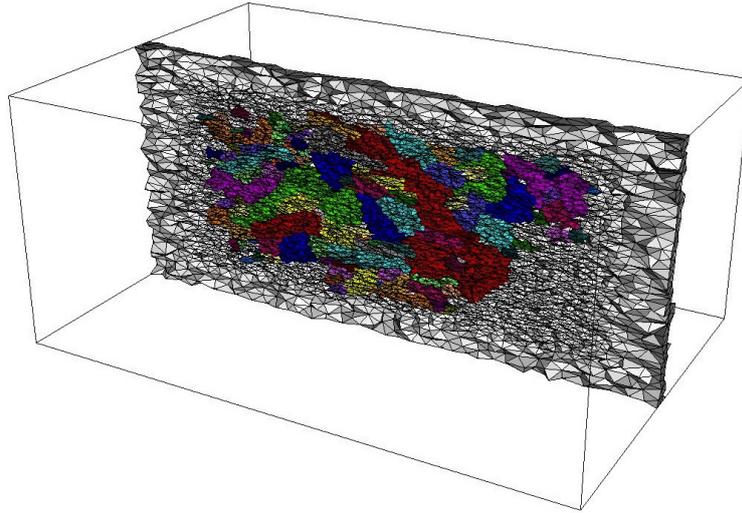
(a)
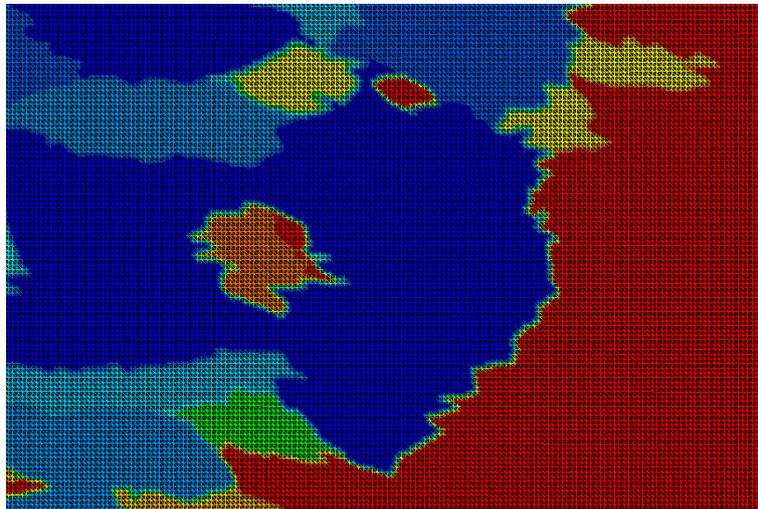
(b)

Fig. 6.9: (a) Inner layer of a 3D microstructure showing the investigated grains in color ; (b) a close-up view of part of the 2D mesh used for the projection

IV Prediction of macrotexture in a model polycrystal

Figure 6.10 illustrates a test case relying on a highly refined isotropic mesh (1175040 elements and 213442 nodes). A polycrystal containing 500 grains is subjected to plain strain compression to more than 90 % thickness reduction. The material parameters in table 6.1 and the boundary conditions given by equation 4.9 are used. In order to reach such strain levels, remeshing is performed whenever it is needed, i.e when the normalized maximum equivalent strain rate becomes too large ($\dot{\boldsymbol{\varepsilon}}^{max}/\dot{\boldsymbol{\varepsilon}}^{avg} > 5$) or when the minimum element quality, defined by equation 4.1, becomes too small ($c < 0.2$).

$C_{11}(GPa)$	$C_{12}(GPa)$	$C_{44}(GPa)$	m	$\dot{\gamma}_0(s^{-1})$	$\tau_0(GPa)$	$\tau_{sat}(GPa)$	$H_0(GPa)$
107.3	60.9	28.3	20.0	0.001	0.1	0.3	0.03

Table 6.1: Material parameters used for the plain strain compression simulation of the model polycrystal

(a) initial mesh

(b) mesh after 55 % height reduction

(c) mesh after 89 % height reduction
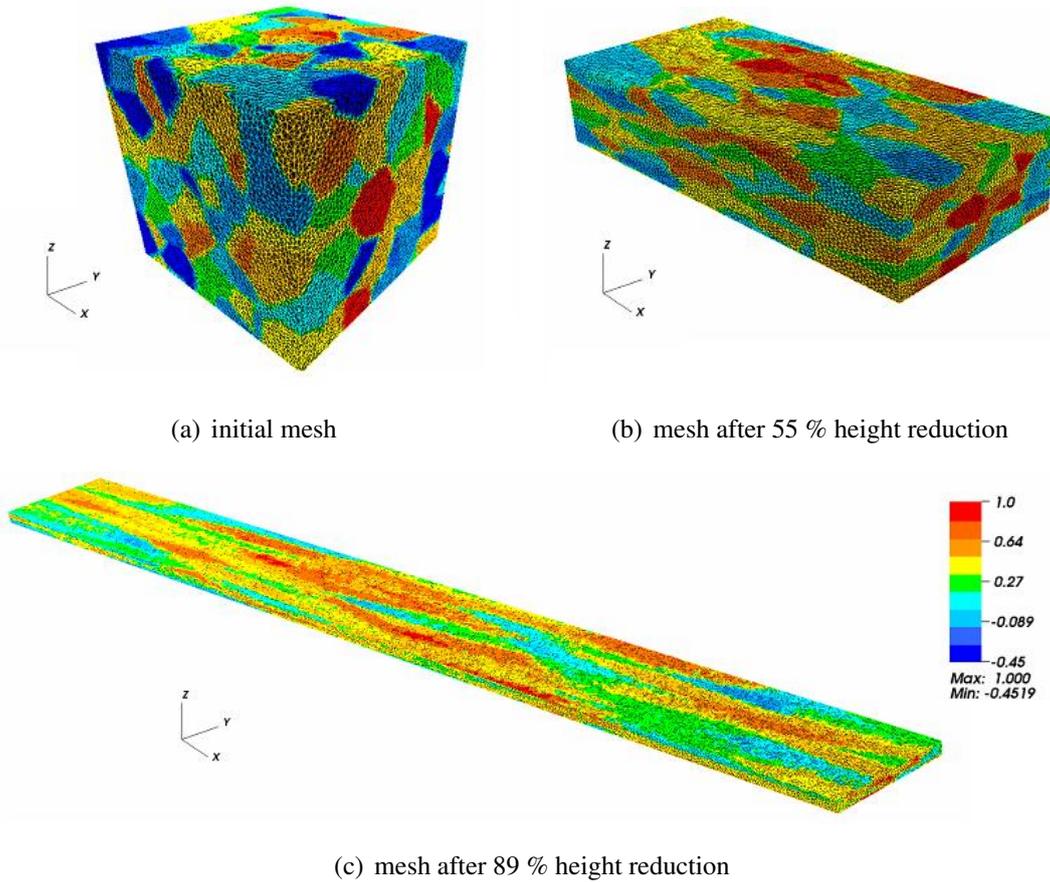
Fig. 6.10: 1st quaternion of a 500 grains polycrystal
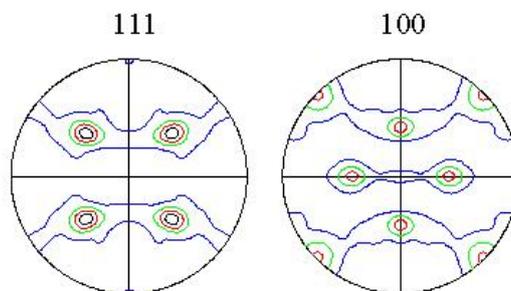
Fig. 6.11: initial 111 and 100 pole figures. Contour lines correspond to the multiples of the random intensity.

(a) Experimental measurement

(b) Taylor full constraint

(c) CPFEM
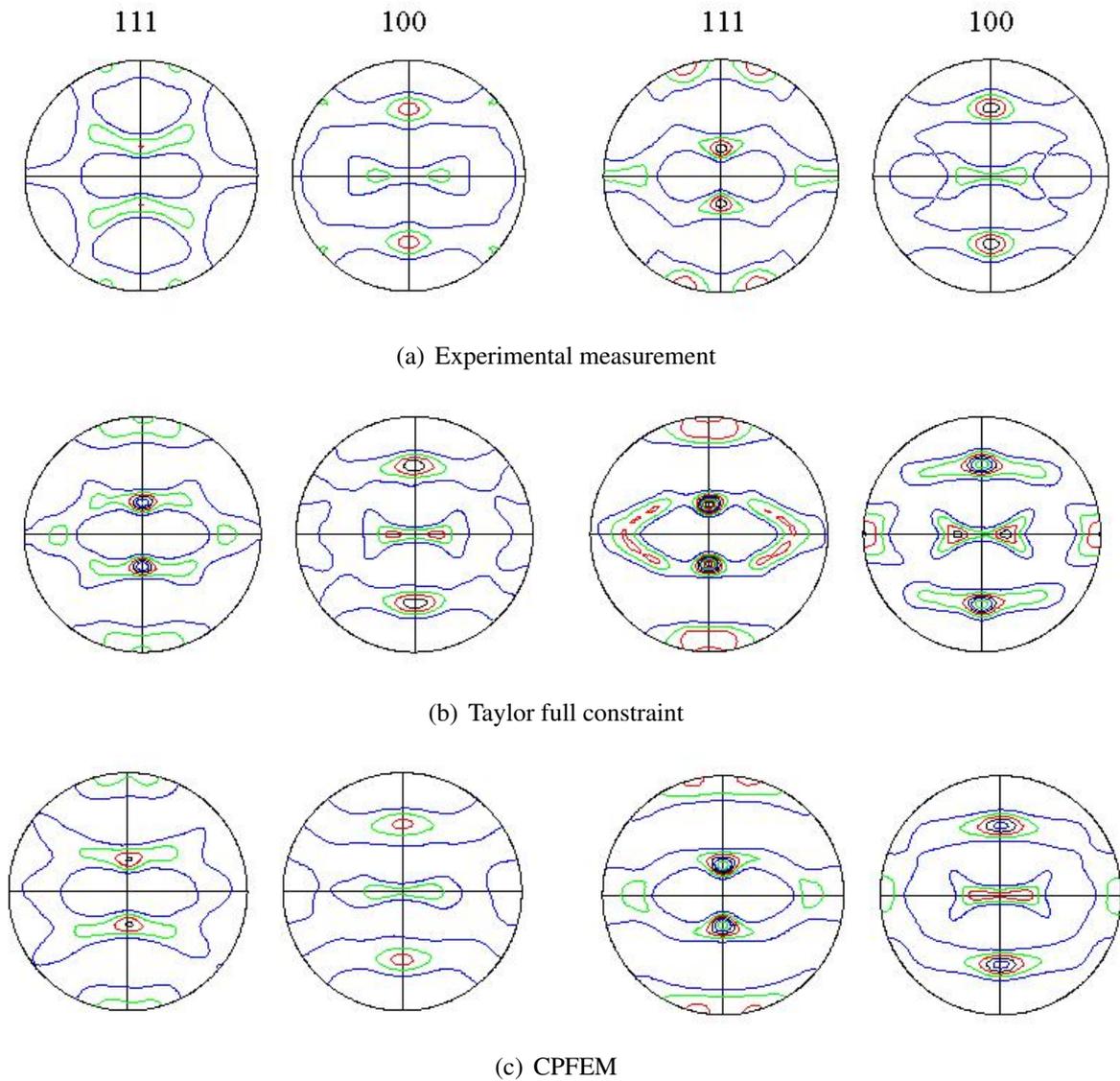
Fig. 6.12: 111 and 100 pole figures after 55 % (left) and 89 %(right) height reductions. Contour lines correspond to the multiples of the random intensity [RESK et al., 2009].

The initial texture of the polycrystal is discretized in order to match the experimental texture of an industrial (AA3104) aluminium alloy [DELANNAY, 2001] while accounting for the heterogeneous grain sizes [MELCHIOR and DELANNAY, 2006]. As seen in figure 6.11, the metal sheet shows a very strong cube {001} <100> texture in the undeformed state. In figure 6.12, the experimental textures measured after 55% and 89% thickness reduction are compared to the textures predicted either by the Taylor "full constraints" model or by CPFEM. As expected, the Taylor model yields intensities which are too pronounced in comparison to the experimental results. Moreover after 89 % height reduction, significant deviations in terms of the position of texture components are observed. On the other hand, CPFEM produces results that are more in line with experimental measurements. These results validate the crystal plasticity framework, described in chapter 2 and 3, at the macroscopic level.

V Detailed comparison between FE simulations and measured microstructure evolutions

V.1 Experimental Setup

Details of the experimental setup can be found elsewhere [QUEY, 2009], only the main points are highlighted in this section. An Al – 0.1 wt % Mn alloy is deformed in channel die compression. The deformation was carried out at a temperature of 400°C and a strain rate of 1 s^{-1}. A split sample method is used to follow 129 grains embedded in the polycrystal (see figure 6.13(a)). A 4×4 mm surface in the middle of the sample perpendicular to the transverse direction was scanned using EBSD with a scanning step of 5 μm. Grains were selected initially following a minimum misorientation angle of 5° giving an average initial grain size of about 300 μm. The same surface was scanned at 25 % and 40 % true strain. Figure 6.13(b) illustrates the grains that were followed during the deformation. These grains presented very small initial average orientation deviation as illustrated in figure 6.14.

(a)   (b)
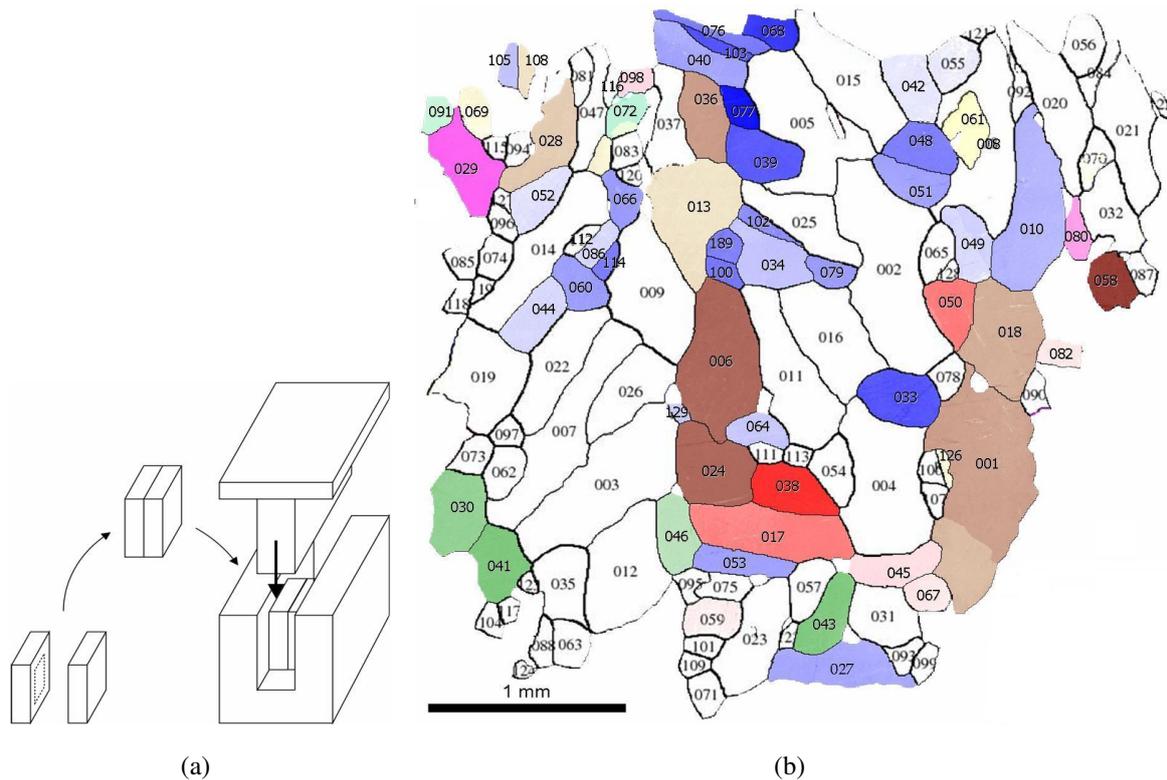
Fig. 6.13: Experimental setup and initial microstructure: (a) split sample in channel die compression; (b) grain structure in the undeformed state showing grain numbering. Grain boundaries (> 5°) are represented by black segments.

The technical difficulties encountered in this technique are numerous. It is worth mentioning that the internal surface is no longer flat after deformation and presents a wrinkled aspect. No polishing was performed and the surface was scanned as is by EBSD. The potential effects

on the measured orientations were investigated and found to be negligible [QUEY, 2009]. Most importantly, two issues related to the rationale of the method are worth highlighting. Firstly, the behaviour of the grains on the split surface can be influenced by the presence of an actual physical split inside the specimen. For pilot specimens, the authors [PANCHANADEESWARAN et al., 1996; QUEY, 2009] removed a few microns from the split surface and showed that the "internal" orientation measurements were quite close to the actual surface measurements. They conclude that the measured grains could be considered as "bulk" grains, while recognizing that such indirect confirmation is far from being decisive. Secondly, the objective of the method is to follow individual grains before and after deformation. Identifying the points belonging to the original grain after deformation seems far from being straightforward as the selection is done manually [PANCHANADEESWARAN et al., 1996]. Microhardness indents performed in selected regions of the surface enable to some extent to follow the deformation of physical regions of the microstructure and to perform somehow the correct mapping of the measured orientations to the original grains [PANCHANADEESWARAN et al., 1996; QUEY, 2009]. It should be noted that such mapping does not take into account the local misorientation, i.e points with misorientations > 15° could be considered as part of the same original grain.

	Min	Max
blue	0.195232	0.586037
green	0.586037	0.976841
yellow	0.976841	1.36765
orange	1.36765	1.75845
red	1.75845	2.14926
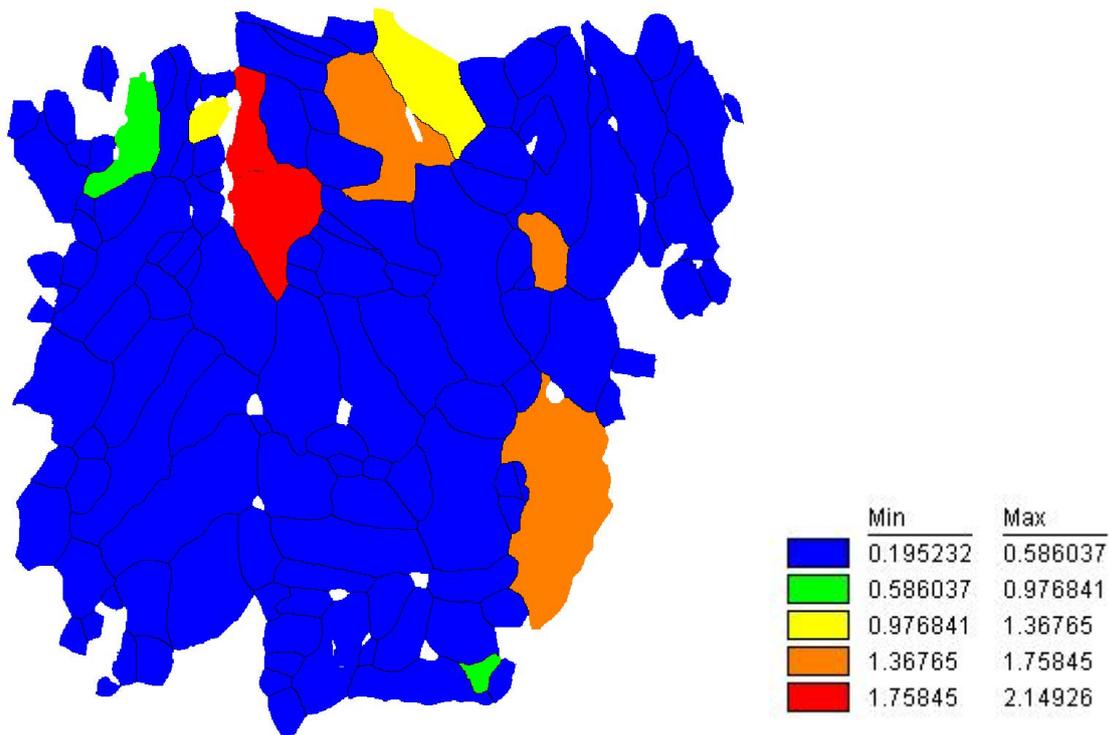
Fig. 6.14: Average orientation deviation for each grain

V.2 Simulations setup

The objective of these simulations is twofold: (i) investigate how well the whole modelling framework (constitutive law, numerical integration, FE solver) performs with respect to

local experimental results, in terms of deformation texture predictions; (ii) investigate the effects of other parameters related to the mesh refinement, the application of the boundary conditions, and the type of microstructure used. The latter two parameters are related to the fact that the scanned 2D area is in fact part of a 3D polycrystalline specimen. In order to compare the obtained results to 3D finite element simulations, the 3D volume surrounding the 2D scan has to be somehow reconstructed or guessed. Moreover, if we are to compare the numerical simulations to actual tests, the rest of the surrounding microstructure has to be guessed, reconstructed or somehow "filled". In the absence of information regarding the third dimension in both the scanned area and the surrounding medium, accurate reconstruction is not an option in our case. One way of generating the 3D microstructure is to assume columnar grains for the scanned area and assume that the surrounding grains have the same average grain size and crystallographic orientation distribution as the scanned grains as in [LEBENSOHN et al., 2008]. In the following section, a columnar microstructure is first assumed for the studied area and different ways of reconstructing the surrounding environment are tested. In the second part, a non-columnar microstructure is investigated as well as the effect of mesh refinement/type on macrotexture and microtexture results. In all simulations, the initial mean orientation of each grain is computed and used as input to the simulations. This is justified by the fact that, before deformation, the grains present very little orientation deviation as seen on figure 6.14. Moreover, as it will be seen subsequently in this chapter, the computation times, even with optimized meshes, are important, even for "numerical" resolutions well above the experimental one. Given the dimensions of the simulated cubic volume $(1 \times 1 \times 1)$, taking into consideration the initially measured orientation at each pixel within a grain would have meant using a mesh with a mesh size h approximately equal to ≈ 0.001. If an isotropic mesh is used to mesh the whole volume, assuming that all tetrahedra are perfectly regular, this would have yielded a mesh with over 8 billion elements. For all simulations, homogeneous strain rate boundary conditions are applied. a cubic volume of $(1 \times 1 \times 1)$ is used, except for the "Slice" test case as explained below. The material parameters, given in table 6.2, corresponding to aluminum, are used. As seen in figure 6.15, the hardening parameters were modified so as to fit the experimental stress-strain curve for the first set of simulations that investigate the effect of different surrounding environments. These parameters are also used for the rest of the simulations as well.

$C_{11}(GPa)$	$C_{12}(GPa)$	$C_{44}(GPa)$	m	$\dot{\gamma}_0(s^{-1})$	$\tau_0(GPa)$	$\tau_{sat}(GPa)$	$H_0(GPa)$
107.3	60.9	28.3	8.0	0.1	0.005	0.010	0.003

Table 6.2: Material parameters
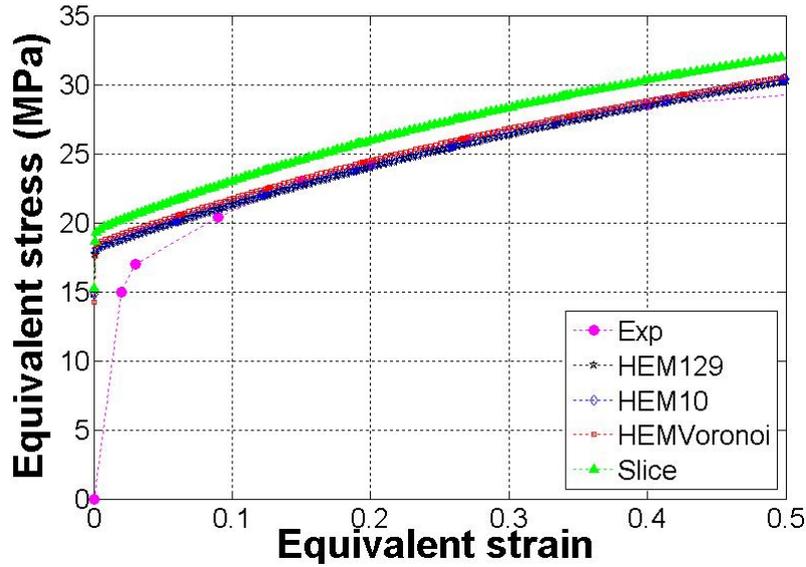
Fig. 6.15: Experimental and simulated stress-strain curves

V.3   Effect of the surrounding medium

In order to reconstruct the surrounding environment, the experimental pixelized EBSD map is first translated into a format compatible with the DIGIMICRO software (see chapter 4 section II). Several simulation cases are tested. In the first approach, the 3D columnar microstructure as represented in figure 6.16(a) is meshed as is. The elements belonging to each grain are assigned the corresponding orientation. The elements belonging to the non-indexed region (the light green region in figure 6.16(a)) are considered as part of a Homogeneous Equivalent Medium (HEM) surrounding the microstructure. In the second approach, the 3D microstructure is embedded in a bigger volume and the HEM corresponds to the non-indexed regions as well as the surrounding cubic volume as seen in figure 6.16(b). Depending on the type of HEM, the simulations cases can be summarized as follows:

1. the "Slice" case corresponding to the first approach. In this case, each element belonging to the HEM is considered as a polycrystal composed of 10 crystals. The orientation of these crystals are selected randomly from the pool of 129 orientations of the indexed grains

2. the "HEM_{129}" case where the microstructure is embedded in a bigger volume (see figure 6.16(b)) corresponding to a Homogeneous Equivalent polycrystalline medium with 129 orientations in each element

3. the "HEM_{10}" case where the microstructure is embedded in a bigger volume corresponding to a Homogeneous Equivalent polycrystalline medium with 10 orientations in each element selected randomly from the pool of 129 orientations

4. the "$HEM_{Voronoi}$" case where the microstructure is embedded in a volume composed of

approximately 1000 grains generated using Voronoi tesselation as seen in figure 6.17 and having the same average size as the considered microstructure. The orientations of these grains are selected randomly. It should be noted that 1000 grains are first generated alone in the cubic volume. Each element of the mesh is then assigned the corresponding crystallographic orientation. The slice is then "embedded" in the generated volume and elements belonging to the grains under investigation are reassigned the proper crystallographic orientation among the 129 orientations based on the level set/ presence function as discussed in chapter 4. So in effect, the surrounding medium is composed of a little less than 1000 grains.

(a)
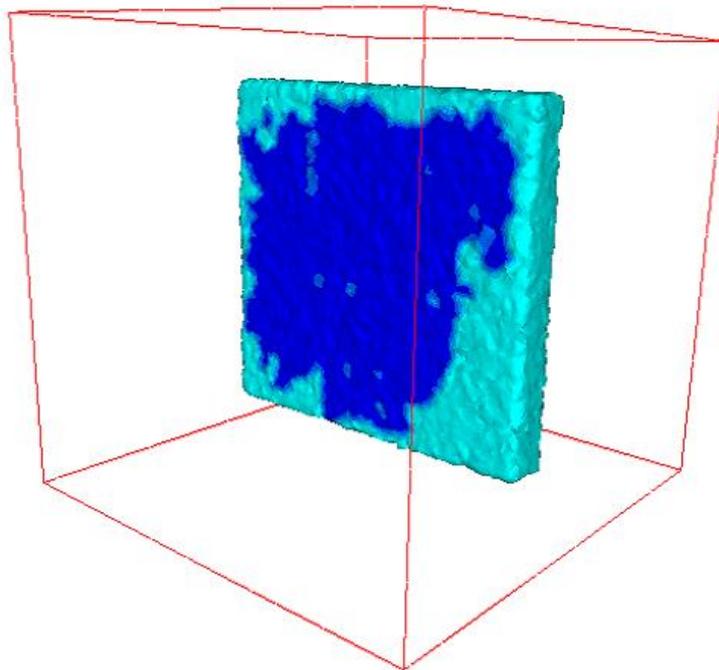
(b)

Fig. 6.16: (a) Generation of a 3D columnar microstructure ; (b) 3D microstructure embedded in bigger volume
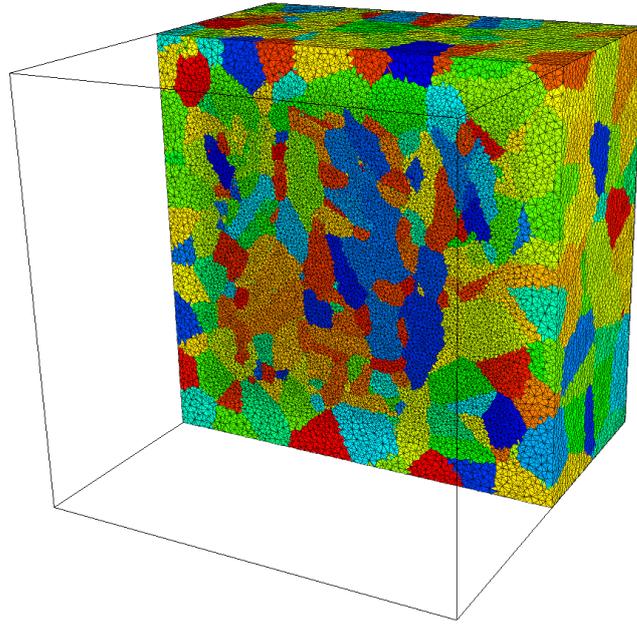
(a)
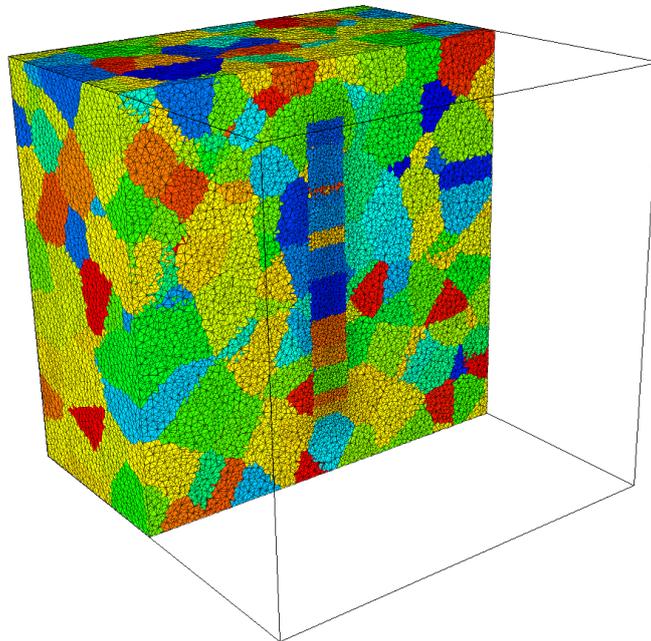
(b)

Fig. 6.17: The HEM$_{Voronoi}$ case: (a) cut along the Y axis, (b) cut along the X axis

For all these cases, the single crystal model is used for the elements belonging to the 129 grains that are under investigation. A standard Taylor FC polycrystal model is used for the HEM$_{129}$ and HEM$_{10}$ cases and for the surrounding medium in the Slice case. Finally the single

crystal model is used for the elements belonging to the surrounding medium in the $\mathrm{HEM}_{Voronoi}$ case. Figure 6.18 shows the mesh used for the Slice case. This mesh yields 138366 elements in the 129 grains (1000 elements / grain). Figure 6.19 illustrates the mesh used for cases 2,3 and 4. In order to optimize computation time, a metric based on the distance function to the inner slice was used, yielding a relatively refined isotropic mesh in the slice and a coarser isotropic mesh in the surrounding volume ($h \approx 0.032$). The total number of elements in this mesh is 484649 elements (87993 nodes), with only 130518 elements in the slice (1000 elements / grain). The meshes for the four cases are therefore equivalent in terms of average mesh size in the inner columnar microstructure under investigation ($h \approx 0.015$). Simulation results are compared to experimental data for a true strain of $\varepsilon = 0.4$.

| (a) | (b) |
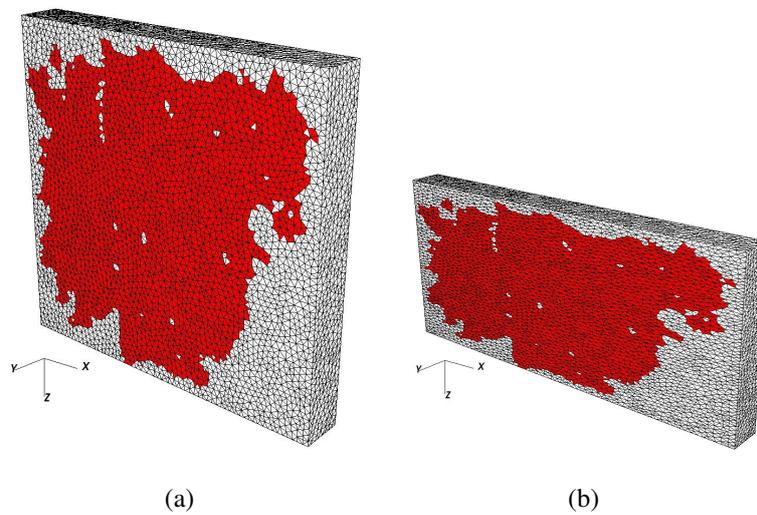
Fig. 6.18: (a) Initial mesh used in the slice case (207951 elements and 40682 nodes); (b) deformed mesh after $\varepsilon = 0.4$

| (a) | (b) | (c) |
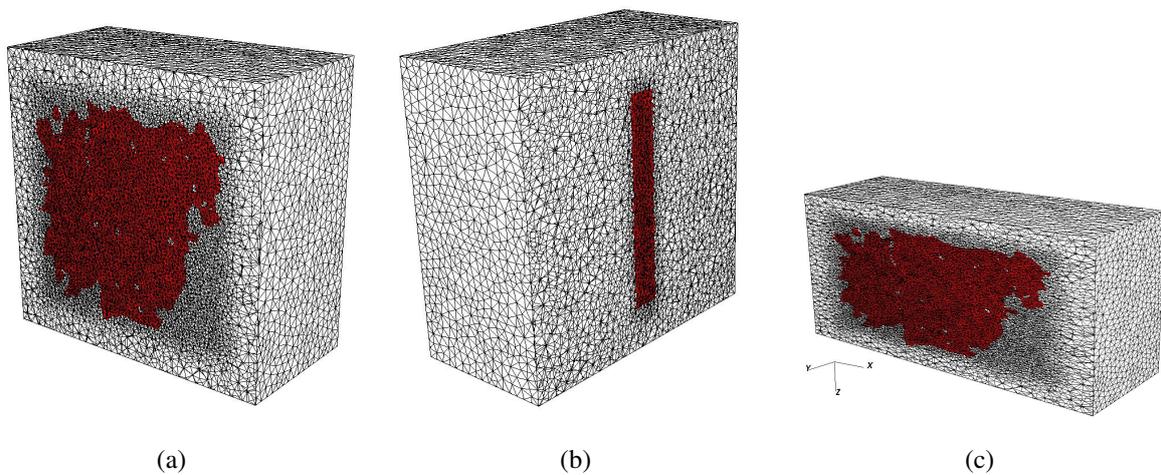
Fig. 6.19: (a) Cut along the Y axis revealing the inner mesh and the microstructure (484649 elements and 87993 nodes); (b) cut along the X axis; (c) cut along the Y axis for $\varepsilon = 0.4$

Computations were performed on 32 processors of the cluster described in chapter 3 section III.5.3. Table 6.3 shows the computation time for the different cases. As expected the computation time is much lower if the slice is not embedded in a bigger volume. Reducing the number of orientation in the polycrystalline model from 129 to 10 leads to a significant reduction in the computation time. Computation time is expected to be higher when a polycrystalline model is used in the surrounding medium instead of simply using a single crystal model. This explains why the HEM$_{Voronoi}$ case has lower computation time than the the HEM$_{10}$ case.

	HEM$_{129}$	HEM$_{10}$	HEM$_{Voronoi}$	Slice
Computation time (min)	2573	959	856	427

Table 6.3: Computation time for different cases, using 32 processors

Computations were carried out without remeshing. The main motivation is to avoid any loss of local orientation information. In chapter 5, it has been shown that the effect of remeshing on global texture evolution is negligible. However, in this section, we are mainly concerned with microtexture analysis involving, among other, orientation deviation computations at the level of each grain. It is expected that remeshing will strongly bias these results. As the strain associated with these analysis is relatively moderate, the computations could be carried out without remeshing. Nevertheless, strain localization is also expected, as seen in chapter 5.

V.3.1   Global texture evolution

Figure 6.20 illustrates the {111} pole figures that were measured experimentally and those which were obtained for the different simulations. As seen, texture evolution is overall well predicted by the different simulations. The intensities, predicted by the simulations, which are higher than the experimental one, suggests lower grain fragmentation and a slower texture evolution in the FE cases. The HEM$_{129}$ and HEM$_{10}$ cases are almost identical while minor differences are observed with HEM$_{Voronoi}$ and Slice case. These results are confirmed by the ODFs shown in figure 6.21. Indeed, the Copper component (sections $\varphi_2 = 25°$ and $\varphi_2 = 45°$) is well captured by all simulations, with higher intensities in the FE cases. Similarly the shift towards the Brass component (section $\varphi_2 = 45°$) is predicted by all simulations, with higher intensities in the FE cases than the experimental result. Also some of the recrystallization component U (section $\varphi_2 = 45°$ bottom left corner and section $\varphi_2 = 90°$ right) initially present, disappears in the experimental predictions, while it remains in the FE cases (section $\varphi_2 = 45°$). The S component (section $\varphi_2 = 25°$) is stronger in the experimental results than in the FE cases. The strengthening of the Rotated cube component (section $\varphi_2 = 90°$) is predicted by CPFEM while the slight shift towards the Goss component (section $\varphi_2 = 90°$) is not revealed by the simulations.

0.5 1 1.5 2 2.5 3.5 4 4.5 5
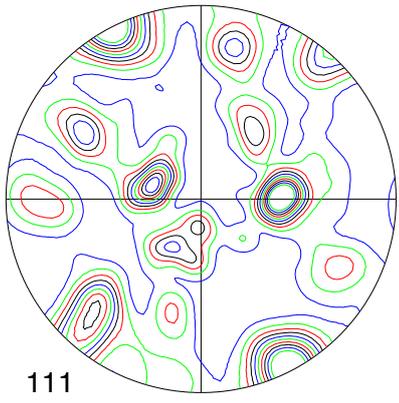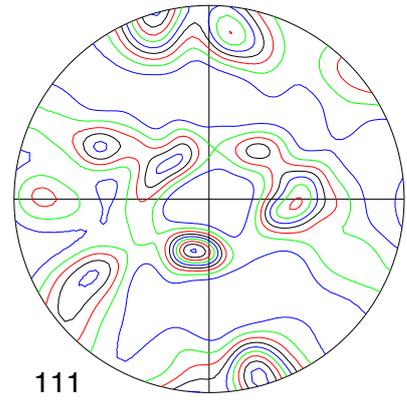
(a) Initial

(b) Experimental results after $\varepsilon = 0.4$
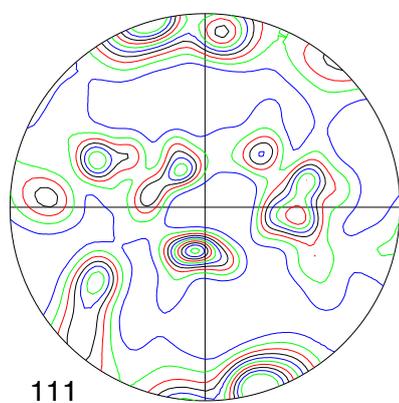
(c) HEM$_{129}$ after $\varepsilon = 0.4$
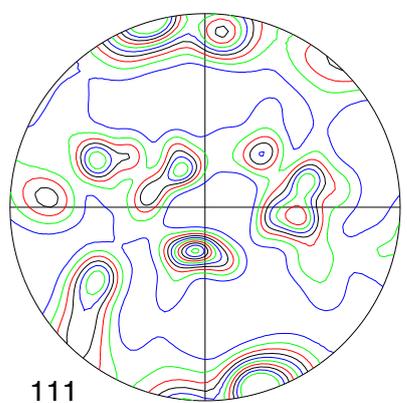
(d) HEM$_{10}$ after $\varepsilon = 0.4$
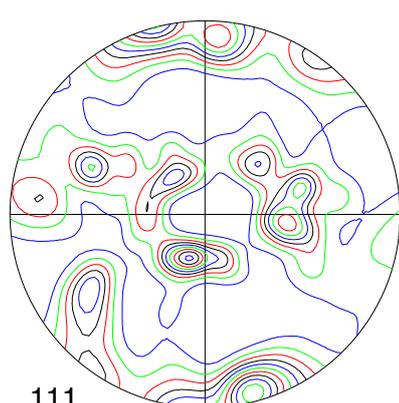
(e) HEM$_{Voronoi}$ after $\varepsilon = 0.4$
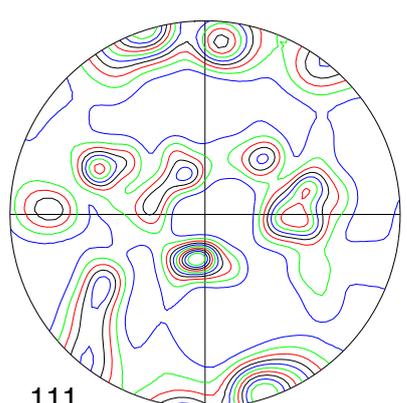
(f) Slice after $\varepsilon = 0.4$

Fig. 6.20: {111} pole figures obtained for different surrounding media.

114

(a) Initial

(b) Experimental results after $\boldsymbol{\varepsilon} = 0.4$

(c) HEM$_{129}$ after $\boldsymbol{\varepsilon} = 0.4$

(d) HEM$_{10}$ after $\boldsymbol{\varepsilon} = 0.4$

(e) HEM$_{Voronoi}$ after $\boldsymbol{\varepsilon} = 0.4$

(f) Slice after $\boldsymbol{\varepsilon} = 0.4$
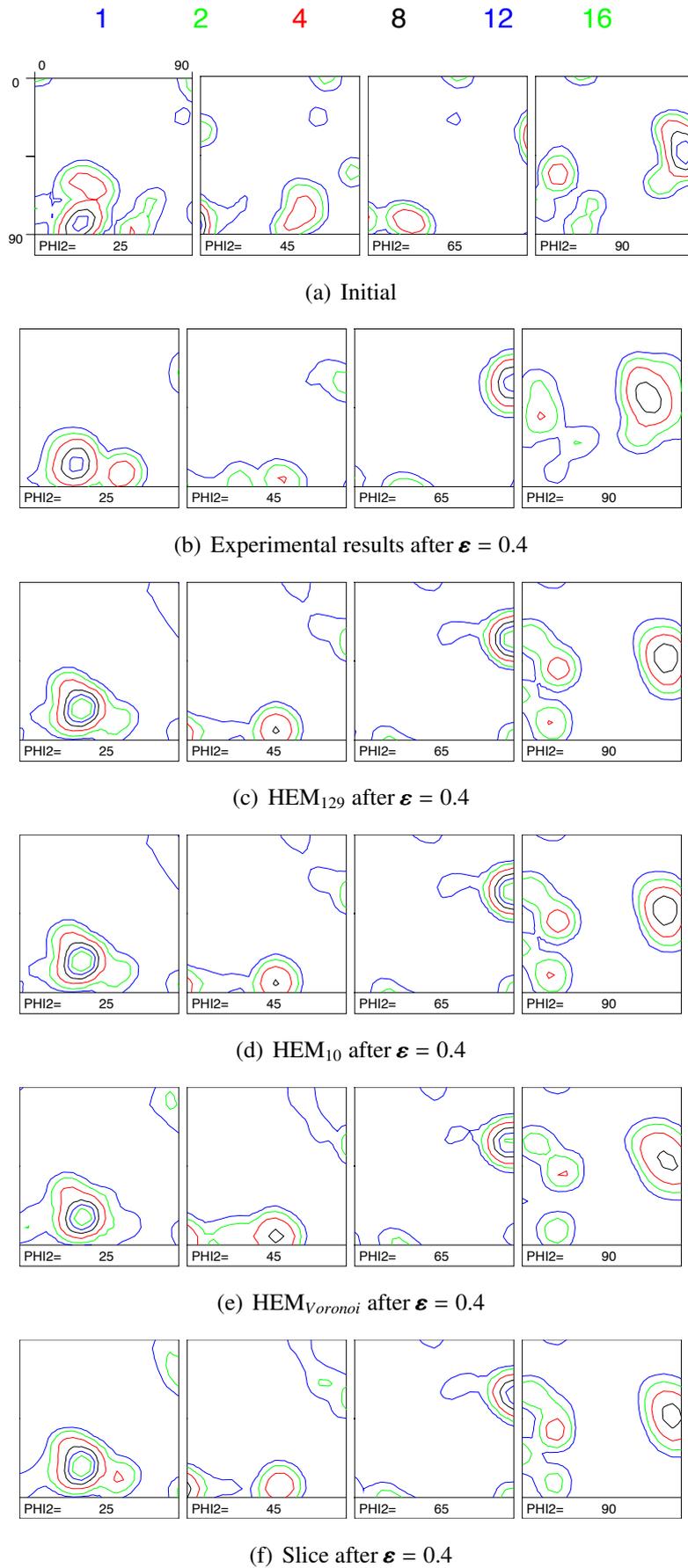
Fig. 6.21: ODF representing texture predictions obtained experimentally and numerically for different surrounding media ($\varphi_2 = 25°, 45°, 65°$ and $90°$).

Figures 6.22 and 6.23, show the texture component maps that were measured experimentally and predicted by the simulations. Compared to pole figure maps or ODF representations, these maps give topological and morphological information. First, as seen, the deformed configuration is overall well predicted by the simulations, but also on a grain by grain basis, i.e the individual shape evolution of the grains is well captured by the simulations. When comparing the different cases, if one is to superimpose the different maps, one can notice minor shape differences between HEM_{129} and HEM_{10} while more discrepancies are observed when compared to the other two cases. For a number of grains, the FE simulations predict well the appearance of certain components. This is the case for Copper for grains 3, 7, 21, 26, 35 and 71. The appearance of Brass in grains 23 and 44 is also predicted. On the other hand, CPFEM fails to predict the appearance of the Goss component in grain 8 and its strengthening in grain 61 (it actually disappears in the FE cases). Also, the finite element results provide in general more concentrated micro-textures than the experimental ones, as it is the case for grains 3,7 and 26. The strong U component in grains 6, 24 and 58 diminishes after deformation in the experimental data as opposed to what is predicted by the simulations. This is also the case for grains 1, 18 and 36. These results suggest slower texture evolution in the CPFEM cases.

The inverse pole figure (IPF) maps 6.24 and 6.25 give yet another insight into the predicting capabilities of our CPFEM framework. Clearly, the maps of the simulations exhibit less fragmentation than the experimental measurements. The FE maps show a more continuous gradient of orientation as opposed to the more patchwork-like aspect of the experimental maps. Nevertheless, the main trends are in general predicted. For example, the behavior of stable grains, like grains 6 and 24, is correctly reproduced. The fragmentation of others is also predicted. The fragmentation of grain 2 in distinct regions is predicted, even though the FE maps do not indicate the correct final experimental orientation. The fragmentation of grain 14 is also clearly visible in the FE cases, even-though the simulations fail to account for the division of the grain into two distinct regions. Regarding the effect of using different approximations for the surrounding medium, there are observable discrepancies on a grain by grain basis, especially between the HEM_{129} and HEM_{10} cases on the one hand, and the $HEM_{Voronoi}$ and the Slice cases on the other hand. Grain 11 and grain 21 for example are quite illustrative. It is important to note that these two grains "feel" the effect of the HEM in a different way. Grain 21 is on the periphery of the studied microstructure and therefore experiences the direct influence of the HEM, as opposed to grain 11, which experiences the effect of the HEM only along the third dimension. The fact that the influence of the HEM is observed regardless of the position of the grain suggests that this third dimension has an influence on the predictions.

Orientation	Orientation
Euler Angles	{hk(i)l}<uv(t)w>
(39.2, 65.9, 26.6)	(1 2 1)<1 -1 1>
(56.8, 77.4, 26.6)	(2 4 1)<1 -1 2>
(64.9, 74.5, 33.7)	(2 3 1)<1 -2 4>
(52.9, 74.5, 33.7)	(2 3 1)<3 -4 6>
(54.7, 90.0, 45.0)	(1 1 0)<1 -1 2>
(0.0, 45.0, 90.0)	(1 0 1)<0 -1 0>
(0.0, 0.0, 0.0)	(0 0 1)<1 0 0>
(90.0, 90.0, 22.6)	(5 12 0)<0 0 1>
(90.0, 45.0, 360.0)	(0 1 1)<0 -1 1>
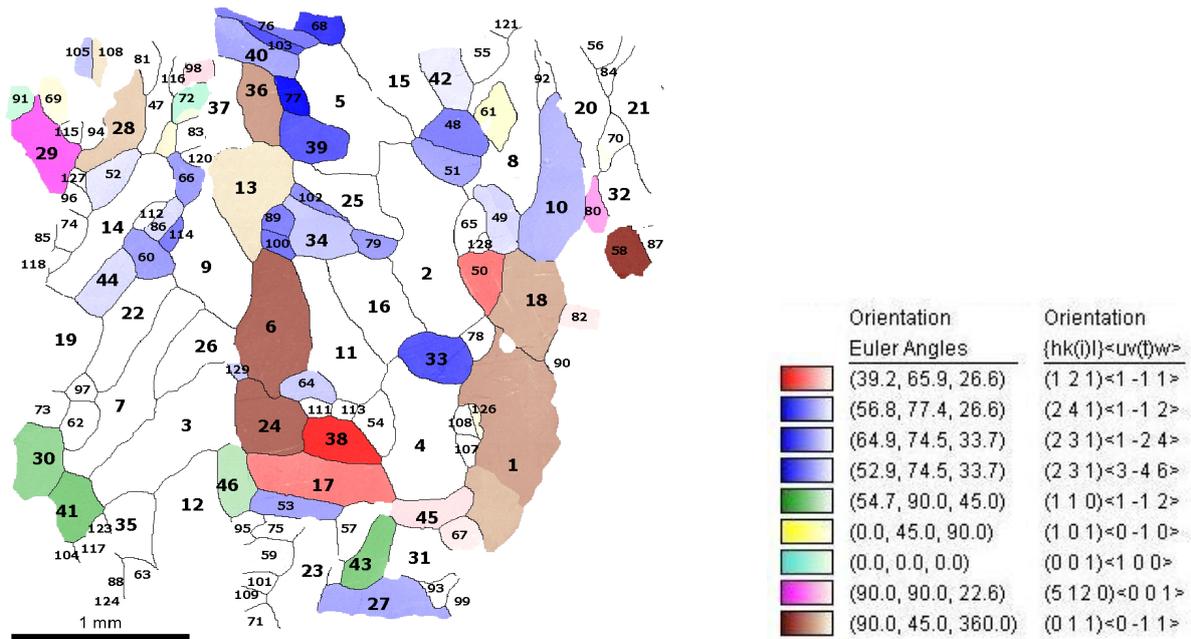
(a) Initial
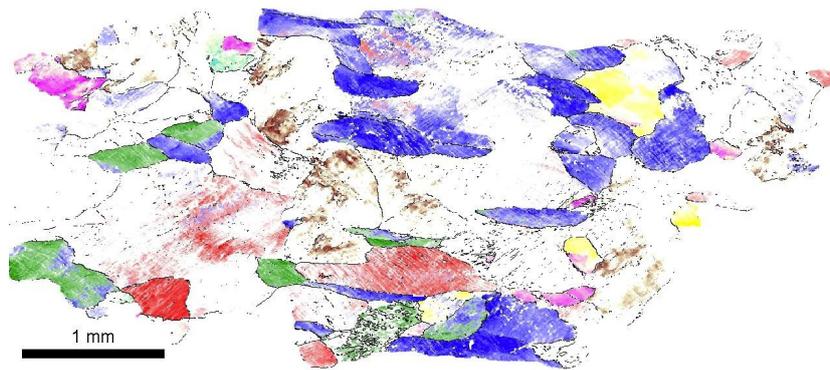
(b) Experimental results after $\varepsilon = 0.4$
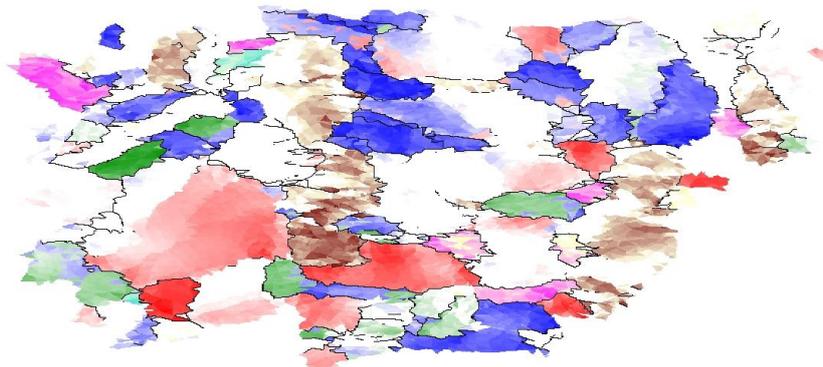
(c) HEM$_{129}$ after $\varepsilon = 0.4$

Fig. 6.22: Deviations from ideal texture components obtained experimentally and for the HEM$_{129}$ case. Colour codes is S: blue, Copper: red, Brass: green, Goss: yellow, Cube: cyan, Rotated Cube: magenta and U: brown. Maximum deviation from ideal components is set to 15°. High angle grain boundaries (>15°) are plotted as black segments

117
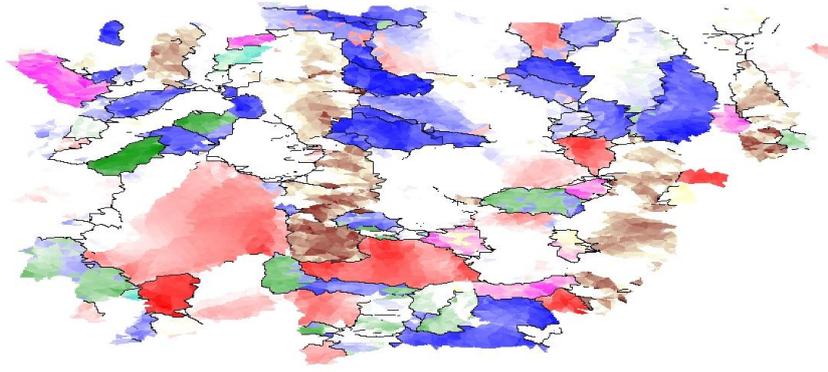
(a) HEM$_{10}$ after $\varepsilon = 0.4$

(b) HEM$_{Voronoi}$ after $\varepsilon = 0.4$

(c) Slice after $\varepsilon = 0.4$

Fig. 6.23: Deviations from ideal texture components obtained for the HEM$_{10}$, HEM$_{Voronoi}$ and Slice cases. Colour codes is S: blue, Copper: red, Brass: green, Goss: yellow, Cube: cyan, Rotated Cube: magenta and U: brown. Maximum deviation from ideal components is set to 15°. High angle grain boundaries (>15°) are plotted as black segments
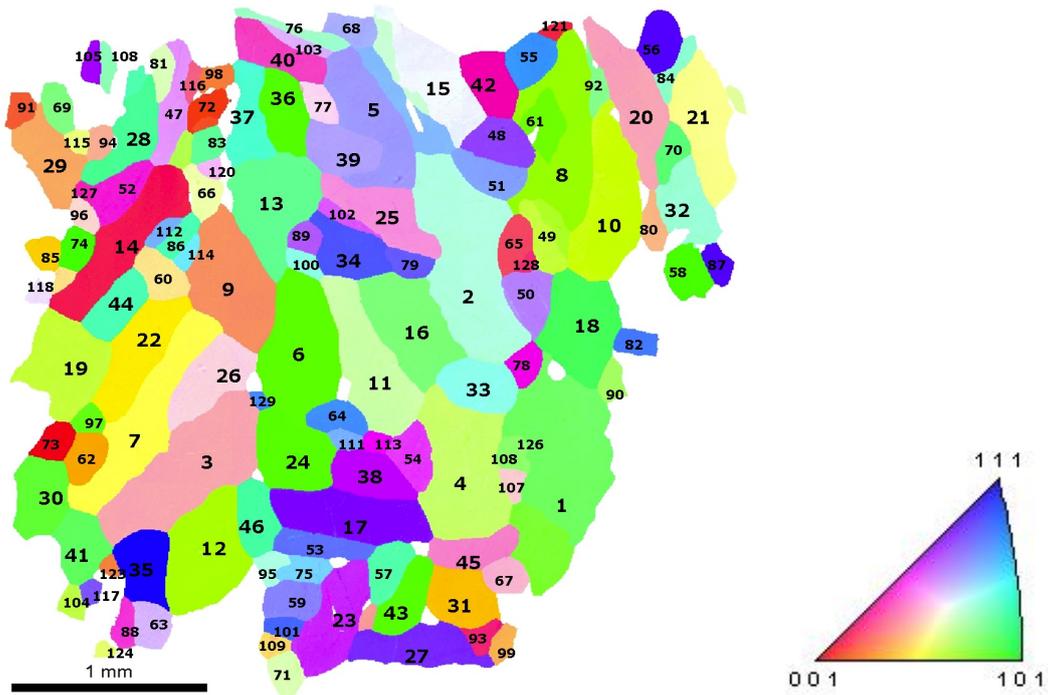
(a) Initial
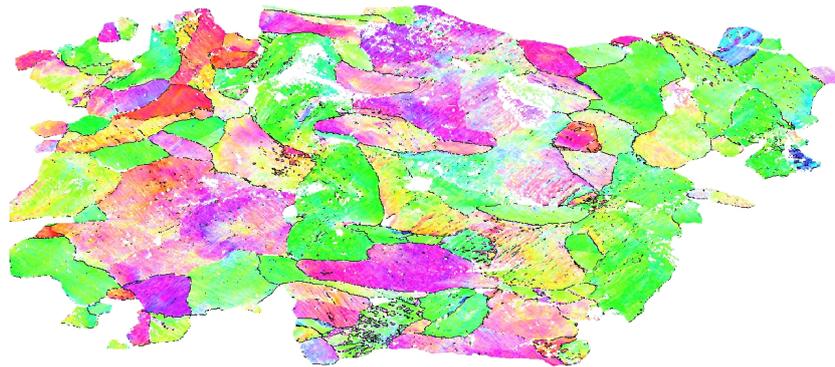
(b) Experimental results after $\varepsilon = 0.4$
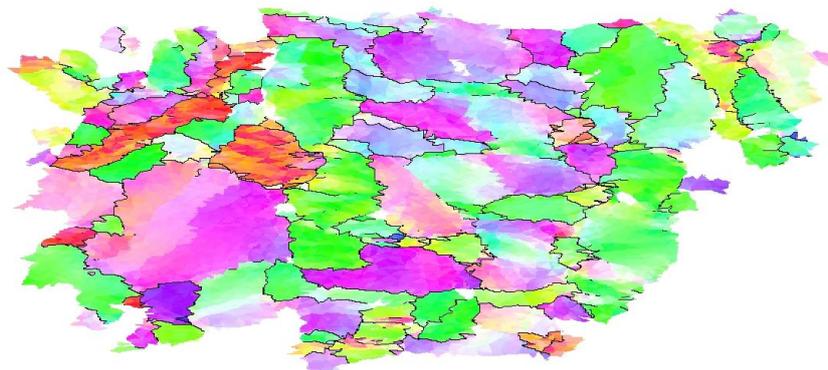
(c) HEM$_{129}$ after $\varepsilon = 0.4$

Fig. 6.24: Inverse pole figure (IPF) maps for sample normal axis obtained experimentally and for the HEM$_{129}$ case. High angle grain boundaries ($>15°$) are plotted as black segments
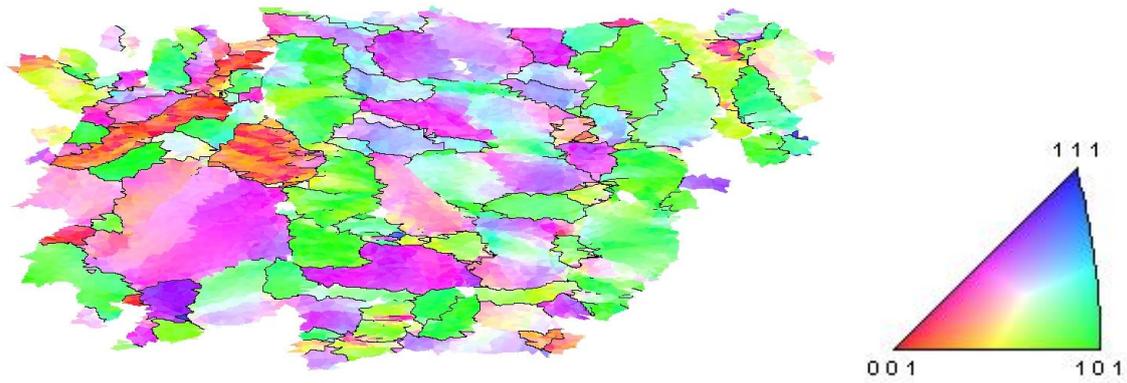
(a) HEM$_{10}$ after $\boldsymbol{\varepsilon} = 0.4$
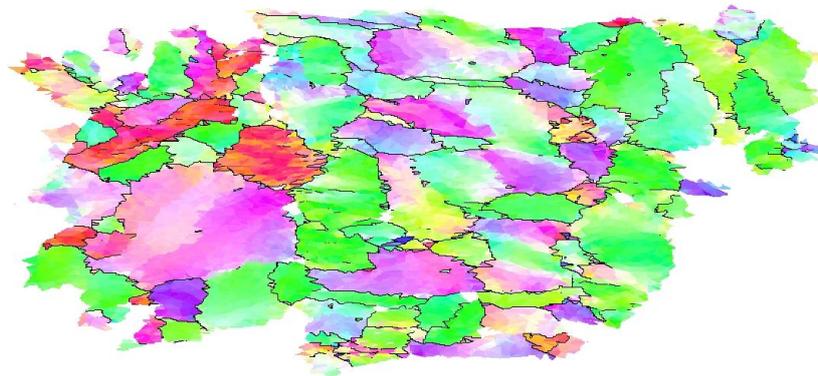
(b) HEM$_{Voronoi}$ after $\boldsymbol{\varepsilon} = 0.4$
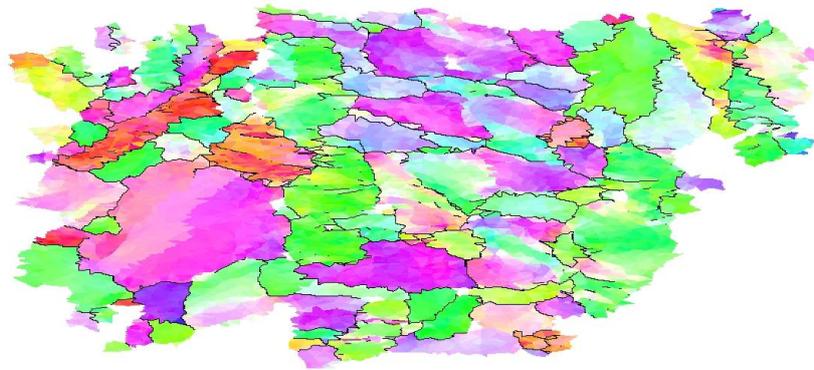
(c) Slice after $\boldsymbol{\varepsilon} = 0.4$

Fig. 6.25: Inverse pole figure (IPF) maps for sample normal axis obtained for the HEM$_{10}$, HEM$_{Voronoi}$ and Slice cases. High angle grain boundaries ($>15°$) are plotted as black segments

V.3.2   Grain subdivision predictions

The mean orientation of the 129 grains is computed using equation 6.2. For every grain, the orientation deviation is computed for every point/element belonging to the grain (see section II.2) and an average orientation deviation is computed for every grain. The relative frequency, among the 129 grains, is then determined for bins of $1°$. The resulting distribution is shown

in figure 6.26. As seen, there is a good correspondence between the simulation results and the experimental ones, although deviations are in general underpredicted. Among all the cases, the HEM$_{Voronoi}$ case yields an overall greater grain fragmentation and is therefore the closest to the experimental data.
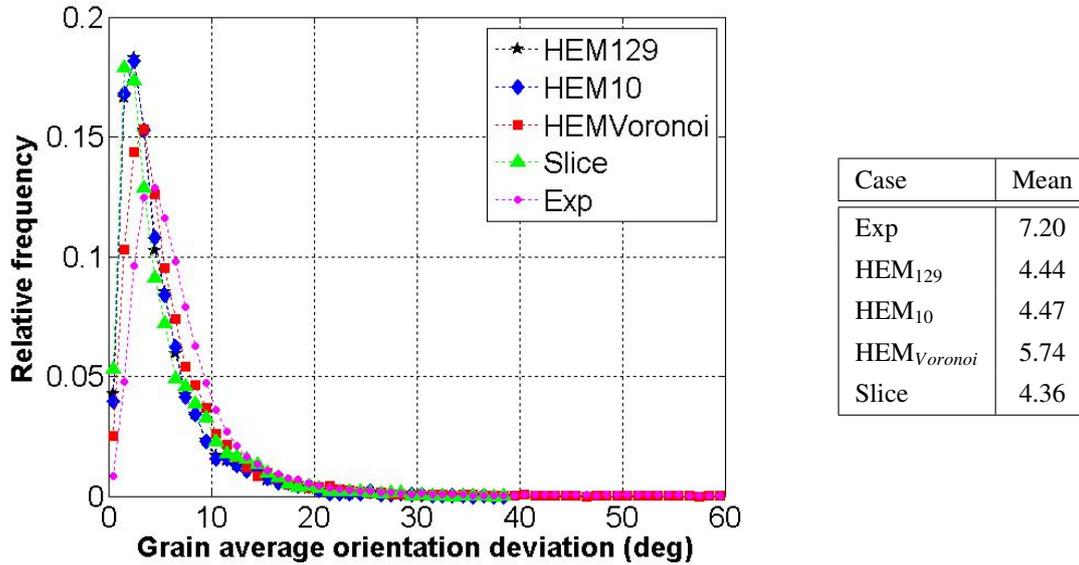
Fig. 6.26: Distribution of grain average orientation deviation

Case	Mean
Exp	7.20
HEM$_{129}$	4.44
HEM$_{10}$	4.47
HEM$_{Voronoi}$	5.74
Slice	4.36

Looking more closely at every grain, figure 6.27 shows the relationship between grain size and average orientation deviation for the experimental data. As mentioned by [LEBENSOHN et al., 2005], the discrete nature of the EBSD technique and the fact that the step size is constant, regardless of grain size, could introduce a bias in the distribution, due to the fact that fewer points are considered in the case of small grains. The figure shows that this is not the case, as small grains could have average orientation deviations higher that $10°$. The observations of [LEBENSOHN et al., 2005], in the case of copper (15% tension), and [PANTLEON et al., 2008] for cold rolled aluminum (38 % reduction), in terms of larger grains exhibiting higher average orientation deviations, are not clearly visible in this figure. Besides, the numerical data in figure 6.28 show that the mesh discretization does not introduce a bias.

Regarding the effect of the HEM approximation, figure 6.29 compares the average orientation spread of the HEM$_{10}$, HEM$_{Voronoi}$ and Slice cases to the experimental ones for all 129 grains and for the first 20 grains for more clarity. The HEM$_{129}$ case is not shown as it yields very close results to the HEM$_{10}$ case. It is observed that, on a grain by grain basis, the results are dependent on the approximation used for the HEM. While the HEM$_{10}$ and Slice cases seem to underpredict the average orientation, the cloud of points in the HEM$_{Voronoi}$ case is more centered. Looking at the 20 first grains, one can also see that, for a given grain, for example grain 11, the three predictions are significantly different ($4.5°$ in the HEM$_{10}$ case, $9.5°$ in the HEM$_{Voronoi}$ case and $7°$ for the Slice case).
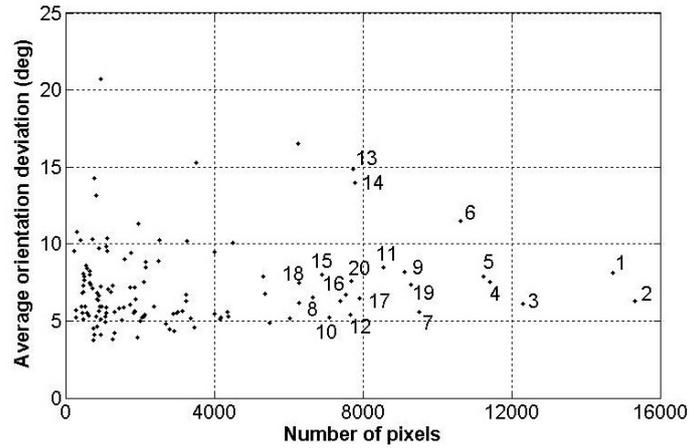
Fig. 6.27: Average orientation deviation as function of grain size (pixels) after deformation for the 129 grains obtained experimentally. The first 20 grains are labelled.
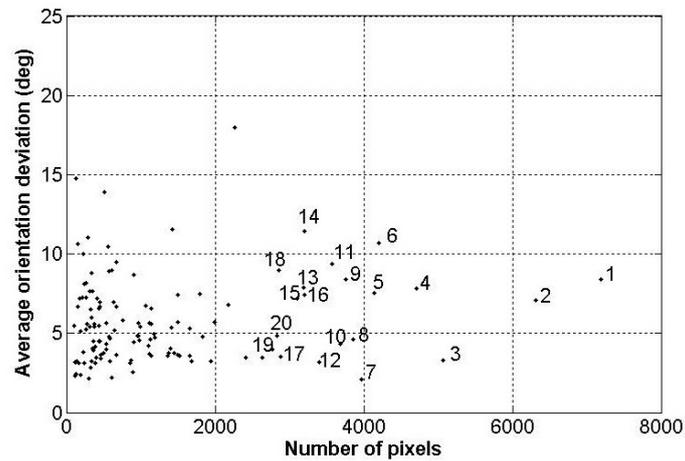
Fig. 6.28: Average orientation deviation as function of grain size (pixels) after deformation for the 129 grains obtained using the Voronoi approximation for the HEM. The first 20 grains are labelled. The number of pixels is representative of the number of elements used to discretize each grain.
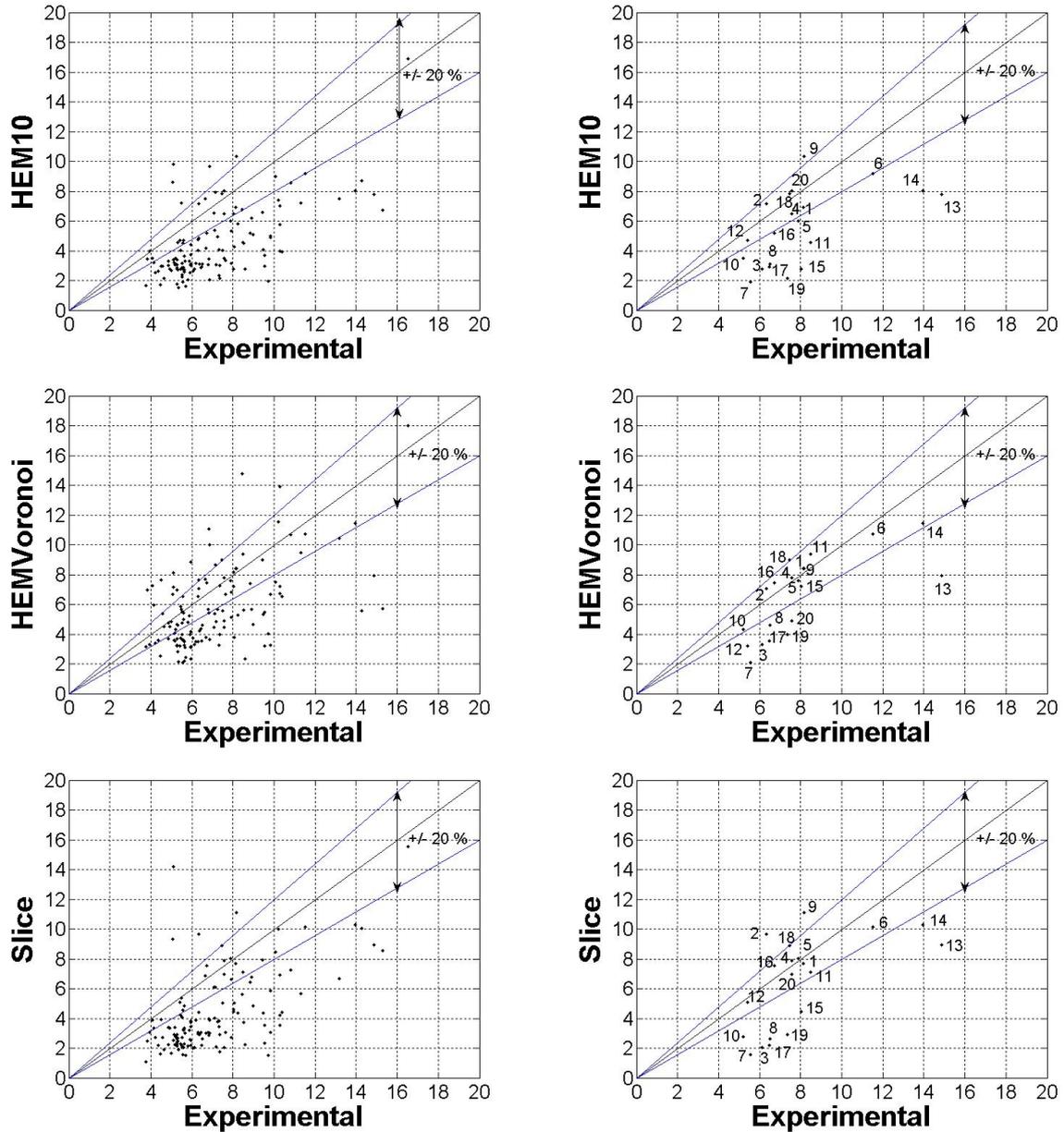
Fig. 6.29: Average orientation deviation for every grain using the HEM$_{10}$, HEM$_{Voronoi}$ and Slice approximations for the HEM (left: all grain; right: the first 20 grains)

V.3.3 Average orientation predictions and orientation deviation distributions for the first ten grains

In order to further investigate the simulation results, the first ten grains were analyzed more closely. Figure 6.30 describes their mean initial and final orientation as predicted by the HEM$_{129}$ simulation and as measured experimentally. The trajectories for grains 2, 3, 5, 6, 7 and 8 seem coherent with the experimental results as opposed to grain 9 for example, where the simulation predicts an evolution in the opposite direction. Also, the simulation predicts results that are quite different from the experimental data for grains 1,4 and 10.
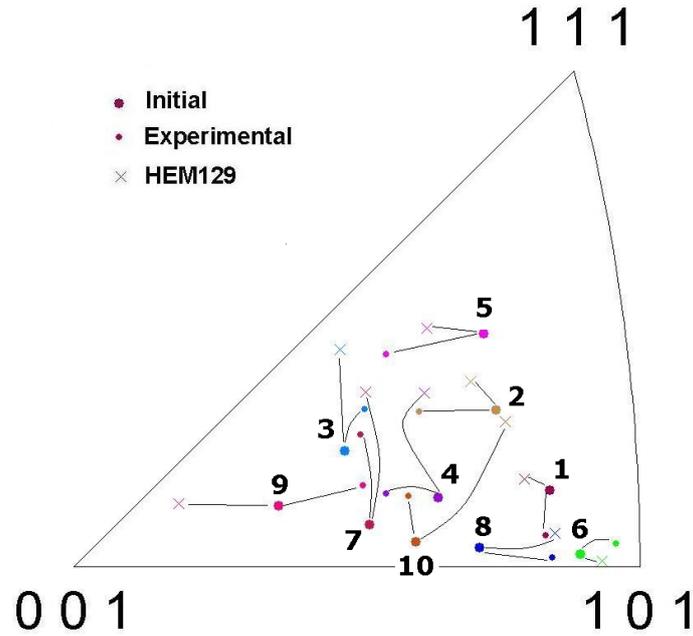
Fig. 6.30: Grain rotation paths (for the mean orientation) obtained experimentally and for the HEM_{129} case.

Figure 6.31 shows that the results are always sensitive to the type of medium selected for surrounding the columnar microstructure, except for the HEM_{129} and HEM_{10} cases which give close predictions. Another way of quantifying the discrepancies obtained on the final mean orientations is to compute the misorientation with respect to the experimental value, as presented in table 6.4. As expected, grain 9 yields a large value, reflecting the information obtained on the inverse pole figure maps 6.30 and 6.31. It is worth mentioning that the $\text{HEM}_{Voronoi}$ case yields a significantly lower misorientation value than the other approximations for grains 2, 3 and 4, while the Slice case is the closest to the experimental value for grains 8, 9 and 10.

Figure 6.29 shows that, although the average orientation deviation could be very close to the experimental measurement, such as for grain 4, this does not mean that the final mean orientation is correctly predicted (see figure 6.30 and 6.31). This is all the more true when we look at the distribution of the average orientation deviation for every grain as in figures 6.32 and 6.33. In figure 6.32(d), the shape of the experimental distribution in grain 4 is well reproduced by the FE cases, although the "tail" of the experimental distribution is not accounted for. The higher deviations obtained experimentally, for all grains in figures 6.32 and 6.33, are consistent with the inverse pole figure map (see figure 6.24(b)), which shows higher fragmentation in the experimental data. It is worth noting, that in the case of grain 9 (see 6.33(c)) the shape (and mean) of the distribution is best matched by the $\text{HEM}_{Voronoi}$ case, although table 6.4 shows that the Slice case yields the smallest misorientation between the final experimental average orientation and the mean value predicted by the simulation. Finally, the distributions, in figures 6.32 and 6.33, show that the location of the grain in the microstructure (i.e grains with a completely determined 2D neighborhood as opposed to peripheral grains like grain 1) is not a determin-

ing factor, regarding how well the predictions conform to the experimental data in terms of orientation deviation. This suggests that the third dimension have an important impact on the predictions.
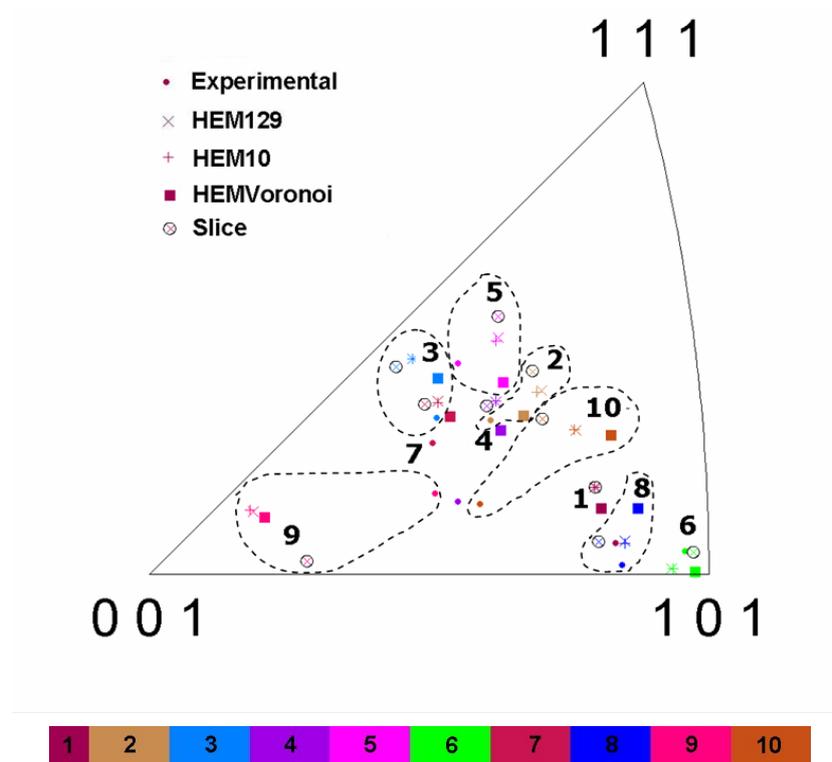
Fig. 6.31: Final mean orientations obtained experimentally and for the different HEM (the color legend corresponds to grains from 1 to 10).

Grain number	HEM$_{129}$	HEM$_{10}$	HEM$_{\text{Voronoi}}$	Slice
1	8.8	8.5	9.6	11.1
2	4.7	4.3	2.9	5.9
3	6.3	6.3	5.5	6.5
4	9.2	9.2	7.1	8.5
5	3.8	3.5	4.6	5.3
6	6.8	6.3	4.6	8.8
7	5.6	5.5	6.0	5.8
8	10.4	10.1	13.6	8.7
9	23.1	23.6	21.4	17.1
10	10.3	10.2	12.5	8.7

Table 6.4: Misorientation between the mean experimental orientation and the mean orientation obtained for each HEM after deformation for the ten first grains.
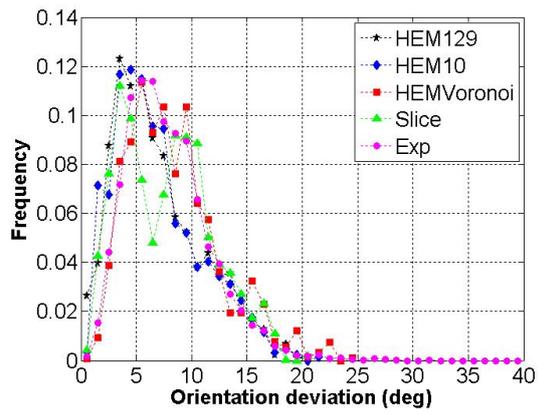
(a) Grain 1   (b) Grain 2
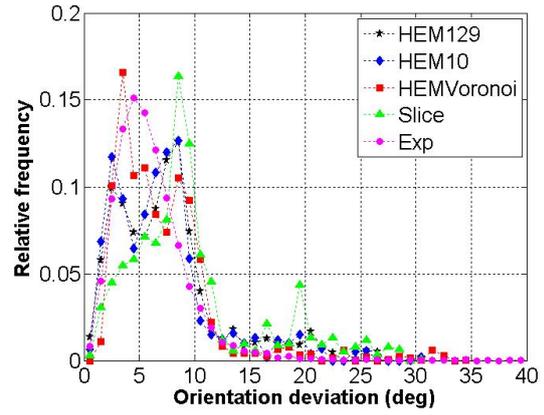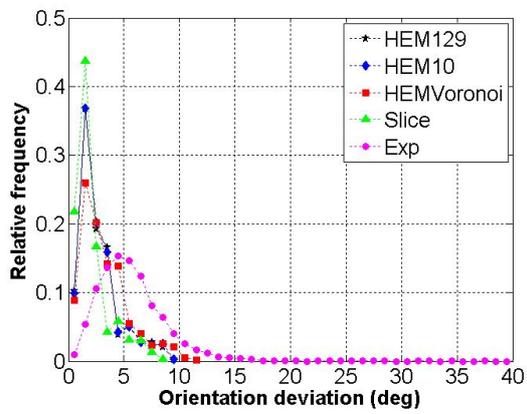
(c) Grain 3   (d) Grain 4
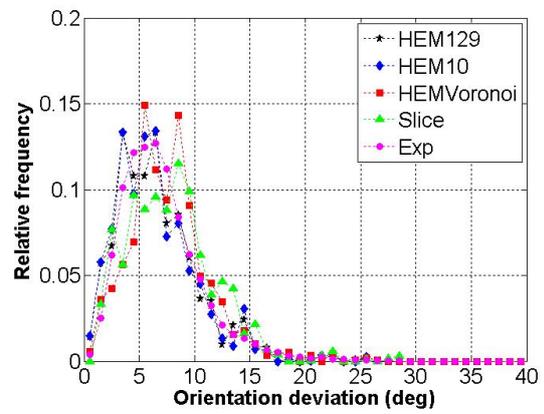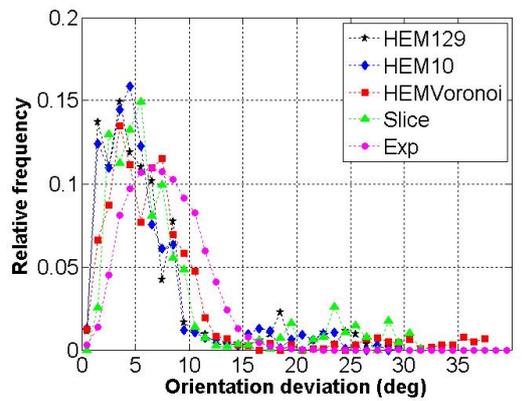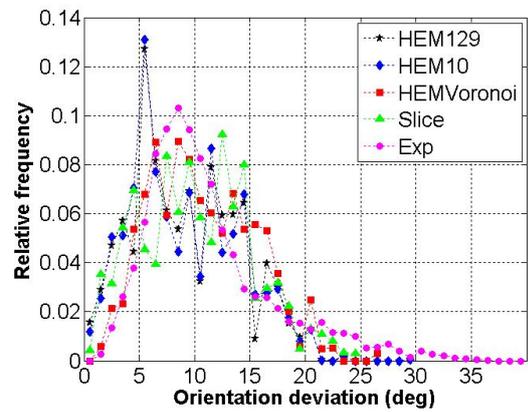
(e) Grain 5   (f) Grain 6

Fig. 6.32: Orientation deviation by grain (grain 1 to 6)

(a) Grain 7

(b) Grain 8

(c) Grain 9

(d) Grain 10
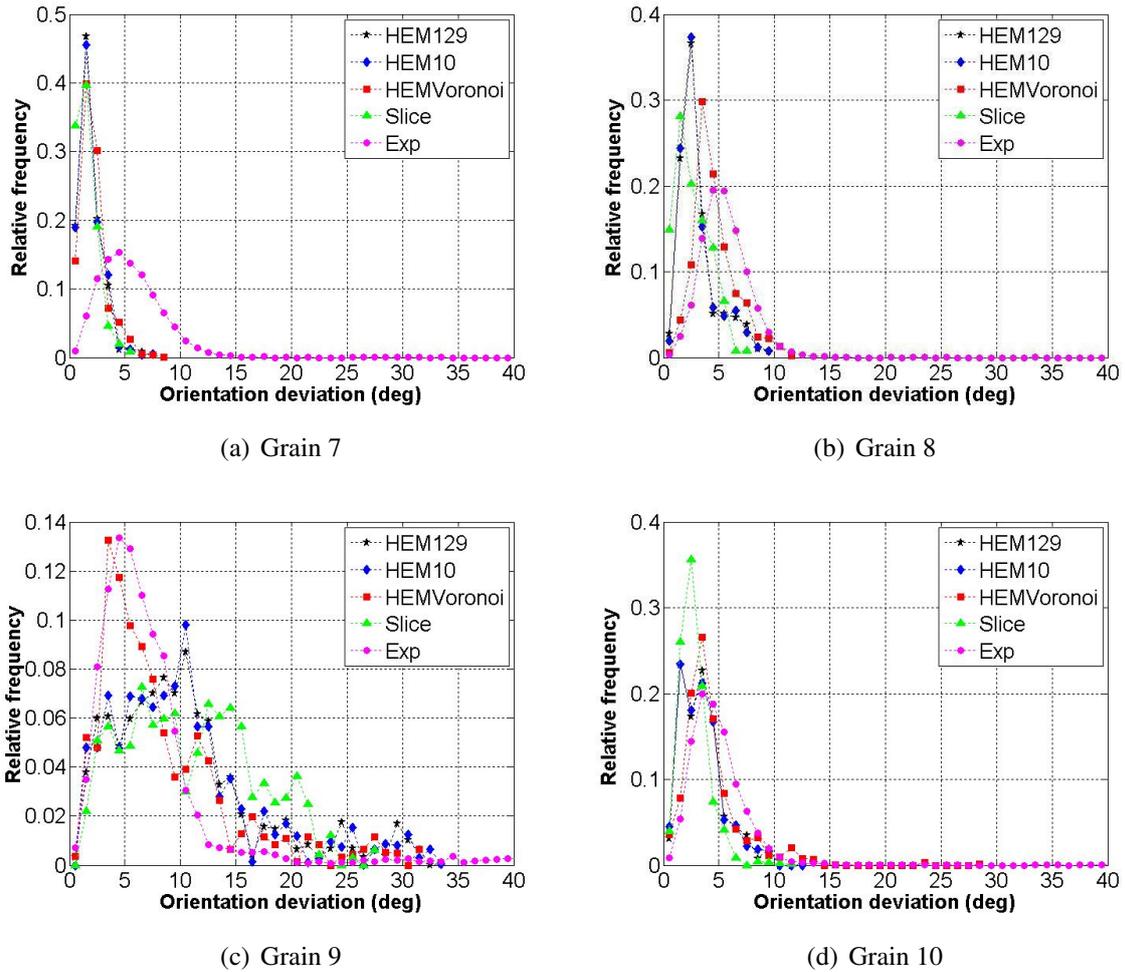
Fig. 6.33: Orientation deviation by grain (grain 7 to 10)

Bearing all the simplifying assumptions regarding the construction of the microstructure, the results presented in this section show that there is a good agreement between the simulations and the experiment in terms of global texture evolution. Moreover, the effect of the approximation used for the HEM on these global results is limited. On the other hand, on a grain by grain basis, there is clearly more discrepancies. Also, these local results have proven to be sensitive to the choice of the surrounding environment.The $HEM_{Voronoi}$ case yields results that are the closest to the experimental ones compared to the HEM_{10} and HEM_{129} cases (see figures 6.26, and 6.29). Also the computation time associated with this case is lower than the other two cases. Compared to the Slice case, the $HEM_{Voronoi}$ case give, on average, results that are closer to the experimental ones (see figures 6.26, and 6.29). The $HEM_{Voronoi}$ distributions in figures 6.32 and 6.33 are, in general, more in line with the experimental ones than those of the Slice case (as illustrated by grain 9). Finally, the simulation setup of the $HEM_{Voronoi}$ case is more physically close to the experimental setting. Moreover, edge effects related to the application of the boundary conditions are avoided. For all these reasons, the $HEM_{Voronoi}$ case is selected for further investigation as presented in the next section.

One of the most clear difference between the results of the simulation and the experimen-

tal ones is the extent of fragmentation, as highlighted in the inverse pole figure maps (see figure 6.24(b)) and in the "tail" of the distributions in figures 6.32 and 6.33. The fragmentation in the FE cases is expected to be linked to the degree of mesh refinement. This refinement can be achieved more optimally, as seen in chapter 5, by using an anisotropic mesh. Therefore in the following section, the effect of mesh refinement and type is assessed, with the objective of evaluating if such efforts lead to an improvement in the predictions. Also, the results of the $HEM_{Voronoi}$ case suggest that, surrounding the microstructure with a more anisotropic environment (compared to the averaged response of the HEM_{129} and HEM_{10} cases), leads to better predictions. The columnar character of the microstructure creates a buffer zone around the central section in the third dimension, preventing strong interaction with the surrounding medium. For this reason, a non-columnar microstructure is also investigated in the following section.

V.4 Effect of mesh refinement and microstructure type

In this section, we investigate the effect of mesh refinement, mesh type and microstructure type. The $HEM_{Voronoi}$ previously investigated was compared to 3 highly resolved computations which are summarized in table 6.5.

Case	Microstructure	Mesh type	# elements in mesh	mesh size in grains	mesh size in surrounding medium
$HEM_{Voronoi}$	columnar	isotropic	484649	$h \approx 0.015$	$h \approx 0.032$
$HEM_{Voronoi2}$	columnar	isotropic	2203334	$h \approx 0.0117$	$h \approx 0.015$
Columnar	columnar	anisotropic	2444166	$h \approx 0.005$	$h \approx 0.032$
Non-columnar	non-columnar	anisotropic	2380190	$h \approx 0.005$	$h \approx 0.032$

Table 6.5: cases for the investigation of mesh refinement and microstructure type

For the isotropic cases, the distance function to the slice is used to generate non-uniform isotropic meshes, yielding a coarser mesh in the surrounding medium and much finer mesh size in the slice. In order to investigate the effect of mesh refinement, a smaller mesh size is chosen for the inner slice in the $HEM_{Voronoi2}$ case. Due to the nature of the metric used to construct this mesh, a smaller mesh size in the surrounding medium is necessary by construction due to the mesh generator capability. For the anisotropic cases, more optimized meshes are used based on the anisotropic metric presented in chapter 4 (see equation 4.5) . The individual distance function for every grain is used to generate the mesh. The refinement thickness e close to the grain boundary is taken large enough to yield a refinement nearly across the full volume of most grains (evidently, this is especially true for small grains). The mesh size in the refinement direction is set to ($h \approx 0.005$). Due to the nature of the metric that we are using, the mesh size

in the other two directions determines the mesh size in the surrounding medium. The mesh size in the other two directions is chosen equal to $h \approx 0.032$ yielding an isotropic mesh in the surrounding medium which is equivalent to the HEM$_{\text{Voronoi}}$ case. Table 6.6 compares the resolution of the different meshes for the first ten grains in 3D. The parameters for the "non-columnar" mesh are the same as the "columnar" case, the difference in numbers of elements is due to the non-columnar nature of the microstructure. The non-columnar microstructure is generated, as explained in chapter 4 section II, by concatenating several 2D layers. These sections are obtained by evolving the experimental 2D section using a Monte-Carlo (MC) algorithm. The final non-columnar microstructure is reconstructed by combining the different layers around a central section, which corresponds to the original 2D experimental section.

Grain number	HEM$_{\text{Voronoi}}$	HEM$_{\text{Voronoi2}}$	Columnar	Non-Columnar
1	5882	14731	34936	21896
2	5165	12648	27904	15602
3	4312	10729	25038	14718
4	3724	9423	21398	10406
5	3413	8293	17323	7068
6	3302	8392	17853	8542
7	3223	7973	15590	8387
8	3026	7583	10376	6528
9	2941	7361	19742	6903
10	2978	7307	16577	8983

Table 6.6: Number of elements per grain for the different meshes for the first ten grains (in 3D).

V.4.1   Global texture evolution

Figures 6.34 and 6.35 represent the global texture evolution predictions. The differences between the HEM$_{Voronoi}$ and HEM$_{Voronoi2}$ cases are insignificant. The effect of refining the mesh, in the slice as well as the surrounding medium, has therefore no influence on the global results. This is also true when comparing these cases to the anisotropic columnar case. The non-columnar case yields slight observable differences. However, the discrepancies are not as striking as one would expect. Also, the inverse pole figure map in figure 6.36 shows, at first, no significant differences.

0.5   1   1.5   2   2.5   3.5   4   4.5   5
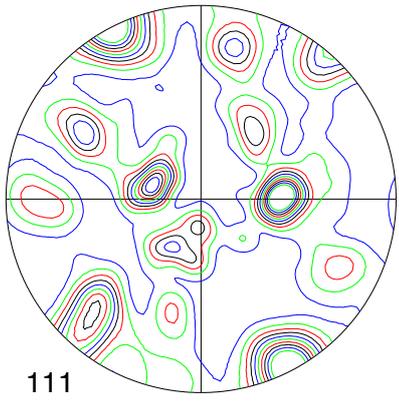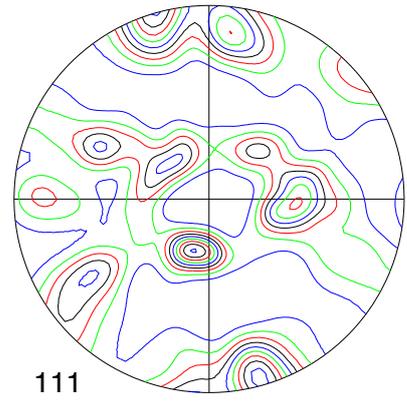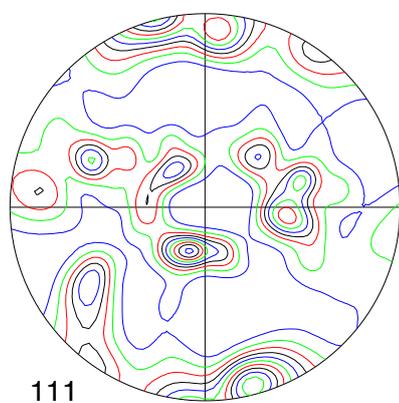
(a) Initial

(b) Experimental results after $\varepsilon = 0.4$
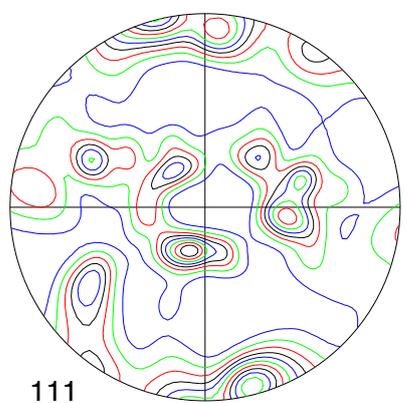
(c) HEM$_{Voronoi}$ after $\varepsilon = 0.4$

(d) HEM$_{Voronoi2}$ after $\varepsilon = 0.4$
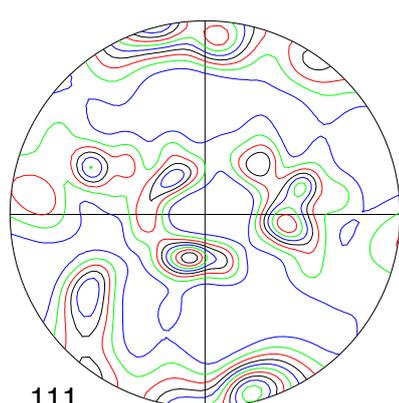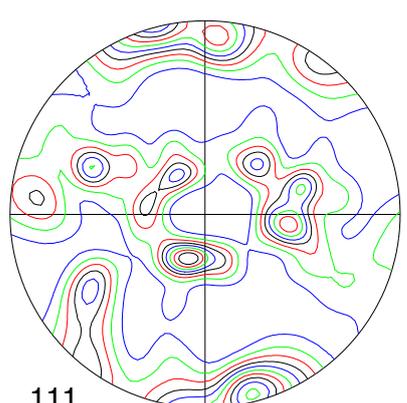
(e) Columnar after $\varepsilon = 0.4$

(f) Non-columnar after $\varepsilon = 0.4$

Fig. 6.34: {111} pole figures obtained for different microstructures and mesh types.

(a) Initial

(b) Experimental results after $\boldsymbol{\varepsilon} = 0.4$

(c) HEM$_{Voronoi}$ after $\boldsymbol{\varepsilon} = 0.4$

(d) HEM$_{Voronoi2}$ after $\boldsymbol{\varepsilon} = 0.4$

(e) Columnar after $\boldsymbol{\varepsilon} = 0.4$

(f) Non-columnar after $\boldsymbol{\varepsilon} = 0.4$
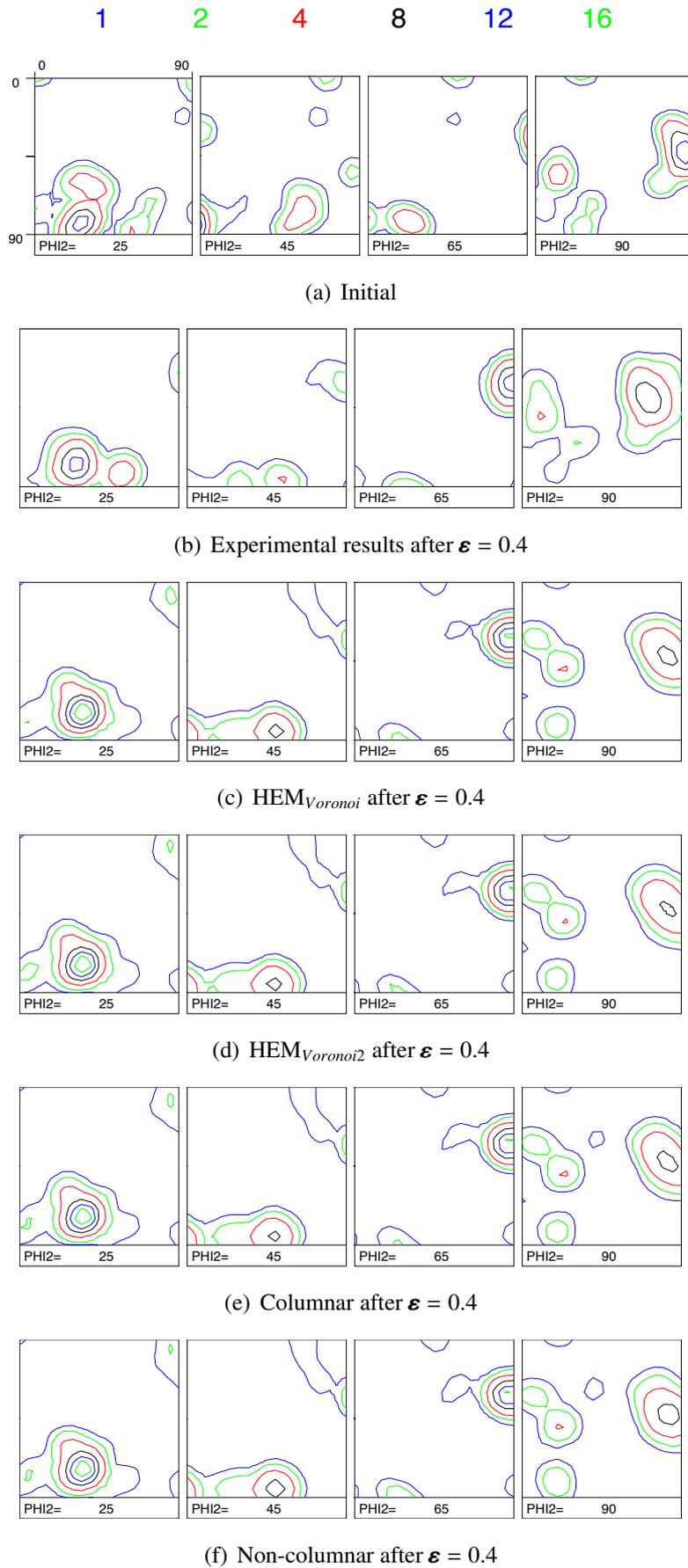
Fig. 6.35: ODF representing texture predictions obtained experimentally and numerically for different microstructures and mesh types ($\varphi_2 = 25°, 45°, 65°$ and $90°$).
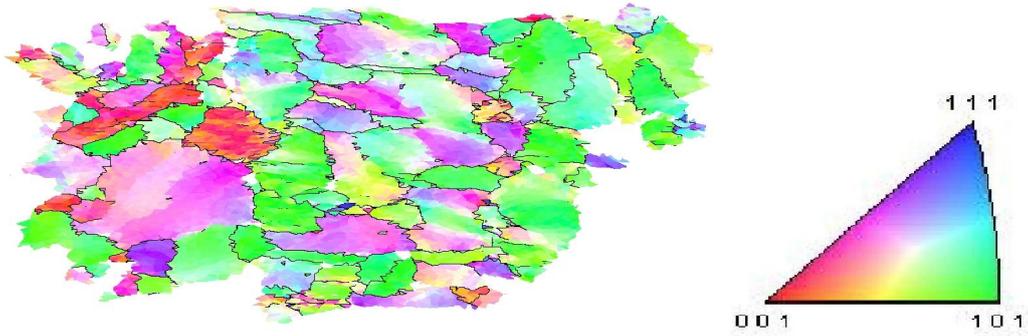
(a) HEM$_{Voronoi}$ after ε = 0.4
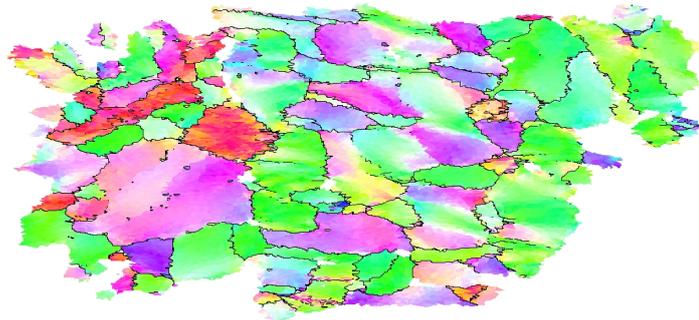
(b) HEM$_{Voronoi2}$ after ε = 0.4
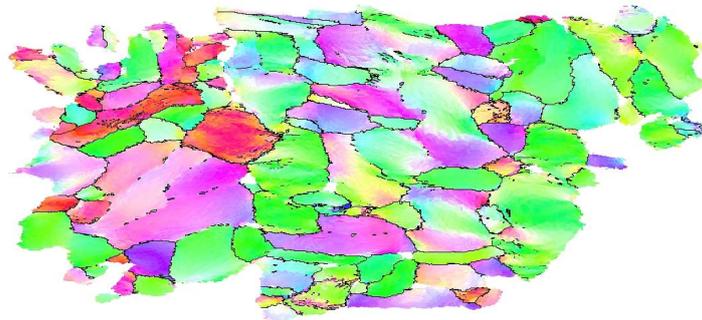
(c) Columnar after ε = 0.4
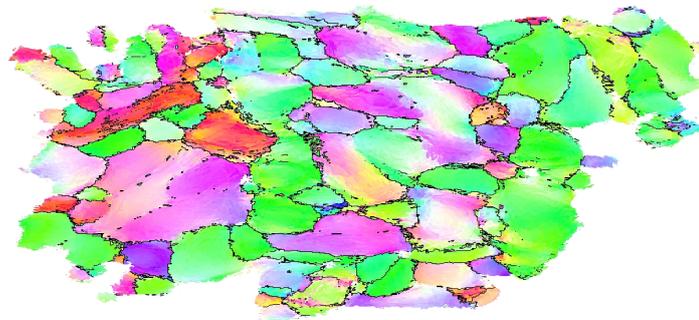
(d) Non-columnar after ε = 0.4

Fig. 6.36: inverse pole figure for sample normal axis. High angle grain boundaries (>15°) are plotted as black segments

V.4.2   Grain subdivision predictions

As seen on figure 6.37, the distributions of the grain average orientation deviation show a very similar shape for all cases. The mean orientation deviation for all grains is very close for all cases and is lower than the experimental value. More differences are observed if we look at the predicted average orientation deviation of every grain with respect to the experimental values, as presented in figure 6.38. For example the fragmentation of grain 18 is overpredicted in the$\text{HEM}_{Voronoi}$, $\text{HEM}_{Voronoi2}$ and Non-columnar cases while the Columnar result is closer to the experimental one. Figure 6.39 is useful for comparing the different simulation cases. As seen, the $\text{HEM}_{Voronoi2}$ predictions are not necessarily larger than those of the less refined isotropic mesh of the $\text{HEM}_{Voronoi}$ case. This is also true when we compare these two cases to the Columnar and Non-columnar one. No evident trend regarding the effect of mesh refinement, mesh type and microstructure type on grain fragmentation, on a grain by grain basis.

Case	Mean
Exp	7.20
$\text{HEM}_{Voronoi}$	5.74
$\text{HEM}_{Voronoi2}$	5.92
Columnar	5.82
Non-columnar	5.93
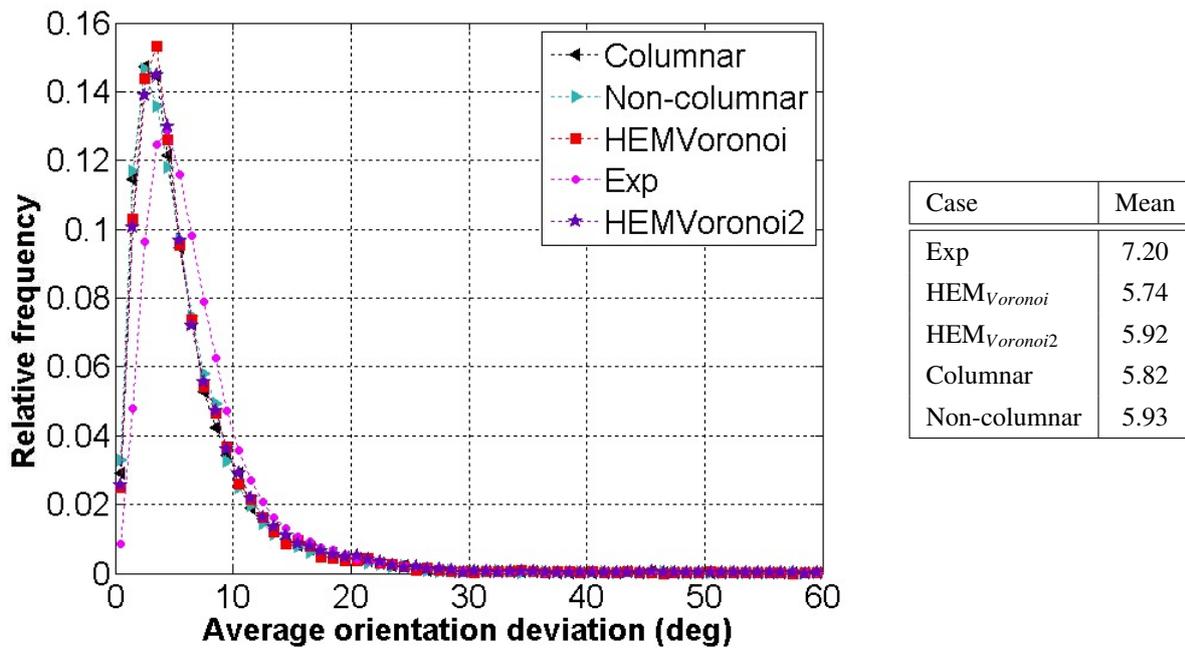
Fig. 6.37: Distribution of grain average orientation deviation
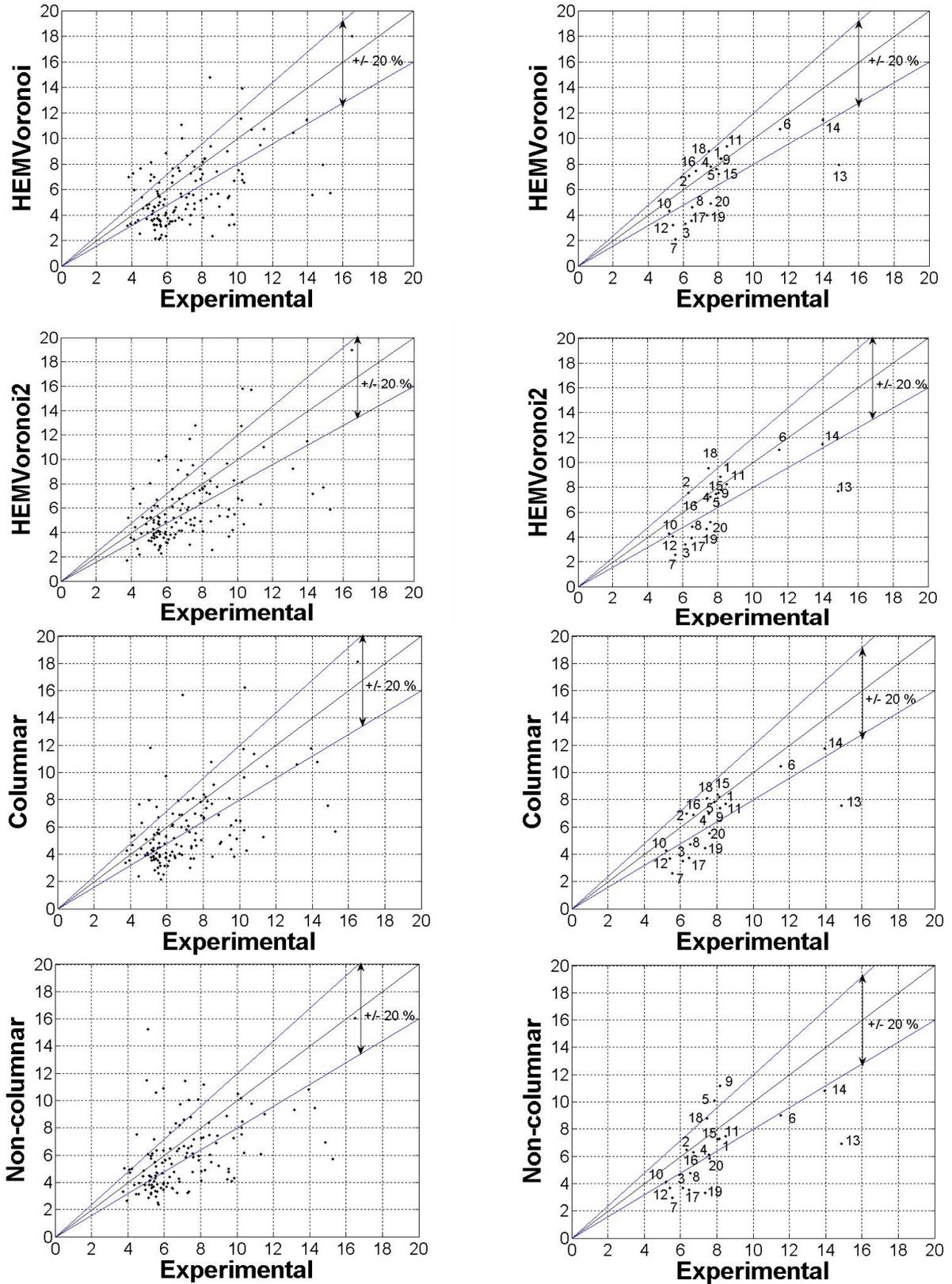
Fig. 6.38: Average orientation deviation for every grain for different microstructures and mesh types.
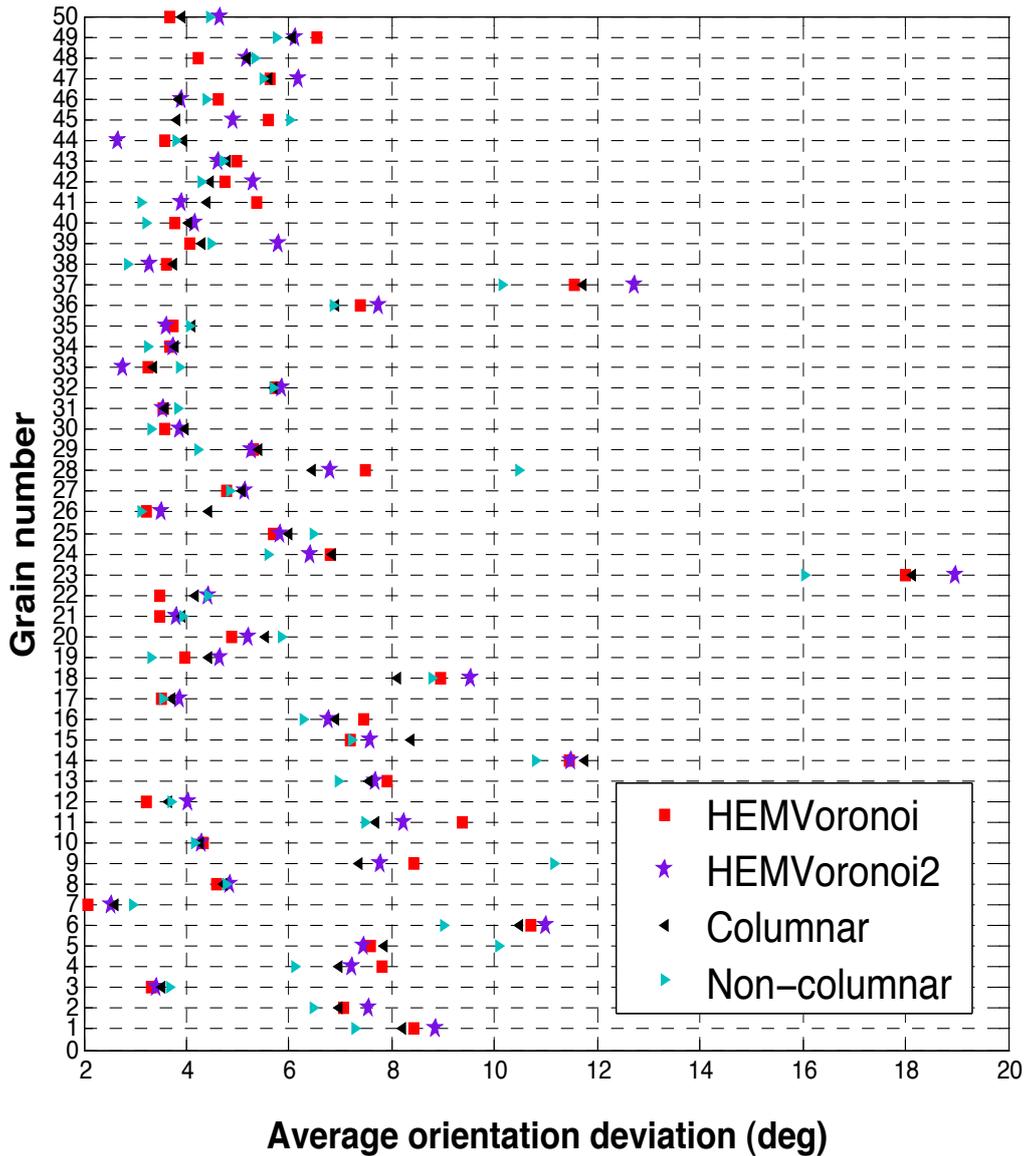
Fig. 6.39: Average orientation deviation for different mesh types and microstructure types for the first 50 grains.

V.4.3 Average orientation predictions and orientation deviation distributions for the first ten grains

The inverse pole figure map in figure 6.40 shows clearly that the mean orientation of each grain is not influenced by mesh refinement, mesh type or microstructure type as might be expected. The final mean orientations of grains 4, 9 and 10 are not predicted by any of these highly resolved crystal plasticity simulations. Nevertheless, the Non-columnar case yields the best results for most of the grains. As seen in table 6.7, the computed misorientation with respect to the final experimental orientation is the smallest in the Non-columnar case for grains 2, 4, 6, 7, 8, 9 and 10. The high misorientation obtained for grain 1, in the Non-columnar case,

corresponds to a rotation about the sample normal axis.
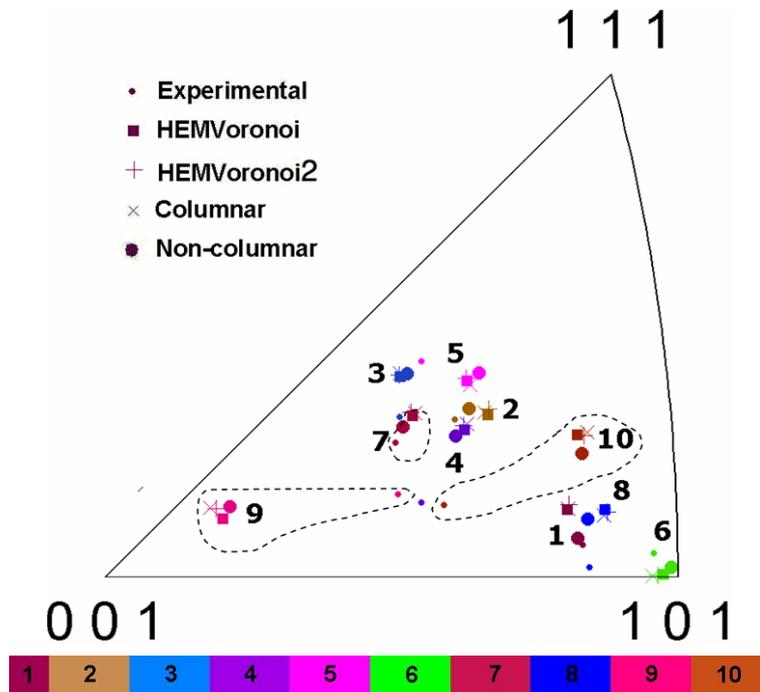
Fig. 6.40: Inverse pole figure for sample normal axis. The color legend corresponds to grains from 1 to 10

Grain number	$HEM_{Voronoi}$	$HEM_{Voronoi2}$	Columnar	Non-columnar
1	9.6	9.8	9.6	11.3
2	2.9	3.0	2.8	1.7
3	5.5	5.6	5.7	6.0
4	7.1	7.4	7.6	6.8
5	4.6	4.6	4.9	5.0
6	4.6	5.1	5.3	3.4
7	6.0	5.9	5.8	5.0
8	13.6	13.9	13.7	11.7
9	21.4	22.6	23.1	20.6
10	12.5	13.1	13.5	12.3

Table 6.7: Misorientation between the mean experimental orientation and the mean orientation obtained for each microstructure and mesh type after deformation for the ten first grains.

The distributions presented in figures 6.41 and 6.42 reveal more insights. Refining the mesh enables to capture the "tail" of the distributions for most grains, as illustrated by the case of grain 7 (see figure 6.42(a)). For other grains, like grain 10, the "tail" of the distribution is improved by mesh refinement, but is best captured by the Non-columnar case (even-though the average orientation deviation predicted by the Non-columnar is lower than the other cases).
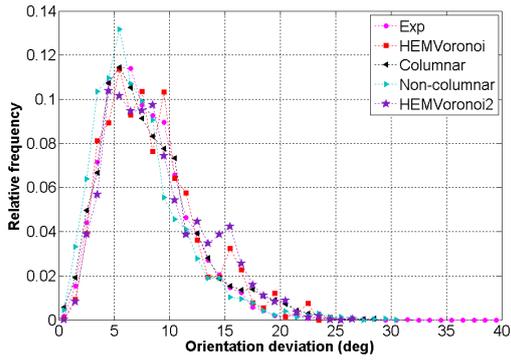
(a) Grain 1
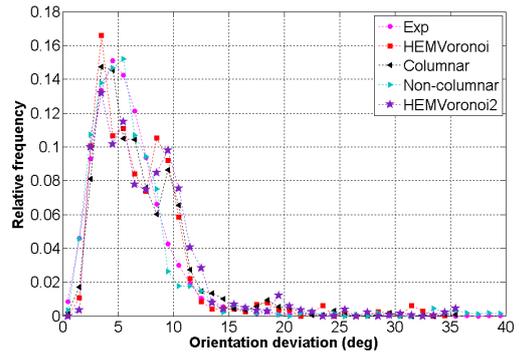
(b) Grain 2
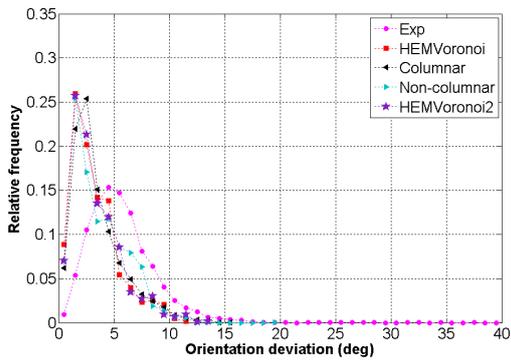
(c) Grain 3
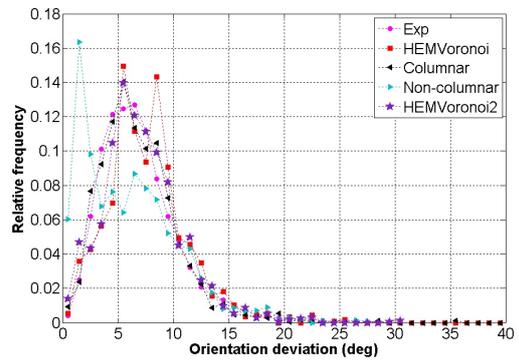
(d) Grain 4
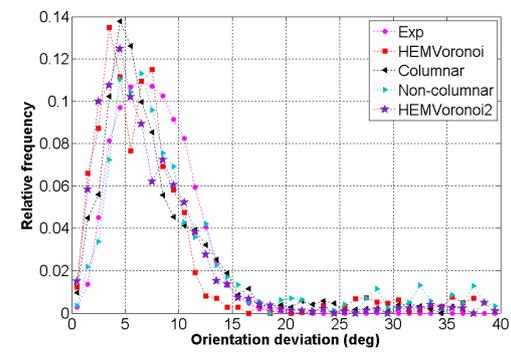
(e) Grain 5
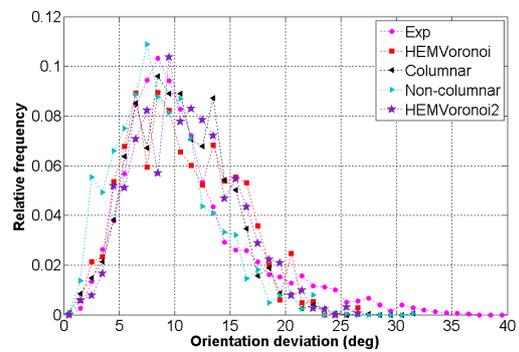
(f) Grain 6

Fig. 6.41: Orientation deviation by grain (grain 1 to 6)

(a) Grain 7   (b) Grain 8

(c) Grain 9   (d) Grain 10
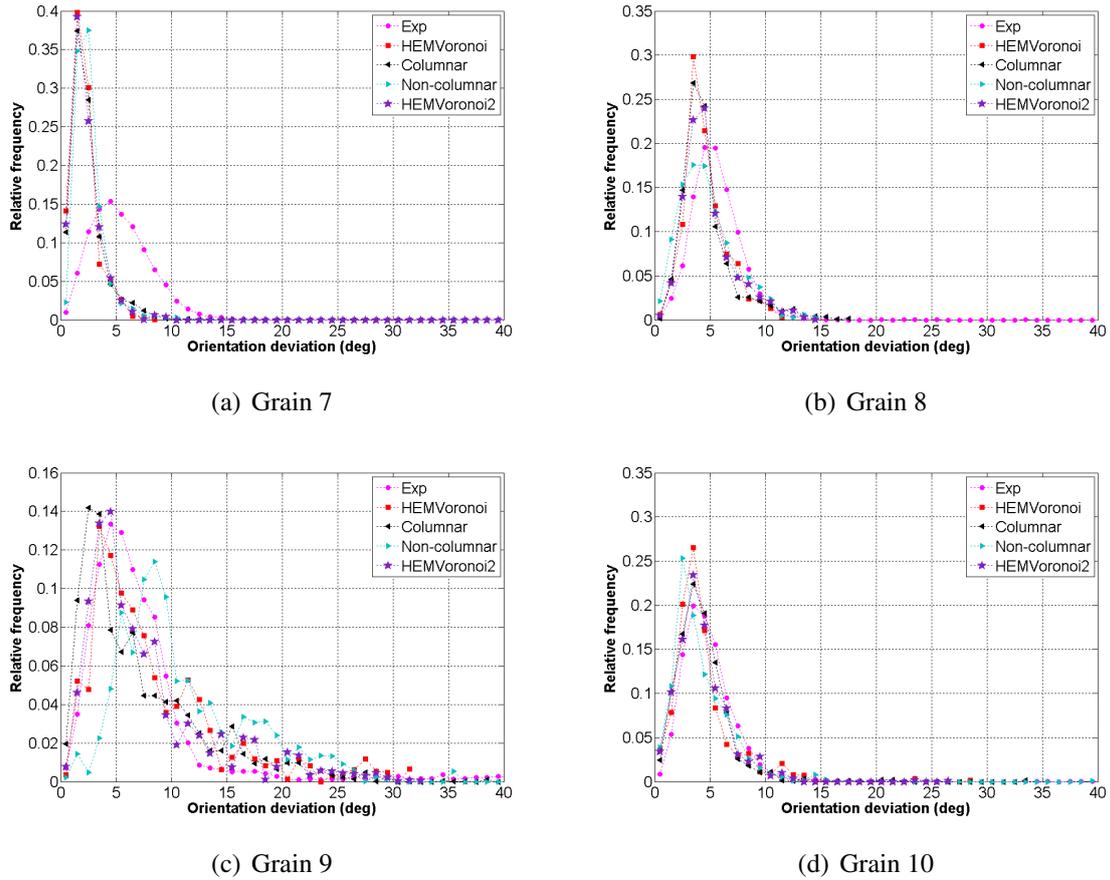
Fig. 6.42: Orientation deviation by grain (grain 7 to 10)

V.4.4 Link between fragmentation and mean orientation predictions for the first ten grains

Firstly, in order to determine if there is a link between the level of fragmentation and the correct prediction of the final mean orientation, figure 6.43 summarizes the results obtained previously for the first ten grains. It is clear from this figure that there is no direct correlation between the error on the prediction of the final mean orientation and how well the different cases account for the average experimental orientation deviation. The Non-columnar case reduces the error on the final mean orientation for grains 4, 6 and 10 while under-predicting the average orientation deviation. It also reduces the error for grain 9, while over-predicting the average orientation deviation. Predicting an average orientation deviation, in the Non-columnar case, that is closer to the experimental value yields improved results for grain 2 and 7 (even if the value remains largely under-predicted for grain 7).

The results obtained so far in terms of orientation deviation do not include any topological information. Orientation deviation maps, as seen in figures 6.44 to 6.53 were obtained with the TSL-OIM software for the first ten grains. Inverse pole figures and inverse pole figure maps are also illustrated. The IPF maps, combined with the discrete IPF figures and the orientation deviation maps, give insights into the degree to which the results reproduce the experimental

measurements or, on the other hand, into possible explanations behind the observed discrepancies. Moreover, the influence of mesh refinement, type and microstructure type is better apprehended.
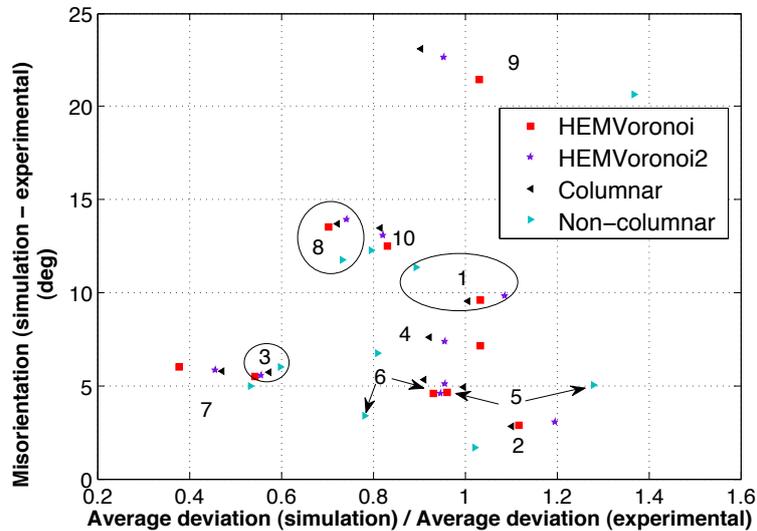
Fig. 6.43: Misorientation between the mean experimental orientation and the mean orientation obtained for all simulations as a function of the ratio of the average orientation deviations

Several general observations can be made. First, some grains have "numerical" shapes significantly different from the experimental ones (grains 1, 6, 8, 9 and 10) . In the FE cases, as the simulations are performed without remeshing, all elements originally belonging to a grain, are identified after deformation using the presence function mentioned in chapter 4 section III.4. No loss of information related to transport of variables during remeshing has intervened, which could occur during the transport of the level set functions or the crystallographic orientations. On the other hand, the experimental grains are selected manually, as mentioned in section V.1 of this chapter. It is worth noting that the number of pixels in each grain, in the experimental scan, obviously decreases after height reduction, i.e we cannot "follow" the evolution of the same pixel before and after deformation, as opposed to the FE simulations. It is also worth noting that, in both instances, the point-to-point misorientation criterion (grain "tolerance" angle) is not used to decide if a pixel / element belongs (or not) to a given grain. Clearly, the procedure for selecting the points / elements belonging to a given grain could explain the discrepancies observed between the experimental and numerical results, in terms of both mean orientation and average orientation deviation. High angle grain boundaries ($> 15°$) and low angle grain boundaries ($> 5°$) are superimposed on the IPF maps for the ten grains for the simulation cases. These boundaries correspond to point-to-point misorientations. The density of these boundaries, especially, low angle ones, is in general significantly higher in the experimental maps compared to the simulation ones (except for grain 9, especially the Non-columnar case). For clarity, the boundaries are not shown for the experimental maps in figures 6.44 to 6.53 but are illustrated in

appendix D. The orientation deviation maps reveal that the spatial distribution corresponding to the simulation cases is, in general, different from the experimental ones, although the statistical distributions, shown in figures 6.41 and 6.42 might be similar. It is important to note that, even if the patterns are sometimes very close for all simulations, the Columnar and Non-columnar cases exhibit much finer description of such pattern, especially near grain boundaries (and a better description of the grain boundaries themselves) as seen for example in figure 6.45. This is related to the use of the anisotropic mesh, which is highly refined in the normal direction to the grain boundaries.

On a grain by grain basis, several remarks can be made. The simulation maps for grain 3 and 7 show two distinct regions located near grain boundaries exhibiting orientation deviations between 5°and 10°(green area in figure 6.46 and 6.50). The same levels of fragmentation are measured experimentally but the maps reveal an intricate mix of low level fragmentation (blue area) and relatively higher level of fragmentation (green area). This highlights the behavior of these grains, in the real microstructure, under the influence of, both their own orientation and their local neighborhood, as opposed to the behavior predicted by the FE simulations. In IPF maps of figure 6.45, grain 2 splits into three regions, with the upper and lower areas that move away from the initial grain orientation. The FE simulations predict correctly the migration of the lower area and the split of the grain, while a much slower development is predicted in the upper area. The final mean orientation is overall well predicted in this case, with the Non-columnar case yielding the best results (see figure 6.43). As mentioned before, even though the split into three regions is tangible in the experimental maps, the orientation field shows thin alternating strips inside these regions, as opposed to the FE simulations. Regarding grain 4, the HEM$_{Voronoi}$, HEM$_{Voronoi2}$ and Columnar cases predict the fragmentation of the grain into three regions, as seen on the IPF maps of figure 6.47. Such behavior is not observed experimentally. The Non-columnar case is closer in that respect to the experimental maps. Grain 5 (figure 6.48) and 6 (figure 6.49) show, for all simulations, results that are in line with experimental measurements. The general spatial distributions of the orientation deviation maps are captured by the FE simulations. The IPF map of figure 6.52 highlights the high fragmentation predicted by the Non-columnar case for grain 9. The shape of the grain predicted by the simulations is particularly different from the experimental one, which could account for the discrepancies observed in terms of mean orientation (see figure 6.43). The orientation deviation map reveals spatial distribution significantly different in the Non-columnar compared to the other simulations. In fact, the Non-columnar case exhibits more differences, in terms of orientation deviation maps, compared to the other three cases for most grains, which highlights the strong influence of the choice of the neighborhood in the third dimension.
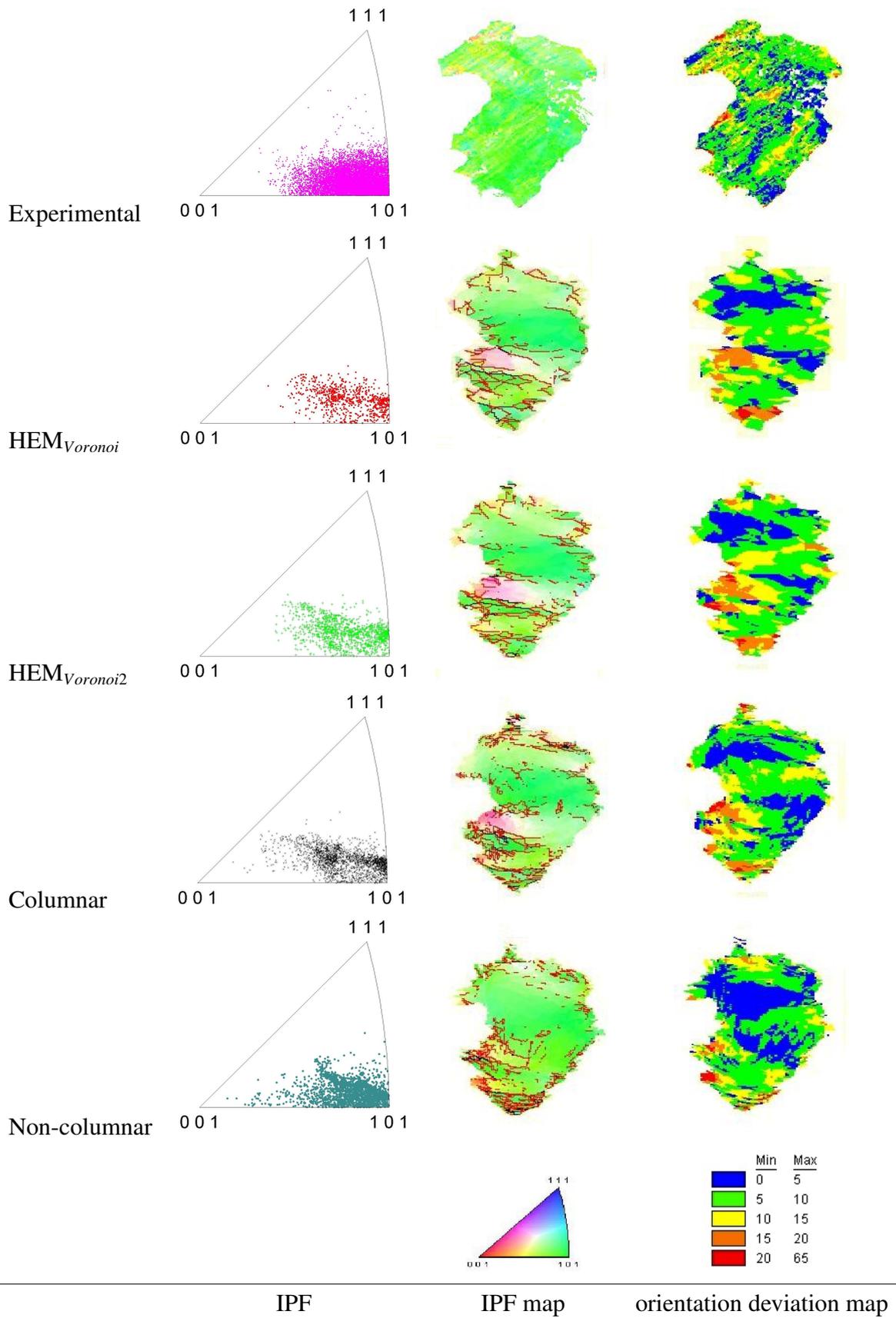
Fig. 6.44: Orientation deviation map and inverse pole figures (sample normal axis) for grain 1. Black and red segments in the IPF maps of the simulations represent high angle (>15°) and low angle grain boundaries respectively (> 5°).
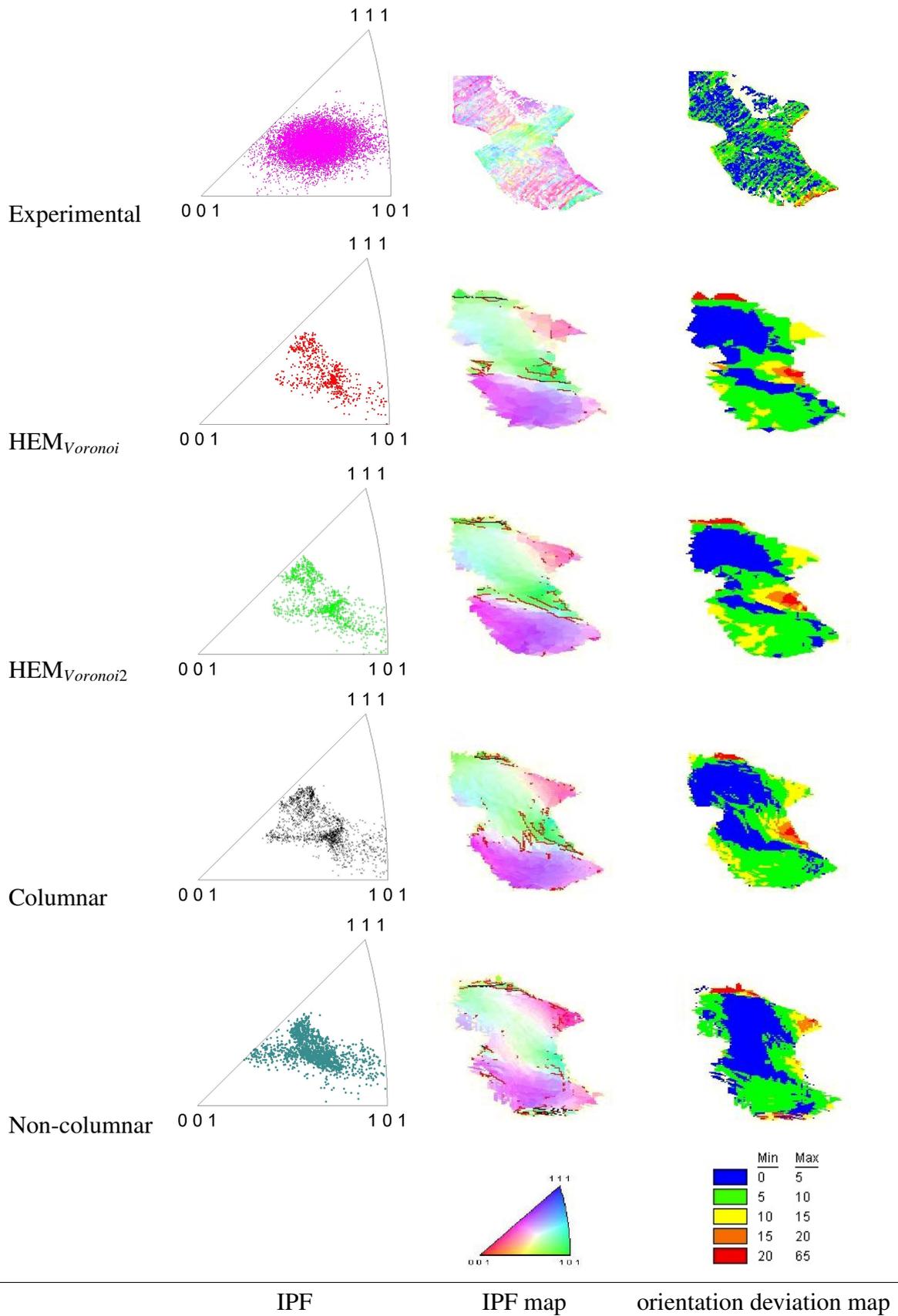
Fig. 6.45: Orientation deviation map and inverse pole figures (sample normal axis) for grain 2. Black and red segments in the IPF maps of the simulations represent high angle (>15°) and low angle grain boundaries respectively (> 5°).
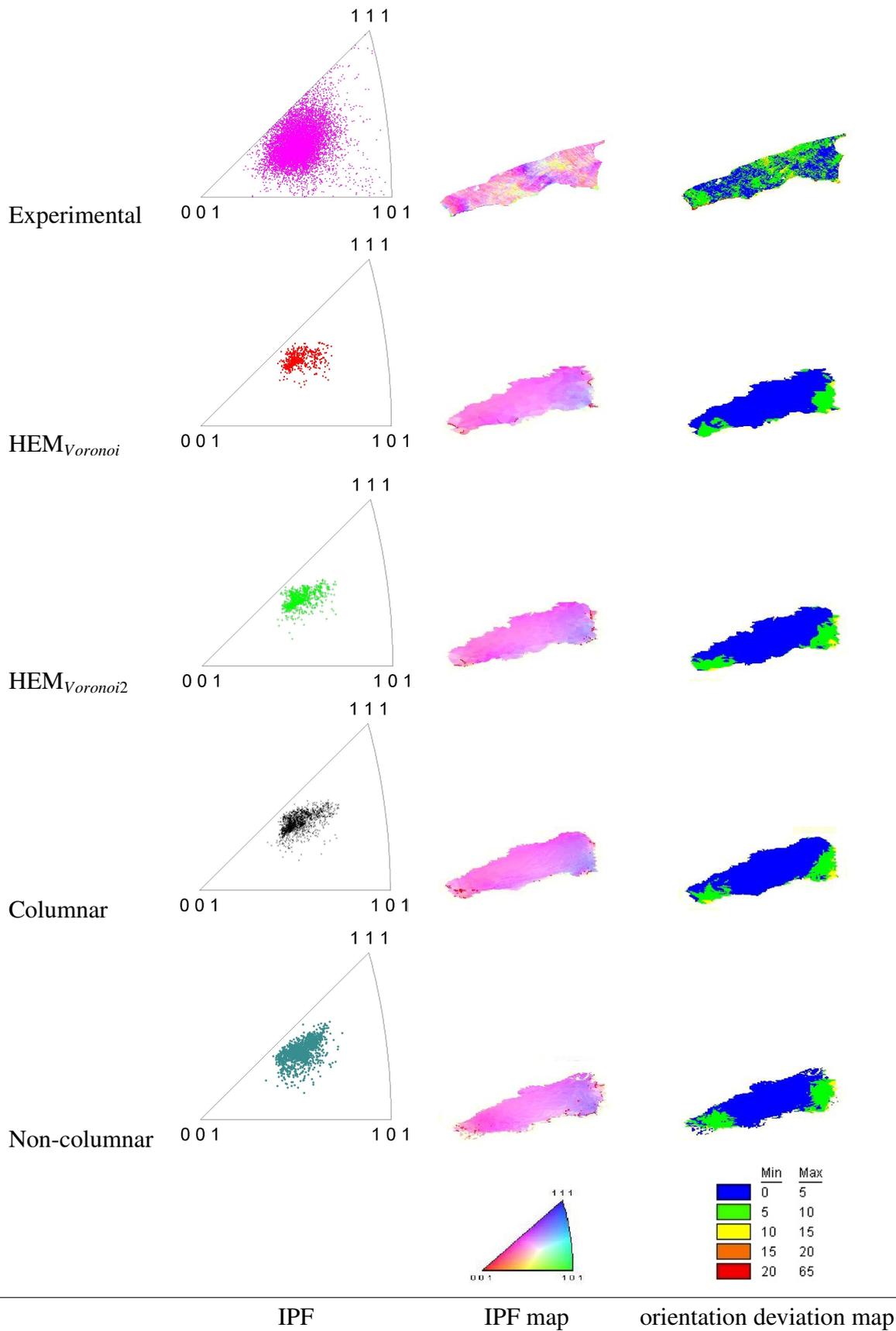
Fig. 6.46: Orientation deviation map and inverse pole figures (sample normal axis) for grain 3. Black and red segments in the IPF maps of the simulations represent high angle (>15°) and low angle grain boundaries respectively (> 5°).
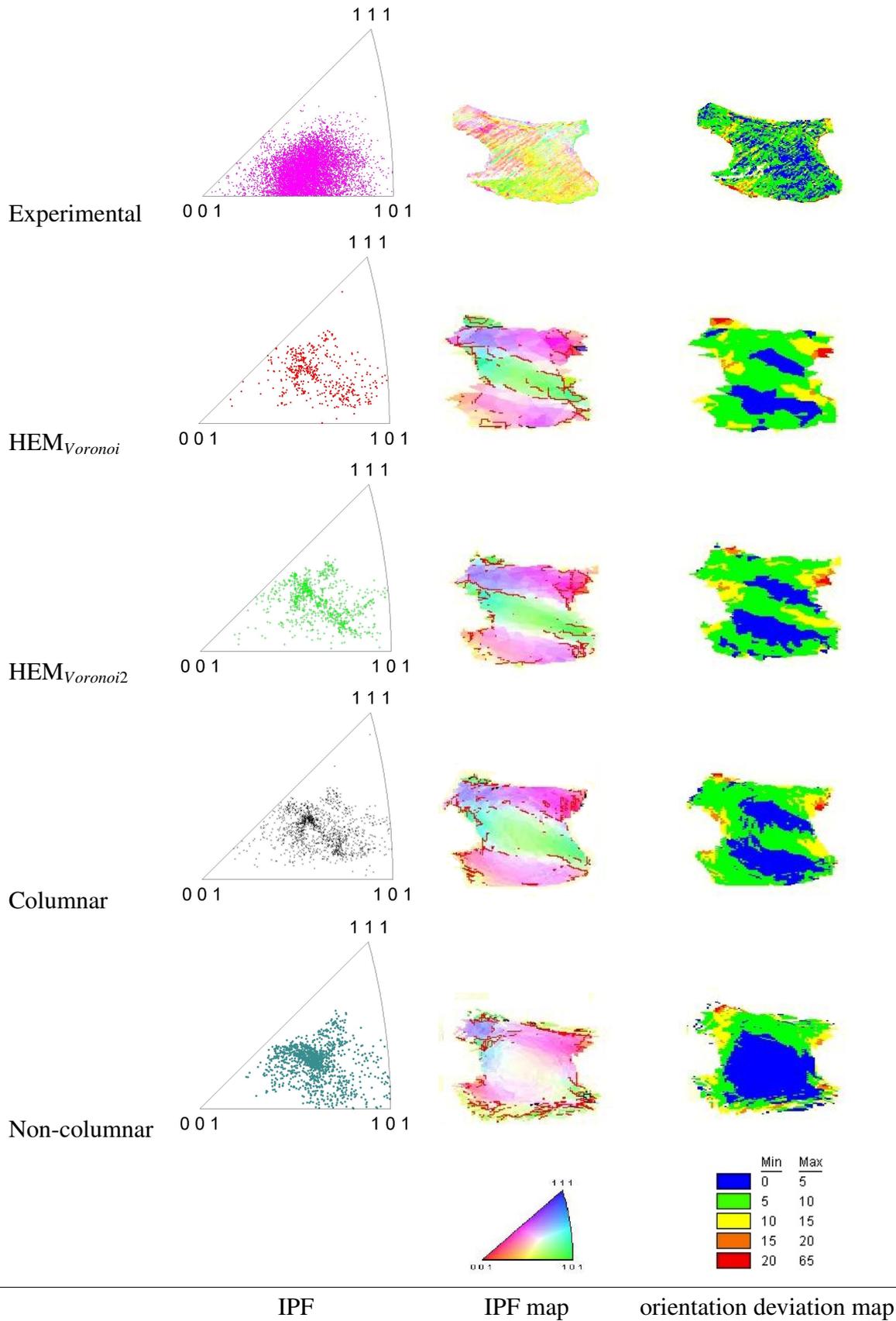
Fig. 6.47: Orientation deviation map and inverse pole figures (sample normal axis) for grain 4. Black and red segments in the IPF maps of the simulations represent high angle (>15°) and low angle grain boundaries respectively (> 5°).
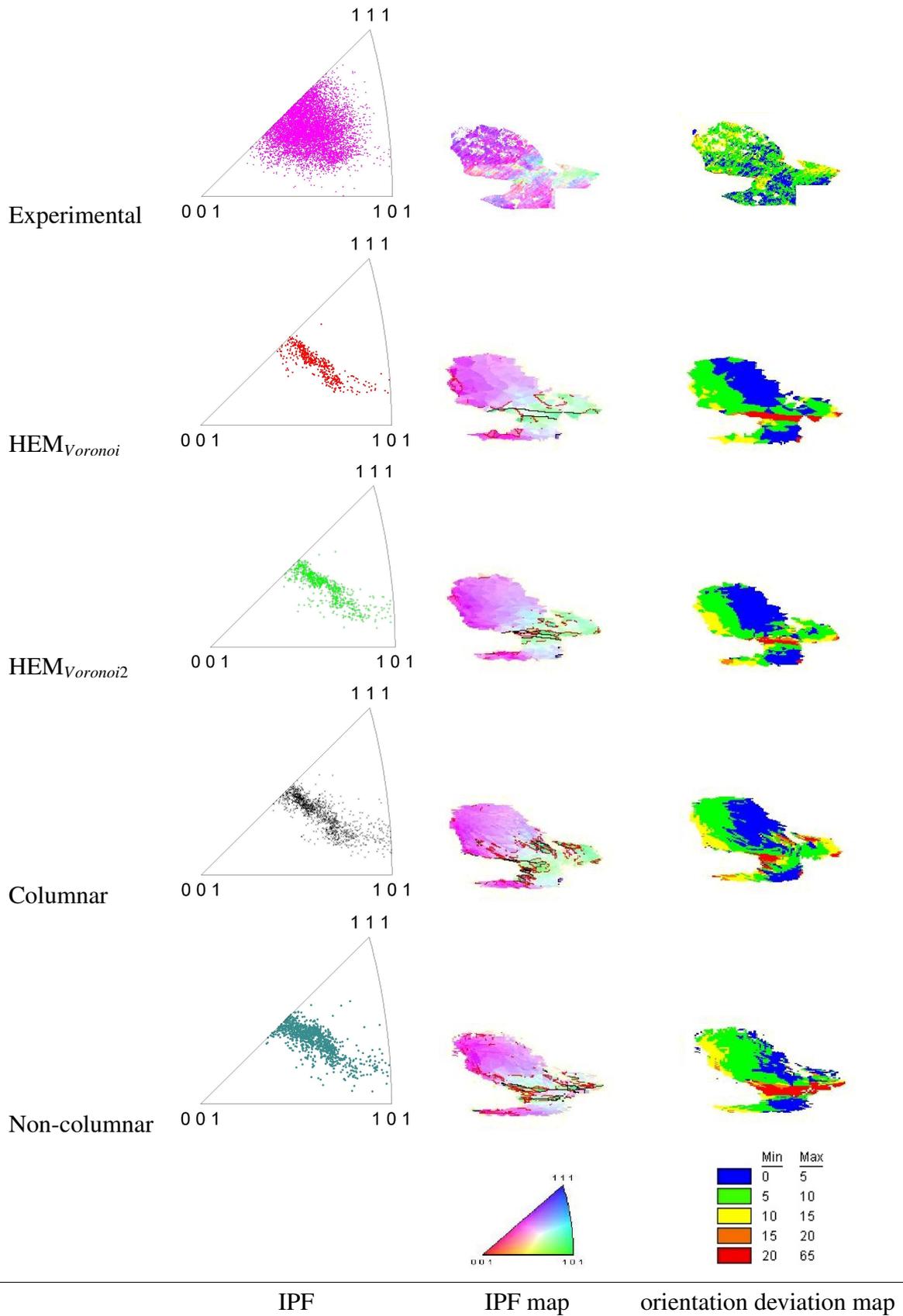
Fig. 6.48: Orientation deviation map and inverse pole figures (sample normal axis) for grain 5. Black and red segments in the IPF maps of the simulations represent high angle (>15°) and low angle grain boundaries respectively (> 5°).
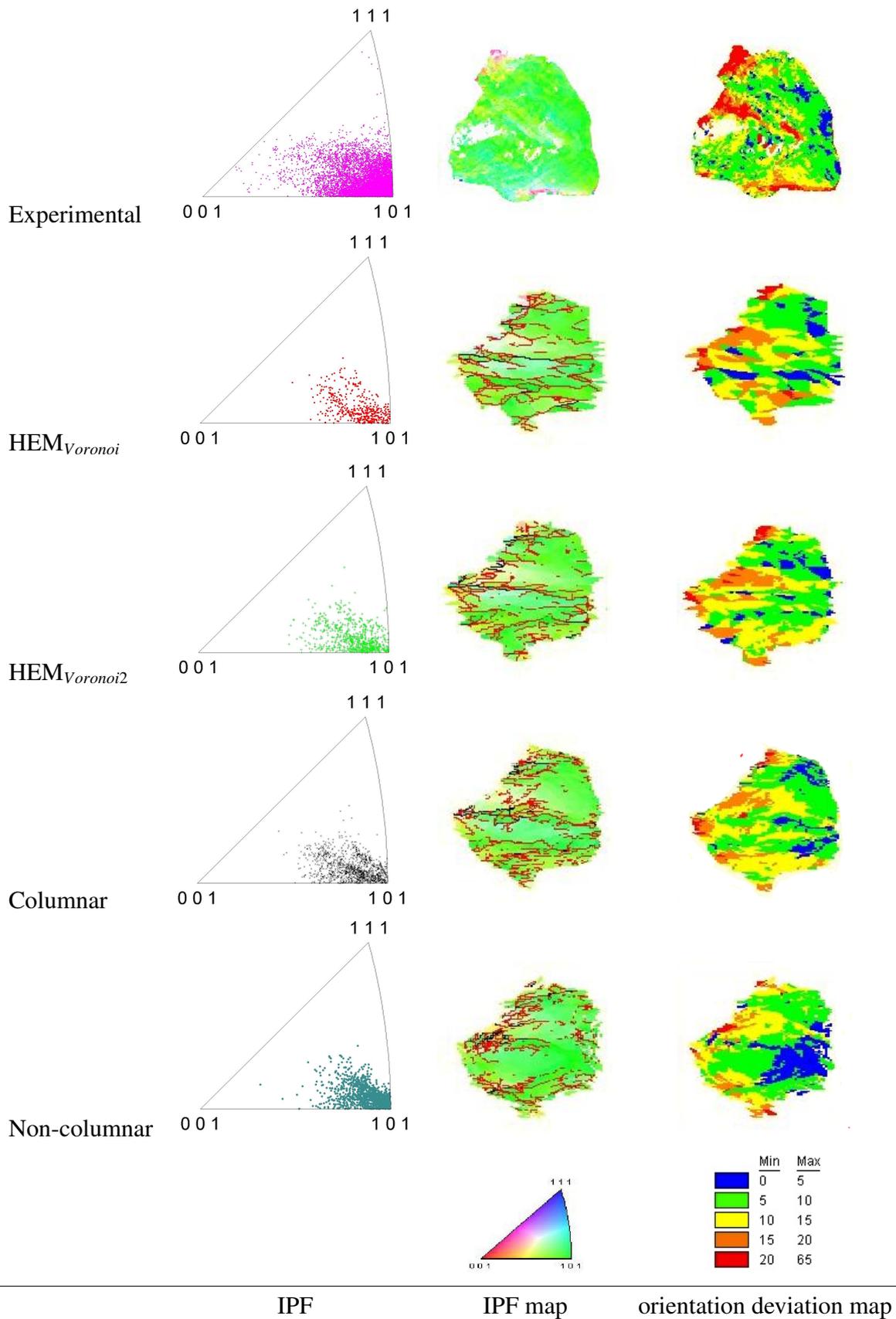
Fig. 6.49: Orientation deviation map and inverse pole figures (sample normal axis) for grain 6. Black and red segments in the IPF maps of the simulations represent high angle (>15°) and low angle grain boundaries respectively (> 5°).
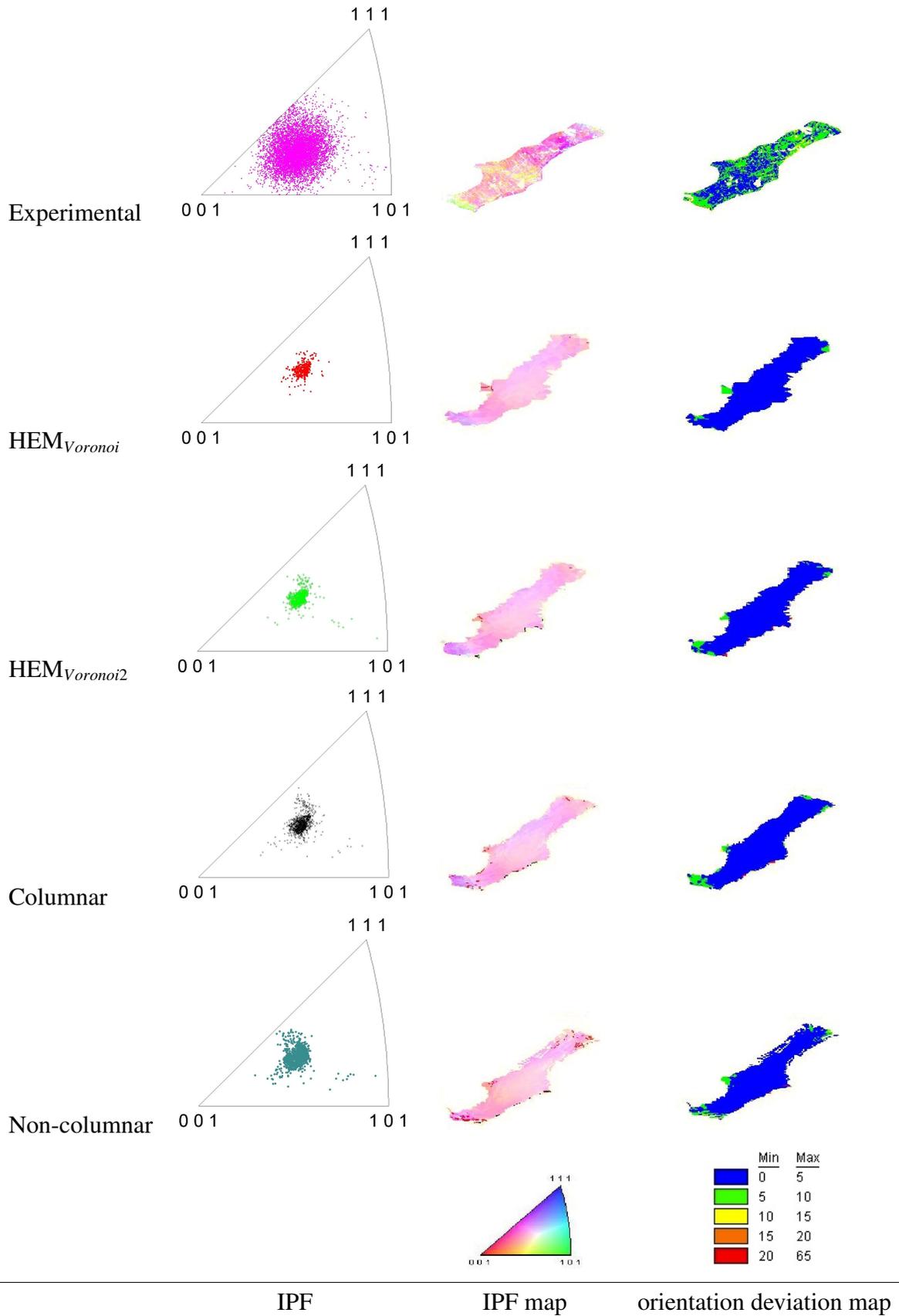
Fig. 6.50: Orientation deviation map and inverse pole figures (sample normal axis) for grain 7. Black and red segments in the IPF maps of the simulations represent high angle (>15°) and low angle grain boundaries respectively (> 5°).

	Min	Max
(blue)	0	5
(green)	5	10
(yellow)	10	15
(orange)	15	20
(red)	20	65

IPF   IPF map   orientation deviation map
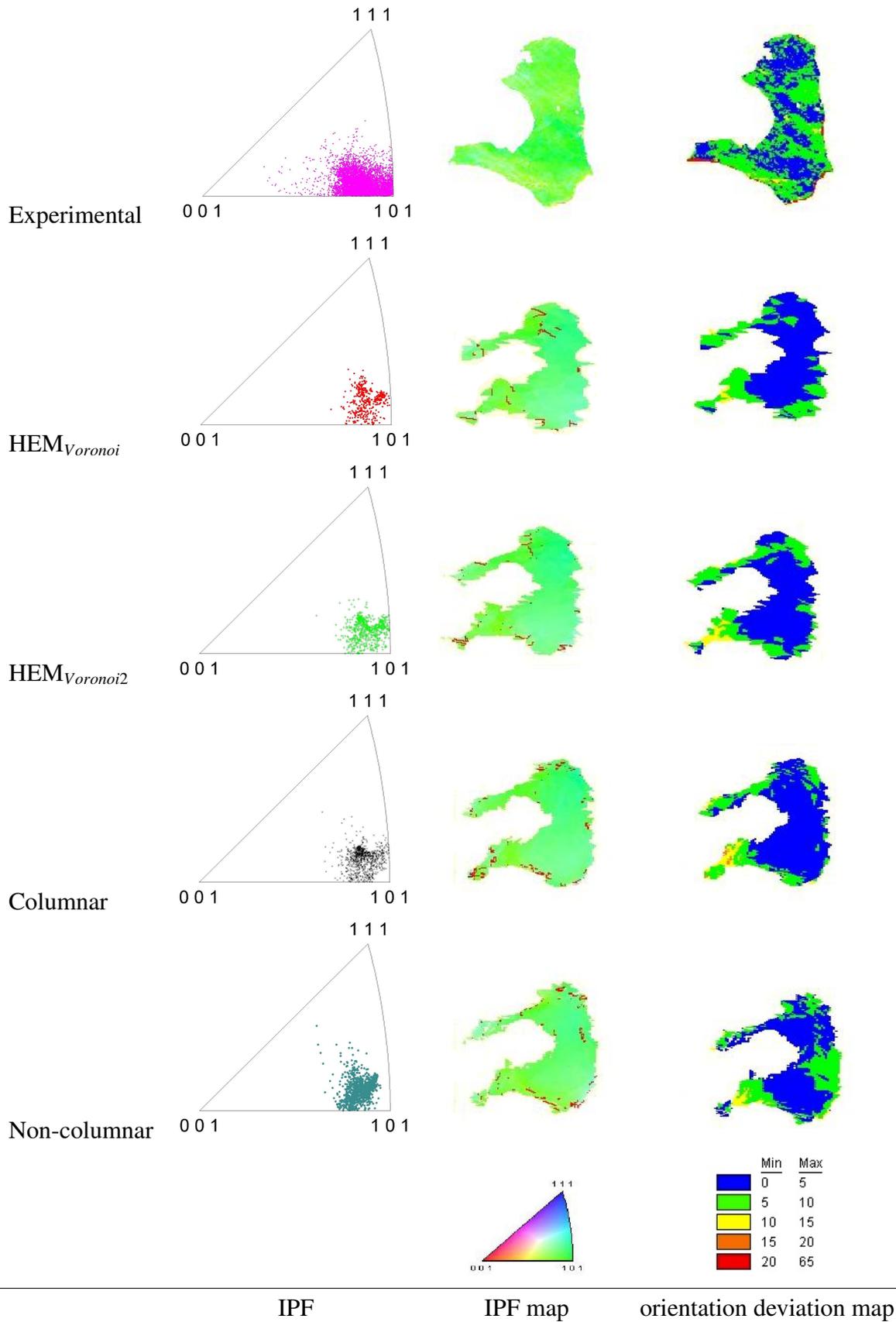
Fig. 6.51: Orientation deviation map and inverse pole figures (sample normal axis) for grain 8. Black and red segments in the IPF maps of the simulations represent high angle (>15°) and low angle grain boundaries respectively (> 5°).
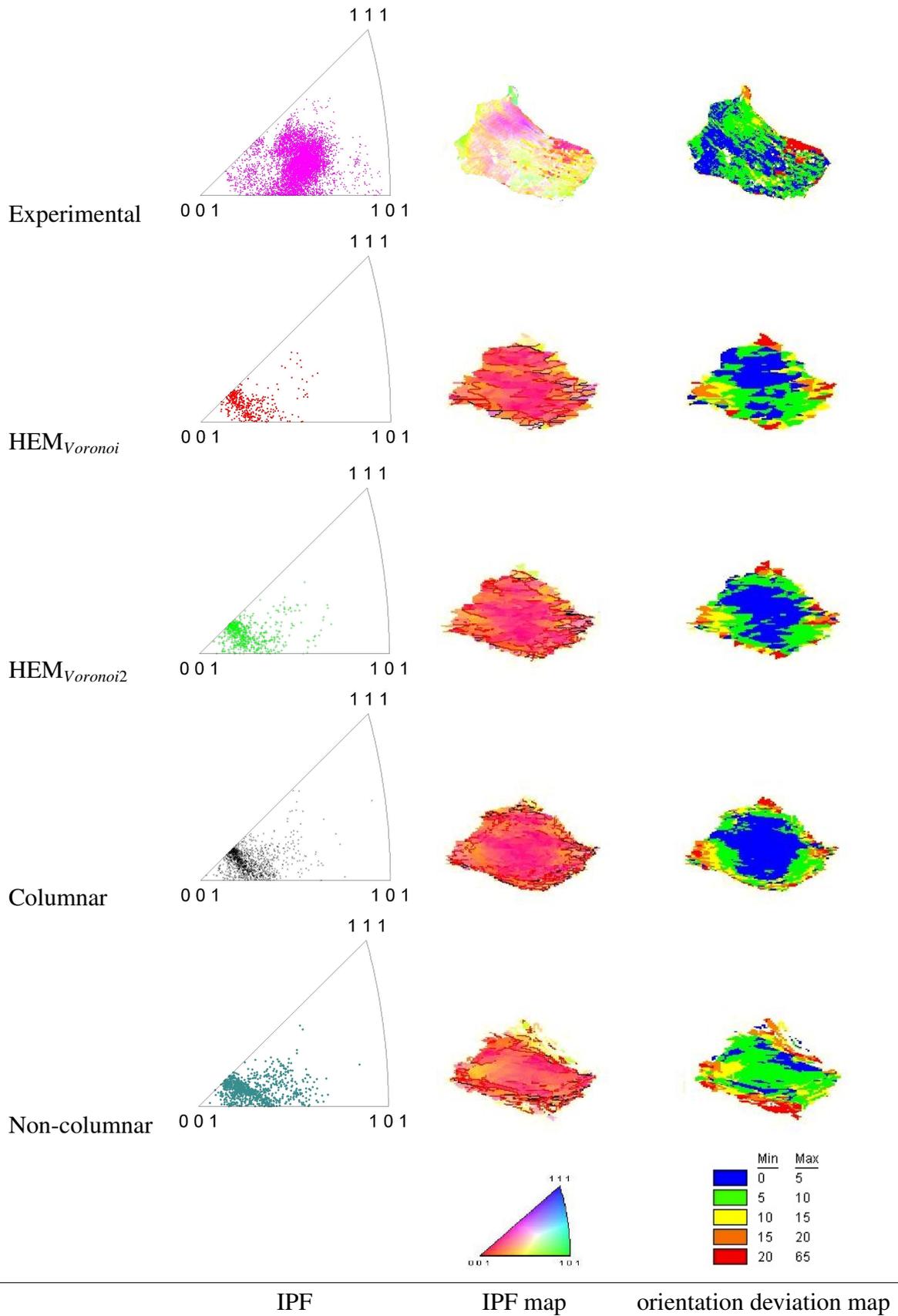
Fig. 6.52: Orientation deviation map and inverse pole figures (sample normal axis) for grain 9. Black and red segments in the IPF maps of the simulations represent high angle (>15°) and low angle grain boundaries respectively (> 5°).
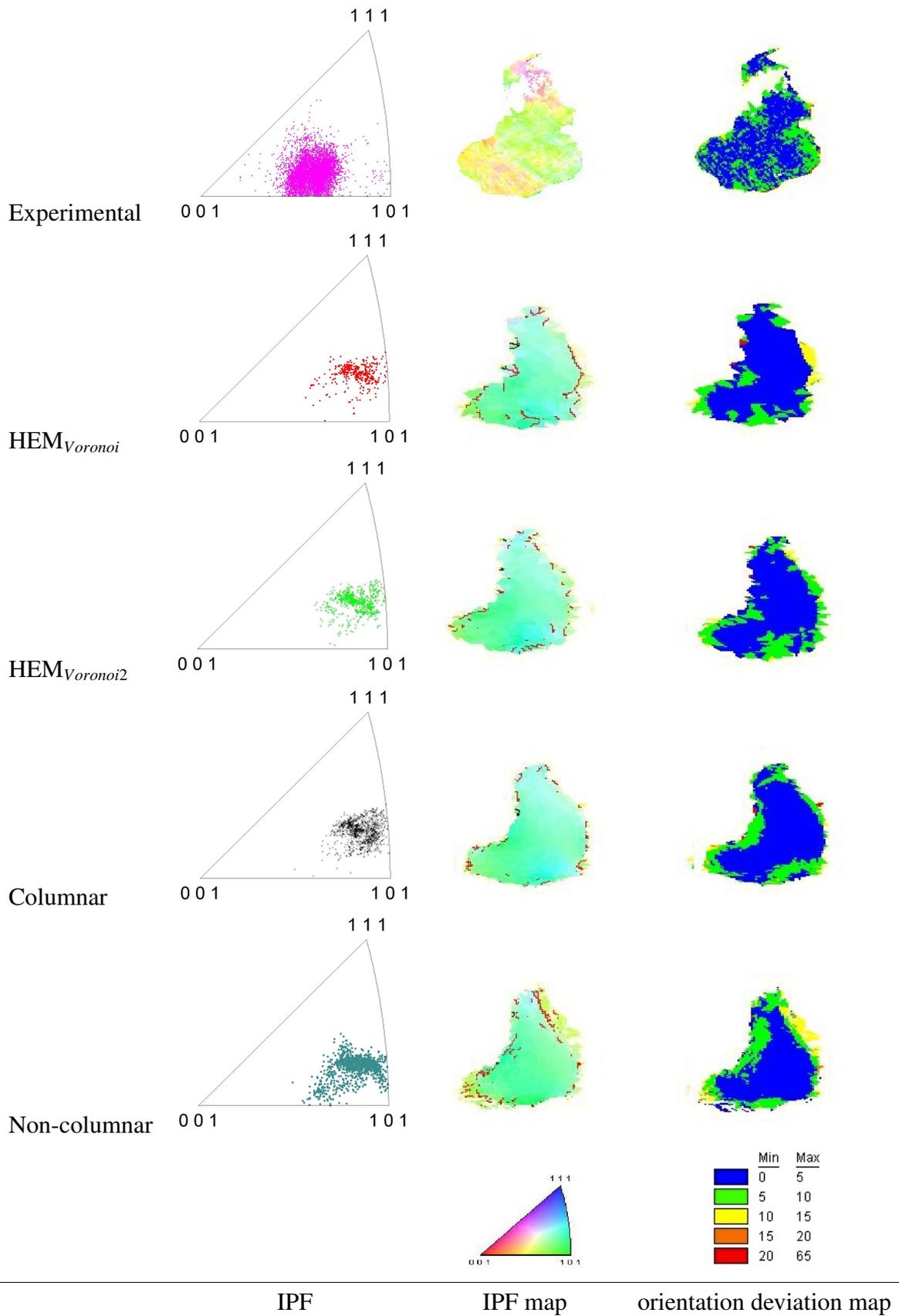
Fig. 6.53: Orientation deviation map and inverse pole figures (sample normal axis) for grain 10. Black and red segments in the IPF maps of the simulations represent high angle (>15°) and low angle grain boundaries respectively (> 5°).

VI Conclusion

The objective of this chapter is to assess the capability of our numerical framework to predict microstructure and texture evolution in polycrystalline aggregates. Such framework, combined with an automatic remeshing tool, enabled the simulation of the rolling of a 500 grains model polycrystal to more than 90 % thickness reduction. The strain levels reached in this simulation have not been reported elsewhere in the literature. Compared to standard polycrystal models such as the Taylor model, such simulations are valuable as they improve global texture predictions [Resk et al., 2009].

The second part of this chapter is dedicated to the macro and microtexture predictions in 129 grains embedded in a polycrystal and followed during deformation using a split sample method [Quey, 2009]. The numerical tools implemented in this work have enabled the construction of a 3D microstructure while "filling" the gaps whenever experimental data was missing. While the numerical framework is fully capable of constructing the actual shape of all grains, the columnar hypothesis was used due to the lack of experimental measurements in the third dimension. As mentioned in the introductory sections of this work, such short circuits are often used in the literature. Also, the microstructure was surrounded by a hypothetical equivalent medium, as the investigated grains were in fact embedded in a polycrystalline aggregate. More specifically, four test cases, corresponding to different approximations of the surrounding medium, were initiallly investigated: Slice, HEM_{129}, HEM_{10} and $HEM_{Voronoi}$.

First results showed that there is globally a good agreement between the simulations and the experiment. Moreover, the influence of the surrounding medium on global texture evolution is not significant. Texture component maps and inverse pole figure maps have also shown an overall agreement with the experimental ones and no striking sensitivity with respect to the HEM. However, upon closer examination, more discrepancies were observed on a grain by grain basis. Grain rotation paths, based on the computation of the mean orientations, as well as grain subdivision predictions, as represented by the average orientation deviation from the mean orientations, did not show a systematic agreement with the experiment and proved to be sensitive to the choice of the surrounding environment. All simulations underestimated the overall fragmentation of the microstructure, with the $HEM_{Voronoi}$ case being the closest. This suggested that relatively low mesh refinement was one the factors that could explain such discrepancies. For this reason, further simulations, based on the Voronoi approximation for the HEM, were performed. Increased mesh refinement was investigated (the $HEM_{Voronoi2}$ case). Anisotropic meshes were also investigated (the Columnar and Non-columnar cases), as they enabled to increase mesh refinement in a optimal fashion, as per the metric presented in chapter 4. Moreover, in order to gain further insight into the effect of grain shape (and consequently grain neighborhood and grain interaction with the surrounding medium in this case), a non-columnar microstructure was investigated (the Non-columnar case).

The discrepancies obtained in terms of global texture evolution were insignificant, even in the case of the non-columnar microstructure. Grain by grain analysis showed more differences. Surprisingly, the HEM$_{\text{Voronoi2}}$ case did not systematically yield greater fragmentation than the HEM$_{\text{Voronoi}}$ case, based on grain average orientation deviation. It is worth noting that the mesh in the HEM$_{\text{Voronoi2}}$ case is finer inside the investigated grains, but also inside the HEM. Refining the mesh inside the HEM could lead to a different interaction behavior. Measurable effects on grain subdivision and mean orientation predictions were found among the four simulations. Nevertheless, the Non-columnar case yielded the largest differences. This is confirmed by the analysis of the first ten grains and the topological orientation deviation maps illustrated at the end of the chapter, where the Non-columnar case often exhibited a different pattern than the other cases. This suggests that neighborhood effects have a stronger influence on the predictions than mesh refinement / mesh type effects. Nevertheless, these maps also showed that the anisotropic mesh, used in the Columnar and Non-columnar cases, enabled a finer description of the orientation deviation pattern, even if the predicted pattern was very close to the other cases (see for example figure 6.45). It is also important to mention that, for the Non-columnar case, such a mesh was even more necessary for a correct description of the hypothetical random shapes of the grains. The orientation deviation maps have also showed that highly resolved FE simulations could sometimes capture the basic features of the experimental pattern, such as the case for grain 5 and 6. The level of fragmentation could also be reproduced while accounted for in a different fashion in the digital microstructure, as it is the case for grain 3 and 7. These maps also illustrated that, even if such highly resolved meshes could be used, the degrees of freedom, available in the "real" microstructure, are far from being reproduced. Besides, remeshing was not performed in these simulations, in order to avoid any loss of local information, which could affect the obtained statistics and spatial distributions. Even though the height reduction achieved in these simulations is moderate, the meshes used are highly refined and strain localization, as shown in chapter 5, occurs. This could introduce some errors in the predictions. A study on the effect of remeshing on local measures should be performed, before performing investigations on cases with remeshing.

There exist several other factors that could account for the discrepancies between simulation and experiment. As mentioned previously, the single crystal model used in this work does not include in its formulation geometrically necessary dislocations (GNDs). The formation of substructure in the presented simulations, evidenced by intragranular misorientations, are the outcome of the FE method and are due to varying slip system activities and, consequently, varying lattice rotations from one element to the other. As mentioned by [Mika and Dawson, 1999], they are similar in that respect to GNDs. However, substructure formation is better apprehended with more "physical" constitutive models that take into consideration the mechanisms, related to long-range (non-local) effects, behind the formation of these GNDs. On another level, the actual 3D microstructure and the real surrounding aggregate are not taken into consideration in

the simulations. The effect of the third dimension (the transverse direction in this case) on the predictions appears to be significant, according to the results presented in this chapter. [ERIEAU, 2003] has showed that the transverse direction has little effect on heterogeneities of strain and stress, which is confirmed by our maps (see appendix C). However, [ERIEAU, 2003] did not investigate the effects on texture evolution. The results presented here show clearly that texture predictions on a grain by grain basis (and global texture to a lesser extent) are affected by the construction assumptions.

Finally, as highlighted by [LEBENSOHN et al., 2005], more refined measures of misorientation should be taken into consideration, in order to characterize, for example its anisotropy, as developed by [PANTLEON et al., 2008]. This could give additional quantitative insights into the reasons behind the discrepancies.

Chapter 7

General conclusion and perspectives

Highly resolved crystal plasticity simulations, based on the finite element method (CPFEM), can be a very useful tool for investigating the micromechanics of polycrystalline aggregates. The work in this thesis, as reflected in the organization of this dissertation, was articulated along two main axes: (i) establishing a robust numerical framework for the simulation of highly resolved polycrystalline aggregates subjected to large strains (chapters 2, 3 and 4); (ii) investigating grain-scale heterogeneities for different applications (chapters 5 and 6).

In chapter 2, the single crystal constitutive model is detailed. The model used is a large strain classical elastic-viscoplastic formulation with optimized numerical integration [DELANNAY et al., 2006]. This model alone is not expected to account for the formation of a substructure, as the formation of geometrically necessary dislocations (GNDs) is not included in the formulation. In chapter 3, in light of standard crystal plasticity models that account for the behavior of the polycrystal, the finite element method is presented as the ultimate polycrystal model. Indeed, stress equilibrium and compatibility is achieved for all grains in a weak numerical sense, as opposed to the Taylor Full Constraint model for example, which assume isostrain deformation in all grains while violating stress equilibrium. The FE formulation is a mixed velocity pressure formulation based on the mini-element (P1+/P1), which makes it flexible enough to model compressible or nearly incompressible materials. An updated Lagrangian scheme is used to deform the 3D polycrystals. The FE framework is implemented in CimLib [DIGONNET et al., 2007], with advanced computational resources that makes it possible to perform parallel computations. In chapter 4, the necessary framework for generating and meshing polycrystalline aggregates is presented. The generation tools presented in this work, based on the DIGIMICRO software or on CimLib, enable the construction of polycrystals with Voronoi based topologies or voxelized data, based on experimental measurements. Most importantly, the specificity of our approach lies in the use of a level set framework which is combined with an unstructured "monolithic" meshing strategy. In that approach, the mesh does not conform to grain boundaries and level set functions are used to implicitly locate grain boundaries. Adaptive meshing, based on these functions, can be performed if the appropriate metric field is constructed [RESK et al.,

2009]. Anisotropic meshes, with refinement in the direction perpendicular to the grain boundaries, are essential for guaranteeing geometric accuracy. The mesh generator can also generate any type of mesh according to the metric field which is supplied to it. This offers flexibility regarding the type of mesh to be used. Depending on the application and the investigated fields, different meshing strategies can be justified, ranging from a standard homogeneous isotropic mesh to highly anisotropic mesh based on the level set function of only one grain. Another important feature related to the flexibility of the mesh generator is the ability to perform remeshing whenever it is needed. Combined with adequate transport of variables after remeshing, automatic remeshing represents a very valuable tool. It is important to note that the fundamental components of the numerical framework, such as the mesh generator and the level set formulation are included in CimLib, while the necessary developments / implementations for adapting them to the case of polycrystalline aggregates have been performed during this work.

In the second part of this dissertation, different applications of CPFEM are examined with the objective of investigating grain-scale heterogeneities. In chapter 5, the deformation energy is used to evaluate such heterogeneities. It is shown that the error related to the distribution of this measure, when comparing the anisotropic mesh to a highly refined isotropic one, is maximum near grain boundaries. It has also been shown that using such anisotropic meshes, with stretched elements along the grain boundaries, offers a good compromise between accuracy and computation time. As demonstrated in chapter 5, such anisotropic refinement is not required for all grain boundaries. Remeshing effects have also been investigated in this chapter. More specifically, it has been shown that remeshing limits strain localization, which may be partially induced by the distribution of mesh qualities, and which ultimately leads to the breakdown of the simulations. The effect of remeshing on global texture evolution has also been evaluated and appeared to be negligible. An application where the computation of the stored energy during deformation is of prime importance, is the simulation of static recrystallization. Energy stored during deformation is the driving force for recrystallization, as discussed in more details in chapter 5. A first modelling effort towards linking the deformation and recrystallization simulation is presented in this chapter [Logé et al., 2008]. A simplified measure of stored energy is used, namely a fraction of the strain energy. A nucleation criterion, based on the gradient of the stored energy, is implemented. The common FE and level set framework ensures that all necessary microstructural information is transferred from the deformation simulation to the recrystallization simulation (namely the energy field and the topology of the microstructure). In chapter 6, a typical CPFEM application, namely the prediction of global texture evolution in a model polycrystal, is presented. This test case validates our CPFEM framework on the macroscropic level and yields the expected improvements compared to the Taylor Full Constraint model. Also, the usefulness of the automatic remeshing tool, in achieving high levels of strain, is demonstrated. A second type of application is presented in the second part of this chapter, namely a direct comparison between an actual microstructure and a digital one, which attempts

to replicate the characteristics of the measured microstructure in a discrete sense (and not in a statistical sense as it is the case for a model polycrystal). Macro and microtexture investigations were performed on bulk grains embedded in a polycrystalline aggregate. The results highlight, on one hand, how well our framework performs with respect to the experiment, and on the other hand, the influence of various numerical parameters / choices on the predictions. Among these parameters are the construction assumptions regarding the investigated microstructure and the properties of its surrounding medium, due to the lack of 3D experimental data. A fictitious homogeneous equivalent medium (HEM) was constructed around the microstructure. Other numerical parameters include mesh refinement and type. A good agreement between simulation and experiment was found in terms of global texture evolution. Also, the results showed that global texture is not significantly sensitive to the numerical parameters mentioned above. However, more discrepancies between simulation and experiment were found on a grain by grain basis. This is in line with the sensitivity of the local results with respect to the approximation chosen for the HEM and with respect to mesh refinement / type and microstructure type. The effect of this latter has been highlighted in comparison to the results obtained with an arbitrary non-columnar microstructure. The "microstructure type" parameter proved to have a more significant impact on the results, not only in terms of grain subdivision predictions and grain mean orientation, but also in terms of topological IPF maps and orientation deviation maps. This suggests that neighborhood effects have a stronger influence on the predictions than mesh refinement / mesh type.

These conclusions stress the importance of being able to experimentally characterize polycrystalline aggregates in 3D before and after deformation. New advances in non-destructive characterization of microtexture and strain fields [KING et al., 2010] in 3D pave the way to more accurate comparisons between FE simulations and experimental data. In this work, 2D results were extracted from the 3D data for direct comparison with the experimental 2D EBSD scans. Nevertheless, 3D microtexture analysis could readily be performed. Intergranular and intragranular misorientation computations could be used for establishing a new nucleation criterion for 3D static recrystallization simulations. In that respect, enriching the single crystal model is in fact important if nuclei positions are to be predicted in a more physical way. Constitutive models developed at lower scales or considering geometrically necessary dislocations (GNDs) would be required to better reproduce local features (shear bands, twin bands, dislocation pile ups, etc.) at the origin of nucleation events. Other perspectives include the simulation of dynamic recrystallization, i.e performing the deformation and recrystallization steps simultaneously.

Bibliography

ACHARYA, A. and BEAUDOIN, A. (2000). Grain-size effect in viscoplastic polycrystals at moderate strains. *Journal of the Mechanics and Physics of Solids*, 48:2213–2230.

AluMATTER (2009). Applications: packaging: beverage cans. `http://www.aluminium.matter.org.uk/content/html/eng/default.asp?catid=&pageid=1`.

ANAND, L. and KOTHARI, M. (1996). A computational procedure for rate-independent crystal plasticity. *Journal of the Mechanics and Physics of Solids*, 44:525–558.

ARSENLIS, A. and PARKS, D. (2001). Modeling the evolution of crystallographic dislocation density in crystal plasticity. *Journal of the Mechanics and Physics of Solids*, 50:1979–2009.

BACHU, V. and KALIDINDI, S. (1998). On the accuracy of the predictions of texture evolution by the finite element technique for fcc polycrystals. *Materials Science and Engineering: A*, 257:108–117.

BALAY, S., GROPP, W. D., MCINNES, L. C., and SMITH, B. F. (1997). Efficient management of parallelism in object oriented numerical software libraries. In *Modern Software Tools in Scientific Computing*, pages 163–202. Birkhäuser Press.

BARBE, F., DECKER, L., JEULIN, D., and CAILLETAUD, G. (2001a). Intergranular and intragranular behavior of polycrystalline aggregates. Part 1: FE model. *International Journal of Plasticity*, 17:513–536.

BARBE, F., FOREST, S., and CAILLETAUD, G. (2001b). Intergranular and intragranular behavior of polycrystalline aggregates. Part 2 : Results. *International Journal of Plasticity*, 17:537–563.

BARRETT, C. S. and LEVENSON, L. H. (1940). The structure of aluminum after compression. *Trans. AIME*, 137:112–127.

BARTON, N., BENSON, D., and BECKER, R. (2004). Crystal level simulations using eulerian finite element methods. In *Materials Processing and Design: Modeling, Simulation and Applications, AIP conference proceedings, NUMIFORM 2004*, volume 712, pages 1624–1629, Columbus, Ohio, USA.

BASSANI, J. L. (1994). Plastic flow in crystals. In *Advances in applied mechanics*, volume 30, pages 191–258.

BASSANI, J. L. (2001). Incompatibility and a simple gradient theory of plasticity. *Journal of the Mechanics and Physics of Solids*, 49:1983–1996.

BATE, P. (1999). Modelling deformation microstructure with the crystal plasticity finite-element method. *Philosophical Transactions of the Royal Society A*, 357:1589–1601.

BATHE, K. J. (1996). *Finite Element Procedures*. Prentice Hall, Englewood Cliffs, NJ.

BAUDIN, T., ETTER, A. L., GERBER, P., SAMET, A., PENELLE, R., and REY, C. (2005). Influence of thermo-mechanical treatments on the stored energy simulated by FEM for two low carbon steels. In *ICOTOM 14: Textures of Materials, pts 1 and 2*, volume 495-497 of *Materials Science forum*, pages 1291–1296.

BEAUDOIN, A. J., DAWSON, P. R., MATHUR, K. K., and KOCKS, U. F. (1995). A hybrid finite element formulation for polycrystal plasticity with consideration of macrostructural and microstructural linking. *International Journal of Plasticity*, 11:501–521.

BERNACKI, M., CHASTEL, Y., DIGONNET, H., RESK, H., COUPEZ, T., and LOGÉ, R. (2007a). Development of numerical tools for the multiscale modelling of recrystallization in metals based on a digital material framework. *Computer Methods in Material Science*, 7:142–149.

BERNACKI, M., DIGONNET, H., RESK, H., COUPEZ, T., and LOGÉ, R. (2007b). Development of numerical tools for the multiscale modelling of recrystallization in metals, based on a digital material framework. In *Materials Processing and Design: Modeling, Simulation and Applications, AIP conference proceedings, NUMIFORM 2007*, volume 908, pages 375–380, Porto, Portugal.

BERNACKI, M., RESK, H., COUPEZ, T., and LOGÉ, R. (2009). Finite element model of primary recrystallization in polycrystalline aggregates using a level set framework. *Modelling and Simulation in Materials Science and Engineering*, 17(6):064006.

BERVEILLER, M. and ZAOUI, A. (1979). An extension of the self-consistent scheme to plastically flowing polycrystals. *Journal of the Mechanics and Physics of Solids*, 26:325–344.

BHANDARI, Y., SARKAR, S., GROEBER, M., UCHIC, M. D., M.DIMIDUK, D., and GOSH, S. (2007). 3d polycrystalline microstructure reconstruction from fib generated serial sections for fe analysis. *Computational Material Science*, 41:222–235.

BHATTACHARYYA, A., KALIDINDI, S. R., EL-DANAF, E., and DOHERTY, R. D. (2001). Evolution of grain-scale microstructure during large strain simple compression of polycrystalline alu-

minum with quasi-columnar grains: OIM measurements and numerical simulations. *International Journal of Plasticity*, 17:861–883.

Bishop, J. and Hill, R. (1951). A theory of the plastic distortion of a polycrystalline aggregate under combined stresses. *Philosophical Magazine*, 42:414–417.

Brahme, A., Alvi, M. H., Saylor, D., Fridy, J., and Rollett, A. D. (2006). 3d reconstruction of microstructure in a commercial purity aluminum. *Scripta Materialia*, 55:75–80.

Brezzi, F. and Fortin, M. (1991). *Mixed and hybrid finite elements methods*, volume Springer Series in Computational Mathematics 15. Springer-Verlag, New York.

Buchheit, T. E., Wellman, G. W., and Battaile, C. C. (2005). Investigating the limits of polycrystal plasticity modeling. *International Journal of Plasticity*, 21:221–249.

Budiansky, B. and Wu, T. T. (1962). Theoretical predictions of plastic strains of polycrystals. In *Proceedings - U.S. National Congress of Mechanics*, volume 4, pages 1175–1185.

Busso, E. and Cailletaud, G. (2005). On the selection of active slip systems in crystal plasticity. *International Journal of Plasticity*, 21:2212–2231.

Busso, E. P., Meissonnier, F. T., and O'Dowd, N. P. (2000). Gradient-dependent deformation of two-phase single crystals. *Journal of the Mechanics and Physics of Solids*, 48:2333–2361.

Cailletaud, G. (1987). *Une approche micromécanique du comportement des polycristaux*. PhD thesis, Université Paris 6, Paris.

Cailletaud, G., Forest, S., Jeulin, D., Feyel, F., Galliet, I., Mounoury, V., and Quilici, S. (2003). Some elements of microstructural mechanics. *Computational Materials Science*, 27:351–374.

Chen, L. Q. (1995). A novel computer-simulation technique for modeling grain-growth. *Scripta Metallurgica et Materialia*, 32:115–120.

Chen, L. Q. (2002). Phase-field models for microstructure evolution. *Annual Review of Materials Research*, 32:113–140.

Cheong, K. S. and Busso, E. P. (2004). Discrete dislocation density modelling of single phase fcc polycrystal aggregates. *Acta Materialia*, 52:5665–5675.

Cheong, K. S., Busso, E. P., and Arsenlis, A. (2005). A study of microstructural length scale effects on the behaviour of fcc polycrystals using strain gradient concepts. *International Journal of Plasticity*, 21:1797–1814.

COLLINS, J. B. and LEVINE, H. (1985). Diffuse interface model of diffusion-limited crystal growth. *Physical Review B*, 31:6119–6122.

COUPEZ, T. (2000). Génération et adaptation de maillage par optimisation locale. *European Journal of Finite Elements*, 9:403–423.

COUPEZ, T. and MARIE, S. (1997). From a direct solver to a parallel iterative solver in 3d forming simulation. *International Journal of Supercomputer Applications*, 11:205–211.

DAWSON, P., BEAUDOIN, A., MATHUR, K., and SARMA, G. (1994). Finite element modelling of polycrystalline solids. *European Journal of Finite Elements*, 3:543–571.

DAWSON, P., MIKA, D., and BARTON, N. (2002). Finite element modeling of lattice misorientations in aluminum polycrystals. *Scripta Materialia*, 47:713–717.

DAWSON, P., MILLER, M., HAN, T. S., and BERNIER, J. (2005). An accelerated methodology for the evaluation of critical properties in polyphase alloys. *Metallurgical and Materials Transactions A*, 36:1627–1641.

DELAIRE, F., RAPHANEL, J., and REY, C. (2000). Plastic heterogeneities of a copper multicrystal deformed in uniaxial tension: experimental study and finite element simulations. *Acta Materialia*, 48:1075–1087.

DELANNAY, L. (2001). *Observation and modelling of grain interactions and grain subdivision in rolled cubic polycrystals*. PhD thesis, K U Leuven, Leuven.

DELANNAY, L., BÉRINGHIER, M., CHASTEL, Y., and LOGÉ, R. (2005). Simulation of cup drawing based on crystal plasticity applied to reduced grain samplings. *Material Science Forum*, 495-497:1639–1644.

DELANNAY, L., JACQUES, P. J., and KALIDINDI, S. R. (2006). Finite element modeling of crystal plasticity with grains shaped as truncated octahedrons. *International Journal of Plasticity*, 22:1879–1898.

DELANNAY, L., LOGÉ, R. E., CHASTEL, Y., and VAN HOUTTE, P. (2002). Prediction of intergranular strains in cubic metals using a multisite elastic-plastic model. *Acta Materialia*, 50:5127–5138.

DELANNAY, L., MELCHIOR, M. A., SIGNORELLI, J. W., REMACLE, J.-F., and KUWABARA, T. (2009). Influence of grain shape on the planar anisotropy of rolled steel sheets - evaluation of three models. *Computational Materials Science*, 45:739–743.

DIARD, O., LECLERCQ, S., ROUSSELIER, G., and CAILLETAUD, G. (2005). Evaluation of finite element based analysis of 3d multicrystalline aggregates plasticity. *International Journal of Plasticity*, 21:691–722.

DIGONNET, H., SILVA, L., and COUPEZ, T. (2007). Cimlib: A fully parallel application for numerical simulations based on components assembly. In *NUMIFORM '07: Materials Processing and Design: Modeling, Simulation and Applications, Pts I and II*, volume 908 of *AIP conference proceedings*, pages 269–274.

DOHERTY, R. D., HUGHES, D. A., HUMPHREYS, F. J., JONAS, J. J., JUUL JENSEN, D., KASSNER, M. E., KING, W. E., MCNELLEY, T. R., MCQUEEN, H. J., and ROLLETT, A. D. (1997). Current issues in recrystallization: a review. *Materials Science and Engineering A*, 238:219–274.

ENGLER, O., CRUMBACH, M., and LI, S. (2005). Alloy-dependent rolling texture simulation of aluminium alloys with a grain-interaction model. *Acta Materialia*, 53:2241–2257.

ERIEAU, P. (2003). *Etude expérimentale et analyse numérique de l'influence des hétérogénéités induites par la déformation à froid sur la recrystallisation primaire d'un acier IF-Ti*. PhD thesis, Ecole Centrale Paris, Paris.

ERIEAU, P. and REY, C. (2004). Modeling of deformation and rotation bands and of deformation induced grain boundaries in if steel aggregate during large plane strain compression. *International Journal of Plasticity*, 20:1763–1788.

ESHELBY, J. (1957). The determination of the elastic field of an ellipsoidal inclusion, and related problems. In *Proceedings - Royal Society of London A. Mathematical and physical sciences*, volume 241, pages 376–396.

FIVEL, M. (1997). *Études numériques à différentes échelles de la déformation plastique des monocristaux de structure cfc*. PhD thesis, Institut National Polytechnique de Grenoble, Grenoble.

FLECK, N. A., MULLER, G. M., ASHBY, M. F., and HUTCHINSON, J. W. (1994). Strain gradient plasticity: theory and experiment. *Acta Metallurgica et Materialia*, 42:475–487.

FRANCIOSI, P., BERVEILLER, M., and ZAOUI, A. (1980). Latent hardening in copper and aluminum single crystals. *Acta Metallurgica*, 28:273–283.

GEORGE, P. L. . and BOUROUCHAKI, H. (1998). *Delaunay Triangulation and Meshing - Application to Finite Element*. Hermes, Paris.

GERKEN, J. and DAWSON, P. (2008). A crystal plasticity model that incorporates stresses and strains due to slip gradients. *Journal of the Mechanics and Physics of Solids*, 56:1651–1672.

GLEZ, J. C. and DRIVER, J. H. (2001). Orientation distribution analysis in deformed grains. *Journal of applied crystallography*, 34:280–288.

GOSH, S., BHANDARI, Y., and GROEBER, M. (2008). Cad-based reconstruction of 3d polycrystalline alloy microstructures from fib generated serial sections. *Computer-Aided Design*, 40:293–310.

GRIMMER, H. (1974). Disorientations and coincidence rotations for cubic lattices. *Acta Crystallographica Section A*, 30(6):685–688.

GROEBER, M., GOSH, S., UCHIC, M., and DIMIDUK, D. (2008a). A framework for automated analysis and representation of 3d polycrystalline microstructures, part 1: Statistical characterization. *Acta Materialia*, 56:1257–1273.

GROEBER, M., GOSH, S., UCHIC, M., and DIMIDUK, D. (2008b). A framework for automated analysis and representation of 3d polycrystalline microstructures, part 2: Synthetic structure generation. *Acta Materialia*, 56:1274–1278.

GROSS, D. and SEELIG, T. (2006). *Fracture mechanics*, chapter Micromechanics and homogenization. Springer Berlin Heidelberg.

GRUAU, C. and COUPEZ, T. (2005). Tetrahedral unstructured and anisotropic mesh generation with adaptation to natural and multidomain metric. *Computer Methods in Applied Mechanics and Engineering*, 194:4951–4976.

GUDMUNDSON, P. (2004). A unified treatment of strain gradient plasticity. *Journal of the Mechanics and Physics of Solids*, 52:1379–1406.

HASSOLD, H. K. and HOLM, T. (1993). An efficient finite temperature algorithm for the quenched potts model. *Computers in Physics*, 7:97–107.

HILL, R. (1965). Continuum micro-mechanisms of elastoplastic polycrystals. *Journal of the Mechanics and Physics of Solids*, 13:89–101.

HILL, R. (1967). The essential structure of constitutive laws for metal composites and polycrystals. *Journal of the Mechanics and Physics of Solids*, 15:79–92.

HOSFORD, W. F. (1993). *The mechanics of crystals and textured polycrystals*. Oxford University Press, New York.

HUANG, Y., QU, S., HWANG, K. C., LI, M., and GAO, H. (2004). A conventional theory of mechanism-based strain gradient plasticity. *International Journal of Plasticity*, 20:753–782.

HUGHES, D. A., LIU, Q., CHRZAN, D. C., and HANSEN, N. (1997). Scaling of microstructural parameters: Misorientations of deformation induced boundaries. *Acta Materialia*, 45:105–112.

HUMPHREYS, F. J. and HATHERLY, M. (2004). *Recrystallization and related annealing phenomena.* Elsevier,Amsterdam.

HUTCHINSON, J. W. (1976). Bounds and self-consistent estimates for creep of polycrystalline materials. In *Proceedings - Royal Society of London A*, volume 348, pages 101–127.

HUTCHINSON, J. W. (1977). Creep and plasticity of hexagonal polycrystals as related to single crystal slip. *Metallurgical Transactions A*, 8:1465–1469.

JACKSON, P. J. and BASINSKI, Z. S. (1967). Latent hardening and the flow stress in copper single crystals. *Canadian Journal of Physics*, 45:707–735.

JAOUEN, O. (1998). *Modélisation tridimensionnelle par éléments finis pour l'analyse thermomécanique du refroidissement des pièces coulées.* PhD thesis, Ecole des Mines de Paris, Sophia Antipolis.

KALIDINDI, S. R., BHATTACHARYYA, A., and DOHERTY, R. D. (2004). Detailed analyses of grain-scale plastic deformation in columnar polycrystalline aluminium using orientation image mapping and crystal plasticity models. In *Proceedings - Royal Society of London A. Mathematical, physical and engineering sciences*, volume 460, pages 1935–1956.

KALIDINDI, S. R., BRONKHORST, C. A., and ANAND, L. (1992). Crystallographic evolution in bulk deformation processing of fcc metals. *Journal of the Mechanics and Physics of Solids*, 40:537–569.

KARMA, A. (2001). Phase-field formulation for quantitative modeling of alloy solidification. *Physical Review Letters*, 87:115701–115704.

KHAN, A. S. and HUANG, S. (1995). *Continuum Theory of Plasticity.* Wiley, New York.

KING, A., HERBIG, M., LUDWIG, W., REISCHIG, P., LAURIDSEN, E., MARROW, T., and BUFFIÈRE, J. (2010). Non-destructive analysis of micro texture and grain boundary character from x-ray diffraction contrast tomography. *Nuclear Instruments and Methods in Physics Research Section B: Beam Interactions with Materials and Atoms*, 268(3-4):291 – 296. X-ray Techniques for Advanced Materials, Nanostructures and Thin Films: from Laboratory Sources to Synchrotron Radiation - Proceedings of the EMRS 2009 Spring Meeting - Symposium R.

KNOCKAERT, R., CHASTEL, Y., and MASSONI, E. (2000). Rate-independent crystalline and poly-crystalline plasticity, application to fcc materials. *International Journal of Plasticity*, 16:179–198.

KOCKS, U. F. (1998a). Kinematics and kinetics of plasticity. In KOCKS, U. F., TOMÉ, C. N., and WENK, H. R., editors, *Texture and anisotropy*. Cambridge University Press, Cambridge.

Kocks, U. F. (1998b). The representation of orientations and textures. In Kocks, U. F., Tomé, C. N., and Wenk, H. R., editors, *Texture and anisotropy*. Cambridge University Press, Cambridge.

Kocks, U. F. and Brown, T. J. (1966). Latent hardening in aluminum. *Acta Metallurgica*, 14:87–98.

Krill, C. E. and Chen, L. Q. (2002). Computer simulation of 3-D grain growth using a phase-field model. *Acta Materialia*, 50:3057–3073.

Kröner, E. (1961). Zur plastischen verformung des vielkristalls. *Acta Metallurgica*, 9:155–161.

Kugler, G. and Turk, R. (2004). Modeling the dynamic recrystallization under multi-stage hot deformation. *Acta Materialia*, 52:4659–4668.

Kugler, G. and Turk, R. (2006). Study of the influence of initial microstructure topology on the kinetics of static recrystallization using a cellular automata model. *Computational Materials Science*, 37:284–291.

Lebensohn, R., Brenner, R., Castelnau, O., and Rollett, A. (2008). Orientation image-based micromechanical modelling of subgrain texture evolution in polycrystalline copper. *Acta Materialia*, 56:3914–3926.

Lebensohn, R., Castelnau, O., Brenner, R., and Gilormini, P. (2005). Study of the antiplane deformation of linear 2-d polycrystals with different microstructures. *International Journal of Solids and Structures*, 42:5441–5459.

Lebensohn, R. and Tomé, C. (1993). A self-consistent anisotropic approach for the simulation of plastic deformation and texture development of polycrystals: application to zirconium alloys. *Acta Metallurgica et Materialia*, 41:2611–2624.

Logé, R., Bernacki, M., Resk, H., Delannay, L., Digonnet, H., Chastel, Y., and Coupez, T. (2008). Linking plastic deformation to recrystallization in metals using digital microstructures. *Philosophical Magazine*, 88(30):3691–3712.

Logé, R., Resk, H., Sun, Z., Delannay, L., and Bernacki, M. (2010). Modelling plastic deformation and recrystallization of polycrystals using digital micro-structures and adaptive meshing techniques. In *Proceedings Metal Forming 2010, submitted for publication in Steel Research international*.

Ma, A., Rosters, F., and Raabe, D. (2006). A dislocation density based constitutive model for crystal plasticity fem including geometrically necessary dislocations. *Acta Materialia*, 54:2169–2179.

MANIATTY, A., LITTLEWOOD, D., LU, J., and PYLE, D. (2007). Modeling of 3d aluminum polycrystals during large deformations. In *Materials Processing and Design: Modeling, Simulation and Applications, AIP conference proceedings, NUMIFORM 2007*, volume 908, pages 393–398, Porto, Portugal.

MARIN, E. and DAWSON, P. (1998a). Elastoplastic finite element analyses of metal deformations using polycrystal constitutive models. *Computer Methods in Applied Mechanics and Engineering*, 165:23–41.

MARIN, E. and DAWSON, P. (1998b). On modelling the elasto-viscoplastic response of metals using polycrystal plasticity. *Computer Methods in Applied Mechanics and Engineering*, 165:1–21.

MELCHIOR, M. A. and DELANNAY, L. (2006). A texture discretization technique adapted to polycrystalline aggregates with non-uniform grain size. *Computational Materials Science*, 37:557–564.

MERRIMAN, B., BENCER, J. K., and OSHER, S. J. (1994). Motion of multiple junctions - A level set approach. *Journal of Computational Physics*, 112:334–363.

MESRI, Y., ZERGUINE, W., DIGONNET, H., SILVA, L., and COUPEZ, T. (2008). Dynamic parallel adaption for three dimensional unstructured meshes: Application to interface tracking. In *Proceedings of the 17th international Meshing Roundtable*, pages 195–212, Pittsburgh PA , USA.

MIKA, D. and DAWSON, P. (1998). Effects of grain interaction on deformation in polycrystals. *Materials Science and Engineering: A*, 257:62–76.

MIKA, D. and DAWSON, P. (1999). Polycrystal plasticity modeling of intracrystalline boundary textures. *Acta Materialia*, 47:1355–1369.

MILLER, M. and DAWSON, P. (1997). Influence of slip system hardening assumptions on modeling stress dependance of work hardening. *Journal of the Mechanics and Physics of Solids*, 45:1781–1804.

MIODOWNIK, M. A. (2002). A review of microstructural computer models used to simulate grain growth and recrystallisation in aluminium alloys. *Journal of Light Metals*, 2:125–135.

MOLINARI, A., CANOVA, G. R., and AHZI, S. (1987). A self consistent approach of the large deformation polycrystal viscoplasticity. *Acta Metallurgica*, 35:2983–2994.

NYE, J. F. (1953). Some geometrical relations in dislocated crystals. *Acta Metallurgica*, 1:153–162.

OSHER, S. and SETHIAN, J. A. (1988). Fronts propagating with curvature-dependent speed - Algorithms based on Hamilton-Jacobi formulations . *Journal of Computational Physics*, 79:12–49.

PANCHANADEESWARAN, S., DOHERTY, R. D., and BECKER, R. (1996). Direct observation of orientation change by channel die compression of polycrystalline aluminum - use of a split sample. *Acta Materialia*, 44:1233–1262.

PANTLEON, W., HE, W., JOHANSSON, T. P., and GUNDLACH, C. (2008). Orientation inhomogeneities within individual grains in cold-rolled aluminium resolved by electron backscatter diffraction. *Materials Science and Engineering A*, 483-484:668–671.

PEETERS, B., HOFERLIN, E., VAN HOUTTE, P., and AERNOUDT, E. (2001). Assessment of crystal plasticity based calculation of the lattice spin of polycrystalline metals for fe implementation. *International Journal of Plasticity*, 17(6):819 – 836.

PEIRCE, D., ASARO, R. J., and NEEDLEMAN, A. (1982). An analysis of non-uniform and localised deformation in ductile single crystals. *Acta Metallurgica*, 30:1087–1119.

PEIRCE, D., ASARO, R. J., and NEEDLEMAN, A. (1983). Material rate dependence and localised deformation in crystalline solids. *Acta Metallurgica*, 31:1951–1976.

POULSEN, H. F., MARGULIES, L., SCHMIDT, S., and WINTHER, G. (2003). Lattice rotations of individual bulk grains, part i: 3d x-ray characterization. *Acta Materialia*, 51:3821–3830.

QUEY, R. (2008). Orientation library: a collection of routines for orientation manipulation. `http://sourceforge.net/projects/orilib`. 2.0 edition.

QUEY, R. (2009). *Suivi de microtextures dans l'aluminium en grandes déformations à chaud*. PhD thesis, Ecole Nationale Supérieure des Mines de Saint Etienne, Saint Etienne.

RAABE, D. (1999). Introduction of a scaleable 3d cellular automaton with a probabilistic switching rule for the discrete mesoscale simulation of recrystallization phenomena. *Philosophical Magazine A*, 79:2339–2358.

RAABE, D. and BECKER, R. C. (2000). Coupling of a crystal plasticity finite-element model with a probabilistic cellular automaton for simulating primary static recrystallization in aluminium. *Modelling and Simulation in Materials Science and Engineering*, 8:445–462 .

RESK, H., BERNACKI, M., CHASTEL, Y., COUPEZ, T., DELANNAY, L., and R.LOGÉ (2008a). Numerical modelling of plastic deformation and subsequent primary recrystallization in a polycrystalline volume element, based on a level set framework. In *WCCM8-ECCOMAS 2008*, Venice, Italy.

Resk, H., Bernacki, M., Coupez, T., Delannay, L., and R.Logé (2008b). Adaptive mesh refinement in crystal plasticity finite element simulations of large deformations in polycrystalline aggregates. In *ICOTOM 15*, Pittsburgh PA, USA.

Resk, H., Delannay, L., Bernacki, M., Coupez, T., and Logé, R. (2009). Adaptive mesh refinement and automatic remeshing in crystal plasticity finite element simulations. *Modelling and Simulation in Materials Science and Engineering*, 17(7):075012.

Ritz, H. and Dawson, P. (2009). Sensitivity to grain discretization of the simulated crystal stress distributions in fcc polycrystals. *Modelling and Simulation in Materials Science and Engineering*, 17(1):015001.

Rollett, A., Lee, S. B., Campman, R., and Rohrer, G. S. (2007). Three-dimensional characterization of microstructure by electron back-scatter diffraction. *Annual Review of Materials Research*, 37:627–658.

Rollett, A. D. (1997). Overview of modeling and simulation of recrystallization. *Progress in Material Science*, 42:79–99.

Rollett, A. D. and Raabe, D. (2001). A hybrid model for mesoscopic simulation of recrystallization. *Computational Materials Science*, 21:69–78.

Rousselier, G., Barlat, F., and Yoon, J. W. (2009). A novel approach for anisotropic hardening modeling, part 1: Theory and its application to finite element analysis of deep drawing. *International Journal of Plasticity*, 25:2383 – 2409.

Sachs, G. (1928). Zur ableitung einer fliessbedingung. *Zeitschrift des Vereins deutscher Ingenieure*, 72:734–736.

Sarma, G. and Dawson, P. (1996). Effects of interactions among crystals on the inhomogeneous deformation of polycrystals. *Acta Metallurgica et Materialia*, 44:1937–1953.

Sarma, G., Radhakrishnan, B., and Dawson, P. (2002). Mesoscale modeling of microstructure and texture evolution during deformation processing of materials. *Advanced Engineering Materials*, 4:509–514.

Sarma, G., Radhakrishnan, B., and Zacharia, T. (1998). Finite element simulations of cold deformation at the mesoscale. *Computational Materials Science*, 12:105–123.

Schmid, E. and Boas, W. (1935). *Kristallplastizität*. Springer Verlag, Berlin.

Schmidt-Baldassari, M. (2003). Numerical concepts for rate-independent single crystal plasticity. *Computer Methods in Applied Mechanics and Engineering*, 192:1261–1280.

Sᴇᴛʜɪᴀɴ, J. (1996). *Level Set methods*. Cambridge University Press, Cambridge.

Sʜᴀʙᴀɴᴀ, A. (2008). *Computational continuum mechanics*. Cambridge University Press, New York.

Sɪᴍᴏ, J. C. and Hᴜɢʜᴇs, T. J. (1998). *Computational inelasticity*. Springer-Verlag, New York.

Sᴜssᴍᴀɴ, M., Sᴍᴇʀᴇᴋᴀ, P., and Osʜᴇʀ, S. (1994). A Level Set Approach for Computing Solutions to Incom- pressible Two-Phase Flow. *Journal of Computational Physics*, 114:146–159.

Sørensen, H. O., Jᴀᴋᴏʙsᴇɴ, B., Kɴᴜᴅsᴇɴ, E., Lᴀᴜʀɪᴅsᴇɴ, E. M., Nɪᴇʟsᴇɴ, S. F., Pᴏᴜʟsᴇɴ, H. F., Sᴄʜᴍɪᴅᴛ, S., Wɪɴᴛʜᴇʀ, G., and Mᴀʀɢᴜʟɪᴇs, L. (2006). Mapping grains and their dynamics in three dimensions. *Nuclear Instruments and Methods in Physics Research B*, 246:232–237.

Tᴀʏʟᴏʀ, G. I. (1938). Plastic strain in metals. *Journal of the Institute of Metals*, 62:307–324.

Vᴀɴ Hᴏᴜᴛᴛᴇ, P. (2005). Deformation texture prediction: from the taylor model to the advanced lamel model. *International Journal of Plasticity*, 21:589–624.

Vᴀɴ Hᴏᴜᴛᴛᴇ, P., Dᴇʟᴀɴɴᴀʏ, L., and Sᴀᴍᴀᴊᴅᴀʀ, I. (1999). Quantitative prediction of cold rolling textures in low carbon steel by means of the lamel model. *Textures and Microstructures*, 31:109–149.

VᴀɴHᴏᴜᴛᴛᴇ, P. V., Lɪ, S., and Eɴɢʟᴇʀ, O. (2004). Taylor-type homogenization methods for texture and anisotropy. In Rᴀᴀʙᴇ, D., Rᴏᴛᴇʀs, F., Bᴀʀʟᴀᴛ, F., and Cʜᴇɴ, L.-Q., editors, *Continuum Scale Simulation of Engineering Materials*. Wiley-VCH, Weinheim.

Vᴏʟᴏᴠɪᴛᴄʜ, P., Cᴀʟᴇʏᴏ, F., Bᴀᴜᴅɪɴ, T., Gᴇʀʙᴇʀ, P., Pᴇɴᴇʟʟᴇ, R., and Rᴇʏ, C. (2005). Monte Carlo modeling of low carbon steel recrystallization: Role of thermo-nnechanical treatment and chemical composition. In *ICOTOM 14: Textures of Materials, pts 1 and 2*, volume 495-497 of *Materials Science forum*, pages 507–512.

Zʜᴀᴏ, H. K., Cʜᴀɴ, T., Mᴇʀʀɪᴍᴀɴ, B., and Osʜᴇʀ, S. (1996). A variational level set approach to multiphase motion. *Journal of Computational Physics*, 127:179–195.

Zʜᴀᴏ, Z., Kᴜᴄʜɴɪᴄᴋɪ, S., Rᴀᴅᴏᴠɪᴛᴢᴋʏ, R., and Cᴜɪᴛɪñᴏ, A. (2007). Influence of in-grain mesh resolution on the prediction of deformation textures in fcc polycrystals by crystal plasticity fem. *Acta Materialia*, 55:2361–2373.

Appendix A

Orientation representation formulae

Given the Euler angles $(\varphi_1, \phi, \varphi_2)$, the rotation matrix is given by:

$$[a] = \begin{bmatrix} \cos\varphi_1 \cos\varphi_2 & -\cos\varphi_1 \sin\varphi_2 & \sin\varphi_1 \sin\phi \\ -\sin\varphi_1 \sin\varphi_2 \cos\phi & -\sin\varphi_1 \cos\varphi_2 \cos\phi & \\ & & \\ \sin\varphi_1 \cos\varphi_2 & -\sin\varphi_1 \sin\varphi_2 & -\cos\varphi_1 \sin\phi \\ +\cos\varphi_1 \sin\varphi_2 \cos\phi & +\cos\varphi_1 \cos\varphi_2 \cos\phi & \\ & & \\ \sin\varphi_2 \sin\phi & \cos\varphi_2 \sin\phi & \cos\phi \end{bmatrix}. \tag{A.1}$$

The angle of rotation w, and the components of a unit vector corresponding to the axis of rotation c are given by:

$$\begin{cases} w = arccos\left[\frac{1}{2}(tr[R] - 1)\right] \\ \\ c_x = \dfrac{R_{32} - R_{23}}{2\sin w} \\ \\ c_y = \dfrac{R_{13} - R_{31}}{2\sin w} \\ \\ c_z = \dfrac{R_{21} - R_{12}}{2\sin w} \end{cases} \tag{A.2}$$

For cubic crystals, there are 24 symmetrically equivalent orientations. Quaternions are used to find the orientation with the smallest angle. The relationship between the quaternion and the axis/angle representation is given by [GRIMMER, 1974]:

$$(q_0, q_1, q_2, q_3) = \left(\cos\frac{w}{2}, c_x \sin\frac{w}{2}, c_y \sin\frac{w}{2}, c_z \sin\frac{w}{2}\right). \tag{A.3}$$

The smallest angle corresponds to the largest q_0. The value of q_0 for all symmetrically equivalent orientations under cubic symmetry is given by [GRIMMER, 1974]:

$$q_0' = q_0 s_0 - q_1 s_1 - q_2 s_2 - q_3 s_3, \tag{A.4}$$

where s_0, s_1, s_2 and s_3 are shown in table A.1. The other components are then determined by the following equation:

$$\begin{cases} q_0' = q_0 s_0 - q_1 s_1 - q_2 s_2 - q_3 s_3 \\ q_1' = q_0 s_1 + q_1 s_0 + q_2 s_3 - q_3 s_2 \\ q_2' = q_0 s_2 - q_1 s_3 + q_2 s_0 + q_3 s_1 \\ q_3' = q_0 s_3 + q_1 s_2 - q_2 s_1 + q_3 s_0 \end{cases} . \tag{A.5}$$

The axis and angle can then be computed by equation A.6.

$$\begin{cases} w = arccos(q_0') \\ c_x = \dfrac{q_1'}{\sin w/2} \\ c_y = \dfrac{q_2'}{\sin w/2} \\ c_z = \dfrac{q_3'}{\sin w/2} \end{cases} . \tag{A.6}$$

In order to compute the misorientation between two crystals, it is first useful to compute the corresponding rotation matrix given by equation A.7 then use the quaternion arithmetics and procedure detailed above.

$$[R] = [R_2][R_1]^T \tag{A.7}$$

	s_0	s_1	s_2	s_3
1	1	0	0	0
2	0	1	0	0
3	0	0	1	0
4	0	0	0	1
5	$1/\sqrt{2}$	$1/\sqrt{2}$	0	0
6	$1/\sqrt{2}$	0	$1/\sqrt{2}$	0
7	$1/\sqrt{2}$	0	0	$1/\sqrt{2}$
8	$1/\sqrt{2}$	$-1/\sqrt{2}$	0	0
9	$1/\sqrt{2}$	0	$-1/\sqrt{2}$	0
10	$1/\sqrt{2}$	0	0	$-1/\sqrt{2}$
11	0	$1/\sqrt{2}$	$1/\sqrt{2}$	0
12	0	$1/\sqrt{2}$	0	$1/\sqrt{2}$
13	0	0	$1/\sqrt{2}$	$1/\sqrt{2}$
14	0	$1/\sqrt{2}$	$-1/\sqrt{2}$	0
15	0	$1/\sqrt{2}$	0	$-1/\sqrt{2}$
16	0	0	$1/\sqrt{2}$	$-1/\sqrt{2}$
17	1/2	1/2	1/2	1/2
18	1/2	1/2	1/2	$-1/2$
19	1/2	1/2	$-1/2$	1/2
20	1/2	$-1/2$	1/2	1/2
21	1/2	1/2	$-1/2$	$-1/2$
22	1/2	$-1/2$	1/2	$-1/2$
23	1/2	$-1/2$	$-1/2$	1/2
24	1/2	$-1/2$	$-1/2$	$-1/2$

Table A.1: Equivalent quaternions under cubic symmetry

Appendix B

Linking plastic deformation and recrystallization simulations (chapter 5)

More details on the recrystallization simulations are found in the following attached papers :

- [Logé et al., 2008] (`http://dx.doi.org/10.1080/14786430802502575`)

- [Bernacki et al., 2009] (`http://iopscience.iop.org/0965-0393/17/6/064006/`)

Linking plastic deformation to recrystallization in metals, using digital microstructures

Roland Logé[a,·], Marc Bernacki[a], Heba Resk[a], Laurent Delannay[b], Hugues Digonnet[a], Yvan Chastel[a], Thierry Coupez[a]

[a] *MINES ParisTech, CEMEF - Center of Materials Forming, CNRS UMR 7635, BP 207, 06904 Sophia Antipolis Cedex, France*
[b] *CESAME – MEMA, Université catholique de Louvain (UCL), bâtiment Euler, av. G. Lemaître 4, 1348 Louvain-la-Neuve, Belgium*

Abstract

Procedures for synthesizing digital polycrystalline microstructures are illustrated, either from 2D statistical data or from 3D deterministic data. Finite element meshes representing the digital microstructures are generated using anisotropic and adaptive mesh refinement close to the grain boundaries. Digital mechanical testing based on crystal plasticity theory provides an estimate of the spatial distribution of strain energy within the polycrystalline aggregate. The latter quantity is used as an input for modelling subsequent static recrystallization, grain boundary motion being described within a level set framework. The kinetic law for interface motion accounts for both the stored strain energy and the grain boundary energy. The possibility to include nucleation events within the level set framework is illustrated, as well as the evolving topology of the grain boundary network. The recrystallization model is tested in different configurations and compared to the Johnson-Mehl-Avrami-Kolmogorov (JMAK) theory.

Keywords*:* digital microstructure; finite elements; meshing; remeshing; crystal plasticity; large deformation; recrystallization; level set; moving boundaries; nucleation, JMAK theory.

1. Introduction

No generic model is currently available to describe the recrystallization behavior of a wide class of metallic alloys. This is due in great measure to the fact that recrystallization, like many similar state-altering processes that are driven by thermal energy and internal energy of structural defects, is really controlled by factors at several length scales. Multiscale modelling is thus a requisite to coming to a better understanding of recrytallization. Important factors over length scales of decreasing size include: (a) grain interactions, which set up stress fields that persist over grain

---

· Corresponding author. Email: Roland.Loge@mines-paristech.fr

dimensions, (b) stress variations within grains due to the presence of dislocation structures, which both perturb the longer range field across the grain and impact the mobility of interfaces through grains, (c) energies and mobilities of interfaces, which control their kinetics, and (d) particles and solutes, interacting with interfaces and modifying their kinetics.

Over the last decade, considerable progress has been made in the numerical simulation of recrystallization phenomena [1]. Common approaches include the Monte Carlo (MC) method [2], the Cellular Automaton (CA) methods [2,3], the phase field method [4] and the level set method [5]. The first two are probabilistic techniques which deliver evolving grain structures. They are associated with a 2D or 3D geometric representation of the microstructure, discretized on a regular grid made of "cells" which are allocated to the grains.

The standard MC method as derived from the Potts model (multistate Ising model) applies probabilistic rules in order to update each cell at each time step of the simulation. The use of this model in 3D is relatively easy and efficient [6]. However the comparison between MC results and experiments is not straightforward [7]. Furthermore, the standard form of the model does not result in a linear relationship between stored energy and migration rate. The CA method, on the other hand, uses physically based rules to determine the rate at which a transformation front propagates across neighbouring cells [3], and can therefore be related to the microstructure and kinetics of a real system. In the case of primary recrystallization the switch rule is simple: an unrecrystallized cell switches to the recrystallized state if one of its neighbours is already recrystallized. A major drawback of the CA method is the absence of appropriate method to treat nucleation phenomena [7].

The two others methods, i.e. the phase field and level set methods, have many common points. They both have the advantage of avoiding numerical difficulties related to interface tracking. The principle of the phase-field model consists in describing the location of phases by introducing an order parameter (the phase field) which varies smoothly from one to zero (or minus one to one) through a diffuse interface [8]. The concept has been extended to deal with more complex problems involving more than two phases and also to model microstructure evolution [9,10]. As for the MC or CA methods, the topological events are treated in a natural way as a result of energy minimization. In the case of 2D ideal normal grain growth, published results illustrate the potential of the approach [9]. However, the main difficulty of this method remains the construction of the free energy density function. Furthermore, the energy minimization of each

order parameter can involve very expensive and intensive calculations, particularly for three-dimensional systems [11]. In contrast, the level set method [12,13] is now commonly used to follow propagating fronts in various models [14]. The level set method has been extended to model the motion of multiple junctions when more than two regions or grains intersect [15].

2. Methodology

This paper proposes a first step in the direction of multiscale modelling of recrystallization in polycrystalline metals, by considering digital microstructures [16-18]. Representative digital microstructures are synthesized with a specific software, based on the construction of Voronoï cells. The distribution of grain sizes and grain shapes is monitored and adapted according to experimental data. In the same way, attributes of grains, such as crystallographic orientation, are sampled so that global properties (e.g. crystallographic texture) are well reproduced. The digital representation of the microstructure is discretized into a finite element mesh, which is then used to model plastic deformation and subsequent recrystallization. The local behaviour of individual microstructure components may be computed through models operating at different scales. For example, grain constitutive models may be derived from the modelling of dislocation populations within the grains, and grain boundary motion may be described by connecting the continuum mechanical and thermal fields to simulations at the atomistic and dislocations levels. Validation of this "digital microstructure" approach is typically done using *in situ* experiments, e.g. synchrotron measurements, where the evolving microstructure can be characterized in 3D before, during and after thermo-mechanical processing.

Previous attempts to use digital microstructures for the modelling of plastic deformation *and* subsequent static recrystallization have been reported by few authors. In [19], a 2D digital sample was meshed, mechanical testing was performed with crystal plasticity finite element simulations, and thermal treatment involving recrystallization was done subsequently using a CA approach [19]. A Monte Carlo (MC) approach can replace the CA approach, as done in [20-23]. In general, the authors do not guarantee that the digital microstructure is representative of a real microstructure because the total number of grains being considered is small. Finite element simulation of plastic deformation is done within updated Lagrangian schemes, which imply that the deformation remains limited in order to avoid that the mesh

degenerates [24,25], as the use of an automatic remeshing procedure is not reported. On the other hand, the finite element mesh needs to be converted into appropriate "voxel" grids for using CA or MC approaches. In doing so, some details of the microstructures may be lost, e.g. those related to grain boundary curvature. This aspect is important if secondary recrystallization is to be modelled after primary recrystallization. Furthermore, in some cases it is useful to simulate further deformation of the digital aggregate following partial recrystallization, e.g. when studying multi-pass (industrial) processing. Transforming the voxel structure back to the finite element mesh then implies a new loss of information (boundary curvature, but also distribution of residual strains/stresses, etc.).

In the approach presented here, there is only one conversion of the initial digital aggregate into a finite element mesh. The digital aggregate can be obtained from experiments, from other simulations, or from a numerical construction. The format is either a Voronoï tessellation or a voxel structure. Discretization into a finite element mesh is done iteratively, by considering the position of the elements with respect to microstructure interfaces (grain boundaries in particular). "Distance functions" updated throughout the deformation simulation allow keeping track of the boundaries. The distance functions uniquely define the topology of the aggregate and the corresponding allocation of properties, even when automatic remeshing operates. The digital heat treatment is performed directly on the finite element mesh using a level set approach. The level set method consists in evolving each distance function using a convection equation, thereby implicitly updating the position of moving interfaces. The velocity of the boundaries is described by a kinetic law taking account of the bulk strain energy and the grain boundary energy, both being related to local crystallographic orientations. When describing primary recrystallization, the influence of the grain boundary energy is neglected with respect to that of the strain energy. The level set approach allows working directly on the deformed mesh, without loosing/distorting any information. The stored energy in particular is directly available and dictates the kinetics of microstructure evolution, with no need to construct a free energy density function (as in phase field methods). Nucleation phenomena are furthermore easy to implement.

The paper is organized as follows. Section 3 explains how distance functions, within a level set framework, can be used for adaptive meshing and remeshing of the microstructure during mechanical testing and subsequent heat treatment. Section 4 presents the construction of digital microstructures and the anisotropic (re-)meshing procedures providing a non uniform mesh size related to the distance functions. In Section 5, mechanical testing is simulated using crystal

plasticity theory. Finally, in Section 6, the level set framework is presented and illustrated with 2D and 3D studies of recrystallization driven by the stored energy. The possibility to nucleate new grains in the context of primary recrystallization is demonstrated as well. Different test cases are discussed with reference to the classical Johnson-Mehl-Avrami-Kolmogorov (JMAK) model.

3. Distance functions and level set framework

A function ϕ, defined in a domain Ω, is called level set if it corresponds, at any points of Ω, to the distance d to an interface Γ. In other words, the interface Γ is given by the zero level of the function ϕ :

$$\begin{cases} \phi(\mathbf{x}) = d(\mathbf{x}, \Gamma), \ \mathbf{x} \in \Omega \\ \Gamma = \left\{ \mathbf{x} \in \Omega, \ \phi(\mathbf{x}) = 0 \right\} \end{cases} \quad . \tag{1}$$

When dealing with a polycrystalline aggregate, an distinct level set function is used for each grain : $\left\{ \phi_i, 1 \le i \le N_G \right\}$, with N_G the total number of grains in the aggregate. The chosen sign convention is $\phi_i \ge 0$ inside the grain G_i, and $\phi_i \le 0$ outside. Figure 1 illustrates a digital sample made of fifty grains, highlighting four particular grains of the microstructure which are displayed using the zero levels of the corresponding level set functions.

When interfaces propagate with a known velocity $\xi(\mathbf{x})$ in Ω, the values of distance functions are updated using a convection equation :

$$\begin{cases} \dfrac{\partial \phi_i}{\partial t} + \xi \cdot \nabla \phi_i = 0 \\ \phi_i(t, \mathbf{x} = 0) = \phi_i^0(\mathbf{x}) \end{cases} \quad \forall i \in \left\{ 1, ..., N_G \right\}. \tag{2}$$

Solving (2) then implicitly updates the position of moving interfaces as a function of time. The method "captures" the interface, rather than tracking it (e.g. see vertex models [27]). Periodic re-initialization of the solution is needed in order to preserve the property of a distance function [15,28].

The level set method is particularly appropriate for handling complex topological events such as the disappearance of grains; no special treatment is needed. A second advantage comes from the fact that intrinsic geometric properties of the front are easily determined from the values of the distance function. Indeed, at any point of the front:

$$\mathbf{n} = \nabla\phi / \|\nabla\phi\|, \qquad \kappa = -\nabla \cdot \mathbf{n} \quad , \tag{3}$$

where $\mathbf{n}$ is a unit vector normal to the interface, which indicates the direction of propagation, and κ the curvature of the interface. The latter quantity is useful when dealing with secondary recrystallization.

4. Automatic meshing of the digital microstructure

2D or 3D polycrystalline microstructures are numerically generated using either a recursive Voronoï tesselation algorithm or an existing pixel/voxel based representation. These microstructures can be optimized according to desired criteria of sizes and shape, as discussed in [29].

Figure 2 illustrates how a 3D initial finite element mesh can be constructed from either a Voronoï structure or a voxel structure. Both Voronoï cells and voxels are easy to divide into tetrahedral elements. In the former case, the obtained mesh is very coarse and will need to be refined. In the latter case, the mesh is on the contrary too fine, and needs to be coarsened. Appropriate refinement of the mesh along interfaces such as grain boundaries is useful to capture the large strain rate/stress gradients developing across those interfaces upon deformation of the microstructure. Such gradients result from the heterogeneous mechanical response of neighbouring grains induced by the crystallographic orientations.

Figure 3 presents a Voronoï tessellation made of 50 grains, and the corresponding finite element mesh, made of tetrahedral elements with heterogeneous sizes and shapes. Anisotropic meshing is used close to the grain boundaries, with a smaller element size in the direction perpendicular to the boundary. A corresponding anisotropic metric is defined, while an isotropic metric is applied in the bulk of the grains. A metric is a symmetric positive tensor $\mathbf{M}$ used to measure the scalar product of two vectors in a stretched, local base :

$$< \mathbf{x}, \mathbf{y} >_{\mathbf{M}} = {}^{t}\mathbf{x}\mathbf{M}\mathbf{y}. \tag{4}$$

If $\mathbf{M}$ is the identity tensor, the scalar product corresponds to the usual one in the Euclidian space.

Anisotropic meshes are built using the MTC algorithm developed by Coupez [30,31]. Mesh generation is topological, in the sense that mesh topology is iteratively improved by considering the quality of the elements. The latter is defined by assigning the highest quality to the elements with all edges of the same length, and the worst quality to elements which

tend to degenerate from a volume to a surface (in 3D), or from a surface to a segment (in 2D). The shape factor $c(e)$ characterizing the quality is normalized within the interval $[0,1]$:

$$c(e) = c_0 \frac{|e|}{l(e)^k} ,$$

(5)

where c_0 is a normalisation coefficient, $|e|$ the volume of the element, $l(e)$ the average length of the element edges and k the space dimension. The volume and lengths are computed with the modified scalar product (Equation 4) when anisotropic meshing is needed. Hence, the MTC algorithm improves the topology of the elements by raising the shape factor of the elements that define this topology.

The definition of the metric field leads to a non-uniform, anisotropic mesh, which is refined close to the grain boundaries. The metric **M** is a tensor whose eigenvalues and eigenvectors define the transformation of an isotropic mesh of size h into an anisotropic mesh with a directional dependence of h. This can be illustrated with a simple configuration of two grains separated by one interface. The direction of mesh refinement is the normal to the interface. To specify the mesh size in that direction, as well as the evolution of mesh size in space, a characteristic length l_0 is introduced. When the distance function is smaller than l_0, the corresponding mesh is considered to be "close" to the interface :

$$\begin{cases} |\phi(\mathbf{x})| > l_0 & \text{far from the interface} \\ |\phi(\mathbf{x})| < l_0 & \text{near the interface} \end{cases} .$$

(6)

The mesh size takes a default value far from the interface, and is reduced in the direction perpendicular to the interface when $|\phi|$ is reduced. For example, the mesh size h may be chosen as

$$\begin{cases} |\phi(\mathbf{x})| > l_0 & \Rightarrow \quad h = h_d \\ |\phi(\mathbf{x})| < l_0 & \Rightarrow h = \dfrac{h_d(m-1)}{ml_0}|\phi(\mathbf{x})| + \dfrac{h_d}{m} \end{cases} .$$

(7)

At the interface the mesh size is reduced by a factor m with respect to the default value h_d. This mesh size then increases steadily to reach the default value h_d at the distance l_0. Such variations in mesh size are directly implemented by varying the corresponding metric **M**.

When dealing with polycrystalline aggregates and multiple interfaces, the above strategy is repeated for each grain. For the nodes at which

$$|\phi_i(\mathbf{x})| > l_0, \ \ 1 \le i \le N_G, \tag{8}$$

there is no direction of refinement, and the mesh is isotropic with $h = h_d$. On the contrary, there may be several directions of refinement when there is more than one level set function for which $|\phi_i(\mathbf{x})| < l_0$, and when the corresponding normal directions $\mathbf{n}_i$ calculated from (3), are not co-linear. These independent vectors are the eigenvectors of the metric defined in (4). For each vector direction the eigenvalue is calculated from the mesh size prescribed in (7), with $\phi(\mathbf{x})$ being the level set function associated to the considered normal. At triple or multiple junctions, the refinement may therefore become isotropic.

Figure 4 illustrates the method which has been applied to a digital microstructure made of one thousand grains. The mesh (2 125 688 nodes, 12 385 889 elements) was obtained after a 26 hours parallel computation on 24 processors of a 98 cores Opteron 280 2,4GHz linux cluster. The refinement of the mesh may become significant when approaching grain boundaries, as already observed in Figure 3 (see enlarged section). In the direction normal to the interface, the length scale is one at which mechanical behaviour may be influenced by the discrete nature of dislocation motion. Nevertheless, traditional crystal plasticity theory is used here (Section 5), thus neglecting some stress concentrators and their potential effect on recrystallisation. Even is this simplified situation, the stored energy field induced by plastic deformation is particularly heterogeneous at the grain boundaries. Besides, strong refinement is needed for the modelling of grain boundary motion in the recrystallization regime. Indeed, in the level set approach (Section 3), the accuracy of the geometric properties of the boundaries, defined by Equations (3), is a direct consequence of the mesh size (see more details in Section 6.1).

5. Digital mechanical testing under large deformations

Mechanical testing is performed using finite element simulations where each integration point of the mesh behaves as a single crystal subjected to finite strain increments. The finite element approach is based on a mixed velocity-pressure formulation with an enhanced (P1+/P1) 4-node tetrahedral element [32]. Classical theory of crystal plasticity [33-36] is

considered, using a slightly modified version of the time integration algorithm developed by Delannay et al. [37]. For computational efficiency, one computes rates of lattice rotation and rates of dislocation slip in a decoupled way.

5.1 Elastic-viscoplastic crystal constitutive law

The main equations described in [37] are briefly recalled. The elastic-viscoplastic formulation is based on a multiplicative decomposition of the deformation gradient tensor, $\mathbf{F} = \mathbf{R}^*\mathbf{U}^{el}\mathbf{F}^p$, where $\mathbf{R}^*$, $\mathbf{U}^{el}$ and $\mathbf{F}^p$ represent, respectively, the rotation of the crystal lattice, the elastic stretch and the deformation by dislocation slip. Under the assumption of infinitesimal elastic strains, i.e. $\mathbf{U}^{el} = \mathbf{I} + \boldsymbol{\varepsilon}^{el}$ where $\boldsymbol{\varepsilon}^{el}$ is symmetric and $\|\boldsymbol{\varepsilon}^{el}\| \ll 1$, the velocity gradient tensor $\mathbf{L} = \nabla\mathbf{v}$ is closely approximated by:

$$\mathbf{L} \cong \dot{\mathbf{R}}^*\mathbf{R}^{*T} + \mathbf{R}^*\left(\dot{\boldsymbol{\varepsilon}}^{el} + \sum_{\alpha}\mathbf{M}^{\alpha}\dot{\gamma}^{\alpha}\right)\mathbf{R}^{*T},$$ (9)

where $\mathbf{M}^{\alpha}$ is the Schmid tensor of slip system α and $\dot{\gamma}^{\alpha}$ the corresponding rate of dislocation slip. Denoting C the anisotropic, fourth-order, elasticity operator, one derives the Cauchy stress tensor $\boldsymbol{\sigma}$ from:

$$\boldsymbol{\sigma} = \mathbf{R}^*\mathbf{T}\mathbf{R}^{*T} \qquad \text{and} \qquad \dot{\mathbf{T}} = \mathbf{C}\dot{\boldsymbol{\varepsilon}}^{el}.$$ (10)

In order to avoid ambiguity in determining the slip rates [38], the viscoplastic expression introduced by [39] is adopted :

$$\dot{\gamma}^{\alpha} = \dot{\gamma}_0\left|\frac{\tau^{\alpha}}{\tau_c}\right|^{1/m} sign(\tau^{\alpha}) \qquad ,$$ (11)

$$\text{with} \qquad \tau^{\alpha} = \mathbf{T}:\mathbf{M}^{\alpha} \quad ,$$ (12)

$$\tau_c = \tau_{c0}\left(1 + \frac{\Gamma_{tot}}{\Gamma_0}\right)^n,$$ (13)

$$\Gamma_{tot} = \int_0^t \sum_{\alpha}\left|\dot{\gamma}^{\alpha}\right|dt.$$ (14)

In (11), $\dot{\gamma}_0$ is a reference slip rate, m the sensitivity exponent, and τ_c the critical resolved shear stress, which evolves with strain according to the hardening law (13), τ_{c0}, Γ_0 and n being material parameters.

5.2 Time integration of the constitutive law in the finite element model

Details of the finite element formulation are available elsewhere [40,32], only the main features are recalled here. The updated Lagrangian scheme is based on a mixed velocity-pressure formulation with an enhanced (P1+/P1) 4-node tetrahedral element. The non linear discretized finite element system is solved within a Newton-Raphson scheme using a preconditioned conjugate residual approach. Unilateral contact with the 'tools' (forming processes context) is treated with a penalty method. In the present study, the average deformation of the digital microstructure, constituting a volume element Ω, is controlled by prescribing the velocity of all nodes lying on the outer boundary Σ of Ω:

$$\mathbf{v} = \overline{\mathbf{L}}\,\mathbf{x}, \tag{15}$$

where $\mathbf{x}$ represent the node coordinates at time t, and $\mathbf{v}$ the velocity that is prescribed.

The principle of virtual work is applied in the deformed configuration Ω at time t. Appropriate conditions are prescribed at the boundary Σ (see above). If $\widetilde{\mathbf{v}}$ denotes a kinematically admissible (virtual) velocity field and $\widetilde{p}$ a virtual pressure field, one writes:

$$\forall\,\widetilde{\mathbf{v}},\ \int_{\Omega}\left(\boldsymbol{\sigma}':\nabla\widetilde{\mathbf{v}}\right)d\Omega - \int_{\Omega}p\left(\nabla\cdot\widetilde{\mathbf{v}}\right)d\Omega - \int_{\Sigma}\left(\mathbf{t}\cdot\widetilde{\mathbf{v}}\right)d\Sigma = 0 \qquad, \tag{16}$$

$$\forall\,\widetilde{p},\ \int_{\Omega}\widetilde{p}\left(\nabla\cdot\mathbf{v} + \frac{\dot{p}}{K}\right)d\Omega = 0\ , \tag{17}$$

where $\boldsymbol{\sigma}$' is the deviatoric part of the Cauchy stress $\boldsymbol{\sigma}$, $p = $ -$tr(\boldsymbol{\sigma})/3$ is the pressure, K the (elastic) bulk modulus, and $\mathbf{t}$ the tension applied to the boundary. While (16) and (17) are solved at time t, $\boldsymbol{\sigma}$ is evaluated at time $t + \Delta t$ [40], and obtained by implicit time integration of Eqs. 9-14, using :

$$\boldsymbol{\sigma}_{t+\Delta t} = \mathbf{R}^{*}\Big|_{t+\Delta t}\left(\mathbf{T}\Big|_{t} + \dot{\mathbf{T}}\Big|_{t+\Delta t}\Delta t\right)\mathbf{R}^{*T}\Big|_{t+\Delta t}. \tag{18}$$

The Newton-Raphson procedure used to solve the finite element problem relies on an algorithmic tangent operator as detailed in [37]. Once a converged velocity field $\mathbf{v}$ is obtained at time t, the geometry of the mesh is updated for the next time increment according to : $\mathbf{x}\big|_{t+\Delta t} = \mathbf{x}\big|_{t} + \mathbf{v}\Delta t$ [40].

5.3 Test case

The objective of the test case is to analyze the spatial distribution of stored strain energy in a digital aggregate, subjected to large deformations. A channel die test has been chosen, and is illustrated in Figure 5.

The digital microstructure is made of $N_G = 50$ grains. Slip is assumed to operate on the 12 {111}<110> slip systems as is typically considered in FCC crystals at room temperature. A 35% reduction in height is applied, and the stored energy is computed from :

$$E = \delta \int \boldsymbol{\sigma} : \nabla \mathbf{v}\, dt , \tag{24}$$

where δ defines the fraction of the strain energy which is stored in the material, i.e. not dissipated into heat. More accurate measures of stored energy could be implemented in the future, by relying on the dislocation density computed within the crystal plasticity approach, e.g. [21,22]. Another simple approach would consist in describing both τ_c (see Equation (13)) and E as a function of the dislocation density ρ [41] :

$$\tau_c = \tau_{c0} + \frac{1}{2} G b \sqrt{\rho} , \tag{25}$$

$$E = \frac{1}{2} \rho G b^2 \quad , \tag{26}$$

where G is the shear modulus of the material. Combining (25) and (26) leads to

$$E = \frac{2}{G} \left(\tau_c - \tau_{c0} \right)^2 . \tag{27}$$

The absolute values of E do not always matter, e.g. only the relative values will play a role in determining the topological evolution of the grain boundary network (see the next section). In those cases, the exact values of G and δ in (27) and (24) do not need to be known.

Figure 6 shows the 3D distribution of the stored energy E, and of the gradient of the stored energy grad(E). The highest values of E and grad(E) usually appear at grain boundaries. The latter are identified by the zero level of the $\{\phi_i, 1 \leq i \leq N_G\}$ functions, as defined in expression (1). One can also notice significant intergranular and intragranular variations of E, which result in maxima of grad(E) mainly at grain boundaries, but also inside some grains. Inversely, most grain boundaries correspond to maxima of grad(E), but not all of them.

These distributions are the consequence of (a) local crystallographic orientations and (b) grain interactions, i.e. neighbourhood effects. They can be used as an input for the modelling of primary recrystallization, keeping in mind that traditional continuum crystal plasticity obviously needs to be enriched, e.g. if nuclei positions are to be predicted. Constitutive models developed at lower scales or considering Geometrically Necessary Dislocations (GNDs) would be required to better reproduce local features (shear bands, twin bands, dislocation pile ups, etc.) at the origin of nucleation events. This work is only a first step in that direction.

6. Digital heat treatment leading to recrystallization

In this section grain boundary motion is modelled using the level set framework described in Section 3. Motion is assumed to be due to the difference in stored energy on either side of the interface, as is the case in primary recrystallization, or when Strain Induced Grain Boundary Migration (SIBM) occurs. When dealing with primary recrystallization, nucleation of new grains need to be modelled as well. Nuclei grow spontaneously since we assume that they have zero stored energy. Position and time of appearance of each new nucleus can be based on different criteria. Let us assume, for simplicity, that they appear in regions with high stored energy, or high gradients of stored energy [42]. A positioning criterion based on local crystallographic misorientations could be defined as well [43], since a nucleus will only grow if the mobility of the associated grain boundaries is high enough. This is usually true for

misorientations larger than 10-15°. Time of appearance of a nucleus is often described by a probability law [44], unless site-saturated conditions are assumed. In the latter case all potential nuclei grow from $t = 0$, i.e. there is no incubation time.

In the simulations described below (Section 6.3), 1000 positions of nuclei are either selected at random or correspond to regions with the highest gradients of stored energy ||grad(E)||. The probability of appearance at each time increment is constant and relatively low ($2 \cdot 10^{-4}$). Grain boundary motion is related to the difference in stored energy E across the boundary. For that purpose only (and *not* for the positioning of the nuclei), a constant value of E is considered in each grain.

6.1 Kinetic law for grain boundary motion

Grain boundary motion is related to a driving force per unit area Δf, and the corresponding velocity ξ defined in (2) is assumed to follow the kinetic relation [42] :

$$\xi = m \Delta f \, \mathbf{n} \qquad , \tag{28}$$

where m corresponds to the grain boundary mobility, and $\mathbf{n}$ to the outside unit normal to the boundary. The mobility is very often written as

$$m = m_0 \exp(Q/RT) \qquad , \tag{29}$$

and it is sensitive to the impurity (solute atom) content in the metal, as well as to the crystallographic nature of the boundary. The driving force is defined by

$$\Delta f = \Delta E - \gamma \kappa, \tag{30}$$

where ΔE is the stored energy difference across the boundary (e.g. according to (24) or (27)), γ the boundary energy, and κ the boundary curvature. It is assumed that the material is highly deformed before it undergoes primary recrystallization. The second term of equation (30), related to the grain boundary energy, is therefore neglected compared to the first term, related to stored strain energy.

Interface motion using level set methods is now of common use [12]. However, in most cases, a single interface is captured, separating only two regions. In [15], the authors have extended the method to the case of multiple junctions, and simulated 2D grain growth due to grain boundary energy only. Each region has its own private level set function, and local normal velocities are defined by the nearest interface. A reassignment step is used to avoid the development of voids and overlapping regions. In a subsequent paper [5], the authors propose to add a constraint to the overall problem which imposes that the addition of all individual surfaces must correspond to the total surface of the domain.

In the present study a new formulation is used, in which (a) bulk stored energies can be taken into account, and (b) the development of voids and overlapping regions is avoided. Individual level set functions are defined for each region, as apparent in (2), and re-initialization steps [12] are periodically performed for each of them as they evolve according to the convection equation [45].

To prevent the development of overlapping regions and/or voids, all meeting interfaces described by distinct level set functions must be assigned the same velocity, i.e. the zero level of the $\phi_i(\mathbf{x})$ functions have to match perfectly. Consequently, the normal $\mathbf{n}$ (and also the curvature κ if considered) to the interface must be computed very accurately from (3), for all $\phi_i(\mathbf{x})$ functions. This in turn requires that the mesh is strongly refined *locally*, close to the interfaces, compared to the bulk of the grains. To avoid the explosion of computational effort, the construction of an anisotropic mesh is required, with the methods discussed in Section 4.

The common velocity at triple or multiple junctions is of particular interest and must be defined according to the kinetic law (28) which only considers a single interface. Figure 7 shows that the direct use of (28) leads to discontinuities of the velocity field at triple junctions, which in turn leads to the development of overlapping regions and/or voids. A smoothing technique is therefore applied (Figure 8), which consists in using the following algorithm :

$$\mathbf{x} \in G_i \Leftrightarrow \phi_i(t, \mathbf{x}) = \max_{1 \le p \le N_G} \left(\phi_p(t, \mathbf{x}) \right)$$

$$\Rightarrow \xi(t, \mathbf{x}) = \sum_{\substack{j=1 \\ j \ne i}}^{N_G} \exp\left(-\eta \left| \phi_j(t, \mathbf{x}) \right| \right) m_{ij} \left(E_i - E_j \right) \mathbf{n}_j(t, \mathbf{x}) \qquad , \qquad (31)$$

where G_i designates the grain of index i, $\forall i \in \{1, ..., N_G\}$, η a positive fixed parameter calibrated to obtain a negligible exponential term outside the anisotropic part of the mesh, m_{ij} the mobility defined in (29) assuming an interface between grains G_i and G_j, and $\mathbf{n}_j$ the outward unit normal at $\mathbf{x}$, calculated from (3) using $\phi = \phi_j(t, \mathbf{x})$. In Figure 8 it is observed that the smoothing technique is not sufficient by itself, it needs to be combined with anisotropic meshing to improve accuracy. The approach is validated in 2D in [45] by comparison with an exact solution of the triple junction problem [46], and when using anisotropic automatic remeshing every few increments. Figure 9 shows that, except for the computational efforts, no specific development is required to extend the above approach in 3D. Finally, Figure 10 illustrates a more complex microstructure evolution in 2D, where grains with the highest E disappear due to the growth of neighbouring grains.

6.2 Nucleation of new grains

Figure 10 has shown that when using front capturing methods for describing interface motion, there is no specific treatment to be used when some regions (grains) disappear. Complex topological evolutions are handled automatically. In a similar way, it is possible to introduce new regions (grains), based on given criteria, which can be based on mechanics, crystallography, etc. Hence, new grains can nucleate during primary recrystallization, with an assumed low (often zero) stored energy. Each of these new grains is described by a new level set function, which evolves subsequently according to the principles described in Section 6.1. A simple way to implement nucleation consists in building a new level set function at a specific time increment and a desired spatial position. For example, the new distance function can be chosen such that the boundary of the nucleus is spherical (3D) or circular (2D), centred around one node of the mesh.

An illustration of this procedure is given in Figure 11, where nucleation has been numerically triggered at the node closest to the triple junction. Spontaneous growth is observed due to the difference in stored energy between the nucleus ($E = 0$) and the surrounding grains.

6.3 Test case

This application considers the channel die test performed on the digital aggregate described in Section 5.3. A 2D section is extracted from the 3D volume shown in Figure 6, leaving us with 24 grains with non uniform stored energy E (see Figure 12) and stored energy gradient grad(E).

The considered digital experiments consist in following the evolution of the recrystallized volume fraction X as a function of time t, for different nucleation criteria, and kinetic relations. Five experiments are considered : (A) all 1000 nuclei start growing from $t = 0$ (site-saturated conditions) with random positions and a uniform constant velocity, (B) nuclei appear with Low Probability in Time (LPT), i.e. $2 \cdot 10^{-4}$, at random positions, and they grow with a uniform, constant velocity, (C) nuclei appear with LPT at random positions, but they grow according to the kinetic relation (28), (D) nuclei appear in LPT and only at the grain boundaries, growth follows (28), (E) nuclei appear in LPT and only at the maxima of grad(E), growth follows (28).

To compare the results of these experiments, reference is made to the JMAK theory [47-49] predicting the recrystallized fraction X as a function of the annealing time t :

$$X = 1 - \exp(-\beta t^n) \quad . \tag{32}$$

In this equation β and n are constant, and n is referred to as the JMAK exponent. Assuming a two-dimensional growth, the JMAK theory predicts $n = 2$ for site-saturated conditions, and $n = 3$ for a low constant nucleation rate. Deviations from these n values and from the linear JMAK kinetics have often been observed experimentally, e.g. [50,51]. A linear kinetics refers to a constant value of n, i.e. a linear JMAK plot displaying $\ln\left[-\ln(1 - X)\right]$ as a function of $\ln(t)$. In experiments (A) to (E), a least-square regression analysis on the numerical data is performed, providing values of n.

Experiments (A) and (B) provide very accurate linear JMAK plots with values of $n = 2$ and 3, respectively. This validates the digital experiment set up. Figures 13 and 14 then show the results of experiments (C), (D) and (E). In each

experiment, a single value of n does not allow fitting the numerical results with sufficient accuracy. It can be noticed that the non uniform stored energy in the aggregate is only responsible for a small deviation from a linear JMAK plot (case C), while the spatial positioning of the nuclei leads to stronger deviations (cases D and E). These results must be placed in the context of repeated discussions in the literature on the reasons of deviations from linear JMAK plots, where several reasons for such deviations have been put forward : heterogeneous distribution of stored energy [50,52], competition between recovery and recrystallization [51,53], anisotropic growth [54,55] due to anisotropic values of mobility m as a function of the crystallographic nature of boundaries, spatial and time distribution of nuclei [55,52]. The present framework has the capability of systematically investigating all these effects, which are expected to have different relative contributions to the overall recrystallization kinetics, depending on the type of material. For example, the heterogeneity of stored energy is expected to increase for metals with hexagonal compact (hcp) lattice, compared to those with cubic crystal symmetries. Experiment C for hcp metals might therefore lead to much stronger deviations from a linear kinetics than the one observed in Figure 14, which is only applicable to FCC metals.

7. Conclusions

In this paper, the use of digital microstructures is illustrated and first numerical developments and results are described. Conversion of digital formats into finite element meshes is facilitated by the use of a level set description of interfaces. Automatic meshing and remeshing operations rely on the values of level set functions, both for spatial localization of the interfaces and for the definition of appropriate metrics for anisotropic mesh generation. The positioning of the interfaces is updated when large plastic strain of the polycrystalline aggregate occurs, even when using automatic remeshing. Computation of the stored energy field within the aggregate, using crystal plasticity based constitutive laws, is the starting point for the subsequent modelling of primary recrystallization using a level set framework. The grain boundary network evolves directly, superposed on the mesh inherited from the digital mechanical testing. The kinetic law is based on the difference in stored strain energy across the interfaces. A special smoothing algorithm is applied to the calculated velocity field, which allows maintaining geometrical compatibility between the different grains, when combined with periodic automatic (anisotropic) remeshing. Nucleation events can be accurately triggered based on

defined criteria, using data calculated during mechanical testing. Overall, the model is able to account for various effects related to microstructure topology, crystallographic features, and mechanical quantities, such that it can be used to decide which mechanisms are the most relevant with respect to experimental data. The selection of the most relevant mechanisms can then be used to develop homogenized, computationally cheaper models, appropriate to a defined material category.

Future work will include more realistic computations of stored energy for specific materials, and the extension of the recrystallization model to 3D aggregates using a statistical number of grains. This will lead to detailed comparisons with experiments, and with other types of model (e.g. Monte Carlo, or phase field models). The proposed approach for describing primary recrystallization could also be extended to grain growth, taking into account grain boundary energy and curvature.

References

[1]   M.A. Miodownik, *A review of microstructural computer models used to simulate grain growth and recrystallisation in aluminium alloys*, J. Light Metals 2 (2002), 125-135.
[2]   A.D. Rollett and D. Raabe, *A hybrid model for mesoscopic simulation of recrystallization*, Comp. Mat. Sc. 21 (2001), 69-78.
[3]   D. Raabe, *Introduction of a scaleable 3D cellular automaton with a probabilistic switching rule for the discrete mesoscale simulation of recrystallization phenomena* , Phil. Mag A79 (1999), 2339–2358.
[4]   L.Q. Chen, *A novel computer simulation technique for modeling grain growth*, Scripta Metall. Mater. 32 (1995), 115-120.
[5]   H.-K. Zhao, T. Chan, B. Merriman and S. Osher, *A variational level set approach to multiphase motion*, J. Computational Physics 127 (1996), 179-195.
[6]   G.N. Hassold and E.A. Holm, *A fast serial algorithm for the finite temperature quenched Potts model*, Comput. Phys. 7 (1993), 97-107.

[7]   A.D., Rollett, *Overview of modeling and simulation of recrystallization*, Progress in Mat. Sci. 42 (1997), 79-99.

[8]   J.B. Collins and H. Levine, *Diffuse interface model of diffusion-limited crystal growth*, Phys. Rev. B31 (1985), 6119-6122.

[9]   L.Q. Chen, *Phase-field models for microstructure evolution*, Ann. Rev. Mater. Res. 32 (2002), 113-140.

[10]   A. Karma, *Phase-field formulation for quantitative modelling of alloy solidification*, Phys. Rev. Letters 8711 (2001), art. no. 115701.

[11]   C.E. Krill, L.Q. Chen, *Computer simulation of 3-D grain growth using a phase-field model*, Acta Mater. 50 (2002), 3057-3073.

[12]   J.A. Sethian, Level Set methods, Cambridge University Press, 1996.

[13]   S. Osher and J.A. Sethian, *Fronts propagating with curvature-dependent speed: Algorithms based on Hamilton-Jacobi formulations*, J. Comp. Phys. 79 (1988), 12-49.

[14]   M. Sussman, *A Level Set Approach for Computing Solutions to Incompressible Two-Phase Flow*, J. Comp. Phys. 114 (1994), 146-159.

[15]   B. Merriman, J. Bence and S.J. Osher, *Motion of Multiple Junctions: A Level Set Approach*, J. Comp. Phys. 112 (1994), 334-363.

[16]   R.E. Logé, Y.B. Chastel, *Coupling the thermal and mechanical fields to metallurgical evolutions within a finite element description of a forming process*, Computer Methods in Applied Mechanics and Engineering 195 (2006), 6843-6857.

[17]   P.R. Dawson, *Computational crystal plasticity*, Int. J. Solids Struct. 37 (2000), 115-130.

[18]   P.R. Dawson, M.P. Miller, T.-S. Han, J. Bernier, *An Accelerated Methodology for the Evaluation of Critical Properties in Polyphase Alloys*, Metall. Mater. Trans. A 36 (2005), 1627-1641.

[19]   D. Raabe and R.C. Decker, *Coupling of a crystal plasticity finite element model with a probabilistic cellular automaton for simulating primary static recrystallization in aluminium*, Model. Simul. Mater. Sci. Eng. 8 (2000), 445-462.

[20]   Ph. Erieau, *Etude expérimentale et analyse numérique de l'influence des hétérogénéités induites par la déformation à froid sur la recristallisation primaire d'un acier IF-Ti*, PhD thesis, Ecole Centrale de Paris, Chatenay Malabry (2003).

[21]   Ph. Erieau and C. Rey, *Modeling of deformation and rotation bands and of deformation induced grain boundaries in IF steel aggregate during large plane strain compression*, Int. J. Plasticity 20 (2004), 1763-1788.

[22]   T. Baudin, A.L. Etter, Ph. Gerber, A. Samet, R. Penelle and C. Rey, *Influence of thermo-mechanical treatments on the stored energy simulated by FEM for two low carbon steels*, Materials Science Forum 495-497 (2005), Pt. 2, 1291-1296.

[23]   P. Volovitch, F. Caleyo, T. Baudin, Ph. Gerber, R. Penelle and C. Rey, *Monte Carlo modeling of low carbon steel recrystallization: role of thermo-mechanical treatment and chemical composition*, Materials Science Forum 495-497 (2005), Pt. 1, 507-512.

[24]   M. Béringhier, R. Logé, L. Delannay and Y. Chastel, *Strategies of transport of microstructural variables for remeshing – application to texture induced mechanical anisotropy in metals*, Computer Methods in Materials Science 6 (2006), 133-139.

[25]   M. Béringhier, L. Delannay, Y. Chastel and R. Logé, *Using Lagrangian particles to efficiently describe microstructure evolution in metal forming – application to texture-induced mechanical anisotropy*, Modelling Simul. Mater. Sci. Eng. 15 (2007), 191-204.

[26]   M. Bernacki, Y. Chastel, H. Digonnet, H. Resk, T. Coupez and R.E. Logé, *Development of numerical tools for the multiscale modelling of recrystallization in metals, based on a digital material framework*, Computer Methods in Materials Science 7 (2007), 142-149.

[27]   D. Weygand, Y. Brechet and J. Lepinoux, *A vertex simulation of grain growth in 2D and 3D*, Adv. Engng. Mater. 3 (2001), 67-71.

[28]   D. Peng, B. Merriman, S. Osher, H. Zhao, M. Kang, *A PDE-Based Fast Local Level Set Method*, J. Comp. Phys. 155 (1999), 410-438.

[29]   A. Brahme, M.H. Alvi, D. Saylor, J. Fridy and A.D. Rollett, *3D reconstruction of microstructure in a commercial purity aluminum*, Scripta Materialia 55 (2006), 75-80.

[30]   T. Coupez, *Génération et Adaptation de maillage par optimisation locale*, La Revue Européenne des éléments finis 9 (2000), 403-423.

[31]   T. Coupez, H. Digonnet, R. Ducloux, *Parallel meshing and remeshing by repartitioning*, Appl. Math. Modeling 25 (2000), 153-175.

[32]   K. Mocellin, L. Fourment, T. Coupez and J.-L. Chenot, *Toward large scale F.E. computation of hot forging process using iterative solvers, parallel computation and multigrid algorithms*, Int. J. for Num. Meth. in Engineering 2 (2001), 473-488.

[33]   R.J. Asaro and A. Needleman, *Texture development and strain hardening in rate dependent polycrystals*, Acta Metall. 33 (1985), 923-953.

[34]   S.R. Kalidindi, C.A. Bronkhorst and L. Anand, *Crystallographic texture evolution in bulk deformation processing of FCC metals*, J. Mech. Phys. Solids 40 (1992), 537-569.

[35]   A.J. Beaudoin, P.R. Dawson, K.K. Mathur and U.F. Kocks, *A hybrid finite element formulation for polycrystal plasticity with consideration of macrostructural and microstructural linking*, Int. J. Plasticity 11 (1995), 501-521.

[36]   E.B. Marin and P.R. Dawson, *On modeling the elastic-plastic response of polycrystalline materials*, Comput. Meth. Appl. Mech. Eng. 132 (1998), 1-21.

[37]   L. Delannay, P.J. Jacques and S.R. Kalidindi, *Finite element modeling of crystal plasticity with grains shaped as truncated octahedrons*, Int. J. Plasticity 22 (2006), 1879-1898.

[38]   P. Van Houtte, *A comprehensive mathematical formulation of an extended Taylor-Bishop-Hill model featuring relaxed constraints, the Renouard-Wintenberger theory and a strain rate sensitivity model*, Textures microstr. 8-9 (1988), 313-350.

[39]   J.W. Hutchinson, *Creep and plasticity of hexagonal polycrystals as related to single crystal slip*, Metall. Trans. A8 (1969), 1465-1469.

[40]   J.-L. Chenot, L. Fourment, K. Mocellin, *Numerical treatment of contact and friction in FE simulation of forming processes*, J. Mater. Process. Technol. 125-126 (2002), 45-52.

[41]   G.B. Sarma, B. Radhakrishnan and T. Zacharia, *Finite element simulations of cold deformation at the mesoscale*, Computational Materials Science 12 (1998), 105-123.

[42]   F.J. Humphreys, M. Hatherly, Recrystallization and Related Annealing Phenomena, Pergamon 2nd edition (2004).

[43]   T. Takaki, A. Yamanaka, Y. Higa, Y. Tomita, *Phase-field model during static recrystallization based on crystal-plasticity theory*, J. Computer-Aided Materials Design 14 (2007), 75-84.

[44]   G. Kugler, R. Turk, *Study of the influence of initial microstructure topology on the kinetics of static recrystallization using a cellular automata model*, Comput. Mater. Sci. 37 (2006), 284-291.

[45]   M. Bernacki, Y. Chastel, T. Coupez, R.E. Logé, *Level set framework for the numerical modelling of primary recrystallization in polycrystalline materials*, Scripta Materialia 58 (2008), 1129–1132.

[46]   F. Reitich, H.M. Soner, *Three-phase boundary motions under constant velocities. I: The vanishing surface tension limit*, Proc. Roy. Soc. Edinburgh 126A (1996), 837-865.

[47]   W.A. Johnson, R.F. Mehl, Trans. Am. Inst. Min. Eng. 135 (1939), 416.

[48]   M. Avrami, J. Chem. Phys. 7 (1939), 1103.

[49]   A.B. Kolmogorov, Akad. Nauk SSSR, Izv. Ser. Mater. 1 (1937), 355.

[50]   M. Oyarzabal, A. Matrinez-de-Guerenu, I. Gutierrez, *Effect of stored energy and recovery on the overall recrystallization kinetics of a cold rolled low carbon steel*, Mater. Sci. Eng. A 485 (2008), 200-209.

[51]   C.W. Price, *Comments on the extent of simultaneous recovery during recrystallization and its effect on recrystallization kinetics*, Scripta Metallurgica 23 (1989), 1273-1276.

[52]   G.J. Liao, R. Le Gall, G. Saindrenan, Experimental investigations into kinetics of recrystallisation of cold rolled nickel, Mater. Sci. Technology 14 (1998), 411-416.

[53]   H.P. Stüwe, A.F. Padilha, F. Siciliano Jr., *Competition between recovery and recrystallization*, Mater. Sci. Eng. A 333 (2002), 361-367.

[54]   Y.A. Andrienko, N.V. Brilliantov, P.L. Krapivsky, Phys. Rev. A 45 (1992), 2263.

[55]   F. Liu, G. Yang, *Effects of anisotropic growth on the deviations from Johnson-Mehl-Avrami kinetics*, Acta Materialia 55 (2007), 1629-1639.
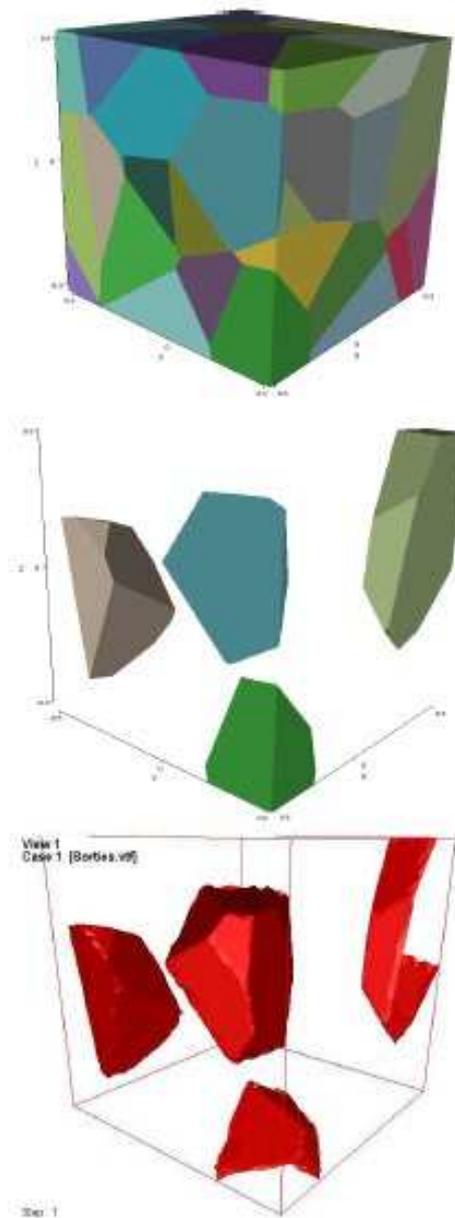
Figure 1 : A 50 grains virtual microstructure generated with the DigiMicro software (see [26]), with four particular grains represented underneath, and the zero levels of the corresponding level set functions shown in red.
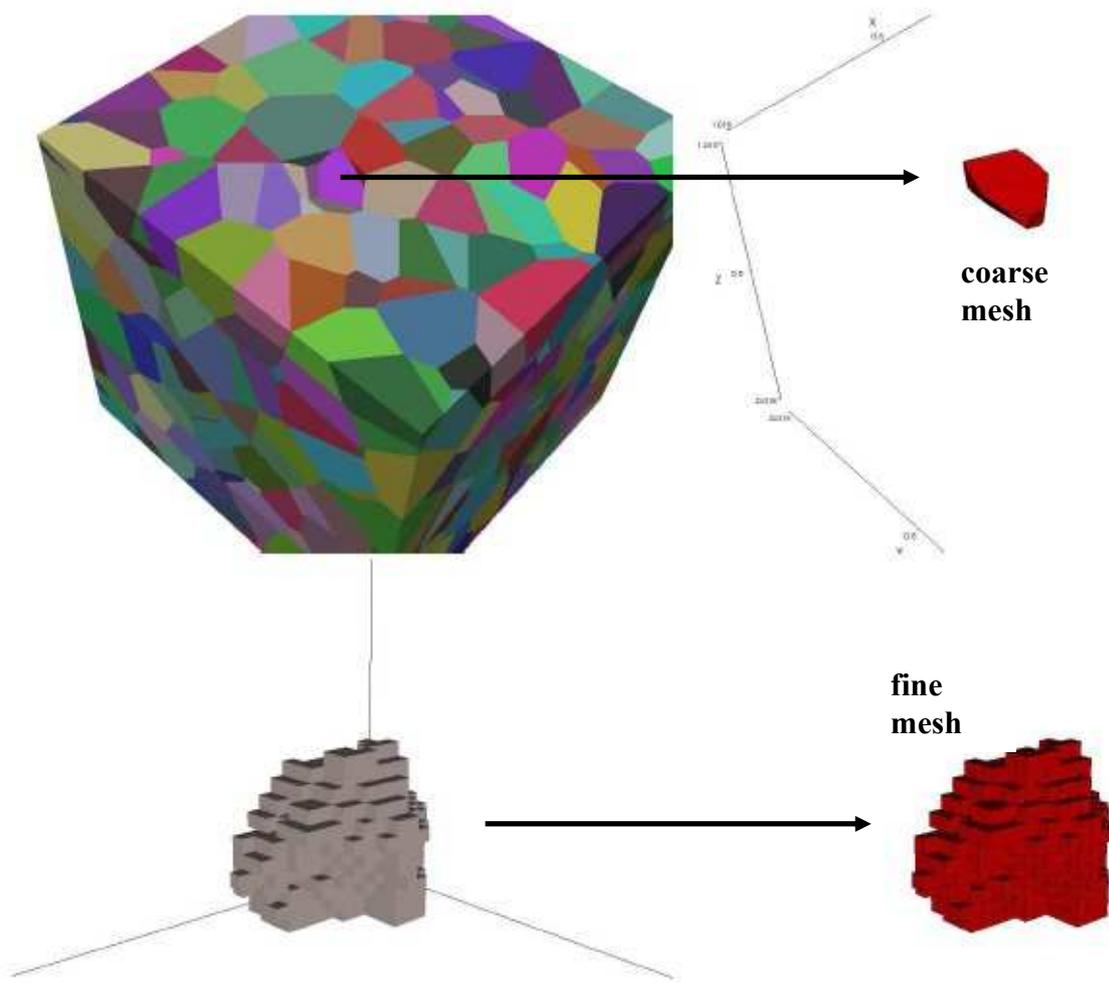
Figure 2 : Conversion of a digital sample into an initial finite element mesh, starting from a Voronoï tessellation (top) or a voxel representation (bottom).
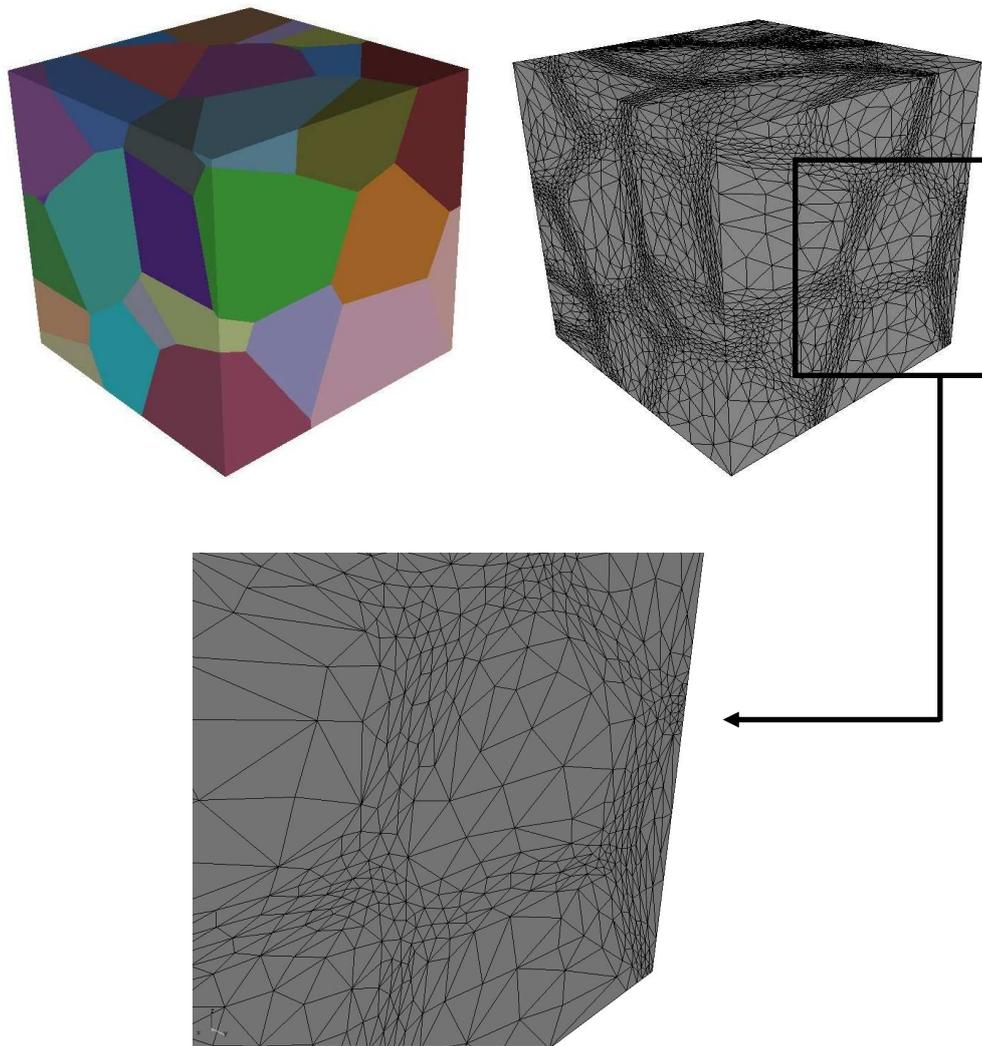
Figure 3 : A 50 grains microstructure and the corresponding finite element mesh (68 631 nodes, 385 494 elements). Anisotropic refining of the mesh is done close to the boundaries according to the $\{\phi_i, 1 \le i \le 50\}$ distance functions, as detailed in the enlarged section (bottom).
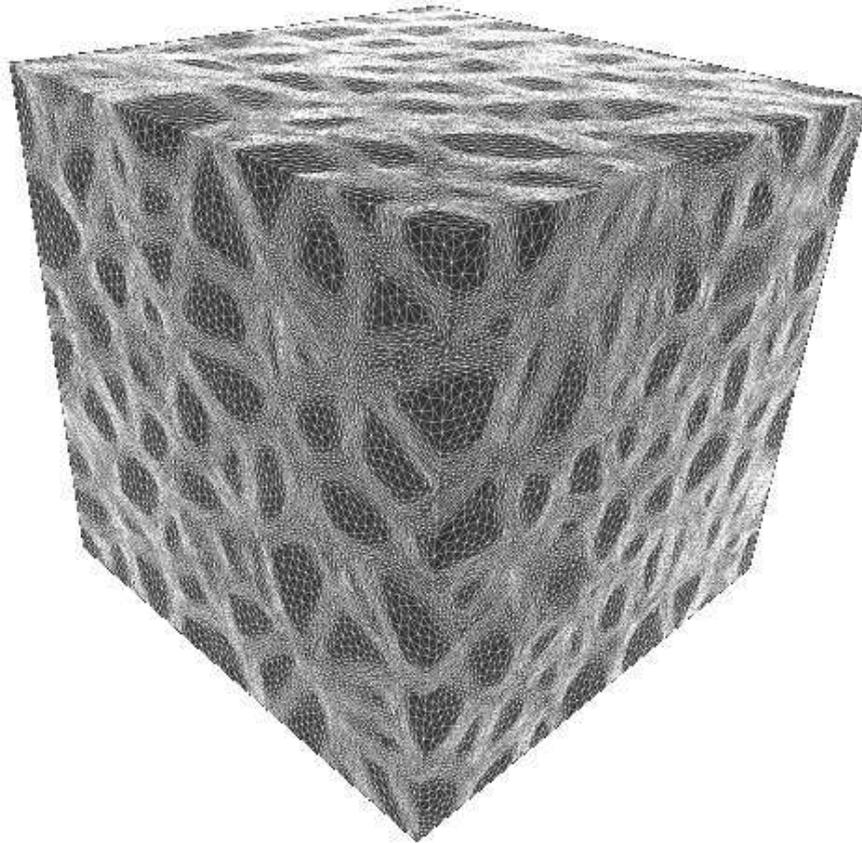
Figure 4 : Anisotropic mesh constructed from a digital microstructure made of 1000 grains
(2 125 688 nodes, 12 385 889 elements)
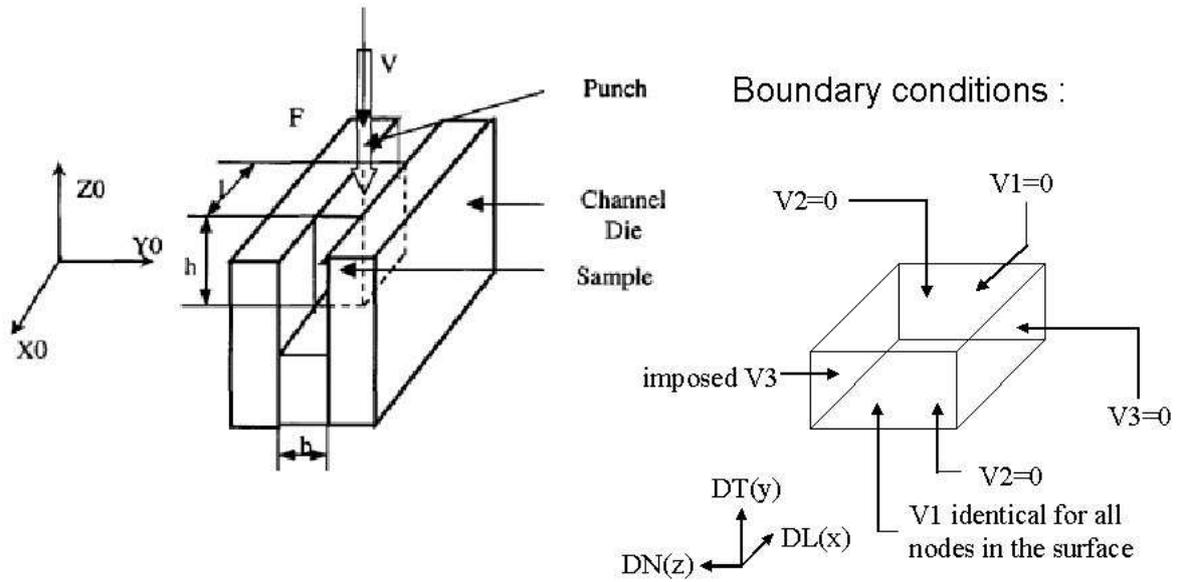
Figure 5 : Channel die test configuration and definition of boundary conditions
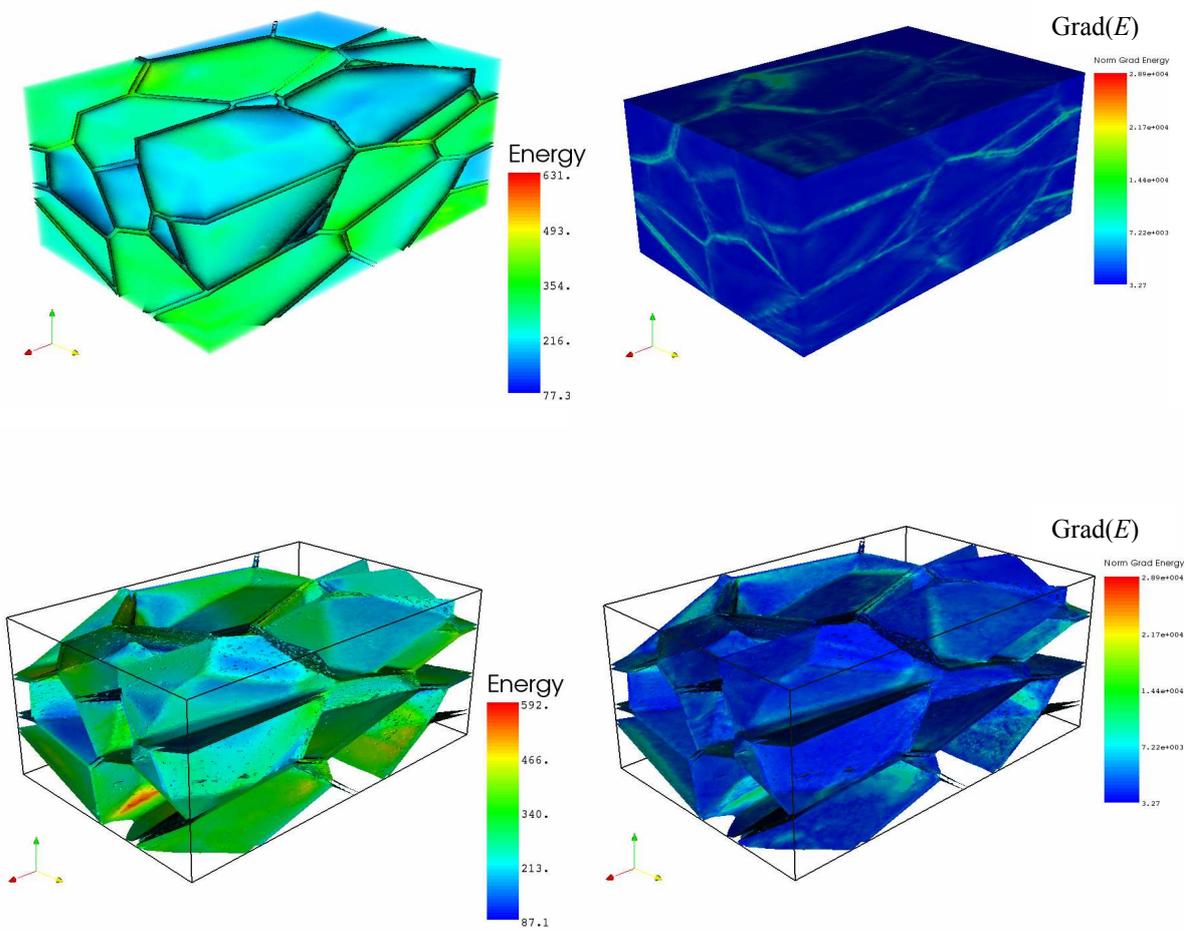
Figure 6 : Distribution of the stored energy E (left) and of the gradient of the stored energy grad(E) (right). Illustrations include the external surfaces of the 3D volume element (top) and internal grain boundaries identified as the zero level of the $\{\phi_i, 1 \leq i \leq N_G\}$ functions (bottom).
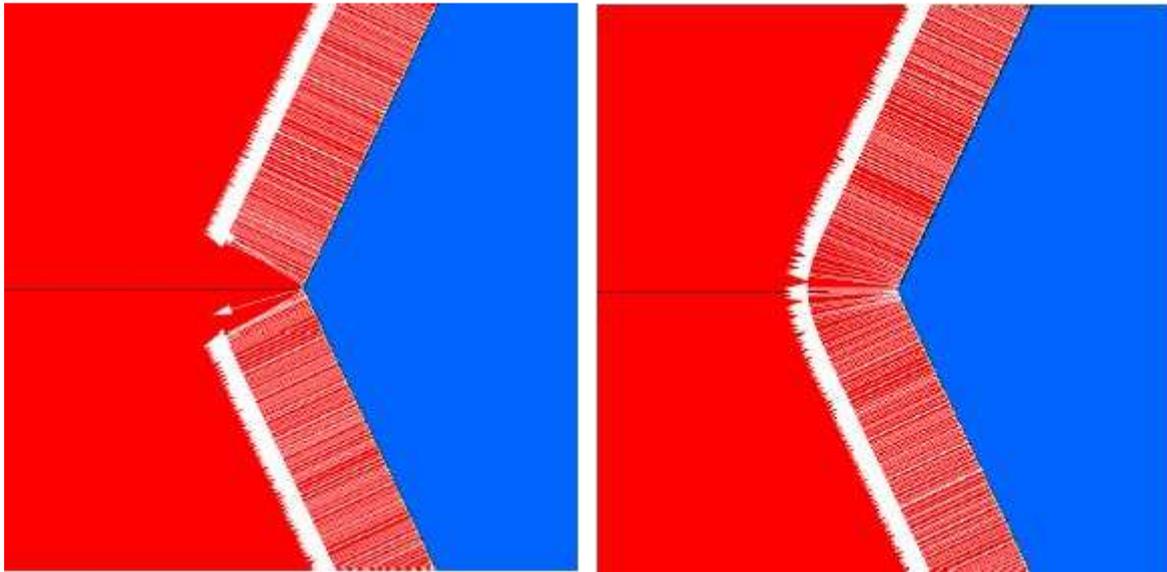
Figure 7 : Triple junction in 2D with a stored energy E lower in the grain on the right ($E_1 = 1$) than in the two grains on the left ($E_2 = E_3 = 2$). Representation of the velocity field with no smoothing (left), and with smoothing (right).
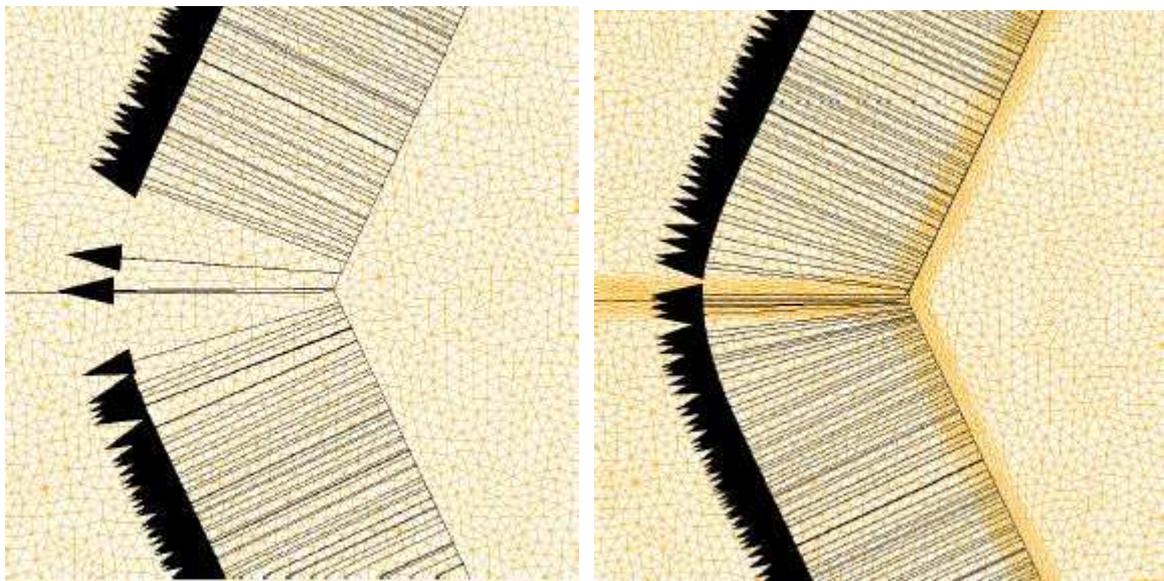
Figure 8 : Effect of the mesh on the velocity field at a triple junction. Isotropic mesh (12 953 nodes, 24 793 elements) on the left, and anisotropic mesh (14 686 nodes, 28 950 elements) on the right.
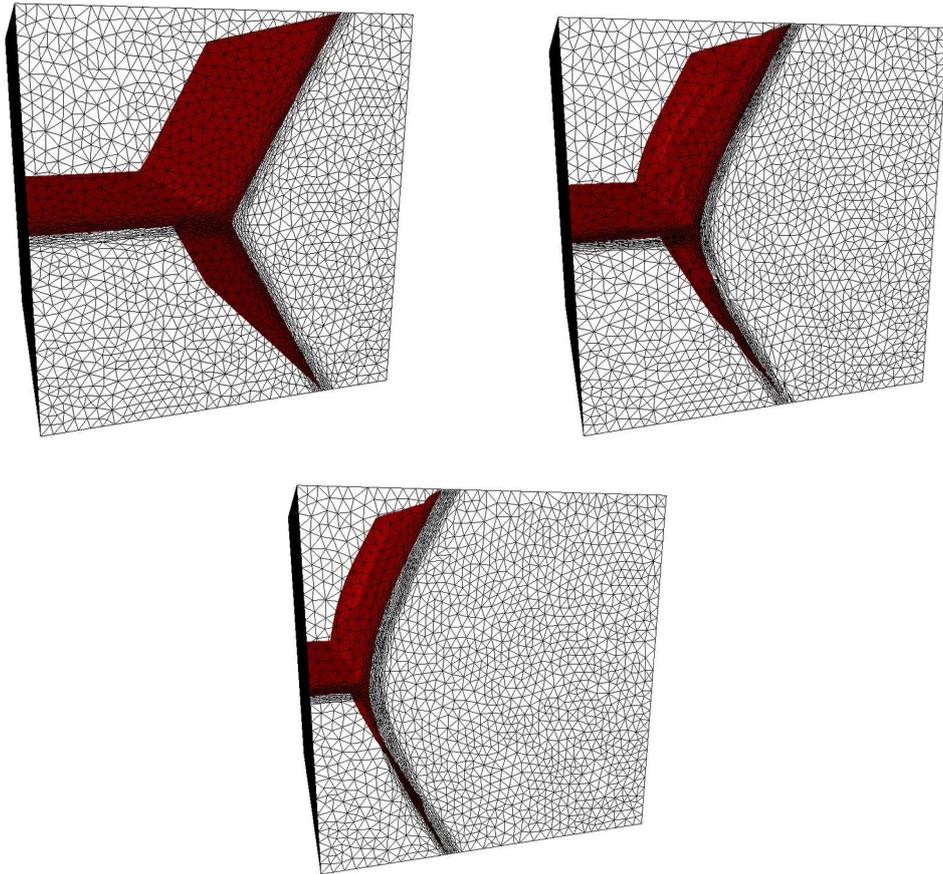
Figure 9 : motion of a triple junction in 3D, equivalent to the 2D representations of Figures 7 and 8.
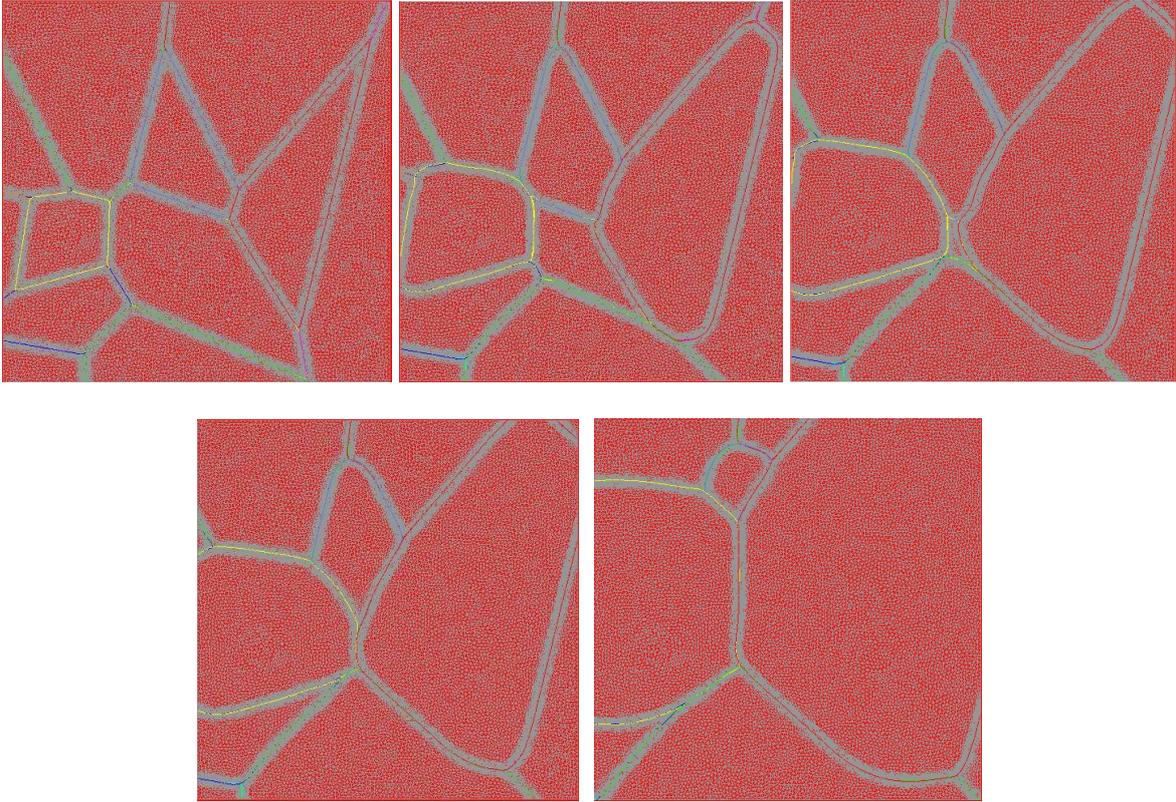
Figure 10 : microstructure evolution of a 12 grains aggregate
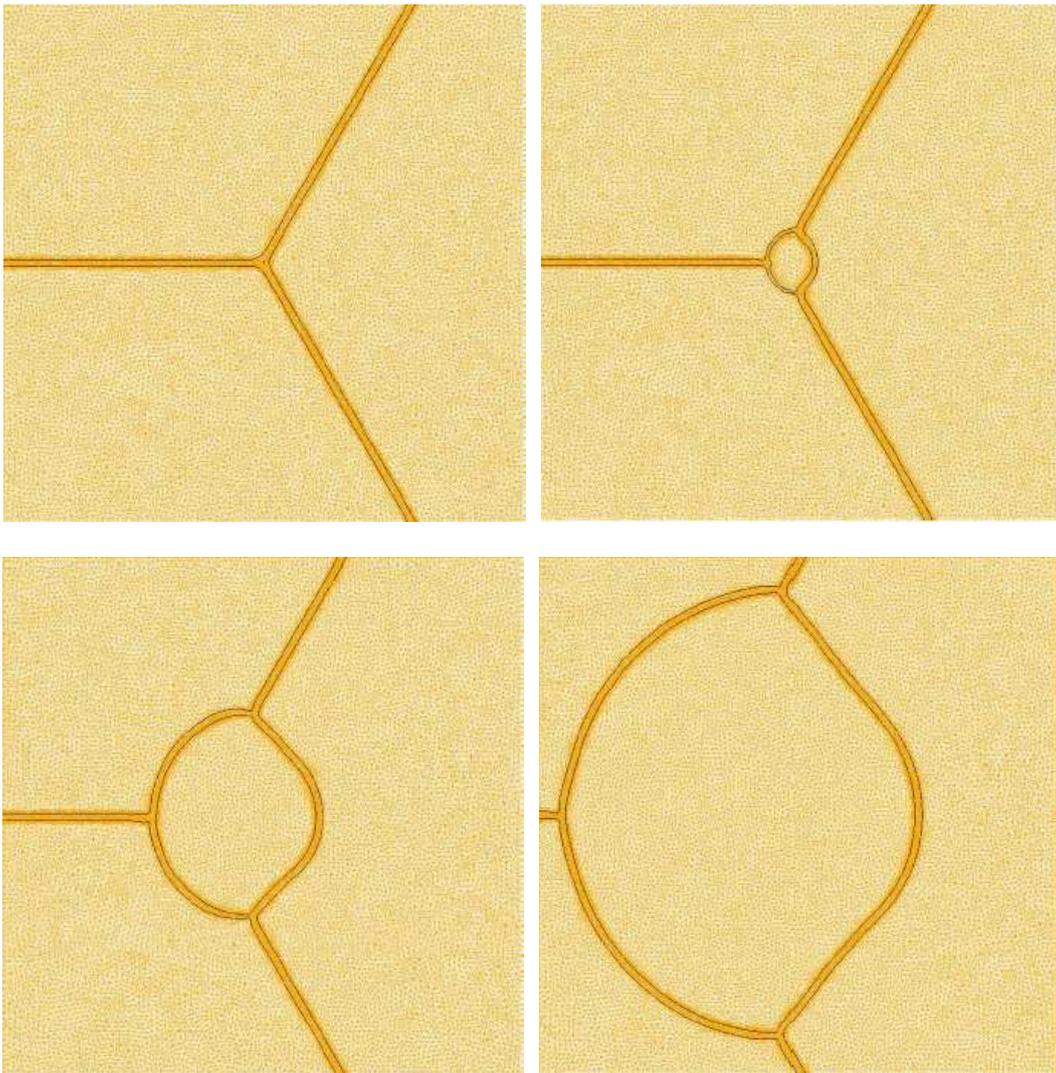
Figure 11 : numerical nucleation and growth at a triple junction
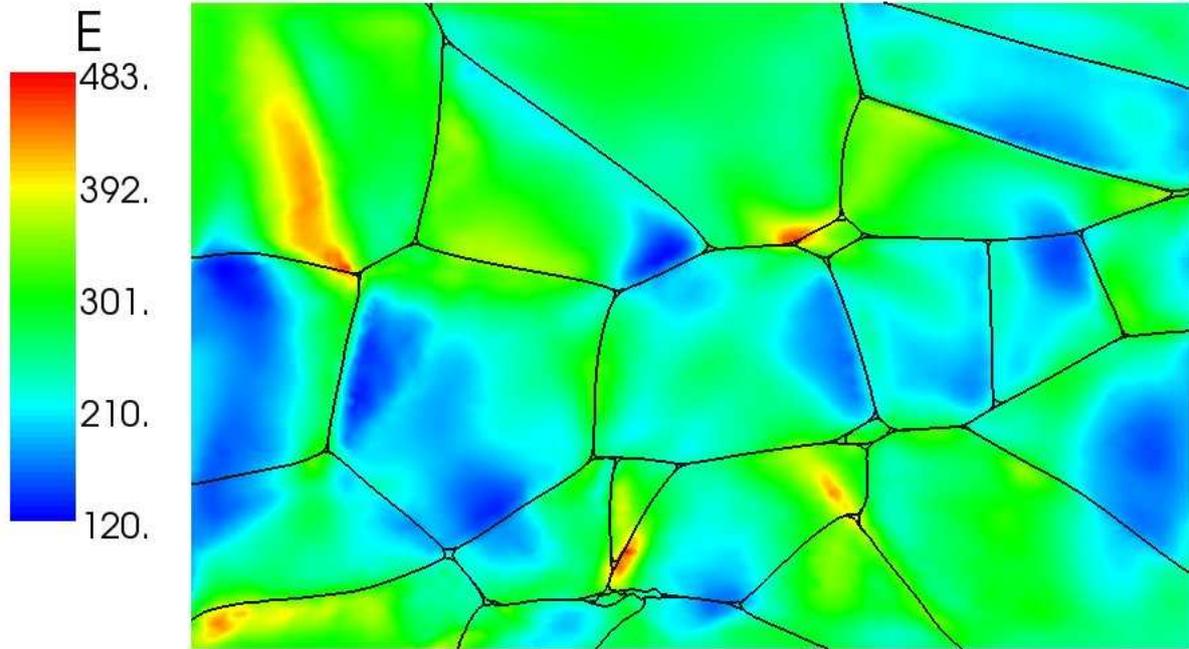
Figure 12 : distribution of the stored energy *E* in a 2D section of the 3D volume of Figure 6.
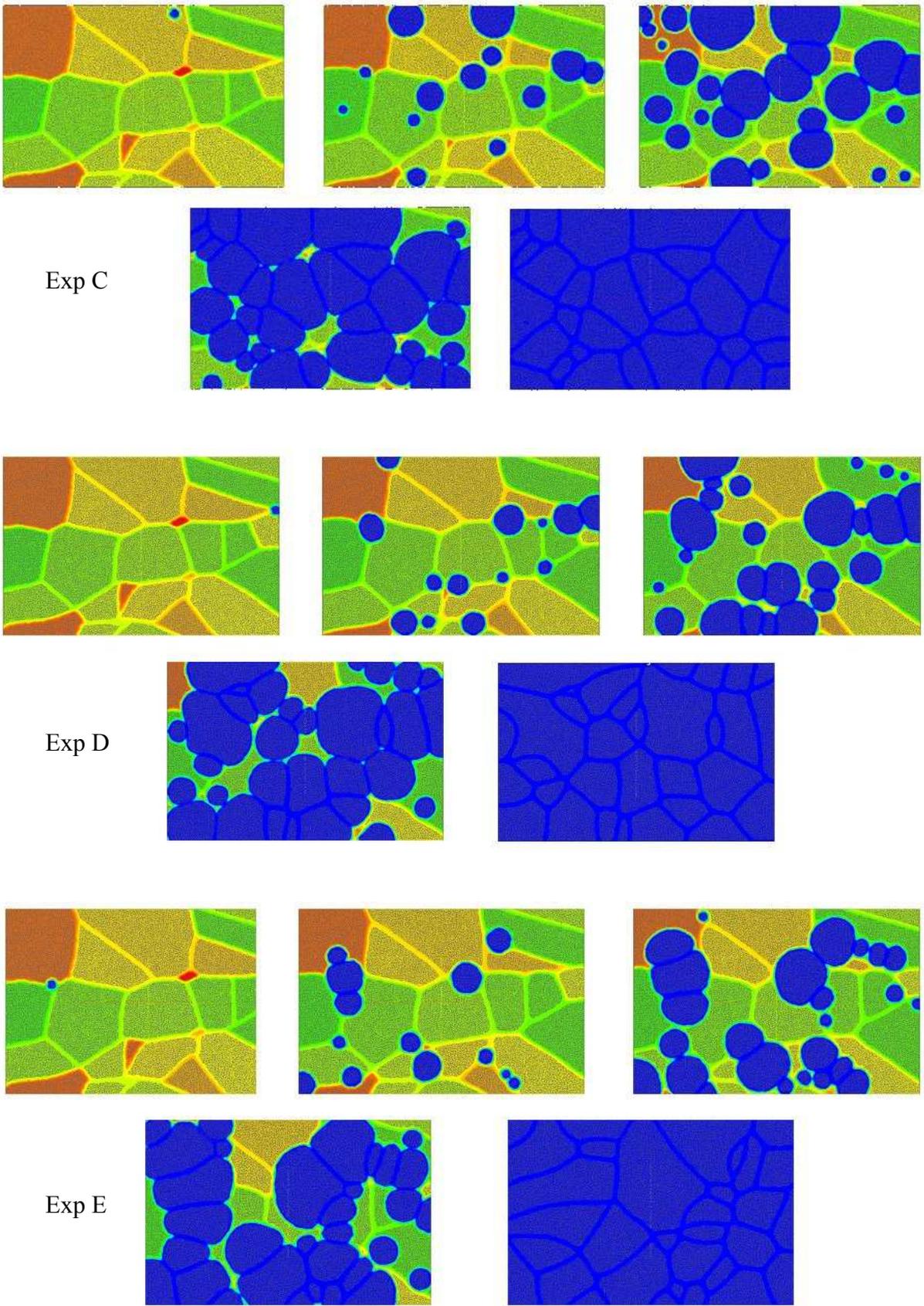
Figure 13 : time evolution of recrystallized volume fraction X (in blue) for experiments C (top), D (middle) and E (bottom)
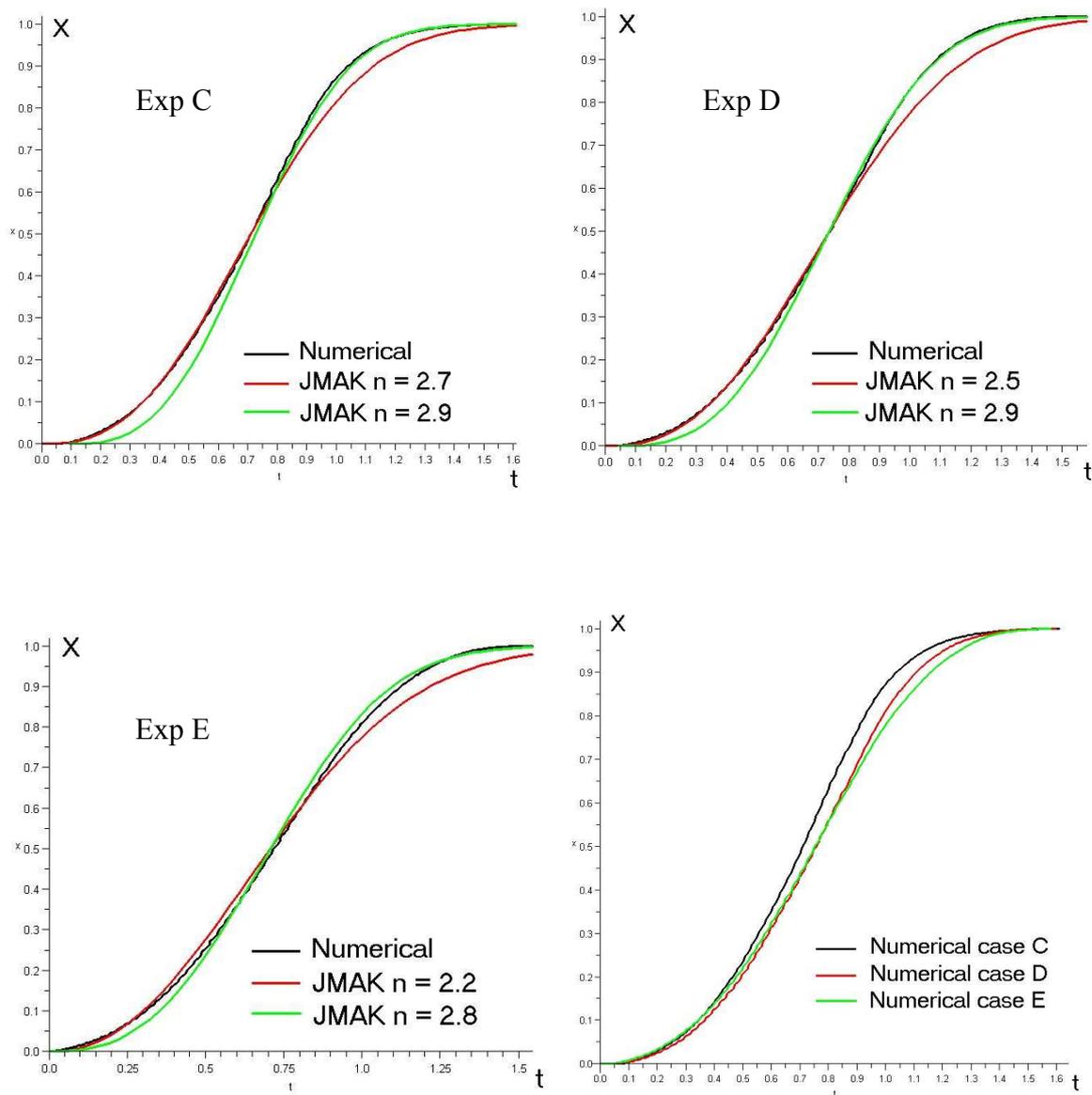
Figure 14 : JMAK approximations of numerical recrystallization kinetics in experiments C, D and E. The JMAK exponent *n* cannot be held constant.

Finite element model of primary recrystallization in polycrystalline aggregates using a level set framework

M Bernacki, H Resk, T Coupez and R E Logé

Centre de mise en forme des matériaux (CEMEF), Mines-Paristech, UMR CNRS 7635, BP 207, 06904 Sophia Antipolis Cedex, France

E-mail : Marc.Bernacki@mines-paristech.fr

Abstract

The paper describes a robust finite element model of interface motion in media with multiple domains and junctions, as the case in polycrystalline materials. The adopted level set framework describes each domain (grain) with a single level set function, while avoiding the creation of overlap or vacuum between these domains. The finite element mesh provides information on stored energies, calculated from a previous deformation step. Nucleation and growth of new grains are modelled by inserting additional level set functions around chosen nodes of the mesh. The kinetics and topological evolutions induced by primary recrystallization are discussed from simple test cases to more complex configurations and compared with the Johnson-Mehl-Avrami-Kolmogorov (JMAK) theory.

1. Introduction

Recrystallization phenomena inevitably occur during thermal and mechanical processes and have a major impact on the final in-use properties of metallic materials. Theories for recrystallization that provide quantitatively correct predictions of crystallographic orientation and grain size distributions have long been sought to fill a critical link in our ability to model material processing from start to finish. To date, no such theory exists. The phenomena of recrystallization seem simple but their mechanisms are not very well understood. Various features of the microstructure contribute to strain energy, particularly defect populations and mismatches in lattice orientation at grain boundaries. On the other hand, kinetics of grain or subgrain boundary motion is controlled not only by the boundary features, but also by the interactions with other defect populations, like dislocations, cells walls, particles or solute atoms. And this kinetics will itself affect the strain energy distribution. In summary, the strain energy distribution factors heavily into the progression of change from old to new grain arrangement, and itself is directly affected by that progression. This dynamic interplay underscores why multiscale models are in principle needed to fully describe recrystallization phenomena in a generic way [1-5].

Historical approaches of recrystallization were based on the Johnson-Mehl-Avrami-Kolmogorov (JMAK) analytical model where equation (1) is used for the description of recrystallization kinetics [6]:

$$X(t) = 1 - \exp(-bt^n), \tag{1}$$

where X is the recrystallized volume fraction, b a constant which depends on nucleation and growth and n the Avrami exponent. If this equation is accurate for very simple loading histories and for some materials, it is no longer the case for complex thermomechanical paths and/or complex microstructures. Heterogeneous nucleation, non-homogeneous stored energy or anisotropic mobility of grain boundaries are only a few of the phenomena to be considered in those cases, especially when the prediction of grain size or crystallographic textures is of concern [1].

Considerable progress has been made in the numerical simulation of recrystallization phenomena since the JMAK approach [7]. In the Microstructural Path Method (MPM) [8], the microstructure was not only characterized by the volume fraction transformed but also by the interfacial area between the recrystallized and unrecrystallized material. This allowed the analysis of more complex grain geometries. Based on the work of Mahin [9], several groups have employed so-called "geometric models" which have extended the analytical methods of the JMAK approach and the MPM to incorporate computer simulation of grain structure evolution. The major disadvantage of these approaches, however, is that they are "blind" approaches: grain growth without regard to the stored energy field into which they intrude.

Monte Carlo (MC) and Cellular Automaton (CA) methods [10] are both probabilistic techniques which deliver grain structures with kinetics: they are associated with 2D or 3D geometric representations of the microstructure, discretized on a regular grid made of "cells" which are allocated to the grains. Both methods have been successfully applied to recrystallization. The standard MC method as derived from the Potts model (multistate Ising model) applies probabilistic rules at each cell in each time step of the simulation. In this model, contrary to the vertex approach, the interfaces between the grains are implicitly defined thanks to the membership of the cells to the various grains. In this context, kinks or steps on the boundaries can execute random walks along the boundaries, which allow changes in curvature to be communicated along the boundaries. The energy of the system is defined by a Hamiltonian which sums the interfacial energy and the topological events appear in a natural way by minimization of this energy, which represents an important advantage of this approach. Moreover, the use of this model in 3D is relatively easy and efficient [11] and can be extended to the recrystallization modelling [10]. However the comparison between MC results and experiments is not straightforward [1]. Furthermore, the standard form of the model does not result in a linear relationship between migration rate and stored energy and the absence of length and time scales can complicate the comparison with the experimental results.

The CA method uses physically based rules to determine the propagation rate of a transformation from one cell to a neighbouring cell [6], and can therefore be readily applied to the microstructure change kinetics of a real system. In the case of recrystallization the switch rule is simple: an unrecrystallized cell will switch to being recrystallized if one of its neighbours is recrystallized. In the standard CA method, the state of all cells are simultaneously updated, which provides efficiency but does not enable the curvature to be a driving force for grain boundary migration [10]. Another major problem of the CA method to model recrystallization is the absence of effective methods for the treatment of nucleation phenomena [1].

Several workers have preferred to define microstructures in terms of vertices. Historically, the vertex models (also called "front tracking" models) described only the grain growth stage and not primary recrystallization [12]. In these models the grain boundaries are considered as continuous interfaces transported by a velocity defined thanks to the local curvature of the grains boundaries. The main idea is to model the interfaces by a set of points and to move these points at each time increment by using the velocity and the normal to the interfaces, which explains the term "front tracking". Complex topological events such as the disappearance of grains or node dissociations are treated thanks to a set of rules which is completed by a repositioning of the nodes. More recently, the vertex model was extended in order to take into account both recrystallization and grain growth [13]. However, even if 2D results for isotropic grain growth seem to show a good agreement with the theory [14], the difficulty remains the non-natural treatment of the topological events, mainly in 3D, where the set of rules becomes very complex and numerically expensive [15]. Moreover, the nucleation modelling remains an open problem.

Other methods suitable for the recrystallization modelling include the phase field model, as in [16], and the level-set method, as in [4,5,17]. These two methods have many common points. They have both the advantage of avoiding the difficult problem of tracking interfaces. More precisely, in both approaches, artificial fields are introduced for the sole purpose of avoiding this difficulty. The initial concept of the phase-field model was to describe the location of two phases by introducing an order parameter (the phase field) which varies smoothly from one to zero (or minus one to one) through a diffuse interface [18]. This concept has been extended to deal with more complex problems involving more than two phases and for modelling microstructure evolution [19,20]. In the case of polycrystalline microstructures, each grain orientation is used as a non-conserved order parameter

field and the free energy density of a grain is formulated as a Landau expansion in terms of the structural order parameters. The grain boundary energy is introduced as gradients of the structural order parameters and the boundaries themselves are represented by an isovalue of the order parameter fields. As for the MC or CA methods, the topological events are treated in a natural way as a result of energy minimization. In the case of 2D ideal normal grain growth, some results illustrate the potential of this approach [19]. However, the difficulties of the method remain: (i) the construction of the free energy density function which must reflect the physical properties of the microstructure and the considered problem; (ii) the very rapid change of the phase field across the diffuse interface which can involve very expensive and intensive calculations, particularly for three-dimensional systems; and (iii) the nucleation modelling which remains, despite recent developments [21], an open problem.

In this paper, a new finite element model based on a level set framework, briefly described in [5], is shown to be effective in modelling primary recrystallization. The model works in 2D and in 3D, and computational cost is reduced thanks to an appropriate mesh refinement around the interfaces. As the interface moves, periodic remeshing is performed such as the refinement zone always coincides with the interface position. In primary recrystallization, the kinetics of interface motion is directly linked to the state variables stored in the mesh, related to the stored strain energy. The formalism also allows to trigger the nucleation of new grains, based on desired criteria (mechanical, crystallographic, etc.). In section 2 the context of the model is introduced. Section 3 then details the finite element approach and the associated level set framework. The associated meshing aspects – automatic meshing and remeshing – are developed in section 4. Numerical results finally illustrate the potential of the method in section 5, through several test cases and comparisons with the JMAK model.

2. Context and equations

It is generally assumed for pure metals that the kinetic law for grain boundary motion is well approximated by [2,22,23] :

$$\vec{v} = M\Delta f \vec{n}, \tag{2}$$

where M corresponds to the grain boundary mobility, Δf to the driving force per unit area, and $\vec{n}$ to the outward unit normal to the grain boundary. Generally, as in [23], M is calculated with:

$$M = \frac{b\delta D_b}{kT} \exp\left(\frac{Q_b}{RT}\right), \tag{3}$$

where b is burger's vector, δ is the characteristic grain boundary thickness, D_b the boundary self diffusion coefficient, Q_b the boundary diffusion activation energy and k the Boltzmann's constant. The driving force Δf is defined by [2,22,23]:

$$\Delta f = \tau \Delta \rho - 2\gamma \kappa, \tag{4}$$

where τ corresponds to the dislocation line energy, $\Delta \rho$ to the total dislocation density difference across the interface, γ to the grain boundary energy and κ to the curvature of the grain boundary. If we assume that the boundary energy is a function of the boundary misorientation, γ can be defined by:

$$\gamma = \frac{\gamma_m}{\theta_m} \theta \left(1 - \ln\left(\frac{\theta}{\theta_m}\right) \right), \tag{5}$$

where θ is the grain boundary misorientation, γ_m and θ_m are the boundary energy and misorientation when the grain boundary corresponds to a high-angle boundary. In first approximation, we can see the normal velocity defined in (2) as a multiple of the curvature of the interface plus the difference of the bulk energies. Considering the three grains configuration (in 2D) of figure 1(a), if each interface Γ_{ij} separates grains G_i and G_j, the oriented normal velocity from G_i to G_j can be defined as:

$$\vec{v}_{ij} \cdot \vec{n}_{ij} = M_{ij} \left(c_{ij} \kappa_{ij} + \left(e_j - e_i \right) \right), \tag{6}$$

with $e_i = \tau \rho_i$ the average stored energy of grain G_i and $c_{ij} = -2\gamma_{ij}$. The triple junction has prescribed angles which can be shown, as in [17], to be defined by:

$$\frac{\sin \alpha_1}{c_{23}} = \frac{\sin \alpha_2}{c_{13}} = \frac{\sin \alpha_3}{c_{12}}, \tag{7}$$

with α_i the angle at the triple junction inside grain G_i. The problem is complex, principally for the treatment of the triple junction where, initially, the curvature is not defined. Moreover, even in the simplified case where only bulk energies are considered, it has been shown that if no further conditions on the motion are imposed, the solution is not unique [24-26]. In [26] it is proved, by considering a particular energy functional, that if the energy of the interfaces are not null ($c_{ij} \neq 0 \ \forall(i, j)$), the time decrease of this functional is equivalent to the condition defined by equation (7). However if we consider only the bulk energy term of the velocity expression, the results are more complex: uniqueness of the solution is not guaranteed. For example, figure 1(a) describes an initial three grains configuration and figure 1(b) and figure 1(c) correspond to two solutions at t=1 for the problem described by equation (6) and this particular geometry. In [26] the authors developed the concept of "vanishing surface tension" solution (called VST solution) by considering the limit problem defined by:

$$\vec{v}_{ij} \cdot \vec{n}_{ij} = \varepsilon M_{ij} c_{ij} \kappa_{ij} + M_{ij}\left(e_j - e_i\right) \ \forall(i, j), \text{ with } \varepsilon \to 0. \tag{8}$$

Using various 2D tests cases and a perturbation analysis, they strongly suggest that the VST solution corresponds to one of the solutions of the considered problem for $\varepsilon = 0$, while it corresponds to the unique solution of the problem for $\varepsilon \to 0$.
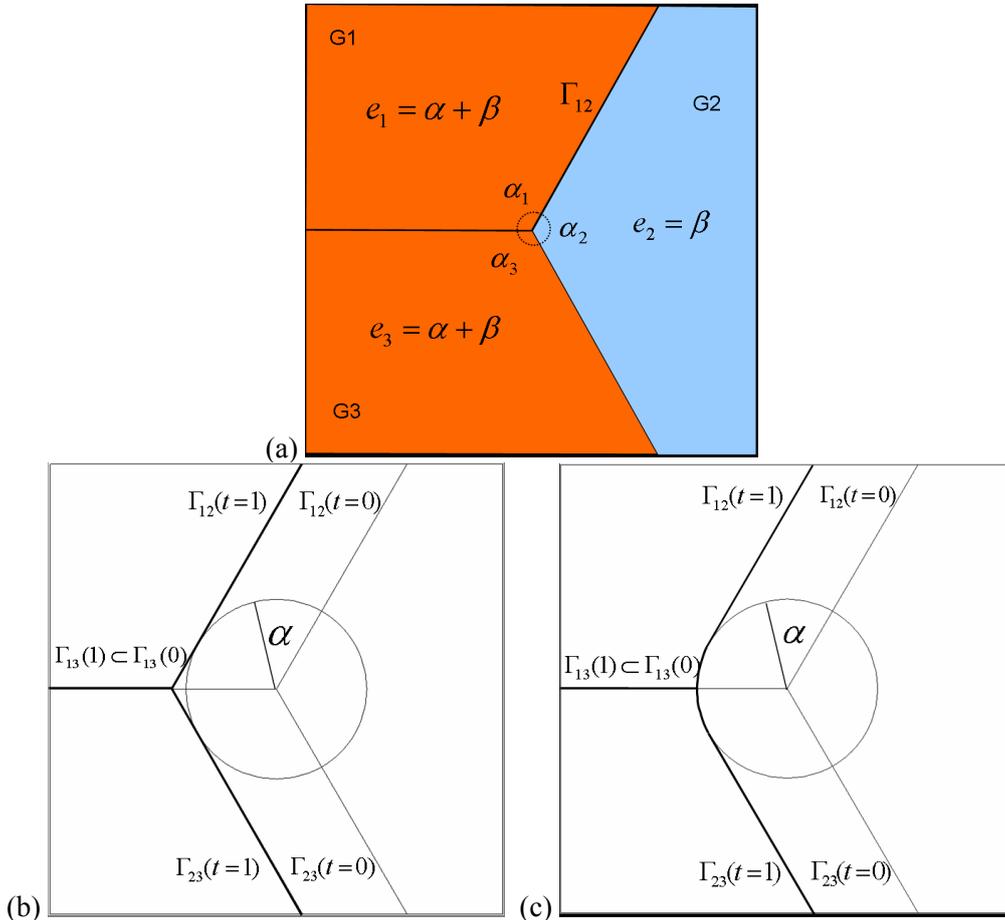
Figure 1. (a) Example of a triple junction configuration; two solutions at t=1 of this configuration for the problem defined by equation (6): (b) the VST solution and (c) another solution.

In this paper, a new algorithm is proposed to model the problem defined by equation (6), in 2D or in 3D, and for any polycrystalline microstructure configuration. The numerical approach is detailed but the treatment of the curvature term at the multiple junction and the simulations with this term will be discussed in a forthcoming publication. The presented approach is based on a level set method [5,25,26], now commonly used to follow propagating fronts in various numerical models [27-29]. In Ref. [25], the authors have extended the standard level set method to model the motion of multiple junctions; the method is appropriate for the case of grain growth, i.e. with zero bulk energies. Each region has its own private level set function, and this function moves each level set with a normal velocity defined by the conditions at the nearest interface. A reassignment step is used to avoid kinematic incompatibilities, i.e. the development of vacuum and overlapping regions. The present model proposes a new formulation accounting for bulk stored energies as well as nucleation events, and still avoiding the development of vacuum and overlapping regions.

3. Finite element model and level set framework

3.1. Introduction

Figure 2 illustrates the procedure of creating a virtual microstructure, and the associated finite element mesh. Figure 2(a) shows a two hundred grains digital sample [3,30-32], made of Voronoï cells, The Voronoï tessellation is fully described by N seeds or Voronoï sites shown in Figure 2(b). Each site s_i defines a Voronoï cell or grain G_i, which consists of all points closer to s_i than to any other site. The conversion of the Voronoï tessellation into a finite element mesh is illustrated in Figure 2(c). The location of the interfaces (grain boundaries) is defined implicitly using a level set framework. For each individual cell or grain, a signed distance function $\phi,$ defined over a domain Ω, gives at any point x the distance to the grain boundary Γ. In turn, the interface Γ is then given by the level 0 of the function ϕ:

$$\begin{cases} \phi(x) = d(x,\Gamma), x \in \Omega \\ \Gamma = \{x \in \Omega, \phi(x) = 0\} \end{cases} \tag{9}$$

Assuming that the domain Ω contains N_G grains, we have $\{\phi_i, 1 \le i \le N_G\}$ with the sign convention $\phi_i \ge 0$ inside grain G_i, and $\phi_i \le 0$ outside grain G_i. The procedure to evaluate these functions at all nodes x of the finite element mesh goes through evaluating the functions

$$\alpha_{ij}(x) = \frac{1}{2}\left\| \overrightarrow{s_i s_j} \right\| - \frac{\overrightarrow{s_i s_j} \cdot \overrightarrow{s_i x}}{\left\| \overrightarrow{s_i s_j} \right\|}, 1 \le i, j \le N_G, j \ne i, \tag{10}$$

which correspond to the signed distance of x to the bisector of the segment $\lfloor s_i, s_j \rfloor$. $\phi_i(x)$ is then defined as:

$$\phi_i(x) = \min_{\substack{1 \le j \le N_G \\ j \ne i}} (\alpha_{ij}(x)). \tag{11}$$

One can also define a global unsigned distance function as:

$$\phi_{glob}(x) = \max\{\phi_i(x), 1 \le i \le N_G\}. \tag{12}$$

This function is positive everywhere and the zero value corresponds to the grain boundary network. Figure 2(c) displays the function $\phi_{glob}(x)$ corresponding to the microstructure of Figure 2(a) and calculated at the nodal points of the finite element mesh (in white).

5
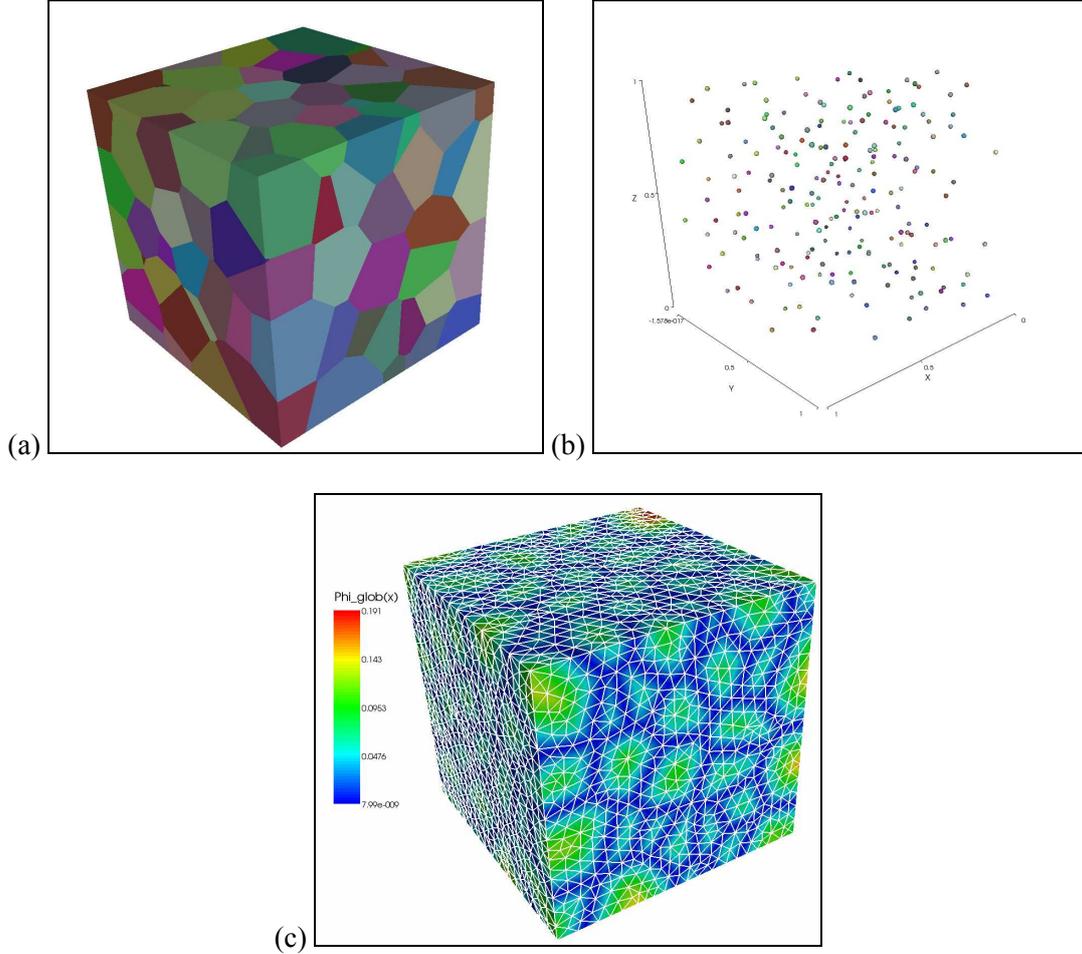
Figure 2. (a) A 200 grains virtual cubic microstructure; the color scale describes the identity of the different grains, (b) the corresponding Voronoï sites, (c) the corresponding $\phi_{glob}(x)$ function for the finite element mesh, the latter appears in white.

If a velocity field $\vec{v}$ is defined over Ω, the motion of the interfaces (or any surfaces defined by a given isovalue of the level set functions) is described by:

$$\begin{cases} \dfrac{\partial \phi_i}{\partial t} + \vec{v} \cdot \nabla \phi_i = 0 \\ \phi_i(t=0,x) = \phi_i^0(x) \end{cases}, \forall i \in \{1,\ldots,N_G\}. \tag{13}$$

At any time t the interface Γ_i of grain G_i is given implicitly by the equation $\phi_i(t,x) = 0$. The expression of $\vec{v}$ in Ω will be detailed in paragraph 3.4. If the initial value of equation (13) is a signed distance function, a priori it is not the case of the solution ($\|\nabla \phi_i(t,x)\| \neq 1$). If one wants to keep the property of a distance function, a re-initialization technique is introduced and applied periodically [28,33], as detailed below.

3.2. Re-initialization

The re-initialization technique consists in building, from a level set function ϕ which is not a signed distance function, a new signed distance function β whose zero isovalue corresponds to the

zero isovalue of ϕ. The most common method to re-initialize level set functions is to solve the following Hamilton-Jacobi equation [28]:

$$\begin{cases} \dfrac{\partial \beta_i}{\partial \tau} + s_i \left(\left\| \nabla \beta_i \right\| - 1 \right) = 0 \\ \beta_i(\tau = 0, x) = \phi_i(t, x) \end{cases}, \text{ with } s_i = sign(\beta_i). \tag{14}$$

In practice, equation (14) is solved periodically, typically every few time steps. Equation (14) can be seen as a pure convective equation. Indeed, if we write $\vec{U}_i = s_i \dfrac{\nabla \beta_i}{\left\| \nabla \beta_i \right\|}$, it becomes:

$$\begin{cases} \dfrac{\partial \beta_i}{\partial \tau} + \vec{U}_i . \nabla \beta_i = s_i \\ \beta_i(\tau = 0, x) = \phi_i(t, x) \end{cases} \tag{15}$$

To define the fictitious time τ, a stability condition is used: $\left\| \vec{U}_i \right\| \Delta \tau = \Delta \tau = h$, where h corresponds to the mesh size. Hence the fictitious time step is usually chosen as h.

To summarize, this algorithm allows to transform a given irregular level set function into a distance function without changing the zero isovalue. This is illustrated in Figure 3: Figure 3(a) represents an irregular level set function with 50 equally spaced isovalues (with the zero level in bold), and figure 3(b) corresponds to the re-initialized level set function.

In this paper, we propose to use a formulation developed in [33] which performs the stage of re-initialization automatically during the resolution of the convection problem. The formulation is recalled below.

3.3 Automatic re-initialization

The idea proposed by this author is to modify equation (13) in order to keep the property of a signed distance function. The parameter $\lambda = d\tau/dt$ is introduced (in practice $\lambda \approx h/\Delta t$), to write the following equality $\dfrac{\partial}{\partial \tau} = \dfrac{\partial t}{\partial \tau} \dfrac{\partial}{\partial t} + \dfrac{\partial x}{\partial \tau} \cdot \nabla = \dfrac{1}{\lambda} (\dfrac{\partial}{\partial t} + \vec{v} \cdot \nabla)$ and to transform equation (14):

$$\dfrac{\partial \beta_i}{\partial t} + \vec{v}.\nabla \beta_i + \lambda s_i \left(\left\| \nabla \beta_i \right\| - 1 \right) = 0. \tag{16}$$

The new formulation with convection and re-initialization becomes:

$$\begin{cases} \dfrac{\partial \phi_i}{\partial t} + \vec{v} \cdot \nabla \phi_i + \lambda s_i \left(\left\| \nabla \phi_i \right\| - 1 \right) = 0 \\ \phi_i(t = 0, x) = \phi_i^0(x) \end{cases}, \forall i \in \{1, \ldots, N_G\}, \tag{17}$$

which can be written as a pure convective problem:

$$\begin{cases} \dfrac{\partial \phi_i}{\partial t} + \left(\vec{v} + \lambda \vec{U}_i \right) \cdot \nabla \phi_i = \lambda s_i \\ \phi_i(t = 0, x) = \phi_i^0(x) \end{cases}, \forall i \in \{1, \ldots, N_G\}. \tag{18}$$

Remark 3.1: the function $s_i = s(\phi_i)$ can take the values 1, -1 or 0 if $\phi_i = 0$. To force equation (18) to be conservative near the interface, the following expression is used:

$$s_i = \frac{\phi_i}{|\phi_i|} \text{ if } \phi_i > \varepsilon \quad , \quad s_i = 0 \text{ if } \phi_i \le \varepsilon \quad , \quad \varepsilon \approx h. \tag{19}$$

Remark 3.2: we refer the reader to [33] for a complete description of the method and its possible extension (regular truncation of the level set functions).

(a)

(b)
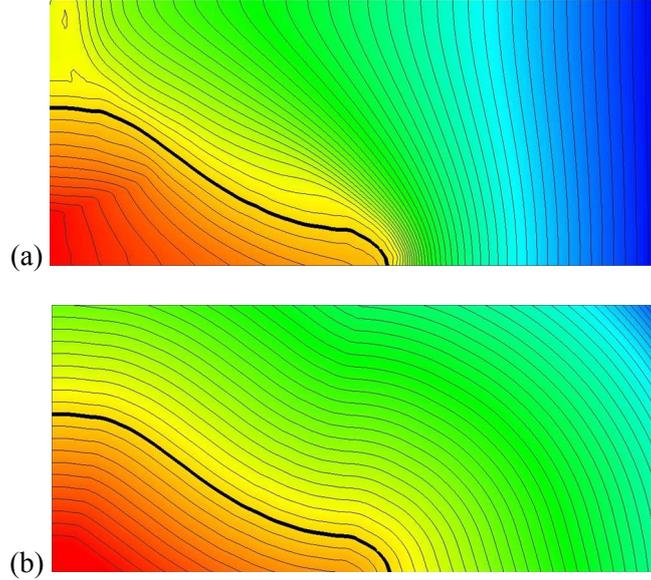
Figure 3. (a) An irregular level set function with 50 equally spaced isovalues and the zero level in bold, (b) the same representation after re-initialization.

3.4 Expression of the velocity field

In the considered problem, the expression of the velocity field is of prime importance. Several comments should be made:

- In order to avoid kinematic incompatibilities (overlapping or vacuum regions), it is necessary to work with the same velocity field for all the level set functions. However the kinetic law defined by equation (6) is built according to parameters which are specific to a single level set function (grain): bulk stored energy difference across the boundary and unit normal (neglecting the curvature term).
- The construction of the velocity field around multiple junctions is critical for a good description of microstructure evolution. On a numerical point of view, it must be as regular as possible.
- The expression (6) of the kinetic law implies a very accurate calculation of the normal to each interface.

The proposed level set framework gives an answer to each of these comments. Concerning the geometric parameters of the interface, it is well known that the level set method is perfectly adapted to their accurate calculation [25]. Indeed, keeping in mind the sign convention described previously, if the function ϕ_i corresponds to the signed distance function of grain G_i:

- The outward unit normal to any isovalue of ϕ_i is defined by:

$$\vec{n}_i = -\frac{\nabla \phi_i}{\|\nabla \phi_i\|} \underset{\|\nabla \phi_i\|=1}{=} -\nabla \phi_i. \tag{20}$$

8

- The curvature of any isovalue of ϕ_i is defined by:

$$\kappa_i = -\nabla \cdot \vec{n}_i \Big|_{\|\nabla\phi_i\|=1} = \Delta\phi_i . \qquad (21)$$

Concerning the definition of the velocity field, it is useful to divide it in two parts: $\vec{v} = \vec{v}_\kappa + \vec{v}_e$. The first part is related to the curvature of the boundary, while the second part refers to the bulk energy term. First of all, some general remarks apply:

- At any time t a given point $M \in \Omega$ of coordinates x, is easily located, i.e. the grain to which it belongs is easily identified. Indeed, as the set $\{G_i \setminus \Gamma_i, 1 \leq i \leq N_G\}$ corresponds to a partition of the domain Ω and with the sign convention described previously, the following results are verified:

$$M \in \Gamma_i \Leftrightarrow \phi_i(t,x) = 0, \qquad (22)$$
$$M \in G_i \setminus \Gamma_i \Leftrightarrow M \notin \bigcup_{j \neq i} G_j \Leftrightarrow \phi_i(t,x) > 0 \Leftrightarrow \forall j \neq i \; \phi_j(t,x) \leq 0. \qquad (23)$$

- The description of an interface by a level set function remains a « fuzzy » description, which means that the zero level of the level set function (the interface) does not inevitably correspond to nodes of the mesh. The point M is located using the following relationship:

$$M \in G_i \Leftrightarrow \phi_i(t,x) = \max_{1 \leq k \leq N_G} (\phi_k(t,x)). \qquad (24)$$

A classical way to build the velocity field $\vec{v}$, for any node of the mesh, is as follows:

- Find i with $\phi_i(t,x) = \max_{1 \leq k \leq N_G} (\phi_k(t,x))$.
- Compare $\phi_i(t,x)$ with a positive fixed parameter ℓ which defines a length scale related to the proximity of the node to the interface:

$$\begin{cases} \text{If } \phi_i(t,x) > \ell \Rightarrow \vec{v}(t,x) = \vec{0} \text{ else} \\ \text{find } j \text{ with } \phi_j(t,x) = \max_{\substack{1 \leq k \leq N_G \\ k \neq i}} (\phi_k(t,x)) \Rightarrow \vec{v}_e(t,x) = M_{ij} f(\phi_i(t,x), \ell)(e_j - e_i)\vec{n}_i(t,x), \end{cases} \qquad (25)$$

with f a decreasing continuous function varying from 1 to 0 when $\phi_i(t,x)$ varies from 0 to ℓ, and M_{ij} the mobility at the interface between grain i and grain j. The main disadvantage of this approach lies in the management of multiple junctions: discontinuous velocity fields are generated, which then lead to convergence problems in the resolution of the convection equation (18). We propose another algorithm which considers, at any point x, all N_G level set functions:

Find i with,

$$\phi_i(t,x) = \max_{1 \leq k \leq N_G} (\phi_k(t,x)) \Rightarrow \vec{v}_e(t,x) = \sum_{\substack{j=1 \\ j \neq i}}^{N_G} M_{ij} \exp(-\alpha|\phi_j(t,x)|)(e_i - e_j)\vec{n}_j(t,x), \qquad (26)$$

with α a positive fixed parameter [5]. Expression (26) leads to a smoother velocity field and avoids topological considerations, i.e. there is no need to identify neighbouring grains at point x. The difference between these two approaches (25) and (26) is illustrated in [5] for the triple junction case of Figure 2, where the smoothing effect of (26) appears clearly when compared to (25). As stated earlier, we do not detail here the method used to estimate the curvatures of the interfaces (defined by the functions $-\Delta\phi$), in particular at multiple junctions where these curvatures are not defined. All

simulations described in section 5 will therefore involve only the stored energy part of the velocity, in the context of primary recrystallization phenomena.

To summarize, the velocity field for primary recrystallization could be defined as follows:

$$\vec{v}(t,x) = \vec{v}_e(t,x) = \sum_{i=1}^{N_G} \sum_{\substack{j=1 \\ j \neq i}}^{N_G} \chi_{G_i}(t,x) M_{ij} \exp\left(-\alpha|\phi_j(t,x)|\right)(e_j - e_i)\nabla\phi_j(t,x), \qquad (27)$$

with $\chi_{G_i}(t,x)$ the characteristic function of the grain G_i. To solve the problem defined by equations (18) and (27), a finite element method based on the C++ library 'Cimlib' [33] is used, with unstructured meshes and a stabilized P1 solver as SUPG or RFB method. The quality of the described approach is strongly related to the accuracy of level set function calculations around the interfaces. Indeed, a little disturbance of the levels around an interface leads to an error in the velocity estimation and consequently in their own evolution. For a given computational cost, optimal accuracy is obtained by using anisotropic meshes, with refinement close to the boundaries [3-5]. The technique to generate anisotropic meshes adapted to a polycrystalline aggregate is presented in section 4.

3.5 Nucleation modelling and disappearance of grains

One of the prominent advantages in using front capturing methods for describing interface motion is that there is no need for specific treatment when some regions (grains) disappear. Complex topological evolutions are handled automatically. In a similar way, it is possible to introduce new regions (grains), based on given criteria. For example, new grains can nucleate during primary recrystallization, with an assumed low (often zero) stored energy.

A very simple method to create a nucleation site is to build a new signed distance function at a desired time increment and at a given spatial position. For example, the new distance function can be such that the boundary of the nucleus is spherical (3D) or circular (2D), centred around one node of the mesh. Each nucleus, described by a new signed distance function, evolves subsequently according to the principles described by equation (27). In particular, spontaneous growth occurs if a zero stored energy is assumed inside the new region. Different rules have been developed for the time and space nucleation laws. For example, at each time step of the simulation, a probabilistic or deterministic law of nucleation can be used considering a set of possible nucleation sites. This set can be chosen in different ways: (i) randomly in the domain Ω, (ii) only at grain boundaries, or (iii) according to specific criteria based on crystallographic or mechanical variables calculated from a previous deformation step of the polycrystal. This last method can be implemented for example when the deformation step is modelled using crystal plasticity based constitutive laws [34].

Instead of nucleating new grains, topological evolutions can also lead to the disappearance of grains. Level set methods automatically manage this type of event, but the numerical cost of the simulation needs to be considered. It is clearly optimized by not taking into account the signed distance functions which correspond to grains which have disappeared. Each level set function indeed leads to a computational effort related to the evaluation of the velocity field according to the kinetic law (27), the resolution of the convection equation together with the re-initialization (18), and the remeshing operations around the interface every few increments. Hence, the problem solved evolves dynamically during the calculation: for each time step, the signed distance functions which become negative on the whole domain (disappearance of the corresponding grain) are excluded from the calculation as well as the corresponding solvers.

Finally, at each time step, the following simplified algorithm concerning the nucleation and the disappearance of grains is used:

- Evaluations of the maximum of each signed distance function and decision to exclude or not the corresponding grain.
- Probabilistic or deterministic rule to choose the new nucleation sites (in agreement with the set of possible sites, and ignoring the part of the domain which is already recrystallized).
- If at least one nucleation site is activated, the corresponding new signed distance functions are built and the signed distance functions of the existing grains, which have an intersection with these new grains, are accordingly modified.

- If at least one site is activated, an anisotropic remeshing operation is performed to obtain an adapted anisotropic mesh around the new grain(s).
- Velocity field re-evaluated in the new topological configuration.

Tests cases illustrating this algorithm will be described in section 5.

4. Generation of finite element meshes

Figure 4(a) and figure 4(b) illustrate an adapted anisotropic mesh to the microstructure detailed in Figure 2. The mesh is made of tetrahedral elements, whose size and shape are not homogeneous. Anisotropic meshing is used along the interfaces of the grains, with a smaller size in the direction perpendicular to the boundary.

(a)   (b)
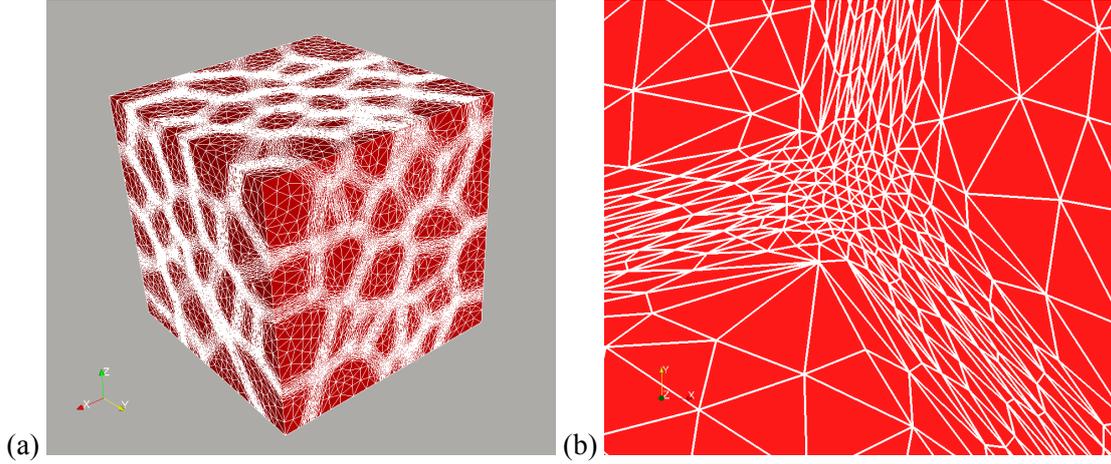
Figure 4. (a) An adapted anisotropic mesh to the microstructure detailed in Figure 2, (b) A zoom on the surface of a triple junction

The technique used to generate such meshes lies in the definition of a metric. A metric is a symmetric positive defined tensor which represents a local base modifying the way to compute a distance, such that:

$$\left\| \vec{u} \right\|_{\mathbf{M}} = \sqrt{{}^{t}\vec{u}\mathbf{M}\vec{u}} \ , \quad <\vec{u}, \vec{v}>_{\mathbf{M}} = {}^{t}\vec{u}\mathbf{M}\vec{v} \ . \tag{28}$$

If $\mathbf{M}$ is the identity tensor, the distance corresponds to the usual one in the Euclidian space. As $\mathbf{M}$ is a symmetric positive defined tensor, it is diagonalizable in an orthonormal basis of eigenvectors and all the eigenvalues are strictly positive. The metric $\mathbf{M}$ can be interpreted as a tensor whose eigenvalues are linked to the mesh sizes, and whose eigenvectors define the direction in which these mesh sizes are applied. Let us consider the simple case of figure 5 with only two grains (hence, one interface). The direction of mesh refinement is the unit normal to the interface (vector $\nabla\phi$ in figure 5). To specify the mesh size in that direction, and its evolution in space, a characteristic thickness E is introduced (see figure 5):

$$\begin{cases} |\phi(x)| < E/2 & \text{near the interface} \\ |\phi(x)| > E/2 & \text{far from the interface} \end{cases} \tag{29}$$

The mesh size takes a default value far from the interface, and is reduced in the direction perpendicular to the interface when $|\phi|$ is reduced. A simple example is given by the following choice of h:

$$\begin{cases} |\phi(x)| \geq E/2 & \Rightarrow \quad h = h_{d} \\ |\phi(x)| < E/2 & \Rightarrow h = \dfrac{2h_{d}(m-1)}{mE}|\phi(x)| + \dfrac{h_{d}}{m} \end{cases} \tag{30}$$

At the interface the mesh size is reduced by a factor m with respect to the default value h_d. This mesh size increases with the distance ϕ to the default value h_d at the distance $E/2$. The unit normal to the interface $\nabla\phi$, and the mesh size h defined by equation (30), lead to the following metric:

$$\mathbf{M} = C(\nabla\phi \otimes \nabla\phi) + \frac{\mathbf{Id}}{h_d^2} \quad \text{with } C = \begin{cases} 0 & \text{if } |\phi| \geq \dfrac{E}{2} \\ \dfrac{1}{h^2} - \dfrac{1}{h_d^2} & \text{if } |\phi| < \dfrac{E}{2} \end{cases} \tag{31}$$

with $\mathbf{Id}$ the identity tensor. This metric corresponds to an isotropic metric far from the interface (with a mesh size equal to h_d for all directions) and an anisotropic metric near the interface (with a mesh size equal to h in the direction $\nabla\phi$ and equal to h_d for the other directions, i.e. in the plane normal to $\nabla\phi$).

When dealing with polycrystalline aggregates and multiple interfaces, the above strategy is repeated for each grain. Combining all information, the number of refinement directions is then evaluated at each node of the mesh. For the nodes at which:

$$|\phi_i(x)| \geq E/2, \quad 1 \leq i \leq N_G, \tag{32}$$

there is no direction of refinement, and the mesh size is isotropic with $h = h_d$. As the number of directions of refinement increases, the mesh size is reduced in one or several directions. This happens when there is more than one level set function for which $|\phi_i(x)| < E/2$, and when the corresponding normal directions $\vec{n}_i$ calculated from equation (20) are not co-linear. A vector base is then constructed from these normals, and refinement is performed along these independent vectors, which are the eigenvectors of the metric. For each vector direction the mesh size is calculated from equation (30), with $\phi_i(x)$ being the signed distance function associated to the considered normal. At triple or multiple junctions, the refinement may therefore become isotropic [35].

Anisotropic meshes are built using the MTC mesher-remesher developed by T. Coupez [36], it is based on local mesh topology optimizations and works for all meshing applications from adaptive remeshing to mesh generation by using a minimal volume principle. MTC improves a mesh topology by considering the quality of the elements. The quality of an element is defined through a shape factor that gives to equilateral triangles the highest quality, while the worst quality corresponds to a triangle which degenerates into a segment (2D). In 3D, degeneration corresponds to a tetrahedron becoming a surface. The element quality is normalised within an interval [0,1], and the shape factor is given by :

$$c(e) = c_0 \frac{|e|}{l(e)^d}, \tag{33}$$

where c_0 is a normalised coefficient, $|e|$ the volume of the element, $l(e)$ the average length of the element edges and d the space dimension. The shape factor takes into account the metric by calculating volume and lengths according to equation (28). More details and illustrations of the robustness and capability of this meshing technique for microstructure are described in [35].
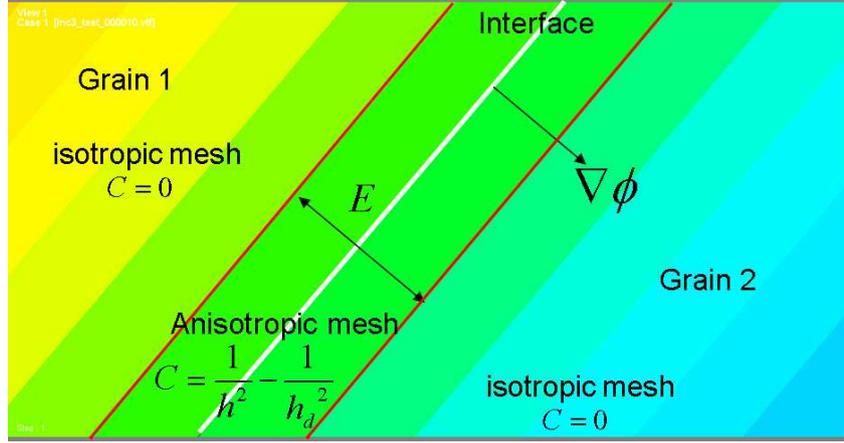
Figure 5. A 2D grain boundary

5. Numerical results

As explained in section 3, the investigated applications study the motion of interfaces under $\vec{v}_e$ caused by the spatial distribution of bulk stored energy, in the context of primary recrystallization. For the sake of simplicity, the mobility is assumed to be a constant equal to one, independent from the crystallographic nature of the interfaces.

5.1 A three grains academic test case

The first test case, which is very classical and instructive [5,26], corresponds to the configuration detailed in figure 1: three straight lines meeting at 120° in an unit square domain. We set $e_1 = e_3 = 2$ and $e_2 = 1$, the challenge is to check the growth of grain 2 at the expense of grains 1 and 3. The time step considered is equal to 1.4e-3 s. Figure 6 shows the comparison, after 20 time steps, of isovalues of ϕ_1 using an adapted anisotropic mesh, with and without re-initialization. This comparison illustrates the need for re-initialization steps of the level set functions to avoid the appearance of discontinuities and associated numerical instabilities. Figure 7 shows the influence of the mesh on the evolution of the distance functions. Lines indicate the $\pm 5 \cdot 10^{-3}$ isovalues of the three distance functions as a function of time, with an isotropic constant mesh size equal to 0.01 and with an adapted anisotropic mesh close to the interfaces. In the latter case, automatic operations of anisotropic remeshing are performed every five time steps in order to track the interfaces and the anisotropic metric was built thanks to equation (31) with $E = 0.015$, $h_d = 0.01$ and $h = 1e - 3$. The bad quality of the results with an isotropic constant mesh underlines the need to work with very fine meshes near the interfaces. Working with anisotropic meshes avoids the use of too fine elements far from the interfaces. At the same time, it is seen in figure 7 that the non uniform anisotropic meshing procedure leads to results which are in very good agreement with one of the exact solutions of this configuration (see [26] or Figure 1), although this solution does not correspond to the VST solution. In terms of accuracy, the $L2$ error between the exact and calculated function defined by $\max\limits_{0 \leq t \leq T_{end}} \left(\max\limits_{1 \leq k \leq N_G} \left(\phi_k(t, x) \right) \right)$ is less than 3%. At the triple junction, the numerical treatment smoothes out the geometrical discontinuity and, as underlined in the introduction, it is a way of imposing the uniqueness of the solution, i.e. the configuration now evolves in a deterministic way. The numerical result is coherent with the construction method of the velocity field, which allows (i) the accurate account of stored energy differences across boundaries, and (ii) regularizing the discontinuous nature of the problem, incompatible with the resolution of the convection equations given by (18). Obviously, the proposed numerical strategy has a cost. On average, there is an approximate 10% difference in terms of number of nodes or elements between the constant isotropic mesh and the non uniform anisotropic mesh. Besides, the cost of successive remeshing operations (typically every 5 time steps) must be added to

this 10% difference. The simulation of Figure 7 was performed on 4 processors of an Opteron 2,4GHz linux cluster in 7min20s with no remeshing, and in 18min32s with automatic anisotropic remeshing. It is therefore important to find a good compromise between numerical cost and desired accuracy.

(a)   (b)
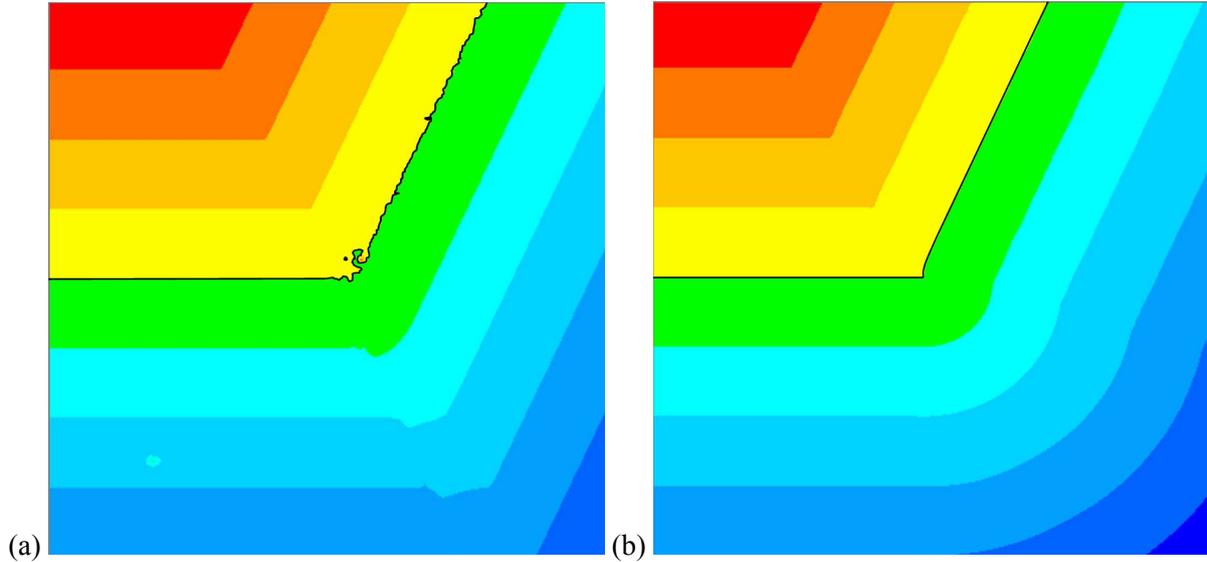
Figure 6. Function ϕ_1 after 20 time steps: (a) without re-initialization and (b) with re-initialization

5.2 *A simple nucleation case*

Figure 8 describes primary recrystallization in a unit square domain, starting from a 25 grains aggregate. A uniform stored energy field is assumed initially, such that the recrystallization front is convected everywhere with a velocity of the same magnitude. A random set of 1000 potential nucleation sites is considered, and a probability of activation of 2.10^{-4} is used at each time step of the simulation. A new activated site is effectively taken into account if it does not belong to the existing recrystallized volume fraction of the domain. Figure 10 illustrates the evolution of the recrystallized volume fraction in white. The computation time is 30 minutes, performed on 8 processors of the cluster described previously. Two hundred time steps were necessary to achieve 100% of recrystallization with an automatic remeshing operation every five time steps and a time step equal to 8.6e-3 s. The anisotropic metric was calculated thanks to equation (31) with $E = 0.04$, $h_d = 0.01$ and $h = 2.66e - 3$. The adopted level set framework, associated with the smoothed definition of the interface velocities, and automatic adapted remeshing operations, is shown here to systematically avoid kinematic incompatibilities (no development of vacuum or overlapping regions [23]). Furthermore, the approach is very effective and natural in the modelling of nucleation events. Comparison can be made with the JMAK theory [6,37,38] predicting the recrystallized volume fraction X as a function of the annealing time t using equation (1). Assuming a two-dimensional growth, the JMAK theory predicts $n=3$ for a low and constant nucleation rate. A linear kinetics refers to a constant value of n; i.e. a linear JMAK plot displaying $\ln[-\ln(1-X)]$ as a function of $\ln(t)$. A least-square regression analysis on the numerical results of Figure 8 was performed, providing $n=2.95$. Figure 9 describes the comparison between the numerical results and the curve obtained by the least-square regression. This result is considered as a validation of our model in 2D.
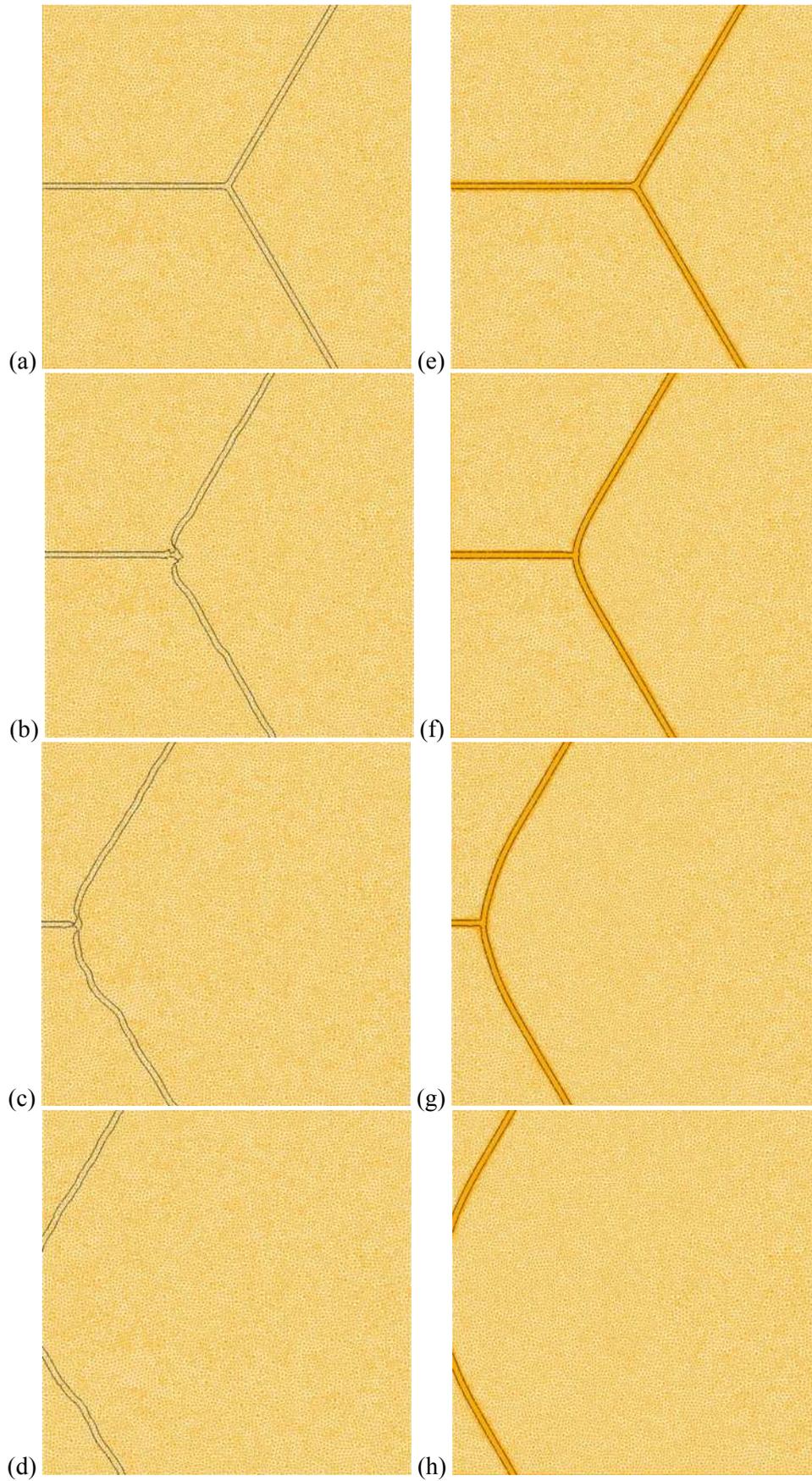
Figure 7. $\pm 5 \cdot 10^{-3}$ isovalues of the three distance functions with isotropic mesh after (a) 0, (b) 120, (c) 300 and (d) 395 time steps and with adapted anisotropic mesh at the grain boundaries (darker orange) after (e) 0, (f) 120, (g) 300 and (h) 395 time steps
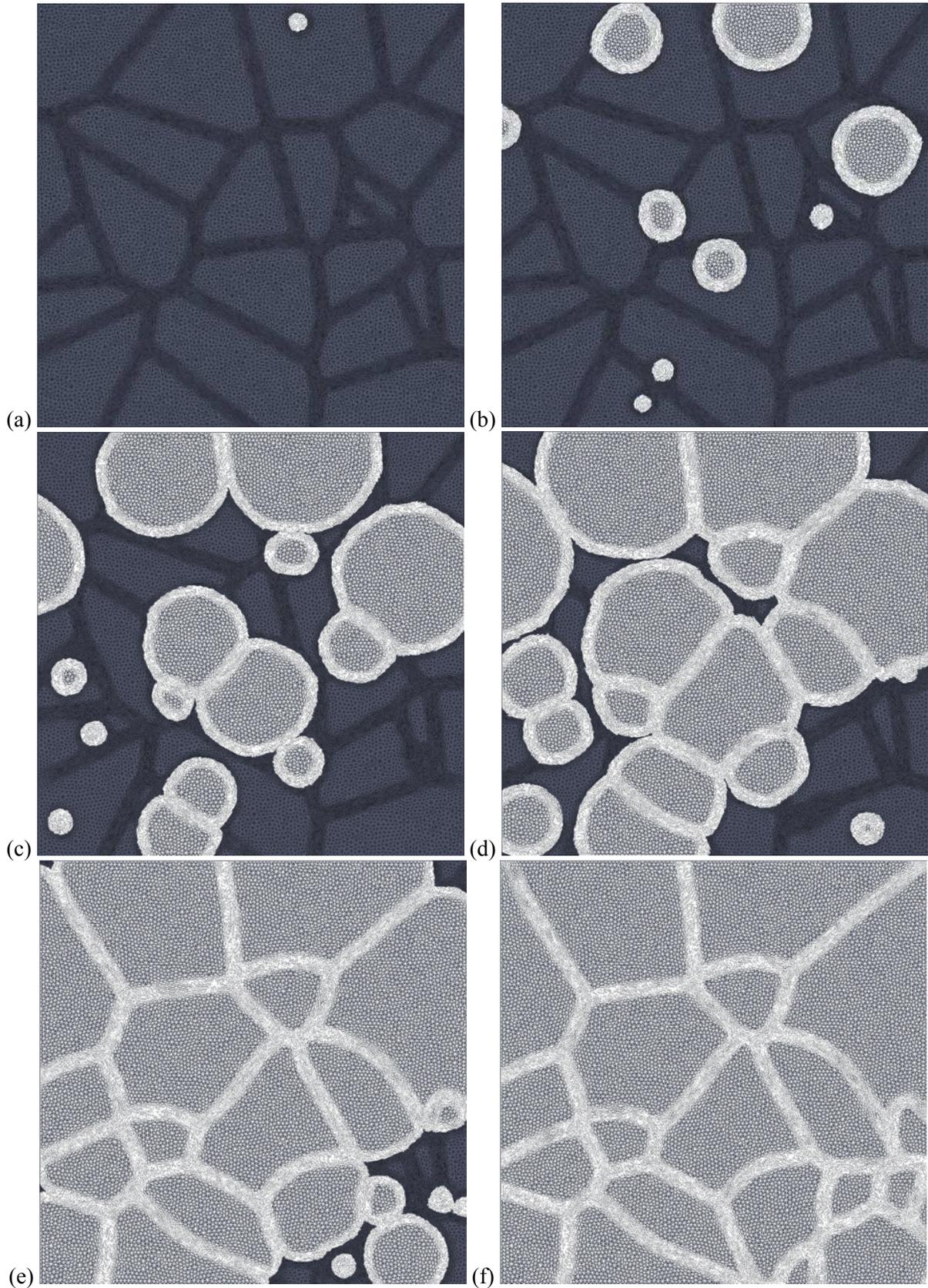
Figure 8. 2D simulation of primary recrystallization with an initial uniform stored energy. Recrystallized part in white corresponding to volume fractions of (a) 1%, (b) 10%, (c) 40%, (d) 60%, (e) 90% and (f) 100%
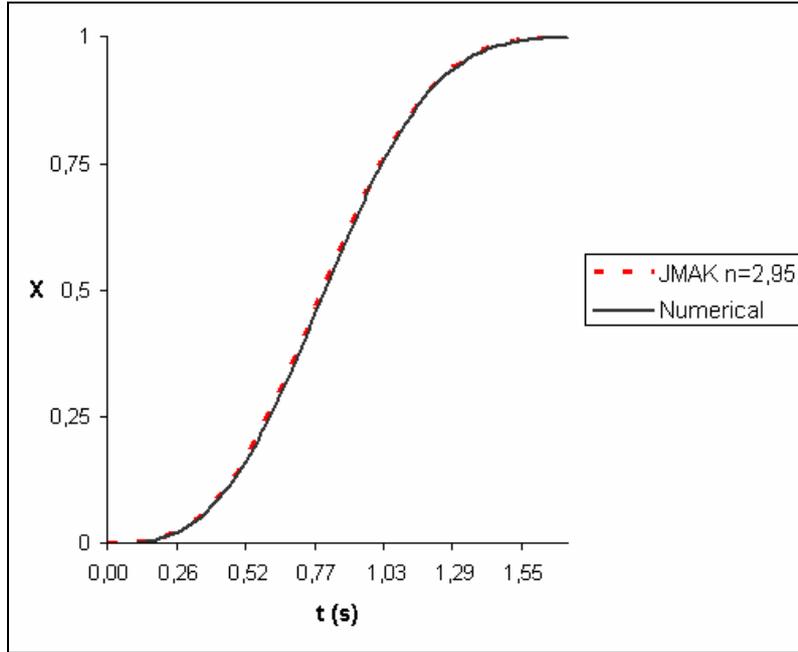
Figure 9. JMAK approximation of the numerical recrystallization kinetics extracted from Figure 8.

5.3 A case with stored energy

A ten grains microstructure in a unit cubic domain is considered, and mechanical testing is performed using finite element simulations where each integration point of the mesh behaves as a single crystal subjected to finite strain increments. The finite element approach is based on a mixed velocity–pressure formulation with an enhanced (P1+/P1) four-node tetrahedral element [39]. Classical theory of crystal plasticity [40,41] is considered, using a slightly modified version of the time integration algorithm developed by Delannay et al. [34,42]. For computational efficiency, one computes rates of lattice rotation and rates of dislocation slip in a decoupled way. The objective of the test case is to analyze the spatial distribution of stored strain energy in a digital aggregate, subjected to large deformations. A channel die test has been chosen. Slip is assumed to operate on the 12 {111}<110> slip systems as is typically considered in fcc crystals at room temperature. For more details, see [34,35]. A 20% reduction in height is applied, and the stored energy is computed from:

$$En = \delta \int \sigma : \nabla \vec{v}\, dt .$$ (34)

with δ the fraction of the strain energy which is stored in the material, considered constant in a first approximation. The stored energy corresponds to defects (dislocations essentially), which represent the driving force for subsequent static recrystallization when performing a heat treatment. Figure 10 illustrates the final stored energy distribution and the corresponding norm of the stored energy gradient $\|\nabla En\|$, together with the adaptive and anisotropic meshing used to model subsequent recrystallization (see section 4 for the meshing strategy). More accurate measures of stored energy could be implemented in the future, by directly relying on dislocation densities computed within the crystal plasticity approach [43].

17
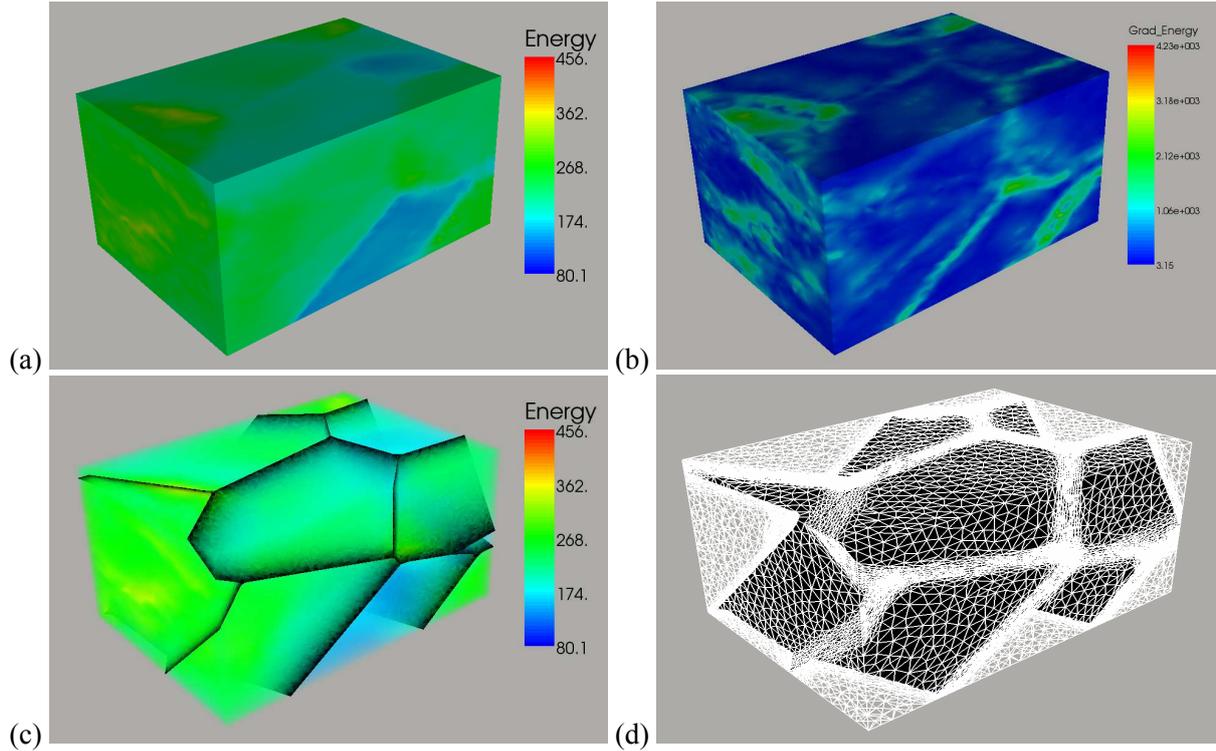
Figure 10. A 3D ten grains microstructure after plastic deformation: (a) external surface view of stored energy, (b) corresponding norm of the stored energy gradient ($\|\nabla En\|$), (c) volumetric view of the stored energy with grain boundaries in black and (d) adaptive and anisotropic meshing in white, grain boundaries in black.

The calculated stored energy field is used as an input to model recrystallization. A normalized average of the stored energy is computed for each grain G_i, and the distribution of $\|\nabla En\|$ is used to define the set of potential nucleation sites. The selection of 1000 potential sites is done by choosing the nodes of the mesh for which $\|\nabla En\|$ is the highest, while considering a safe distance between two neighbouring nuclei equal to 3 times the average element size. As for the previous test case, a probability of activation of 2.10^{-4} is used at each time step, and 1200 time steps were simulated to achieve 100% of recrystallization with a time step equal to 3e-3 s. Figure 11 illustrates the increasing recrystallized volume fractions and the corresponding recrystallized front in blue. The simulation was performed in 6 hours on 16 processors of the cluster described previously and the final microstructure is made of 27 grains. The anisotropic metric was calculated thanks to equation (31) with $E = 0.1$ for the anisotropic thickness, $h_d = 0.05$ and $h = 6.66e - 3$.

Comparisons with the JMAK theory were performed again, and are described in Figure 12. A first simple comparison was done with no consideration of the stored energy field, with a random choice of nucleation sites. A least-square regression analysis on the numerical results provided a JMAK exponent n=3.91 (Figure 12(a)), while the theoretical value is n=4 in 3D. This result validates our method in 3D. The second case, illustrated by Figure 12(b), corresponds to the numerical recrystallization kinetics of the numerical simulation described by Figure 11. Interestingly, in this case, a single value of n does not allow fitting the numerical results with sufficient accuracy. This result must be placed in the context of repeated discussions in the literature on the reasons of deviations from the standard JMAK theory. Heterogeneous distribution of stored energy [44], and, spatial and time distribution of nuclei [45] can explained these deviations. These can be studied in details with the present level-set model.

18
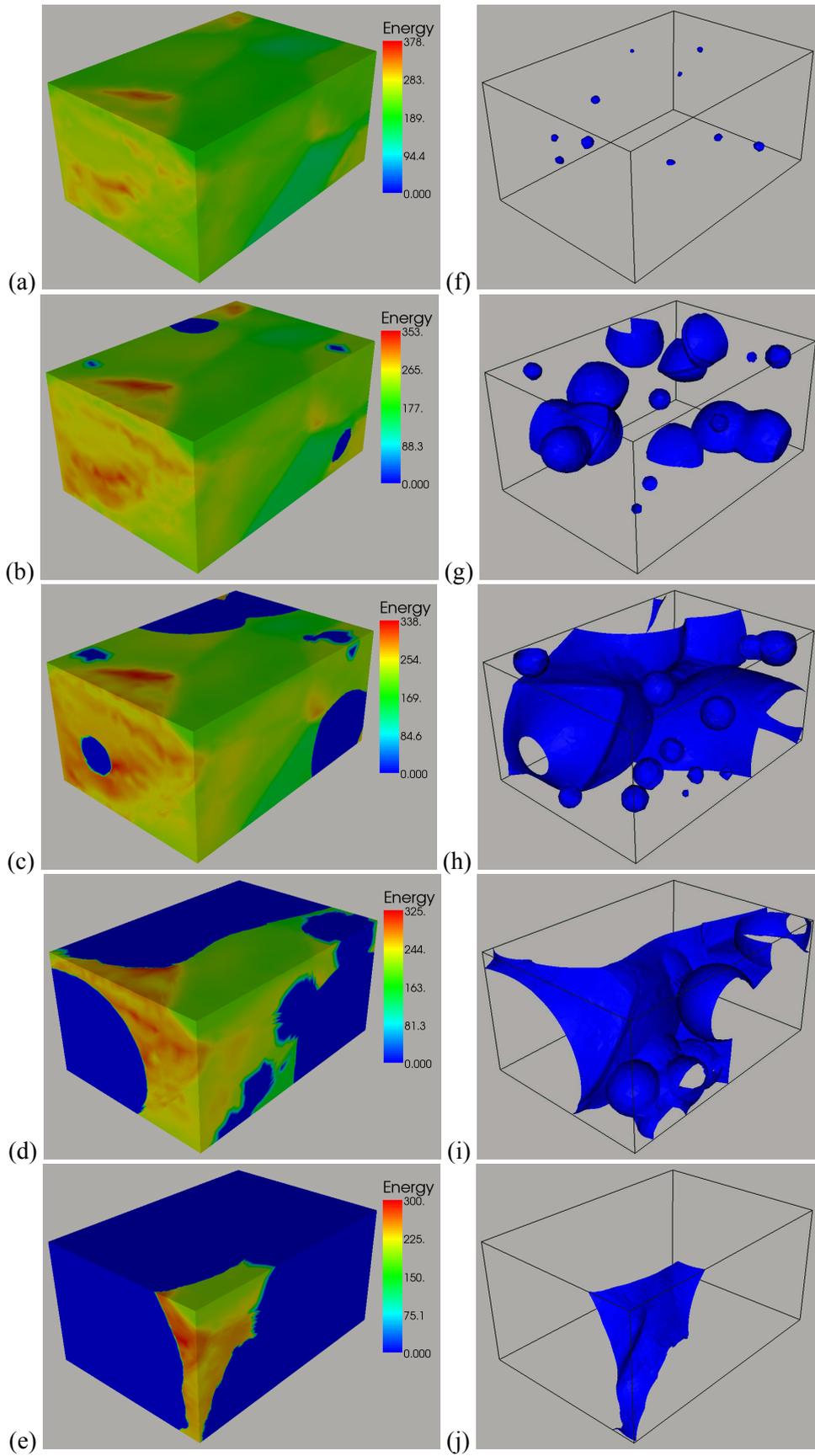
Figure 11. 3D recrystallization with a non uniform initial stored energy field: external surface view of the stored energy for recrystallized volume fractions of (a) 1%, (b) 15%, (c) 58%, (d) 80%, (e) 95%, and corresponding recrystallized front in blue (f-j).

(a)

(b)
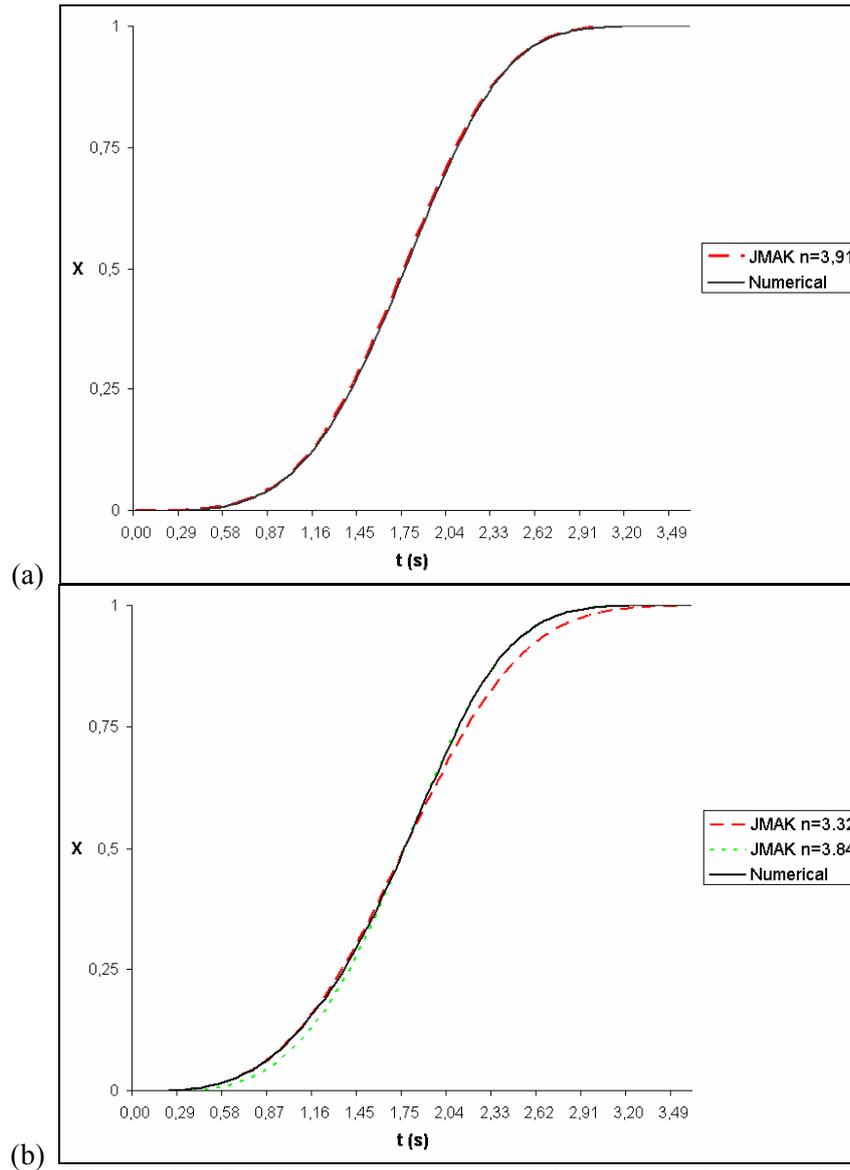
Figure 12. JMAK approximations of the numerical recrystallization kinetics extracted from Figure 11: (a) random choice of nucleation sites, low and constant nucleation rate of 2.10^{-4}; (b) considering the non uniform stored energy field and choosing nucleation sites at highest values of $\left\|\nabla En\right\|$.

6. Conclusion

It has been shown that a finite element model associated to a level set framework, using adaptive anisotropic automatic remeshing, is a promising tool to describe primary recrystallization in a polycrystalline material. A special smoothing algorithm is applied to the calculated velocity field, which allows avoiding the appearance of vacuum or overlapping regions. The method allows efficient and natural modelling of nucleation phenomena. On going work is currently addressing:

- The modelling of primary recrystallization with stored energy due to prior deformation steps, modelled with crystal plasticity and 3D aggregates composed of a statistical number of grains.
- Comparisons with experiments and other models, like the Monte-Carlo or phase field methods.

- The respective influences of initial microstructure topology, stored energy field, and local crystallographic orientations, on the nucleation and growth kinetics involved in static recrystallization.
- The extension of the method to model grain growth and discontinuous dynamic recrystallization.

References

[1] Rollett A D 1997 Overview of modeling and simulation of recrystallization *Progress in Mat. Sci*. **42** 79-99

[2] Kugler G and Turk R 2006 Study of the influence of initial microstructure topology on the kinetics of static recrystallization using a cellular automata model *Comp. Mat. Sc.* **37** 284-291

[3] Bernacki M Chastel Y Digonnet H Resk H Coupez T and Logé R E 2007 Development of numerical tools for the multiscale modelling of recrystallization in metals, based on a digital material framework *Comp. Met. in Mat. Sc.* **7** 142-149

[4] Logé R E Bernacki M Resk H Digonnet H and Coupez T 2007 Numerical modelling of plastic deformation and subsequent recrystallization in polycristalline materials, based on a digital material framework *Recrystallization and Grain Growth III proceedings* Korea 1133-1138

[5] Bernacki M Chastel Y Coupez T and Logé R E 2008 Level set method for the numerical modelling of primary recrystallization in the polycrystalline materials *Scripta. Mater.* **58** 1129-1132

[6] Raabe D 1999 Introduction of a scaleable 3D cellular automaton with a probabilistic switching rule for the discrete mesoscale simulation of recrystallization phenomena *Phil. Mag. A* **79** 2339-2358

[7] Miodownik M A 2002 A review of microstructural computer models used to simulate grain growth and recrystallisation in aluminium alloys *J. Light Metals* **2** 125-135

[8] Vandermeer R A and Rath B B 1989 Modeling recrystallization kinetics in a deformed iron single crystal *Metall.Trans.* **20A** 391-401

[9] Mahin K W Hanson K and Morris J W 1980 Comparative analysis of the cellular and Johnson-Mehl microstructures through computer simulation *Acta Metall.* **28** 443-453

[10] Rollett A D and Raabe D 2001 A hybrid model for mesoscopic simulation of recrystallization *Comp. Mat. Sc.* **21** 69-78

[11] Hassold G N and Holm E A 1993 A fast serial algorithm for the finite temperature quenched Potts model *J. Comput. Phys.* **7** 97-107

[12] Nagai T Ohta S Kawasaki K and Okuzono T 1990 Computer simulation of cellular pattern growth in two and three dimensions *Phase Trans.* **28** 177-211

[13] Piekos K Tarasiuk J Wierzbanowski K and Bacroix B 2007 Generalized vertex model-Study of Recrystallization in copper *Recrystallization and grain growth III proceedings* Korea 1157-1162

[14] Maurice C 2001 2- and 3-d curvature driven vertex simulations of grain growth *Recrystallization and grain growth proceedings* Berlin 123-134

[15] Weygand D Brechet Y and Lepinoux J 2001 A vertex simulation of grain growth in 2D and 3D *Adv. Engng. Mater.* **3** 67-71

[16] Chen L Q 1995 A novel computer simulation technique for modeling grain growth *Scripta Metall. Mater.* **32** 115-120

[17] Zhao H K Chan T Merriman B and Osher S 1996 A variational level set approach to multiphase motion *J. Comp. Phys.* **127** 179-195

[18] Collins J B and Levine H 1985 Diffuse interface model of diffusion-limited crystal growth *Phys. Rev.* **B31** 6119-6122

[19] Chen L Q 2002 Phase-field models for microstructure evolution *Ann. Rev. Mater. Res.* **32** 113-140

[20] Karma A 2001 Phase-field formulation for quantitative modelling of alloy solidification *Phys. Rev. Letters 8711* **115701**

[21] Takaki T Yamanaka A Higa Y and Tomita Y 2008 Phase-field model during static recrystallization based on crystal-plasticity theory *J. Comp.-Aided Mater. Des.* **14** 75-84

[22] Humphreys F J and Haterly M 1995 Recrystallization and related annealing phenomena *Oxford: Pergamon Press*

[23] Kugler G and Turk R 2004 Modeling the dynamic recrystallization under multi-stage hot deformation, *Acta Mat.* **52** 4659-4668

[24] Taylor J E 1995 The motion of multiple-phase junctions under prescribed phase-boundary velocities *J. Differ. Eq.* **119** 109-136

[25] Merriman B Bence J and Osher S J 1994 Motion of Multiple Junctions: A Level Set Approach *J. Comp. Phys.* **112** 334-363

[26] Reitich F and Soner H M 1996 Three-phase boundary motions under constant velocities. I: The vanishing surface tension limit *Proc. of the Roy. Soc. of Edinburgh* **126A** 837-865

[27] Sethian J A 1996 Level Set methods *Cambridge University Press*

[28] Osher S and Sethian J A 1988 Fronts propagating with curvature-dependent speed: Algorithms based on Hamilton-Jacobi formulations *J. Comp. Phys.* **79** 12-49

[29] Sussman M Smereka P and Osher S 1994 A Level Set Approach for Computing Solutions to Incompressible Two-Phase Flow *J. Comp. Phys.* **114** 146-159

[30] Dawson P R 2000 Computational crystal plasticity *Int. J. Solids Struct.* **37** 115-130

[31] Dawson P R Miller M P Han T S and Bernier J 2005 An Accelerated Methodology for the Evaluation of Critical Properties in Polyphase Alloys *Metall. Mater. Trans. A* **36** 1627-1641

[32] Logé R E and Chastel Y 2006 Coupling the thermal and mechanical fields to metallurgical evolutions within a finite element description of a forming process *Comp. Meth. in Appl. Mech. and Eng.* **195** 6843-6857

[33] Coupez T 2007 Convection of local level set function for moving surfaces and interfaces in moving flow *NUNIFORM'07 proceedings* Plenary lecture 61-66

[34] Logé R Bernacki M Resk H Delannay L Digonnet H Chastel Y and Coupez T 2008 Linking plastic deformation to recrystallization in metals using digital microstructures *Phil. Mag.* **88** 3691-3712

[35] Resk H Delannay L Bernacki M Coupez T and Logé R Adaptive mesh refinement and automatic remeshing in crystal plasticity finite element simulations *to appear in Modelling and Simulation in Materials Science and Engineering*

[36] Coupez T Digonnet H and Ducloux R 2000 Parallel meshing and remeshing by repartitioning *Appl. Math. Modeling* **25** 153-175

[37] Johnson W A and Mehl R F 1939 Reaction kinetics in processes of nucleation and growth *Trans. Am. Inst. Miner. Eng.* **135** 416-458

[38] Avrami M 1939 Kinetics of Phase Change. I. General Theory *J. Chem. Phys.* **7** 1103-1112

[39] Mocellin K Fourment L Coupez T and Chenot J-L 2001 Toward large scale F.E. computation of hot forging process using iterative solvers, parallel computation and multigrid algorithms *Int. J. Num. Methods. Eng.* **2** 473-488

[40] Kalidindi S R Bronkhorst C A and Anand L 1992 Crystallographic evolution in bulk deformation processing of FCC metals *J. Mech. Phys. Solids* **40** 537-569

[41] Marin E B and Dawson P R 1998 Elastoplastic finite element analyses of metal deformations using polycrystal constitutive models *Comput. Meth. Appl. Mech. Eng.* **165** 23-41

[42] Delannay L Jacques P J and Kalidindi S R 2006 Finite element modeling of crystal plasticity with grains shaped as truncated octahedrons *Int. J. Plast.* **22** 1879-1898

[43] Baudin T Etter A L Gerber P Samet A Penelle R and Rey C 2005 Influence of thermo-mechanical treatments on the stored energy simulated by FEM for two low carbon steels *Mater. Sci. Forum* **495/497** 1291-1296

[44] Oyarzabal M Matrinez-de-Guerenu A and Gutierrez I 2008 Effect of stored energy and recovery on the overall recrystallization kinetics of a cold rolled low carbon steel *Mater. Sci. Eng. A* **485** 200-209

[45] Liu F and Yang G 2007 Effects of anisotropic growth on the deviations from Johnson–Mehl–Avrami kinetics *Acta Mater.* **55** 1629-1639

Appendix C

Stress and strain heterogeneities for different HEM approximations (chapter 6)
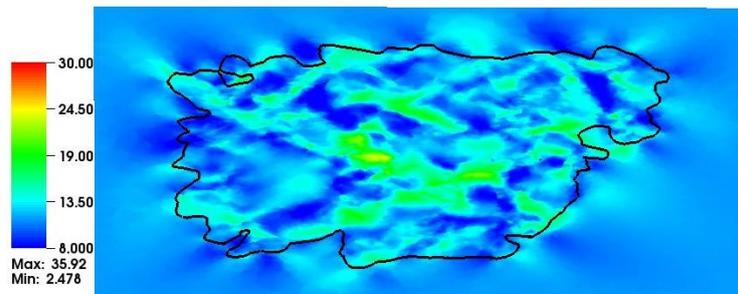
(a) HEM$_{129}$ after $\boldsymbol{\varepsilon} = 0.4$
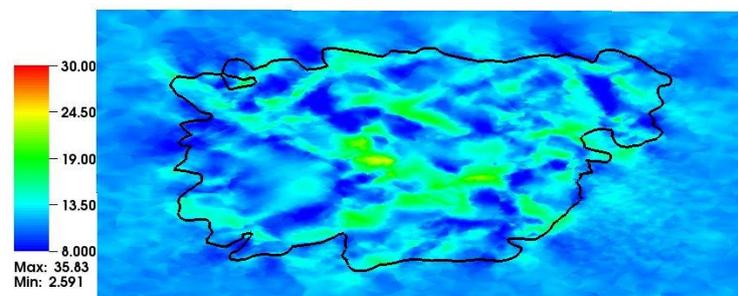
(b) HEM$_{10}$ after $\boldsymbol{\varepsilon} = 0.4$
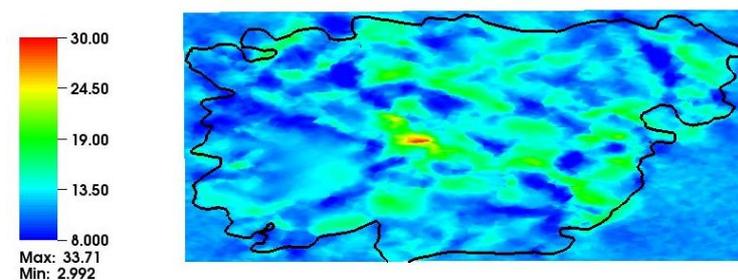
(c) Slice after $\boldsymbol{\varepsilon} = 0.4$

Fig. C.1: Energy distribution
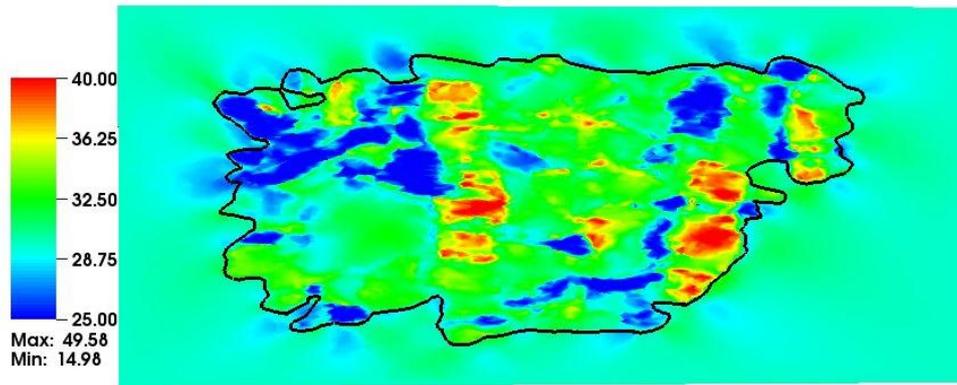
(a) HEM$_{129}$ after $\boldsymbol{\varepsilon} = 0.4$
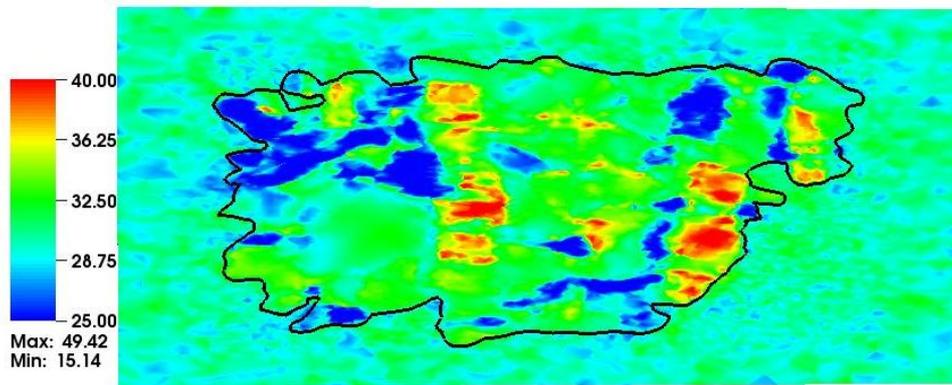
(b) HEM$_{10}$ after $\boldsymbol{\varepsilon} = 0.4$
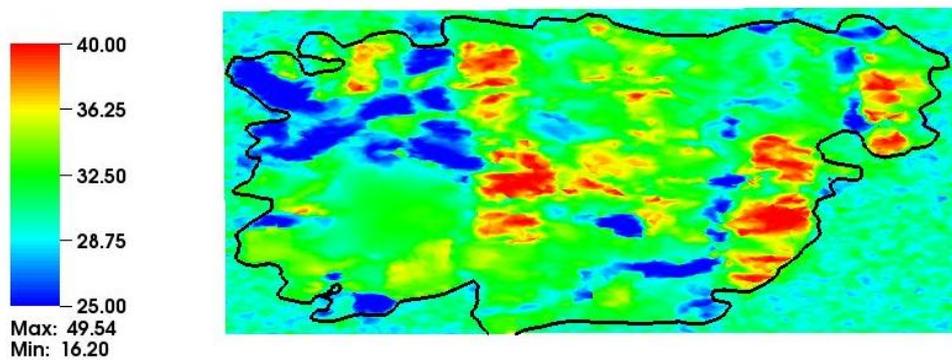
(c) Slice after $\boldsymbol{\varepsilon} = 0.4$

Fig. C.2: Equivalent stress
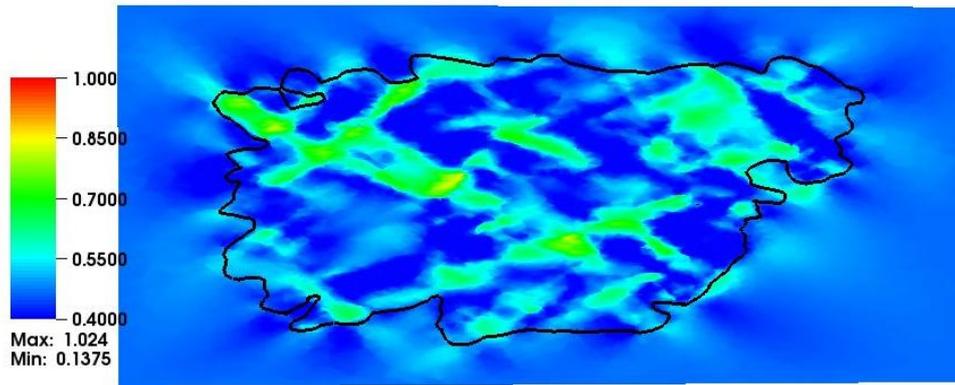
(a) HEM$_{129}$ after $\boldsymbol{\varepsilon} = 0.4$
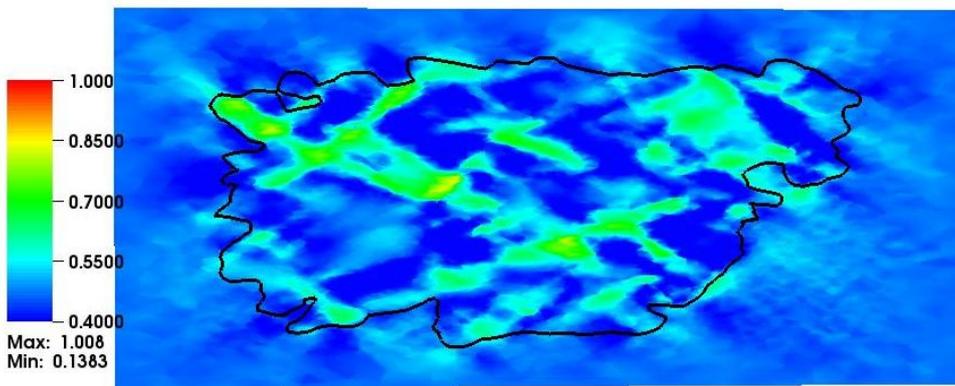
(b) HEM$_{10}$ after $\boldsymbol{\varepsilon} = 0.4$
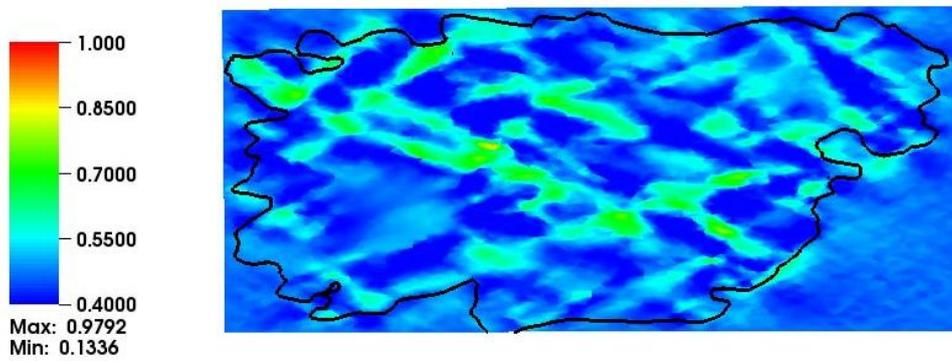
(c) Slice after $\boldsymbol{\varepsilon} = 0.4$

Fig. C.3: Equivalent strain
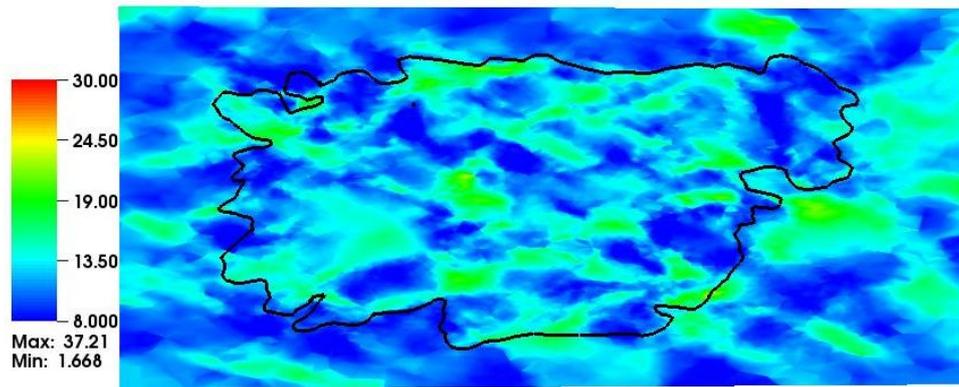
(a) HEM$_{Voronoi}$ after $\varepsilon = 0.4$
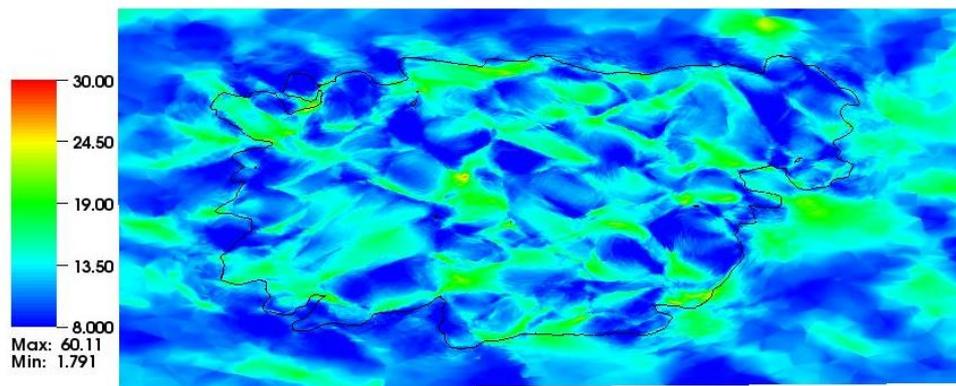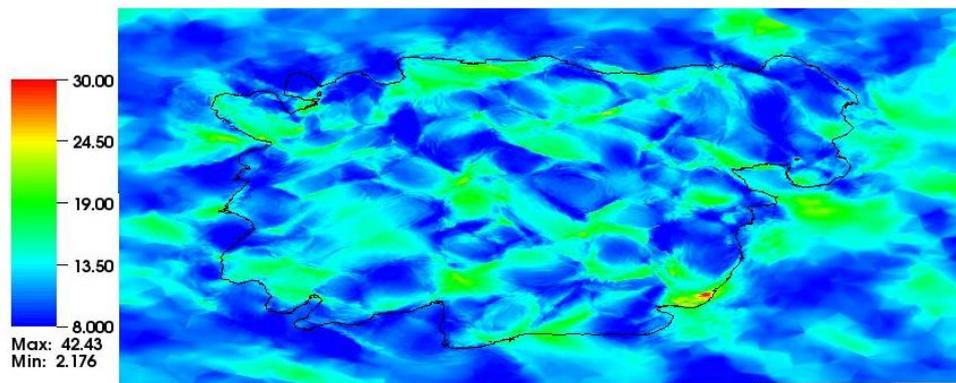
(b) Columnar after $\varepsilon = 0.4$

(c) Non-columnar after $\varepsilon = 0.4$

Fig. C.4: Energy distribution
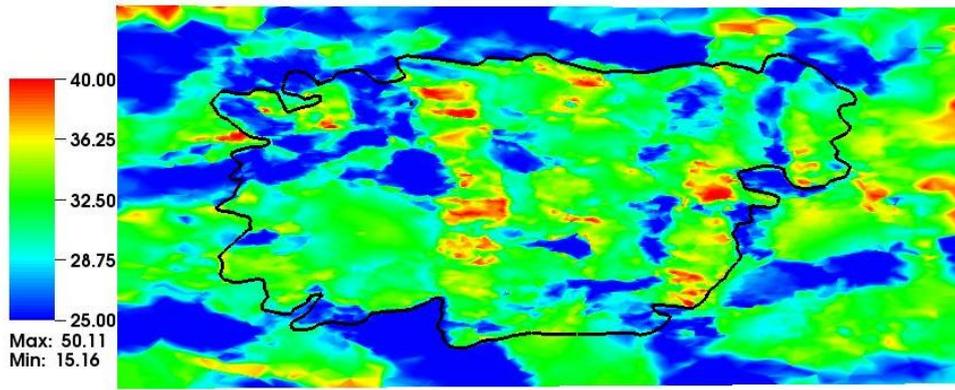
(a) HEM$_{Voronoi}$ after $\boldsymbol{\varepsilon} = 0.4$
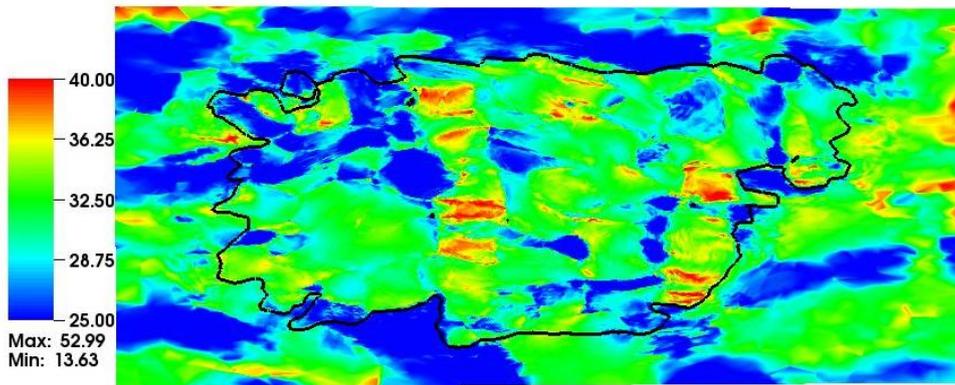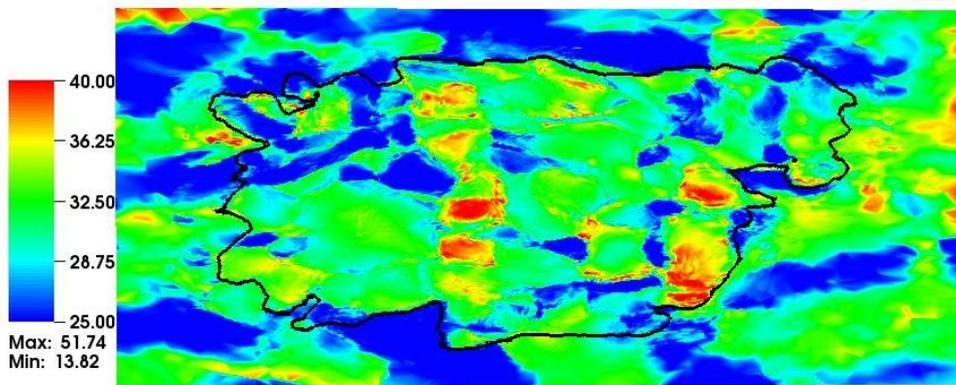
(b) Columnar after $\boldsymbol{\varepsilon} = 0.4$

(c) Non-columnar after $\boldsymbol{\varepsilon} = 0.4$

Fig. C.5: Equivalent stress distribution
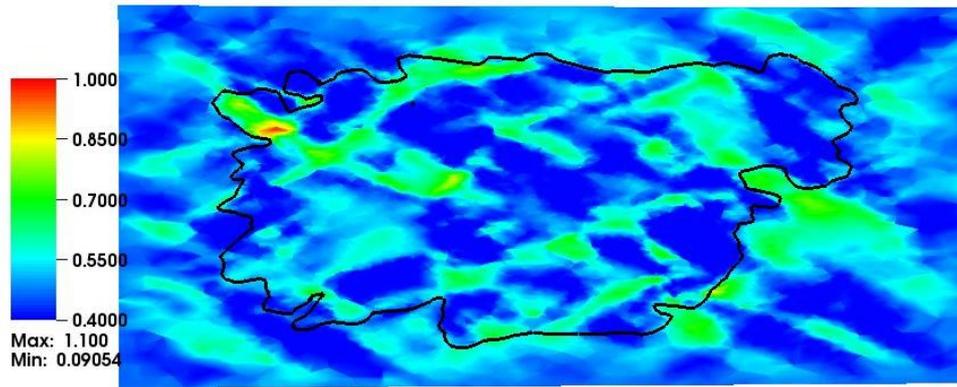
(a) HEM$_{Voronoi}$ after $\boldsymbol{\varepsilon} = 0.4$
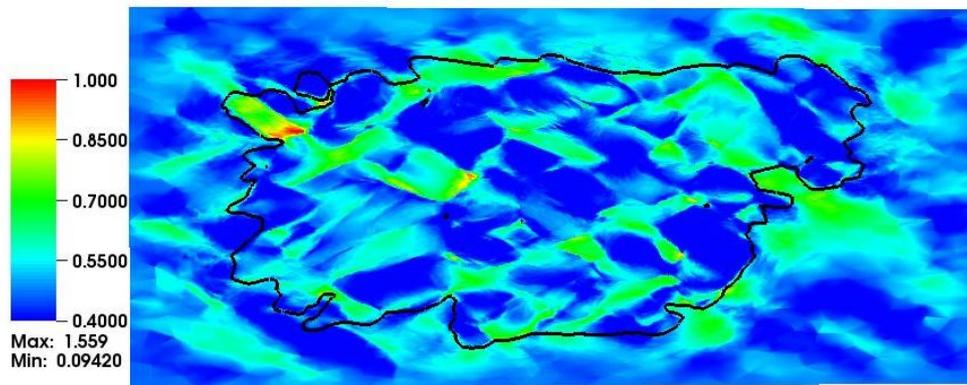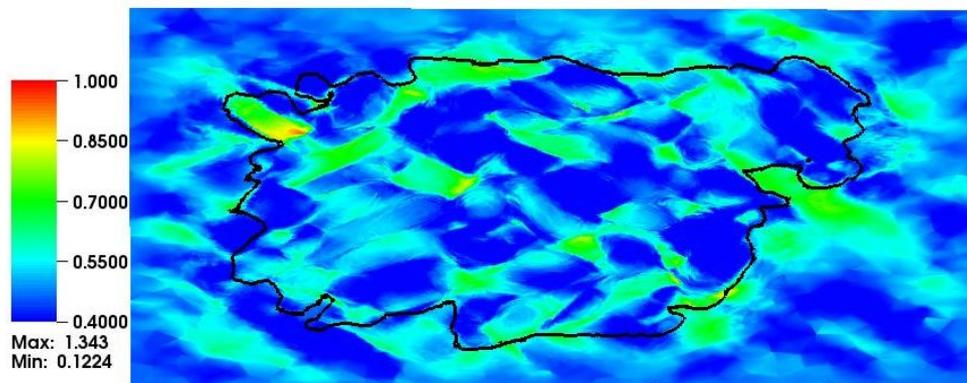
(b) Columnar after $\boldsymbol{\varepsilon} = 0.4$

(c) Non-columnar after $\boldsymbol{\varepsilon} = 0.4$

Fig. C.6: Equivalent strain distribution

235

Appendix D

OIM maps for the experimental microstructure (chapter 6)

(a) Grain 1   (b) Grain 2   (c) Grain 3   (d) Grain 4

(e) Grain 5   (f) Grain 6   (g) Grain 7   (h) Grain 8

(i) Grain 9   (j) Grain 10
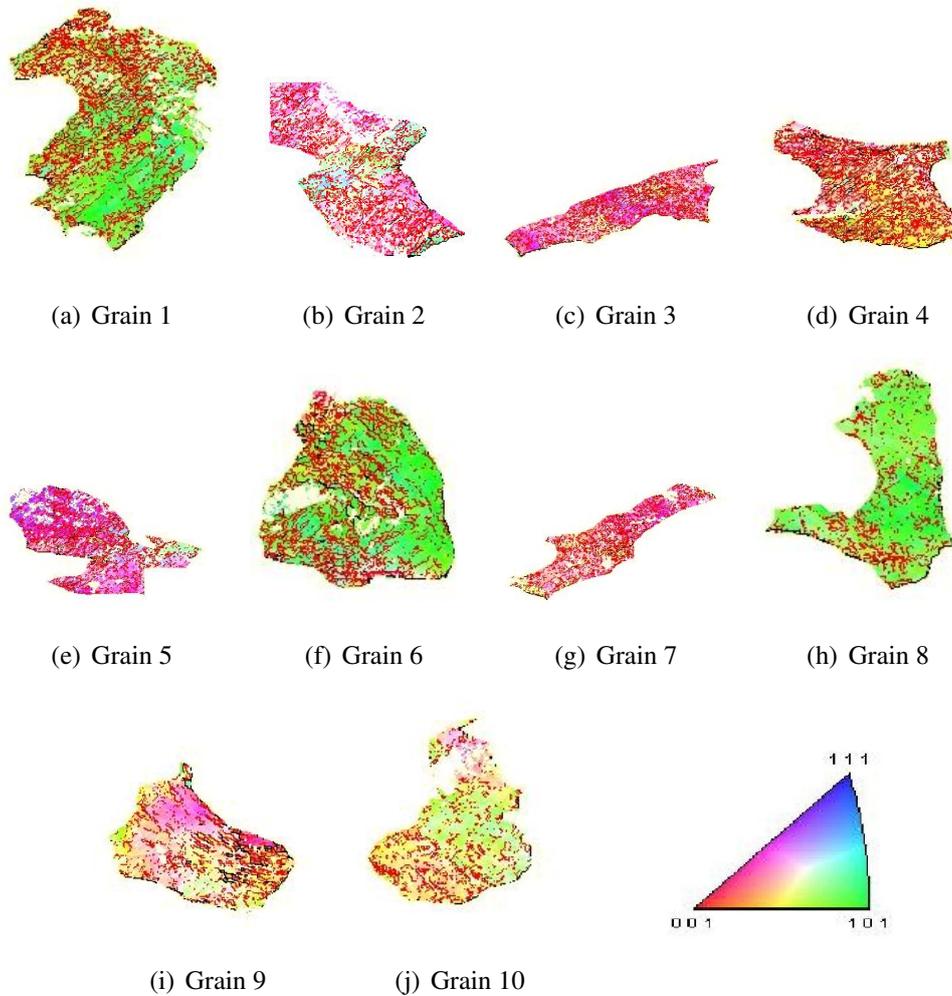
Fig. D.1: Experimental inverse pole figure (IPF) maps for sample normal axis for the first ten grains of the experimental microstructure in chapter 6. Black and red segments represent high angle (>15°) and low angle grain boundaries respectively (> 5°).

Finite element modelling of grain-scale heterogeneities in polycrystalline aggregates

Abstract: Macroscopic properties of crystalline solids depend inherently on their underlying microscopic structure. Studying the mechanisms operating at the microstructural scale during the various thermomechanical processes to which such materials may be subjected offers a valuable insight into their final in-use properties. The objective of this work is to investigate grain scale heterogeneities in polycrystalline aggregates subjected to large strains using the Crystal Plasticity Finite Element Method (CPFEM). For this purpose, highly resolved simulations, where each grain is represented explicitly, are needed. The first part of this work is devoted to a detailed account of the numerical framework implemented for such simulations. A classical elastic-viscoplastic crystal plasticity model is combined to a non-linear parallel finite element framework. The discretization of the digital microstructures is performed using non-conforming unstructured meshes. Most importantly, a level set approach is used to describe grain boundaries and to guide an adaptive anisotropic meshing strategy. Automatic remeshing, with appropriate transport of variables, is introduced in the proposed framework. In the second part of this work, the robustness and flexibility of our approach is demonstrated via different CPFEM applications. The deformation energy is used to assess heterogeneities in polycrystalline aggregates, highlighting the need to perform adaptive meshing so as to achieve a good compromise between accuracy and computation time. These grain-scale heterogeneities are to be accurately predicted during the deformation simulation if subsequent static recrystallization modelling is to be performed. An example of linking between the deformation and static recrystallization steps, using the proposed common approach, is illustrated. In terms of global texture predictions, the CPFEM framework is validated for a highly resolved model polycrystal subjected to more than 90 % thickness reduction in rolling. The importance of automatic remeshing in avoiding excessive mesh distortion, in such applications, is demonstrated. Most importantly, microtexture analysis is performed on digital microstructures that correspond, in a discrete sense, to an actual microstructure observed experimentally. Intragranular misorientation predictions and virtual 2D orientation maps are compared to the experimental ones, highlighting the difficulties pertaining to the validation of such grain-scale predictions.

Modélisation par Éléments Finis des hétérogénéités à l'échelle granulaire au sein d'agrégats polycristallins

Résumé : Les matériaux cristallins, notamment métalliques, sont des matériaux hétérogènes. Leurs propriétés macroscopiques sont fondamentalement déterminées par leurs caractéristiques micro-structurales. L'étude des mécanismes opérant à l'échelle du grain permet de mieux comprendre et ainsi mieux contrôler les caractéristiques des pièces fabriquées afin de réduire leur coût et optimiser leur performance. Cette thèse s'inscrit dans le cadre de la méthode dite "CPFEM" qui couple la plasticité cristalline à la méthode des Éléments finis (EF). L'objectif de ce travail est d'étudier les hétérogénéités à l'échelle du grain au sein d'agrégats polycristallins soumis à de grandes déformations. Pour ce faire, une représentation explicite de la microstructure est nécessaire. Le travail réalisé, ainsi que ce manuscrit, s'articule autour de deux axes principaux : Dans le chapitre 2, le comportement du matériau est modélisé par une loi élastoviscoplastique cristalline, qui ne prend cependant pas en compte le développement d'une sous-structure dans sa formulation. Cette loi est couplée à une formulation EF mixte en vitesse pression. L'approche EF, détaillée dans le chapitre 3, peut être considérée comme le modèle polycristallin idéal vu le respect, au sens numérique faible, de l'équilibre des contraintes et la compatibilité des déformations. Dans le chapitre 4, l'approche utilisée pour construire, représenter et discrétiser un volume polycristallin est détaillée. La microstructure est représentée, soit par des polyèdres de Voronoi, soit par des voxels, si elle est construite à partir de données expérimentales. L'agrégat polycristallin est discrétisé avec une approche "monolithique", où un seul maillage, non structuré et non-conforme aux interfaces entre les grains, est utilisé. Une approche level set permet alors de décrire l'interface entre les grains de façon implicite et sert de base pour la construction d'un maillage adaptatif anisotrope. Le remaillage, avec un transport approprié des variables du problème, se fait de façon naturelle et automatique si la carte de métrique, associée au maillage, est calculée avant la procédure de remaillage. Dans le chapitre 5, les hétérogénéités inter- et intragranulaire sont appréhendées à travers une étude de la distribution d'une fraction de l'énergie de déformation. Cette fraction est considérée, dans une première approche, comme étant représentative de l'énergie stockée durant la déformation. Une analyse de sensibilité, au degré et au type de maillage utilisé, permet de mettre en évidence l'apport d'une stratégie de maillage anisotrope. Ces données locales sont particulièrement importantes à calculer lors de la déformation d'agrégats polycrystallins si l'objectif est de modéliser le phénomène de recristallisation statique qui suit l'étape de déformation. Un cas test 3D permet d'illustrer le chaînage de la simulation de la déformation et de la recristallisation, toutes deux réalisées dans le même cadre numérique. Dans le chapitre 6, notre approche numérique est, dans un premier temps, validée à l'aide d'un cas test de laminage pour un polycrystal statistiquement représentatif d'une texture expérimentale. Une réduction d'épaisseur de plus de 90 % est réalisée. Le remaillage, dans ce type d'application, s'avère plus que nécessaire. Dans la seconde partie de ce chapitre, une étude approfondie de la microtexture, développée au sein de microstructures virtuelles, est effectuée. Dans ce cas, ces microstructures "digitales" correspondent à une microstructure réelle dans un sens discret. Les prédictions de désorientations, d'orientations cristallographiques moyennes ainsi que les cartes d'orientation 2D virtuelles, sont comparés à l'expérience à l'échelle de chaque grain, mettant ainsi en évidence les facteurs à l'origine de certaines des différences observées.

Mots clés : Plasticité Cristalline, Éléments Finis, Grandes Déformations, Level Set, Remaillage, Microtexture, Macrotexture, Recristallisation, Calcul Parallèle